Instituto de Ciencia de Materiales de Sevilla
(Centro Mixto CSIC-Universidad de Sevilla)

TESIS DOCTORAL

PROPIEDADES FOTOFUNCIONALES DE NANOESTRUCTURAS SUPERFICIALES DE ÓXIDOS PREPARADAS MEDIANTE PLASMA Y HACES DE IONES

PABLO ROMERO GÓMEZ

SEVILLA 2011

PROPIEDADES FOTOFUNCIONALES DE NANOESTRUCTURAS SUPERFICIALES DE ÓXIDOS PREPARADAS MEDIANTE PLASMA Y HACES DE IONES

Memoria para optar al grado

de Doctor por la Universidad de Sevilla

Sevilla, Febrero 2011

Fdo. Pablo Romero Gómez

Director de la Tesis Doctoral:

Dr. Agustín Rodríguez González-Elipe
Profesor de Investigación del CSIC
Isnt. De Ciencia de Materiales de Sevilla

Tutora de la Tesis Doctoral:

Dra Adela Muñoz Páez
Catedrática de Química Inorgánica
Universidad de Sevilla

A mis padres

A Esther, Carlos, Daniel y Euge.

Esta tesis ha sido realizada en el Instituto de Ciencia de Materiales de Sevilla (CSIC-US) dentro del grupo "Superficies, Intercaras y Láminas Delgadas", bajo la dirección del Prof. Agustín R. González-Elipe.

Este trabajo de tesis ha dado lugar a las siguientes publicaciones:

- "*Surface nanostructuring of TiO_2 thin films by high energy ionirradiation*" **Romero-Gomez, P**.; Palmero, A.; Ben, T.; Lozano, J. G.; Molina, S. I.; González-Elipe, A. R., *Physical Review B 82, 2010, 115420.*
- "*Plasma Deposition of N-TiO_2 Thin Film*". **Pablo Romero-Gomez**, Angel Barranco, José Cotrino, Juan P. Espinós, Francisco Yubero, Agustín R. Gonzalez-Elipe.capítulo publicado en el libro "Industrial Plasma Technology". Editores: Y.Kawai, H.Ikegami,N.Sato, A. Matsuda, K. Uchino, M. Kuzuya, A. Mizuno WILEY-VCH, Weinheim, Alemania, 2010, pags. 349-355.
- "*Band gap narrowing vs. formation of electronic states in the gap in N-TiO_2 thin films*" **P. Romero- Gómez**, Said Hamad , J.C. González, A. Barranco, J.P. Espinós, J. Cotrino1, A.R. González-Elipe. *J. Phys. Chem. C*, 2010, Article ASAP (DOI: 10.1021/jp104634j).
- "*Chemical State of Nitrogen and Visible Surface and Schottky Barrier Driven Photoactivities of N-Doped TiO_2 Thin Films*" **P. Romero- Gómez**; V. Rico; A. Borrás; A. Barranco; J. P. Espinós; J. Cotrino; and A. R. González-Elipe. *J. Phys. Chem. C* 2009, 113, 13341–13351.
- "*Enhanced Schottky-barrier Photoactivity in bilayer films with buried Rutile-*Anatase heterojunctions" **Romero-Gomez P**.; Borras A.; Barranco A.; Espinos J.P.; Gonzalez-Elipe, ChemPhysChem, 2010 (DOI: 10.1002/cphc.201000734)
- "*Tunable Nanostructure and Photoluminescence of Columnar ZnO Films Grown by Plasma Deposition*" **Romero-Gomez, P**.; Toudert, J.; Sanchez-Valencia, J.; Borras, A.; Gonzalez-Elipe, A.; Barranco, A., *J. Phys. Chem. C*, 2010, 114 (49), pp 20932–20940.

Otros trabajos publicados durante el transcurso de esta tesis:

- "*Surface nanostructuring of TiO_2 thin films by ion beam irradiation*" **P. Romero-Gomez**, A. Palmero, F. Yubero, M. Vinnichenko, A. Kolitsch and A.R. Gonzalez-Elipe. *Scripta Materialia* 2009,60,574-577.
- "*Wetting angles and photocatalytic activities of illuminated TiO_2 thin films*". V. Rico, **P. Romero**, J.L. Hueso, J.P. Espinós, A.R. Gonzalez-Elipe. Catalysis Today 143, 2009, 347‑354.
- "*Improved Non-Covalent Biofunctionalization of Multi-Walled Carbon Nanotubes Using Carbohydrate Amphiphiles with a Butterfly-Like Polyaromatic Tail*" Mohyeddin Assali, Manuel Pernía Leal, Inmaculada Fernández, **Pablo Romero-Gomez**, Rachid Baati, and Noureddine Khiar, *Nano Res.*3, 2010, 764–778.
- "*Tilt angle control of nanocolumns grown by glancing angle sputtering at variable argon pressures*" J. M. García-Martín, R. Alvarez, **P. Romero-Gómez**, A. Cebollada, and A. Palmero. *Appl. Phys. lett* 97, 2010, 173103
- *"On the microstructure of thin films grown by an isotropically directed deposition flux*" R. Alvarez, **P. Romero-Gomez**, J. Gil-Rostra, J. Cotrino, F. Yubero, A. Palmero and A. R. Gonzalez-Elipe. *J. Appl. Phys*. 108, 2010, 064316.
- "*Supported plasma-made 1D heterostructures: perspectives and applications*" Ana Isabel Borras, Manuel Macias-Montero, **Pablo Romero-Gomez** and Agustin Rodriguez Gonzalez-Elipe. *J. Phys. D: Appl. Phys*. 43 (2010).

AGRADECIMIENTOS

Antes de empezar la descripción de esta memoria de tesis me gustaría expresar mi más sincero agradecimiento a todas aquellas personas que han contribuido a la realización de esta tesis, tanto científicamente como personalmente, es decir, a mis maestros, compañeros y amigos.

Todos ellos han colaborado de una forma u otra al resultado final de este trabajo. Este es el momento de agradeceros todo lo aprendido y vivido.

Al **Prof. Agustín R. González-Elipe**, director de esta tesis, le agradezco casi todo lo que he aprendido. Gracias por tu apoyo incondicional y por haberme empujado con tanto ímpetu. Sinceramente, ¡te estaré eternamente agradecido!

Al **Dr. Alberto Palmero Acebedo** por haberle ampliado los márgenes a esta tesis, además de haber sido un gran compañero en el transcurso de la misma. ¡Muchas gracias! Para mí has sido mi codirector de la tesis.

Para realizar un trabajo de investigación en un campo tan multidisciplinar como es el caso de esta tesis, creo que es necesaria la colaboración constante con expertos en los diferentes ámbitos. Por ello, quiero agradecer a los doctores Said Hamad Gómez, Angel Barranco, Víctor Rico, José Cotrino, Ana Borras, Johann Toudert, Teresa Ben, Francisco Yubero, Juan Carlos González, Mycola Vinnichenko y al Prof. Juan Pedro Espinós por su ayuda científico-técnica. Especialmente quiero agradecerles al **Dr. Johann Tourdet**, a la **Dra. Ana Borras**, pero sobre todo, al **Prof. Juan Pedro Espinos** su papel fundamental en la investigación realizada. Otros doctores que me han ayudado a lo largo de la tesis son los doctores Leopoldo, Adela, Ángel Justo, Hernán Míguez y Juan Carlos Sánchez (algún día te pagaré las cervezas que te debo). Gracias a todos.

También me gustaría agradecerles la ayuda prestada a los diferentes especialistas de los servicios generales, como es el caso de José María, Olga, Cristina (ya no, ¡enhorabuena!), Paco, Santi y Mari Carmen.

Part of my formation has been outside Spain. I would like to thank Frank and Stefan for helping me during my stay in Dresden, and for making me discover excellent German beers. También recordaré con agrado los excelentes momentos vividos con los Dr Alberto (Palmero + Escudero) en el extranjero.

Desde un punto de vista personal he vivido durante tiempo con muchos compañeros de viaje, los cuales me han dado muchas vivencias que en general espero recordar sólo las positivas, aunque uno siempre aprende de todo. Por ello quiero agradecerle su compañía a María Alcaire Martín, Rafael Álvarez, Toñy Terriza, Gabriel Lozano, José Alejandro, Silvia Colodrero, Jorge G., Manuel M., Lola González, Marco, Carolina, Julián P., Pedro C., Ana, W. Yesid, Triana, Olalla, Nuria, Patricia, Nieves, Said, Coco, Regla, Iwona, Youssef, Curro, Carmen (gracias por acordarte de mí), Pepe M., Javi Ferrer (jugón), Vanda Godinho A., Juanra, Rebeca, José Carlos, Alberto, Ana Transfer, Víctor, Marga, Sonia, Fátima, Rosa, Silvia, David, Luis, Santi, Óscar, Carlos, Alberto, Rafa, Antonio, a mis innumerables compañeros de piso, a todos los jugones del baloncesto y/o fútbol y al resto de compañeros del Instituto.

Quiero resaltar los buenos momentos vividos durante el transcurso de esta tesis con Lola, Gabriel, Alex, Silvia, Julián etc. Además, no me queda otra que agradecer a ENCANTADORA (María), ESTUPENDA (Toñi), Manuel (sin palabras), Youssef, Víctor C. R. y Pedro todo lo vivido/aprendido durante este tiempo, como la ayuda de algunos de vosotros en ciertos momentos complicados, así que no me queda otra que daros mil gracias a los 10 y etc. Deseo de corazón que todo os vaya muy bien en vuestro futuro tanto personal como laboral, aunque espero seguir disfrutando de todos vosotros en mi futuro. Siempre os tendré un especial cariño.

Cambiando de tercios. También quiero agradecer a todos mis colegas/familia que me han ayudado moralmente en el transcurso de esta tesis.

Un apunte. Antes de que la tesis empezase, tenía muy claro el camino que quería escoger en mi vida laboral. Este pensamiento se lo debo a mi primer profesor. Muchas gracias **D. Francisco Romero Escobar** (mi padre). También agradecerle a él y a su mujer Dña. Ana María Gómez Guerrero de Escalante (mi madre) los sacrificios que han hecho por mí, por todos mis hermanos (gracias a vosotros también, especialmente a Esther) y, en general, por toda su familia. También quiero darles las gracias a mi compañera inseparable Macarena y a mi prima Eu.

Para finalizar vuelvo al principio. Quiero volver a darle las gracias a mi director de tesis Agustín por su imprescindible ayuda en todos los artículos publicados, por su apoyo científico/moral, por su constancia, por su personalidad de la cual espero haber aprendido algo y, en general, por ser el motor que hace que las cosas funcione. Humildemente, gracias de nuevo.

"El que no posee el don de maravillarse ni de entusiasmarse
más le valdría estar muerto, porque sus ojos están cerrados."

Einstein, Albert

(1879-1955) Físico Alemán

"El experimentador que no sabe lo que está buscando
no comprenderá lo que encuentra."

Claude Bernard

(1813-1878) Fisiólogo francés.

Esta Tesis Doctoral ha sido elaborada en la modalidad “compendio de publicaciones” de acuerdo a la normativa interna del departamento de química inorgánica de la universidad de Sevilla aceptada el día 02 de Octubre de 2009.

Según este acuerdo, los criterios para la elaboración de Tesis Doctorales en esta modalidad son:

1. La Memoria de la Tesis Doctoral deberá contener necesariamente los siguientes apartados: Introducción, Discusión Global de Resultados para el conjunto de publicaciones presentadas y Conclusiones Generales.

2. Junto a la Memoria deben aportarse, para cada una de las publicaciones presentadas, informe firmado por cada uno de los autores de la publicación, en el que expresamente se indique que el trabajo descrito ha sido realizado fundamentalmente por el/la doctorando/a que presenta la Memoria en cuestión y que en su conjunto forma parte del trabajo Doctoral del/de la candidato/a.

A continuación se presentan los informes, firmados por cada uno de los autores, correspondientes a las publicaciones que forman parte de esta Tesis Doctoral.

Este informe verifica que:

El trabajo titulado " *Surface nanostructuring of TiO_2 Thin Films by High Energy Ion Irradiation* ", publicado en la revista *Phys. Rev. B 82, 115420 (2010)*, cuyos autores son *P. Romero-Gomez, A. Palmero, T.Ben, J.G. Lozano, S.I. Molina, A.R. González-Elipe*, ha sido realizado fundamentalmente por el doctorante Pablo Romero Gómez y forma parte de su Tesis Doctoral.

Alberto Palmero Acebedo (A.Palmero)	Teresa Ben Fernández (T.Ben)
Juan Gabriel Lozano (J.G. Lozano)	Sergio Ignacio Molina Rubio (S.I. Molina)
Agustín Rodriguez González-Elipe (A.R. Gonzalez-Elipe)	

Este informe verifica que:

El capítulo titulado "*Plasma Deposition of N-TiO_2 Thin Film* ", publicado en el libro *Industrial Plasma Technology, WILEY-VCH, Weinheim, Alemania, 2010, pags. 349-355* cuyos autores son *Pablo Romero-Gomez, Angel Barranco, José Cotrino, Juan P. Espinós, Francisco Yubero, Agustín R. Gonzalez-Elipe* , ha sido realizado fundamentalmente por el doctorante Pablo Romero Gómez y forma parte de su Tesis Doctoral.

Ángel Barranco Quero (A.Barranco)	José Cotrino Bautista (J.Cotrino)
Juan Pedro Espinós Manzorro (J.P. Espinós)	Francisco Yubero Valencia (F.Yubero)
Agustín Rodriguez González-Elipe (A.R. Gonzalez-Elipe)	

Este informe verifica que:

El trabajo titulado *"Chemical State of Nitrogen and Visible Surface and Schottky Barrier Driven Photoactivities of N-Doped TiO_2 Thin Films "*, publicado en la revista J. Phys. Chem. C 2009, 113, 13341–13351 , cuyos autores son P. Romero- Gómez; V. Rico; A. Borrás; A. Barranco; J. P. Espinós; J. Cotrino; and A. R. González-Elipe , ha sido realizado fundamentalmente por el doctorante Pablo Romero Gómez y forma parte de su Tesis Doctoral.

Victor Rico Gavira (V.Rico)	Ana Borrás Martos (A.Borrás)
Ángel Barranco Quero (A.Barranco)	Juan Pedro Espinós Manzorro (J.P. Espinós)
José Cotrino Bautista (J.Cotrino)	Agustín Rodriguez González-Elipe (A.R. Gonzalez-Elipe)

Este informe verifica que:

El trabajo titulado "Band gap narrowing vs. formation of electronic states in the gap in N-TiO_2 thin films ", publicado en la revista J. Phys. Chem. C (DOI. 10.1021/jp104634j) en el año 2010, cuyos autores son P. Romero-Gómez, Said Hamad, J.C. González, A. Barranco, J.P. Espinós, J. Cotrino, A.R. González-Elipe, ha sido realizado fundamentalmente por el doctorante Pablo Romero Gómez y forma parte de su Tesis Doctoral.

Said Hamad Gómez (Hamad S.)	Juan Carlos González González (J.C. González)
Angel Barranco Quero (Barranco A.)	Juan Pedro Espinós Manzorro (J.P. Espinós)
José Cotrino Bautista (J.Cotrino)	Agustín Rodriguez González-Elipe (A.R. Gonzalez-Elipe)

Este informe verifica que:

El trabajo titulado "Enhanced Photoactivity in bilayer films with buried Rutile-Anatase heterojunctions ", publicado en ChemPhysChem, cuyos autores son P.Romero-Gomez, A. Borras, A. Barranco, J.P. Espinos, A. R. Gonzalez-Elipe , ha sido realizado fundamentalmente por el doctorante Pablo Romero Gómez y forma parte de su Tesis Doctoral.

Ana Borras Martos (Borras A.)	Angel Barranco Quero (Barranco A.)
Juan Pedro Espinós Manzorro (J.P. Espinós)	Agustín Rodríguez González-Elipe (A.R. Gonzalez-Elipe)

Este informe verifica que:

El trabajo titulado " Tunable Nanostructure and Photoluminescence of Columnar ZnO Films Grown by Plasma Deposition ", publicado en la revista Journal of Physical Chemistry C, cuyos autores son Pablo Romero-Gómez, Johann Toudert, Juan R. Sánchez-Valencia, Ana Borrás, Angel Barranco and Agustín R. Gonzalez-Elipe, ha sido realizado fundamentalmente por el doctorante Pablo Romero Gómez y forma parte de su Tesis Doctoral.

Johann Toudert	Juan R. Sánchez-Valencia Sanchez-Valencia J.R.
Ana Borrás Martos (Borras A.)	Angel Barranco Quero (Barranco A.)
Agustín Rodriguez González-Elipe (A.R. Gonzalez-Elipe)	

ÍNDICE

Índice General

CAPÍTULO 1 – INTRODUCCIÓN Y OBJETIVOS 15

1.1-OBJETIVOS DEL TRABAJO DE TESIS 17

1.2- INTRODUCCIÓN Y PRESENTACIÓN DEL TEMA DE TESIS 19

1.3- LÁMINAS DELGADAS Y NANOESTRUCTURACIÓN SUPERFICIAL 22

1.3.1- Implantación iónica y nanoestructuración superficial 24

1.3.2- Deposición de películas delgadas de N-TiO2 mediante plasma CVD 27

1.3.3- Preparación de capas delgadas y nanoestructuras superficiales de ZnO mediante plasma CVD 30

1.4. PROPIEDADES FOTOFUNCIONALES DEL TiO_2 y ZnO 33

1.4.1-Fotoactividad del TiO_2 34

Absorción de luz 34

Migración y recombinación de portadores 36

Barrera de Schottky 37

1.4.1.1-Control del mojado superficial 39

1.4.1.2-Procesos fotocatalíticos 41

1.4.2-El problema de las intercaras anatasa-rutilo 41

1.4.3-Sensibilización del TiO_2 con luz visible 43

1.4.4-Fotoluminiscencia del ZnO 44

1.5-CONSIDERACIONES METODOLÓGICAS 46

1.5.1-Celda de fotodegradación de colorantes 46

1.5.2-Ángulo de contacto bajo irradiación 48

1.5.3-Deposición de películas delgadas de N-TiO_2 mediante plasma 49

1.5.4-Diagnosis de plasma 51

1.5.5-Métodos de implantación iónica y nanoestructuración superficial 53

1.5.6 Cálculos de la estructura electrónica 55

1.6-ESTRUCTURA DE LOS RESULTADOS DEL TRABAJO DE TESIS 59

1.7-BIBLIOGRAFÍA..... 61

CAPÍTULO 2 - NANOESTRUCTURACIÓN SUPERFICIAL USANDO ACELERADORES DE PARTÍCULAS 67

TITLE: **Surface nanostructuring of TiO_2 Thin Films by High Energy Ion Irradiation** 70

Abstract..... 70

Introduction 71

Experimental..... 73

Results and discussion 75

Conclusions 87

References 89

CAPÍTULO 3 - CONTROL DE LAS CONDICIONES DEL PLASMA . 93

TITLE**: Plasma Deposition of N-TiO2 thin films** 96

Abstract..... 96

Introduction 97

Experimental setup and diagnostic techniques 97

Ressults and discussion 99

References 106

CAPÍTULO 4 - SINTESIS Y PROPIEDADES DE CAPAS NANOESTRUCTURADAS N-TiO_2 109

TITLE: **Band gap narrowing vs. formation of electronic states in the gap in N-TiO_2 thin films** 112

Abstract 112

Introduction 113

Experimental 116

Results 120

Discussion 138

Conclusions 143

References 145

Supporting information 150

TITLE: **Chemical state of nitrogen and visible surface and Schottky barrier driven photo-activities of N-doped TiO_2 thin films** 157

Abstract 157

Introduction 158

Experimental 160

Result 165

Discussion 179

Conclusions 182

References 183

Supporting information 187

CAPÍTULO 5 - EL PROBLEMA DE LA INTERCARA ANATASA-RUTILO 191

TITLE**: Enhanced Photoactivity in bilayer films with buried Rutile-Anatase heterojunctions** 194

Abstract 194

Introduction 195

Results and discussion 196

Conclusions 203

Experimental 204

References 206

Supporting information 209

CAPÍTULO 6 – SINTESIS Y PROPIEDADES DE CAPAS NANOESTRUCTURADAS DE ZnO 213

TITLE**: Tunable Nanostructure and Photoluminescence of Columnar ZnO Films Grown by Plasma Deposition** 216

Abstract 216

Introduction 217

Experimental 218

Results and discussion 221

Conclusions 239

References 241

Supporting information 246

CAPÍTULO 7 – RESUMEN Y DISCUSIÓN GLOBAL DE RESULTADOS 249

7. DISCUSION GLOBAL DE RESULTADOS 251

7.1 Nanoestructuración superficial usando aceleradores de partículas..... 251

7.2 Control de las condiciones del plasma..... 253

7.3 Síntesis y propiedades de capas nanoestructuradas N-TiO_2 255

7.4. El problema de la intercara anatasa-rutilo 260

7.5 Síntesis y propiedades de capas nanoestructuradas de ZnO 262

CAPÍTULO 8 – CONCLUSIONES GENERALES 265

APÉNDICES 271

Apéndice I..... 273

Apéndice II 288

Índice de figuras

Figura 1.1.- Esquema general de los sistemas nanoestructurados estudiados..... 18

Figura 1.2.- Ejemplos de sistemas nanoestructurados ordenados según el número de dimensiones dentro del orden de los nanómetros (*1D, 2D, 3D*)..... 20

Figura 1.3.- Aplicaciones fotofuncionales relacionadas con esta tesis..... 21

Figura 1.4.- Esquema general del trabajo de tesis 22

Figura 1.5.- Ejemplos de materiales nanoestructurados utilizando diferentes estrategias de deopsición. (a) PLD con sustrato de ópalos, (b) aceleradores de partículas, (c) PECVD y (d) PVD-GLAD. 23

Figura 1.6.- Resultados obtenidos de la simulación mediante el programa SRIM de la implantación de iones N^+ en una matriz de TiO_2. A la izquierda se muestra el perfil de concentración utilizado. A la derecha se muestra los parámetros de la simulación utilizados, así como el rendimiento del desbastado superficial de la muestra..... 25

Figura 1.7.- Esquema comparativo de las nanoestructuras observadas en la bibliografía mediante implantación iónica y las nanoestructuras obtenidas en esta tesis..... 26

Figura 1.8.- Etapas y procesos principales en los procesos de crecimiento de recubrimientos mediante técnicas de PECVD 27

Figura 1.9.- Resultados de la de caracterización de un plasma. A la izquierda se presenta la curva característica del plasma medida mediante la sonda de Lagmuir. A la derecha se presenta el espectro de emisión medido mediante espectroscopia óptica de emisión 29

Figura 1.10.- Ejemplos de nanoestructuras crecidas mediante PECVD. A la izquierda se muestran estructuras formadas por nanotubos de carbono. En el centro se muestra una imagen de fibras $Ag@TiO_2$. A la derecha se observan nanocolumnas de TiO_2..... 30

Figura 1.11.- Diferentes microestructuras de ZnO y métodos de deposición utilizados 31

Figura 1.12.- Esquema de procesos de fotoactivación de semiconductores de banda ancha. (a) proceso de fotoexcitación del semiconductor. (b) proceso de separación del par e^-/h^+ en TiO_2. (c) proceso de recombinación e^-/h^+ y la correspondiente emisión de un fotón debido a la recombinación del excitón en el caso del ZnO..... 33

Figura 1.13.- Espectro ultravioleta visible de la radiación solar en la superficie terrestre 35

Figura 1.14.- Esquema de bandas de semiconductor tipo n..... 37

Figura 1.15.- Esquema de formación de la barrera de Schottky..... 38

Figura 1.17.- Esquema representativo del equilibrio de fuerzas cohesivas-adhesivas..... 39

Figura 1.18.- Esquema de las energías intersuperficiales gota-superficie 40

Figura 1.19.- Esquema de una bicapa de TiO_2 crecida sobre el sustrato. A-TiO_2 se refiere a una capa Anatasa y R-TiO_2 se refiere a una capa de Rutilo 42

Figura 1.20.- Procesos de desexcitación por emisión del semiconductor ZnO. A la izquierda se muestran las dos emisiones encontradas al registrar el espectro uv-vis. En el centro se muestra un esquema de bandas simplificado, con la posición de todos los estados electrónicos en el gap designadas teóricamente con la notación de Kröger-Vink. A la derecha se presenta la deconvolución de la banda de emisión en el visible de ZnO asociada a defectos de oxígeno y Zinc 45

Figura 1.21.- Ensayo de fotodegradación de colorante. A la izquierda se muestra el espectro UV-visible del metacrilato para justificar su uso como filtro del UV. En el centro un esquema de el experimento utilizado. A la derecha la evolución del pico de absorción del naranja de metilo durante los experimentos realizados..... 47

Figura 1.22.- Imagen del dispositivo experimental utilizado (a) y de la geometría de una gota depositada sobre una capa de TiO_2 (b) 48

Figura 1.23.- Esquema sistema de deposición de películas delgadas PECVD 49

Figura 1.24.- Precursores de Titanio utilizados para el crecimiento de las películas N-TiO_2. (a) TTIP, (B) TDEAT, (C) TDMAT 50

Figura 1.25.- Esquema del sistema de burbujeo para precursores de baja presión de vapor 51

Figura 1.26.- Portamuestras del acelerador de partículas para implantar a 45º 53

Figura 1.27.- Esquema de un implantador iónico[88] 54

Figura 1.28.- Esquema general de la tesis 60

Figure 2.1.- Cross-sectional SEM micrographs of irradiated anatase thin films: a) sample #1 (100-N^+-RT) in Table 2.I, b) sample #2 (100-O^+-RT) in Table 2.I..... 76

Figure 2.2.- SEM micrographs of irradiated anatase thin films: a) top view of sample #3 (50-N^+-RT) in Table 2.I, b) top view of sample #3 (50-N^+-RT) after its annealing at 700 K, and c) cross-sectional image of sample #3 (50-N^+-RT) after its annealing at 700 K, and d) top view of sample #4 (50-N^+-700) in Table..... 77

Figure 2.3.- Characterization results of samples #3 (50-N^+-RT) and #4 (50-N^+-700) in Table 2.I: a) X-ray difraction diagrams of an as-deposited TiO_2 thin film along with those of samples #3 (50-N^+-RT) and #4 (50-N^+-700) in Table 2.I, and a reference spectrum. b) N1s photoemission spectra of samples #3 (50-N^+-

RT) and #4 (50-N^+-700), and c) Transmission spectra of samples #3 (50-N^+-RT) and #4 (50-N^+-700) along with that of a reference sample 79

Figure 2.4.- Chemical analysis of sample #3 (50-N^+-RT) in Table 2.I. a) Nitrogen intensity profiles obtained through the EELS spectra, b) cross-sectional HAADF image of the surface scaled with figure 2.4a, and c) EELS spectra for the positions given by the horizontal arrows in figure 2.4b (slashed and continuum curves correspond to the slashed and continuum arrows) 80

Figure 2.5- Chemical analysis of sample #4 (50-N^+-700) in Table 2.I. a) Nitrogen intensity profiles obtained through the EELS spectra, b) cross-sectional HAADF image of the surface scaled with figure 2.5a, and c) EELS spectra for the positions given by the horizontal arrows in figure 2.5b (slashed and continuum curves correspond to the slashed and continuum arrows) 82

Figure 2.6.- Proposed model for the void production, growth, coarsening and opening to the surface to explain the different surface nanostructures formed during ion implantation 84

Figure 2.7.- SEM micrographs of TiO_2 anatase thin films: a) cross-sectional view of sample #5 (50-F^+-RT) in Table 2.I, b) top view of sample #6 (50-F^+-700), c) cross-sectional view of sample #7 (50-S^+-700), and d) top view of sample #7 (50-S^+-700)..... 86

Figure 3.1.- OES spectrum recorded in the region from 300 to 400 nm for a $N_2/O_2/H_2$ (65, 12, 23 %) and N_2/O_2 plasmas..... 101

Figure 3.2.- N1s photoemission spectra recorded for two N-doped TiO_2 thin films prepared with (left) a N_2/O_2 (12, 88 %) and (right) a $N_2/O_2/H_2$ (65,12,23%) plasma at 523 K..... 104

Figure 4.1.- Schematic representation of the Ti precursors utilized for the synthesis of the N-TiO_2 thin films by plasma deposition 116

Fig. 4.2.- N1s spectra recorded for a series of N-TiO_2 thin films prepared with the TDMAT precursor and different percentages of N_2 in the plasma as indicated. Note that some spectra are affected by a multiplication factor to bring them into a common scale 122

Figure 4.3.- Fitted (gray line) and experimental (black line) N1s normalized spectra of selected N-TiO_2 thin films prepared at 523 K with the TDMAT (left) and the TTIP (right) precursors and different percentages of N_2 in the plasma gas. Elemental bands used for fitting are plotted in gray..... 124

Figure 4.4.- N/Ti ratio determined from the intensities of the N1s and Ti2p photoelectron peaks as a function of the percentage of nitrogen in the O_2+N_2 mixture used as plasma gas. The dashed line is included to guide the eyes 125

Figure 4.5.- Set of absorption spectra recorded for a series of N-TiO_2 thin films prepared at 523 K with the TDMAT precursor and different percentages of nitrogen in the plasma gas as indicated in each particular panel. The gray color spectrum included for comparison in each panel corresponds to the absorption spectrum of a pure TiO_2 thin film 126

Figure 4.6.- Values of the absorption threshold plotted against the percentage of nitrogen in the plasma gas for N-TiO_2 thin films prepared with the TTIP, TDMAT and TDMAT precursors at 523 K. The dashed line is included to guide the eyes 128

Figure 4.7.-Top) Refraction index and bottom) Extinction coefficient curves determined for N-TiO_2 thin films prepared at 523 K by using TDMAT as a precursor and different percentages of N_2 in the mixture used as plasma gas as indicated. The star points to the region whose reproduction is only possible by admitting an oscillator around 375 nm 129

Figure 4.8.- Structures of the three type of N centers studied. a) Substitutional defect, N_s , in which a N atom replaces a O atom. b) Interstitial defect, N_i, in which the N atom is located in an interstitial place, and the O atom is also displaced from its original site. c) Substitutional-interstitial defect, N_{si}, in which the N atom occupies the same position as in the case of the N_s defect, and the O atom occupies an interstitial place 131

Figure 4.9.- Density of states plots of the six N-TiO_2 systems studied, showing the two spin components separately. **a** and **b** correspond to the two systems with substitutional N doping (N_s), with 2 N atoms located at close and separated positions, respectively. **c** and **d** correspond to the two systems with interstitial N doping (N_i), with 2 N atoms located at close and separated positions, respectively, respectively. **e** and **f** correspond to the two substitutional-interstitial N configurations (N_{si}), with 2 N atoms located at close and separated positions, respectively, respectively. The bands are plotted in such a way that the origin of the energy (0 eV) is placed at the bottom of the conduction band. The two vertical dashed lines are placed to indicate HOMO-LUMO gap in TiO_2. The vertical solid line indicate the highest occupied orbital of the system, which in the case of N-TiO_2 corresponds to new gap states generated by the presence of nitrogen in the lattice 135

Figure 4.10.- Partial density of states plots of N, Ti and O in the gap states for the six studied N-TiO_2 systems with the labelling a)-f) being the same than in Fig. 4.9. The oxygen contribution is differentiated for the oxygen atoms close to the nitrogen and the rest of oxygen atoms of the lattice. The total densities of states plotted in Figure 4.9 are calculated as the sum of these partial densities of states. The vertical solid line indicates the highest occupied orbital of the system 136

Figure 4.11.- Evolution of the wetting angle as a function of the illumination time with visible and UV lights and then left in the dark for N-TiO_2 samples prepared with 85% (top) and 97% (bottom) of N_2 in the plasma gas. The lines are plotted to guide the eyes 138

Fig. 4.12.- Cross section views of thin films A-F and that of the REF sample. Sample E has a microstructure very similar to that of sample C 166

Fig. 4.13.- XRD of samples A-F and that of the REF sample included for comparison. Peaks due to the anatase and rutile phases are indicated in the form of patterns..... 168

Figure 4.14.- (Top) Raman spectra in the zone between 200 and 800 cm^{-1} for samples A-F compared with that of the reference anatase sample; the peaks attributed to the rutile phase are indicated. (Bottom) Raman spectra in the zone of the main peak of anatase at around 150 cm^{-1}..... 169

Fig. 4.15.-UV-vis absorption spectra of samples A-F compared with that of the reference thin film. The asterisk in some of the plots indicates the presence of a specific absorption feature 172

Figure 4.16.- N1s fitted photoemission spectra of samples A-F..... 174

Figure 4.17.- Evolution of the wetting angle for the REF and E thin films (left) and samples A and F (right) subjected sequentially to illumination with visible, UV+vis and then left in the dark. The curves are plotted to guide the eyes 177

Figure 4.18.- Evolution of the concentration of methyl orange dye in an illuminated solution of this molecule in the presence of the thin films. Curves corresponding to experiments with UV+vis (top) and visible (bottom) illumination are reported. The curves upon UV+vis illumination have been corrected by the curve of a solution of the dye in the presence of a bare substrate of Si without thin film 178

Figure 5.1.- Cross section SEM micrographs of a series of anatase thin films deposited on Si(100) (left) and of the anatase layers in the rutile-anatase bilayer thin films (right). The thicknesses of the anatase layers are indicated by labels. Due to the high compactness and very low electrical conductivity of the rutile layer no details of its microstructure are observed..... 197

Figure 5.2.- Selected XRD diagrams of a series of anatase thin films deposited on Si(100) (left) and of the anatase layers in the rutile-anatase bilayer thin films (right). The thicknesses of the anatase layers are indicated by labels. The pattern of a rutile thin film is also included for comparison..... 198

Figure 5.3.- Selected Raman spectra of a series of anatase thin films deposited on Si(100) (left) and of the anatase layers in the rutile-anatase bilayer thin films (right). The thicknesses of the anatase layers are indicated by labels 199

Figure 5.4.- Top) Photo-activated decolouration curves of the methyl orange dye as a function of the illumination time for different anatase thickness in the RABs. Results for anatase (d > 200 nm) and rutile (d ~ 400 nm) films are shown as references. Bottom, Plot of the kinetic constant k as a function of the anatase thickness for the RAB, SAL and rutile thin films..... 200

Figure 5.5.- Top) Evolution with the illumination time of the wetting angle measured on the surface of anatase surfaces in RABs thin films with different thickness of the anatase layer. Results for pure anatase (d > 200 nm) and rutile (d ~ 400 nm) thin films are included as references. Bottom) Plot of the kinetic constant k2 as a function of the anatase thickness for the RAB, SAL and rutile thin films 202

Figure 6.1.- SEM cross section and plan view (insets) micrographs of the ZnO films grown with a O_2 plasma and at different substrate temperatures: (a) 300 K (O_2 300K 550nm), (b) 410 K (O_2 410K 450nm) and (c) 475 K (O_2 475K 400nm) 222

Figure 6.2.- (a) θ–2θ x-ray diffraction spectra of the films grown with a O_2 plasma at various substrate temperatures , (b) evolution of the ZnO crystal size along the vertical axis determined from the (002) peak width, (c) evolution of the angular position of the (002) wurtzite diffraction peak as a function of the substrate temperature. The dotted lines in (b) and (c) are a guide for the eye. The dashed line in (c) represents the angular position of the (002) peak of a stress free ZnO wurtzite crystal, taken from JCPDS tables..... 224

Figure 6.3.- (a) Room temperature photoluminescence spectra of the thin films grown with a O_2 plasma at different substrate temperatures (The vertical dotted line representing the 378 nm wavelength has been drawn in each figure as a guide to the eye), (b) Spectra of the UV photoluminescence of two selected films and their corresponding Gaussian components. The peak at 378 nm is attributed to the recombination of free excitons and the others to phonon replicas. (c) Visible photoluminescence spectra of two selected films and their corresponding Gaussian components 226

Figure 6.4.- SEM cross-section view of the O_2 410K 1730nm film (inset : SEM surface view) 229

Figure 6.5.- (a) θ–2θ x-ray diffraction spectra of films presenting different thicknesses grown with a O_2 plasma at a substrate temperature of 410 K. The vertical dashed line represents the angular position of the (002) peak of stress free ZnO wurtzite bulk crystal. (b) Reflectance spectra of the five films and corresponding best fits, (c) n and k spectra extracted for the five effective ZnO layers using the multilayer structures depicted in table 6.2. The vertical dotted lines correspond to wavelengths of 280 nm (excitation wavelength during PL experiments) and 375 nm (typical of the UV PL band) 230

Figure 6.6.- (a) Room temperature photoluminescence spectra of the thin films grown with a O_2 plasma at 410 K presenting different thicknesses and optical quality factor evolution versus thickness, (b) Spectra of the UV photoluminescence of two selected films and their corresponding Gaussian components, (c) Visible photoluminescence spectra of two selected films and their corresponding Gaussian components 234

Figure 6.7.- SEM cross section and plan view (insets) micrographs of the ZnO films grown at 475 K substrate temperature and with different plasmas: (a) O_2 plasma (O_2 475K 400nm), (b) O_2/H_2 plasma (O_2/H_2 475K 800nm), (c) O_2/Ar plasma (O_2/Ar 475K 700nm), (d) O_2/ N_2 plasma

(O_2/ N_2 475K 300nm)..... 236

Figure 6.8.- (a) θ–2θ x-ray diffraction spectra of the films grown at a 475 K substrate temperature and with different compositions of the plasma. (b) Evolution of the ZnO crystal size along the vertical axis determined from the (002) peak width as a function of the plasma composition. The dotted line is a guide for the eye. (c) Evolution of the angular position of the (002) wurtzite diffraction peak as a function of the plasma composition. The dashed line represents the angular position of the (002) peak of stress free wurtzite ZnO crystal 237

Figure 6.9.- (a) Room temperature photoluminescence spectra of the thin films grown with at 475 K with various plasmas, (b) Spectra of the UV photoluminescence and Visible photoluminescence spectra of a film grown in a O_2/H_2 plasma and the corresponding Gaussian components 239

Figura 7.1.- Esquema representativo de los sistemas Anatasa y Rutilo para diferentes espesores de la capa Anatasa. A) $d_{Anatasa} > 130$ nm; B) $d_{Anatasa}=d_{max\text{-}fotoactividad}$ y C) $d_{Anatasa} < 130$ nm. Izquierda) capa de anatasa depositada directamente sobre un sustrato aislante. Derecha) capa de anatasa depositada directamente sobre un sustrato de rutilo. Por simplicidad las diferencias entre "*band gap"* y función de trabajo entre anatasa y rutilo no son consideradas. La contribución del rutilo a la fotoactividad de los sistemas se asume despreciable y las bandas se representan por líneas rectas 261

Índice de Tablas

Table 2.I.- Irradiation conditions for each sample along with the measured resistivity of the films 74

Table 3.1.- Ion density, electron temperature and plasma potential of different plasmas used in the present work 100

Table 3.2.- Plasma species detected by OES 102

Table 4.1.- Relevant distances (in Å) involved in the three types of defects studied: N_i, N_s and N_{si}. The distance between the two defects in the unit cell is taken into account by labeling with C and S the structures in which the N atoms are close and separated respectively 132

Table 4.2.- Summary of main properties of samples 161

Table 6.1.- Label, plasma conditions and substrate temperature during the growth of the ZnO films and thickness as determined by optical reflectance measurements. Due to the crudeness of the model used to fit the reflectance data, errors of a few tens of nanometers are expected in the determination of the thickness 216

Capítulo 1

Introducción y Objetivos

1.1 OBJETIVOS DEL TRABAJO DE TESIS

El trabajo realizado durante el transcurso de esta tesis persigue la generación y estudio de nanoestructuras superficiales con aplicaciones fotofuncionales. Esta tesis pretende ampliar el conocimiento, tanto en la formación de nuevas nanoestructuras, como respecto de sus posibles aplicaciones fotofuncionales o la mejora de dichas propiedades.

Para la formación de las nanoestructuras superficiales se han escogido dos métodos. En primer lugar, se utiliza un acelerador de partículas de media energía para implantar aniones en muestras de TiO_2 con el propósito de modificar la nanoestructura superficial, así como la composición de las capas. En segundo lugar, se pretende controlar el crecimiento de nanoestructuras de TiO_2 y ZnO mediante deposición química desde fase vapor asistida por plasma (PECVD). Con ello se pretende controlar la nanoestructura y composición de los óxidos estudiados. Para entender el crecimiento de las muestras crecidas mediante PECVD, se estudian los plasmas utilizados en los procesos de crecimiento de capas delgadas.

Para tener un buen control de las nanoestructuras formadas, se deben tener en cuenta los siguientes puntos:

- Propiedades ópticas. Controlar el índice de refracción y el coeficiente de extinción de las nanoestructuras.
- Controlar la estructura cristalina de las nanoestructuras.
- Control microestructural de la nanoestructura.

Con estas premisas y estrategias, se pretende estudiar:

1.1.1- GENERACIÓN Y CARACTERIZACION DE NANOESTRUCTURAS SUPERFICIALES

1. La primera aproximación a los problemas plantean generar sistemas consistentes en la formación de nanoestructuras de TiO_2 modificadas con aniones mediante aceleradores de partículas. Además de la modificación nanoestructural, se pretende modificar la composición superficial de la muestra. La comprensión de los procesos que controlan la formación de la nanoestructura es otro aspecto fundamental a considerar en este punto (figura 1.1.a).
2. Otro aspecto es generar sistemas consistentes en el control nanoestructural y de la composición superficial de muestras TiO_2 crecidas mediante plasmas que

contienen nitrógeno en su composición y/o en el precursor utilizado (figura 1.1.b).

3. La generación de sistemas consistes en la formación de bicapas rutilo-anatasa crecidas mediante la técnica de deposición PECVD y sus propiedades fotocatalíticas es otro de los puntos objeto de estudio de este trabajo (figura 1.1.c).
4. Finalmente la preparación de nanoestructuras de ZnO mediante PECVD y el estudio de su fotoluminiscencia es el último punto de interés de este estudio (figura 1.1.d).

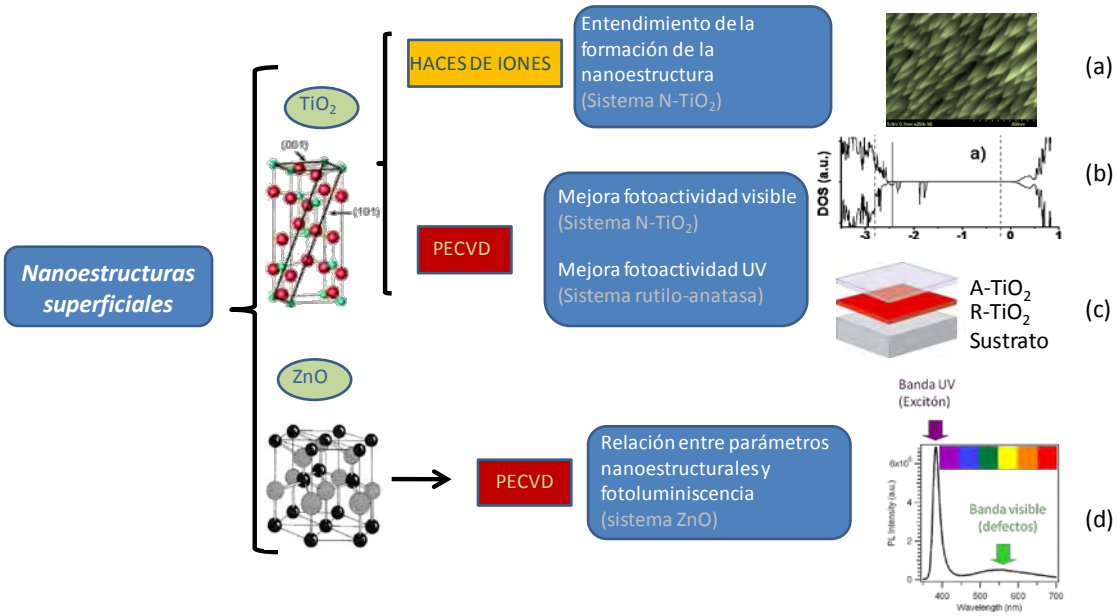

Figura 1.1. Esquema general de los sistemas nanoestructurados estudiados.

1.1.2- PROPIEDADES SUPERFICIALES FOTOFUNCIONALES DE NANOESTRCTURAS

Con los dos primeros sistemas estudiados, el objetivo es conseguir que las muestras presenten fotoactividad en el visible bien en el test fotocatalítico y/o mojado superficial. Las causas de esa foto-actividad se han analizado mediante el estudio teórico usando cálculos ab-initio de las posibles especies de nitrógeno capaces de generar la fotoactividad en el visible.

En el tercer caso se pretende explicar el aumento de la fotoactividad que se observa en sistemas mezcla de fases anatasa-rutilo, frente a sistemas de una única fase.

Finalmente en el último sistema estudiado, el objetivo es conocer la relación existente entre las características de la nanoestructura superficial obtenida y la fotoluminiscencia del ZnO.

1.2- INTRODUCCIÓN Y PRESENTACION DEL TEMA DE TESIS.

En las últimas décadas, uno de los aspectos más interesantes en la investigación y desarrollo de nuevos materiales ha perseguido la fabricación de materiales funcionales para su implementación en dispositivos con aplicaciones en diversos campos tecnológicos.[1]

La fabricación de materiales con al menos una de sus dimensiones en el orden de los nanómetros es necesaria para la miniaturización de componentes, lográndose además la consecución de nuevas propiedades no alcanzables con los materiales tradicionales[2]. Un ejemplo clásico del uso de nanomateriales es en el campo de la microelectrónica, donde elementos de tamaño "*nano*" forman parte de los distintos componentes de los dispositivos[3]. Un parámetro fundamental para el control final de las propiedades de los sistemas, una vez escogido el tipo de material a utilizar, es el control de su nanoestructura superficial del mismo, persiguiéndose exaltar y controlar algunas de sus propiedades. Aspectos fundamentales de la nanoestructura superficial de un material son su rugosidad y porosidad.[4]

Una categorización clásica de los nanomateriales atiende al número de dimensiones espaciales dentro del rango de los nanómetros. Según la misma, los nanomateriales nanoestructurados se denominan *1D, 2D* y *3D*, según tengan una, dos o tres dimensiones en el orden de los nanómetros. La figura 1.2 muestra esquemáticamente algunos ejemplos de nanomateriales según esta división.

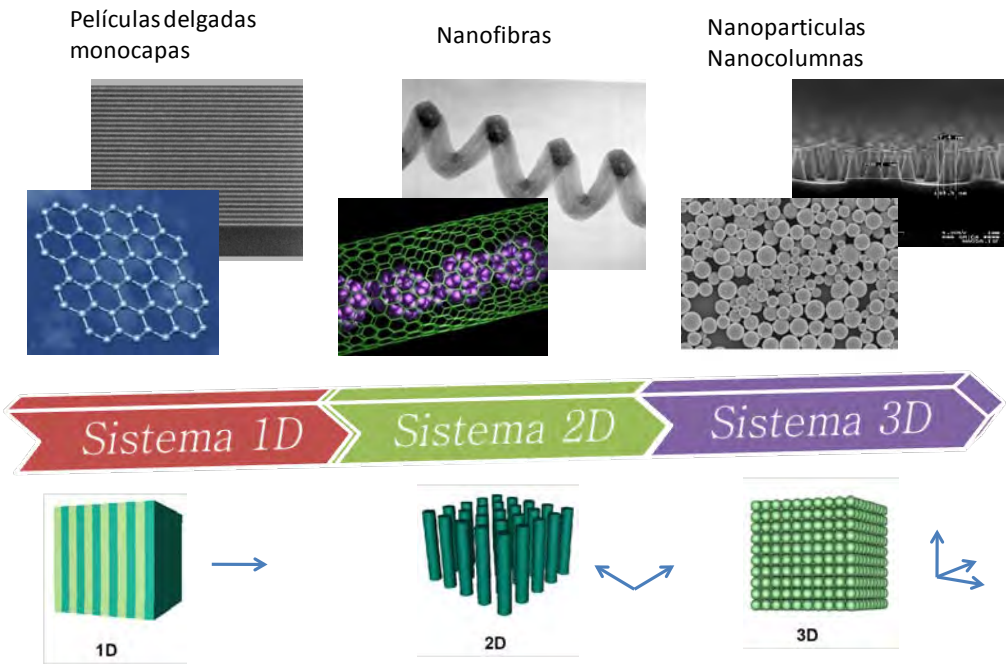

Figura 1.2. Ejemplos de sistemas nanoestructurados ordenados según el número de dimensiones dentro del orden de los nanómetros (*1D, 2D, 3D*).

Los sistemas 1D seleccionados en la figura 1.2 muestran ejemplos de multicapas de películas delgadas y grafeno. Entre los sistemas 2D destacamos ejemplos de nanofibras o nanotubos. Para sistemas 3D se destaca el desarrollo de nanopartículas.

En este trabajo de tesis doctoral se abordan diversos procesos de nanoestructuración superficial de capas delgadas de materiales fotofuncionales, es decir, nanomateriales cuya respuesta o aplicación final viene determinada por su activación mediante fotones.

Debido a sus propiedades fotofuncionales, los materiales escogidos son los semiconductores de banda ancha, Óxido de Titanio (TiO_2) y Óxido de Zinc (ZnO). El TiO_2, es un material de gran interés debido a sus propiedades fotocatalíticas[5] y de control del mojado superficial.[6] Aplicaciones importantes del mismo en estos campos son la descontaminación de compuestos orgánicos y el desarrollo de superficies autolimpiables, respectivamente. Por otro lado, el ZnO tiene un gran interés debido a sus propiedades de fotoluminiscencia en condiciones ambientales[7], una característica que propicia su uso para el desarrollo de sensores fotónicos de gases[8], diodos electroluminiscentes[9] o láseres de UV[10]. Un esquema del contexto de uso de estos materiales para las aplicaciones indicadas se recoge en la figura 1.3.

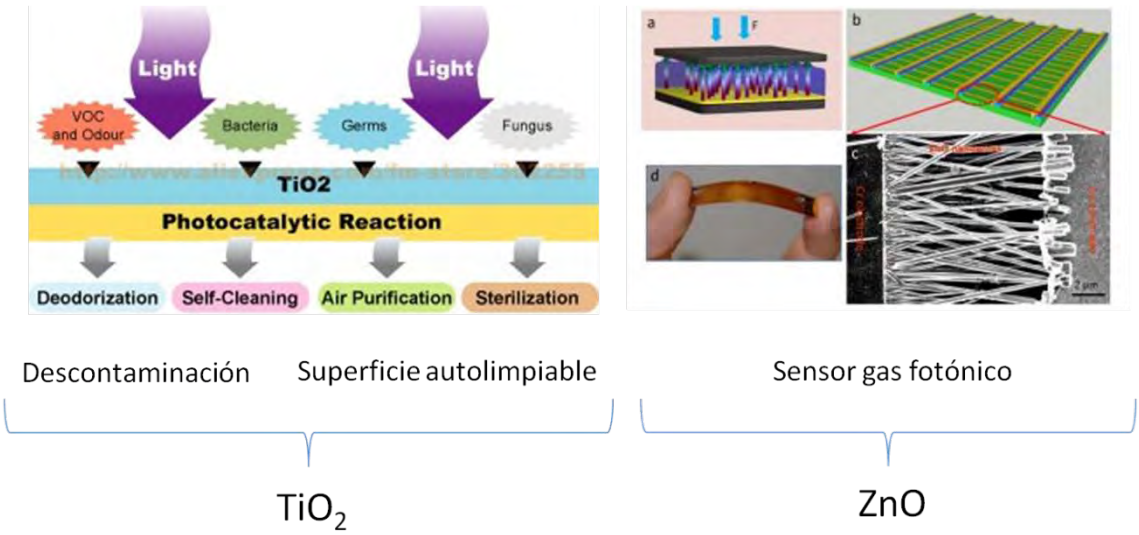

Figura 1.3. Aplicaciones fotofuncionales relacionadas con esta tesis.

En la parte izquierda de la figura 1.3 se destacan algunas aplicaciones del TiO_2 como son desodorización, superficies autolimpiables, purificación de aire y esterilización, destacándose las aplicaciones de descontaminación y el desarrollo de superficies autolimpiables, ya que son las aplicaciones estudiadas durante esta tesis. En la parte derecha, se ejemplifica un prototipo de sensor fotónico de gases basado en ZnO, el cual, consiste en un conjunto de nanohilos de gran porosidad.

En función de las consideraciones anteriores, este trabajo de tesis se divide en dos bloques fundamentales. Uno de ellos, trata del control nanoestructural del material a fin de crear nanoestructuras superficiales utilizando diferentes métodos de nanoestructuración. El otro, trata sobre las aplicaciones de estas nanoestructuras para su implementación en dispositivos y aplicaciones fotofuncionales. La organización general del trabajo realizado se recoge en la figura 1.4.

Según este esquema 1.4, el trabajo realizado parte de de la elección de la nanoestructura a estudiar así como del material el cual se desea nanoestructurar. A continuación se plantea la técnica utilizada para controlar la formación de la nanoestructura superficial deseada. En este caso, se ha utilizado dos metodologías. Por un lado, se ha tratado de controlar la nanoestructura superficial mediante el proceso de deposición química desde fase vapor asistida por plasma de microondas (MW-PECVD)[11]. Por otro lado, se ha utilizado un a celerador de partículas, cuyo uso para nanoestructuración superficial apenas se ha estudiado en la literatura para otros materiales[12]. Una vez caracterizada adecuadamente la nanoestructura superficial obtenida y las propiedades de las capas

obtenidas, se estudiaron algunas aplicaciones de las mismas en diversos campos de interés tecnológico, siempre con especial referencia a las propiedades fotofuncionales de los materiales escogidos.

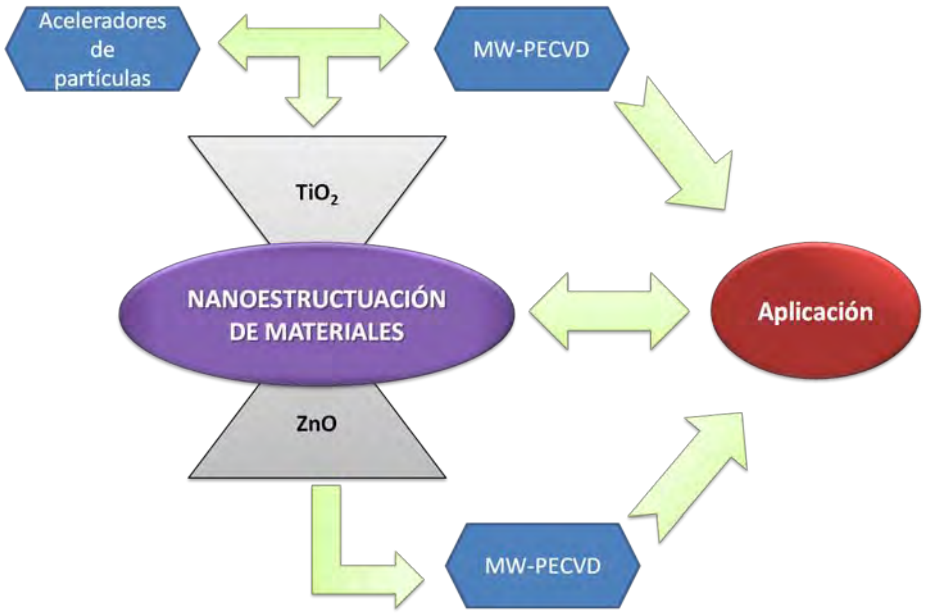

Figura 1.4. Esquema general del trabajo de tesis.

1.3-LÁMINAS DELGADAS Y NANOESTRUCTURACIÓN SUPERFICIAL

Dentro del contexto anteriormente expuesto, este trabajo se ha ordenado en función del tipo de proceso de nanoestructuración utilizado y del tipo de material que se va a nanoestructurar.

En la bibliografía reciente se muestran innumerables artículos que intentan nanoestructurar superficies y láminas delgadas. Algunos ejemplos de interés encontrados en la bibliografía o desarrollados en el transcurso de esta tesis se muestran la figura 1.5.

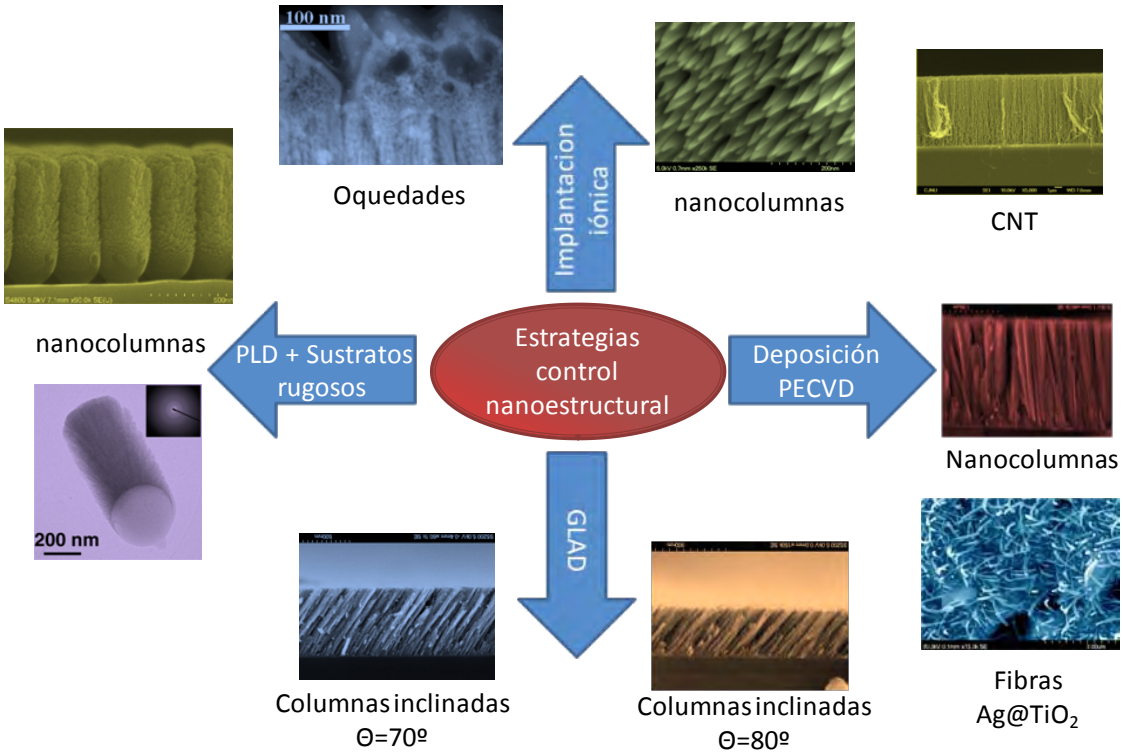

Figura 1.5. Ejemplos de materiales nanoestructurados utilizando diferentes estrategias de deposición. (a) PLD con sustrato de ópalos, (b) aceleradores de partículas, (c) PECVD y (d) PVD-GLAD.

En esta figura 1.5 se muestra cómo mediante diferentes técnicas se pueden conseguir una gran variedad de nanoestructuras de diferentes materiales. Los ejemplos recogidos en la misma se refieren a muestras crecidas utilizando cámaras de deposición por laser pulsado (PLD) con ópalos como sustrato[13], deposición de películas mediante evaporación en configuración rasante ("Glancing Angle Deposition (*GLAD)*" según su denominación en inglés),[14] laminas delgadas crecidas mediante PECVD controlando el tamaño de poro,[11] generación de nanotubos de carbono[15] o bien, la generación de nanocolumnas (nanorods) o oquedades (voids)[16] en la superficie mediante el bombardeo con iones de alta energía.

Tal y como se ha mencionado, dentro de las diferentes técnicas utilizadas para nanoestructurar la superficie de muestras de TiO_2 y ZnO, en esta tesis se van a desarrollar particularmente dos. Por un lado, la utilización de aceleradores de partículas con energía en el orden de decenas de keV. El propósito de esta aproximación es generar oquedades ("*Voids*") o estructuras tipo esponja ("*sponge-like*")[17] similares a las reportadas en la bibliografía para otros materiales diferentes al estudiado en esta tesis.[18] Un desarrollo original de los trabajos aquí realizados, se refiere a la utilización de

aceleradores de partículas para obtener estructuras formadas por nanocolumnas ("*nanorods*") en las superficies irradiadas. Por otro lado, se utilizó la técnica PECVD asistida por plasma de microondas, la cual ha demostrado ser capaz de general capas finas con tamaño de poro controlado,[11] así como de inducir el crecimiento de fibras core@shell[19] o incluso el crecimiento de nanotubos de carbono.[15] Otro objetivo planteado durante la tesis persigue la modificación de la composición de las muestras de TiO_2 incorporando nitrógeno en su estructura, simultáneamente a su nanoestructuración. Los resultados obtenidos han puesto de manifiesto que, en determinadas circunstancias, es posible realizar ese control simultáneo de ambos tipos de características, lográndose las composiciones finales bien definidas en los casos que así lo requerían.

A continuación, se discuten con más detalle las técnicas utilizadas para nanoestructurar la superficie de los diferentes materiales estudiados.

1.3.1- Implantación iónica y nanoestructuración superficial

La implantación iónica mediante aceleradores de partículas consiste en hacer incidir un haz de iones de alta energía sobre la superficie del material que se desea modificar. Para tener una cierta selectividad superficial, este tipo de proceso se lleva a cabo mediante el uso de aceleradores de partículas con energías comprendidas entre 10 KeV y 500 KeV, consiguiendo perfiles de implantación de los iones del orden de las decenas o centenas de nanómetros en profundidad.[20]

Previamente a l a realización de los experimentos es posible calcular el perfil en profundidad de los iones implantados en la matriz, así como diversos parámetros asociados a la energía del ion. Para ello, se utiliza el programa de cálculo computacional de acceso libre SRIM (http://www.srim.org/). Con el mismo se puede hacer una estimación teórica de la influencia de distintos parámetros experimentales para conseguir un perfil dado de concentración de iones y/o daño (energía depositada) en la matriz. Este tipo de análisis requiere definir parámetros tanto del acelerador, como son la energía del haz incidente, ángulo de incidencia y tipo de ion, como la densidad del material donde se desea realizar la implantación. Un ejemplo de estas simulaciones se muestra la figura 1.6. En la simulación se muestra un perfil de implantación de nitrógeno en una matriz cuya densidad es 3.8 g/cm^3, pudiéndose aproximar mediante

un perfil tipo Gaussiano. Este programa, y por consiguiente el modelo en el que se basa, tienen en cuenta las múltiples colisiones que tiene el ion primario al penetrar dentro de la matriz que se desea modificar, así como fenómenos de desbastado superficial ("sputtering" según su denominación en inglés) y transferencia de energía y momento a los átomos de la matriz. El desbastado superficial se produce al extraer del blanco bombardeado átomos superficiales que se excitan por colisiones secundarias con otros átomos excitados del sistema.

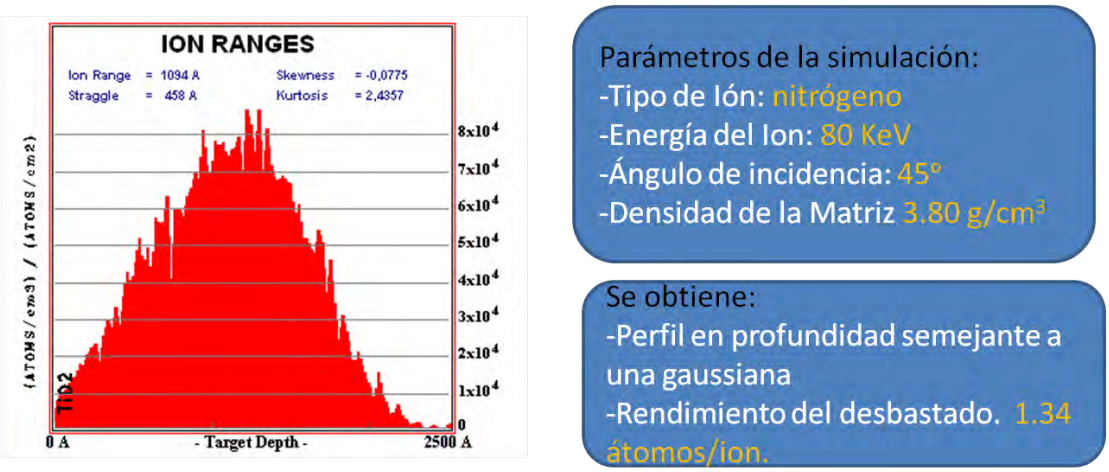

Figura 1.6. Resultados obtenidos de la simulación mediante el programa SRIM de la implantación de iones N^+ en una matriz de TiO_2. A la izquierda se muestra el perfil de concentración utilizado. A la derecha se muestra los parámetros de la simulación utilizados, así como el rendimiento del desbastado superficial de la muestra.

La implantación iónica, está considerada una técnica de postratamiento, ya que persigue la modificación de muestras previamente crecidas. Una ventaja a resaltar de la misma en relación con nuestro trabajo es la posibilidad de cambiar la composición de los materiales implantados con alta precisión.

Tradicionalmente se ha utilizado la implantación iónica para el dopado de semiconductores, cuyas principales aplicaciones se encuentran en el campo de la microelectrónica.[21-22] Esto se debe, al control exhaustivo que se consigue de las dosis al implantar. Más recientemente, se está estudiando cómo utilizar esta técnica para nanoestructurar materiales en la zona de implantación. Como se ha comentado anteriormente, en publicaciones recientes se ha podido comprobar la formación de

nanoestructuras tipo esponja (*sponge-like*) u oquedades (*Voids*) dentro de materiales como Ge[16] Si[23], InSb[24], GaN[25] o GaSb[16].

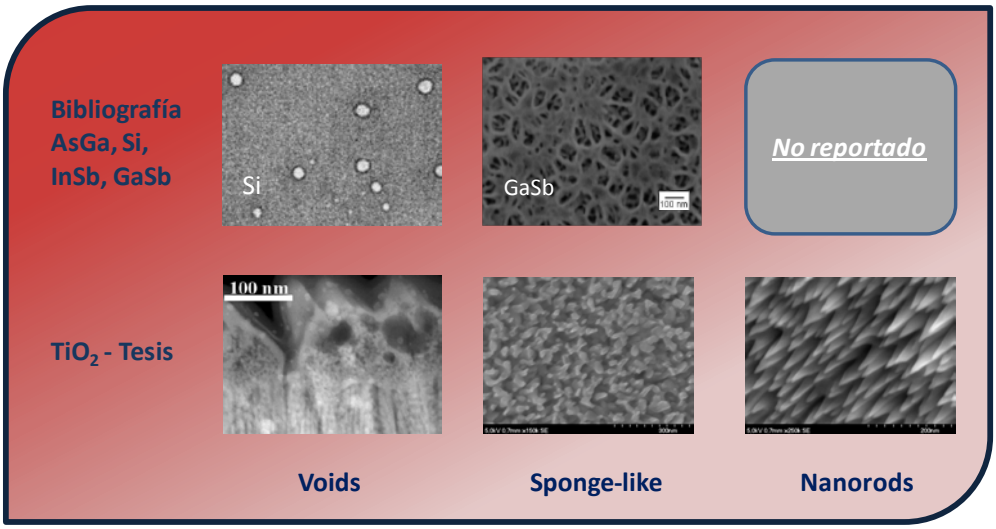

Figura 1.7. Esquema comparativo de las nanoestructuras observadas en la bibliografía mediante implantación iónica y las nanoestructuras obtenidas en esta tesis.

En la figura 1.7 se muestran tres casos de nanoestructuración bien diferenciados. En la bibliografía, se tienen reportados casos de estructuración tipo *voids* o *sponge-like* para diferentes materiales. Una estructura semejante se ha encontrado también aquí para el TiO_2. Sin embargo, para este material se ha podido también verificar la posibilidad de nanoestructurar su superficie con la formación de "*nanorods*" orientados según el haz de incidencia. Creemos que este resultado puede abrir un campo de estudio nuevo que permitirá la nanoestructuración de superficies mediante aceleradores de partículas.

En el estudio realizado en esta tesis se ha pretendido la nanoestructuración superficial de películas de TiO_2 usando diferentes elementos durante la implantación. Los elementos escogidos poseen diferente afinidad química con la matriz de TiO_2. Un parámetro experimental que ha demostrado ser muy importante es la temperatura de la muestra durante la implantación, habiéndose verificado que la temperatura controla la movilidad de átomos de la red, favoreciendo determinados procesos de nanoestructuración. Otros factores que se han considerado son el desbastado superficial y el efecto del ángulo de incidencia de los iones. Todo ello ha permitido crear nuevas nanoestructuras en el TiO_2, habiéndose propuesto un modelo que explica la formación de dichas nanoestructuras mediante implantación iónica.

Este trabajo de investigación se publicó en la revista "*Physical review B*" (Volumen 82, página 115420, año 2010), y ha sido seleccionado por la revista "Virtual Journal of Nanoscale Science & Technology" (http://www.vjnano.org), editada por el instituto americano de física, como artículo destacado en su número del mes de Septiembre del año 2010.

1.3.2-Deposición de películas delgadas de N-TiO_2 mediante plasma CVD

La técnica PECVD consiste en la descomposición en fase vapor de un precursor mediante la acción de un plasma. Por lo tanto, el crecimiento de una capa por PECVD implica la introducción de un precursor en la cámara de reacción, su activación, fragmentación y reacción mediante el uso de un plasma. Un esquema de las etapas y procesos de este procedimiento se recoge en la figura 1.8.

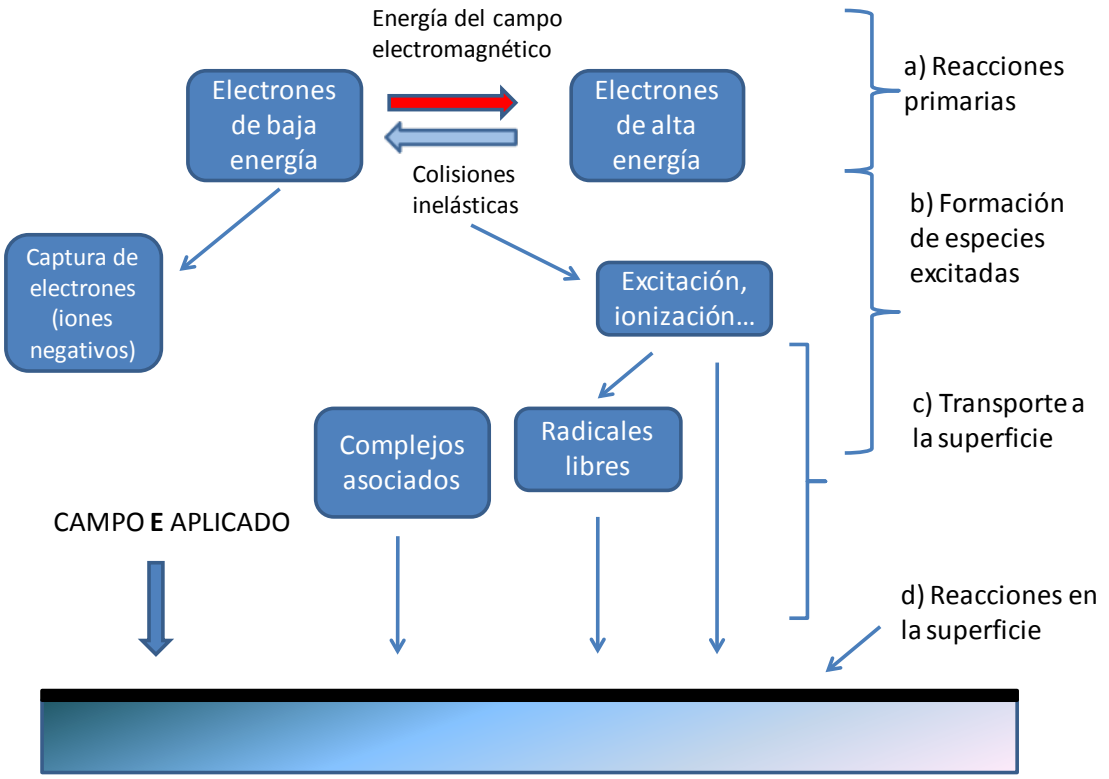

Figura 1.8. Etapas y procesos principales en los procesos de crecimiento de recubrimientos mediante técnicas de PECVD.

Durante la deposición, se producen diferentes procesos de intercambio energético como son la absorción de energía del campo electromagnético por parte de los electrones o la captura de electrones dando lugar a iones negativos. El conjunto de esos procesos forma parte de las reacciones primarias que ocurren en el plasma. Además se producen colisiones inelásticas entre las especies del plasma y las moléculas volátiles del precursor usado, produciendo la formación de especies altamente excitadas (iones y/o radicales libres) capaces de actuar como especies precursoras del recubrimiento. Estas especies son trasladadas a la superficie al tiempo que tienen lugar diferentes reacciones secundarias inelásticas y elásticas como son los procesos de interacción ión-radical o fotón-átomo/molécula. Por último, se producen fenómenos de absorción de las especies reactivas provenientes del precursor en la superficie del sustrato, además de procesos de recolocación (difusión y/o nucleación principalmente). Las componentes residuales provenientes del precursor volátil son extraídas de la cámara en fase gaseosa.

El método de activación del plasma escogido viene caracterizado por su excitación mediante una descarga de microondas (2,45 GHz), con una configuración en remoto. Esta configuración permite minimizar el bombardeo a la película por los iones positivos del plasma. Una ventaja importante de la técnica PECVD es que posibilita el crecimiento de películas a temperaturas bajas.[26] En paralelo, dependiendo de los parámetros del proceso, es posible conseguir la nanoestructuración de la película,[11] mejorándose también su adherencia sobre el sustrato.[27]

Los plasmas generados mediante esta técnica se pueden caracterizar midiendo sus parámetros fundamentales como son: tipo de especies iónicas y neutras formadas, temperatura electrónica, densidad electrónica etc. los cuales, dan una idea del tipo de especies y energía de la mismas que llegan a la película.[28] Este análisis es fundamental si se quiere incorporar un tipo dado de especies o átomos a la película.

Para la caracterización de los parámetros básicos del plasma se pueden utilizar diversas técnicas. Una de ellas es la sonda de Langmuir, capaz de medir parámetros del plasma como la temperatura y densidad de los electrones, función de distribución electrónica, potencial del plasma o potencial flotante.[29] Otra técnica de gran interés es la espectroscopia óptica de emisión (OES), capaz de detectar las diferentes especies excitadas del plasma,[30] así como corroborar las medidas de temperaturas electrónicas obtenidas mediante la sonda de Lagmuir[31]. En la figura 1.9 se muestran tanto una curva

característica del plasma medida mediante la sonda de Langmuir como un espectro óptico de emisión del mismo, para un plasma producido con una mezcla de N_2 e H_2 como gas plasmogeno a una presión de $5 \cdot 10^{-3}$ torr.

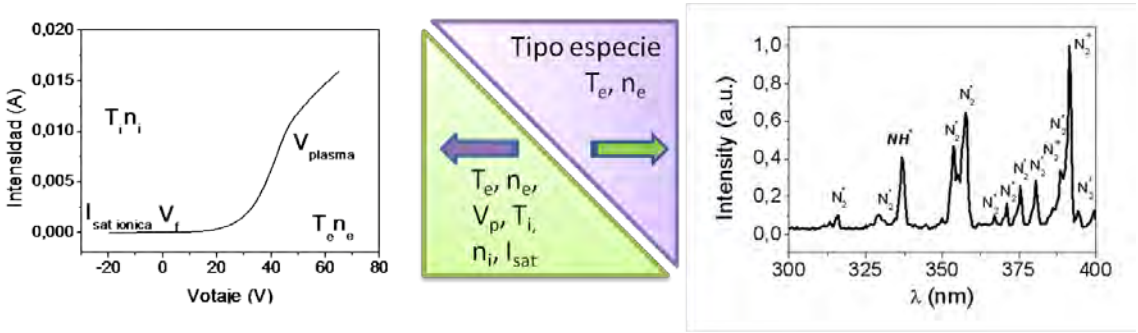

Figura 1.9. Resultados de la de caracterización de un plasma. A la izquierda se presenta la curva característica del plasma medida mediante la sonda de Langmuir. A la derecha se presenta el espectro de emisión medido mediante espectroscopia óptica de emisión.

Tradicionalmente, la técnica PECVD se ha utilizado para crecer capas de óxidos controlando sus espesores e índice de refracción, atendiendo fundamentalmente a su uso para aplicaciones ópticas.[27] En la actualidad está también cobrando especial relevancia, el uso de este tipo de técnica, para crecer materiales nanoestructurados. Ejemplos recientes de esta aproximación son el crecimiento de nanotubos de carbono (CNT)[15] o el crecimiento de nanocolumnas[11] o nanofibras Ag@TiO_2.[19] Estas últimas se han desarrollado en el laboratorio donde se ha realizado esta tesis. Algunos ejemplos de nanoestructuras crecidas mediante PECVD se muestran en la figura 1.10.

En esta figura, se muestran tres ejemplos de materiales nanoestructurados cuyas estrategias de crecimiento están bien diferenciadas. Por un lado, los nanotubos de carbono que se crecen utilizando una semilla metálica, desde la cual se generan los nanotubos.[15] Por otro lado, las fibras Core@Shell de TiO_2 con plata, cuyo mecanismo de crecimiento consiste en la oxidación y reducción de plata previamente depositada sobre el sustrato, generando procesos de estrés, que conllevan la formación de un hilo de plata (*core*) que posteriormente será recubierto por el óxido (*Shell*).[19] Por último nanocolumnas que crecen dependiendo de fenómenos como efectos de sombra de los primeros nucleos sobre las partículas de plasma incidentes[32] o la movilidad de esas partículas durante el crecimiento.

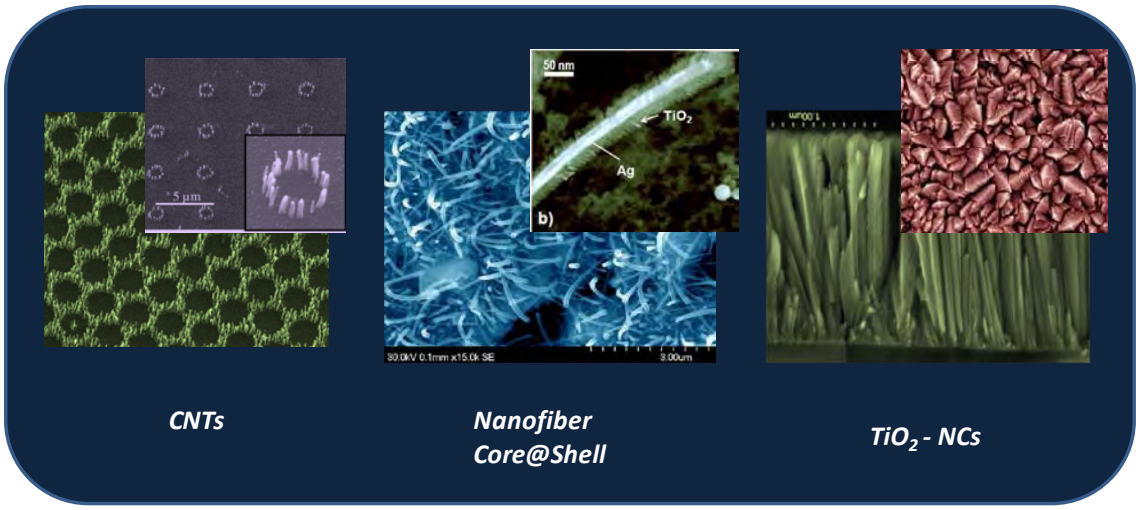

Figura 1.10. Ejemplos de nanoestructuras crecidas mediante PECVD. A la izquierda se muestran estructuras formadas por nanotubos de carbono. En el centro se muestra una imagen de fibras Ag@TiO_2. A la derecha se observan nanocolumnas de TiO_2.

La elección en este trabajo de tesis del método PECVD para la preparación de capas nanoestructuradas se ha debido a dos motivos. Por un lado, a la posibilidad que ofrece para controlar las características químicas del plasma, lo que permite crecer óxidos de titanio con diferentes cantidades de nitrógeno en su estructura. Por otro lado, su capacidad de usarse para controlar la nanoestructura de las capas en función de los parámetros experimentales durante el proceso de deposición. Estas perspectivas sobre el control del proceso se han demostrado ciertas a lo largo de este trabajo en el cuál se han preparado películas de TiO_2 con microestructura y estructura controlada que han resultado adecuados para su uso efectivo en aplicaciones fotocatalíticas, control del mojado superficial etc.

Los resultados obtenidos se presentan en el capítulo 4 de esta tesis correspondientes a un trabajo publicado en la revista "The Journal of Physical Chemistry C" (DOI. 10.1021/jp104634j, año 2010).

1.3.3- Preparación de capas delgadas y nanoestructuras superficiales de ZnO mediante plasma CVD

El ZnO es un material de gran interés debido a la gran variedad de aplicaciones que presenta.[8-10] Su preparación en forma de capa es indispensable para muchas de sus aplicaciones, utilizándose una gran variedad de métodos con este propósito.[33-36] Entre

los métodos utilizados para el crecimiento de estos materiales destaca el uso de los métodos químicos por vía húmeda,[36] capaces de general ZnO en forma de película delgada, fibras u otras nanoestructuras. Una alternativa a esta forma de fabricación es el crecimiento de estos nanomateriales de ZnO mediante métodos de vía seca.[8,10] La ventaja esencial de estos métodos reside en la posibilidad de eliminar más fácilmente los residuos líquidos generados durante el crecimiento de las películas, además de su relativa fácil implementación a escala industrial. Algunas micrografías de diferentes nanoestructuras de ZnO se muestran en la figura 1.11.

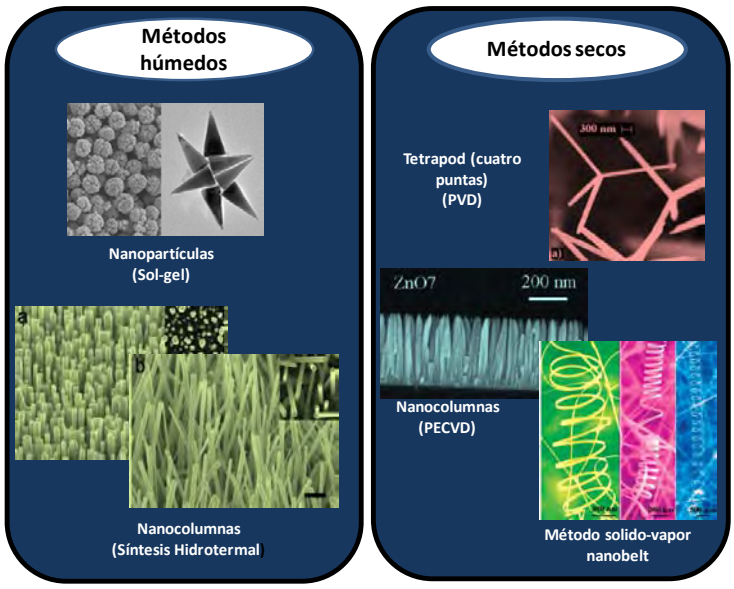

Figura 1.11. Diferentes microestructuras de ZnO y métodos de deposición utilizados.

En la figura 1.11 se muestran diferentes microestructuras de ZnO dependiendo del método de síntesis, discriminando si se trata de un método húmedo o seco. Para los métodos húmedos se muestran los casos de nanopartículas crecidas mediante Sol-gel[37] o nanocolumnas crecidas mediante un método hidrotermal.[38] Para el caso de métodos secos se muestran ejemplos de *"nanobelt"* crecido mediante procesos solido-vapor,[39] nanocolumnas crecidas mediante PECVD[40] o *"tetrapod"* crecidos mediante evaporación-PVD.[41]

En trabajos previos en el laboratorio donde se ha realizado esta tesis, se puso de manifiesto que la técnica de PECVD asistida por microondas, permite controlar la nanoestructura y propiedades de transporte eléctrico de capas de ZnO,[42] siendo un punto importante del estudio su dopado con aluminio para conseguir buena conductividad eléctrica y alta transparencia.

Para tener un control efectivo de la deposición PECVD se requiere conocer la composición de las especies del plasma, así como otros parámetros básicos, como son su temperatura electrónica e iónica y sus densidades electrónica e i ónica. Estos parámetros pueden ser modificados mediante cambios en la presión de la cámara durante el crecimiento de la película o bien cambiando la composición del plasma. Este último parámetro experimental permite además generar diferentes especies en el plasma capaces de controlar la ruptura del precursor al incorporar otras especies al plasma o bombardear la película al cambiar la temperatura electrónica. En trabajos precedentes, se ha estudiado cómo un plasma rico en O_2 produce una alta concentración de especies O atómico capaces de descomponer de forma efectiva el precursor.[11] Por otro lado, se ha podido comprobar cómo la adición de Ar al plasma produce un mayor bombardeo iónico sobre la película lo que se traduce en cambios microestructurales de la misma. Finalmente, se verificó que la temperatura del sustrato produce cambios en la movilidad de las especies del plasma que llegan al sustrato produciendo en general, una densificación de las capas. Este tipo de resultados previos han servido en esta tesis como punto de partida para entender los procesos del crecimiento de nanoestructuras superficiales en capas de ZnO crecidas mediante PECVD. Así, Un control exhaustivo de todos estos parámetros ha permitido fabricar capas con una gran variedad de texturas, estructuras y ordenación nanoestructural. El estudio de cómo la luminiscencia de las capas se ve afectada por dichos parámetros ha sido también un objetivo preferente de este trabajo, al que nos referimos con más detalle en la sección 1.4.4.

En efecto, un control exhaustivo de la nanoestructura es muy relevante para capas de ZnO, ya que dicha nanoestructuración determina el control de la fotoluminiscencia de este óxido, así como la posibilidad de modificar dicha emisión en presencia de una molécula o agente externo. Esta posibilidad es la que permite su uso para el desarrollo de sensores fotónicos.[8]

Los resultados obtenidos se presentan en el capítulo 6 de esta tesis correspondientes a un trabajo publicado en la revista "The Journal of Physical Chemistry C" (DOI. 0.1021/jp103902u, año 2010).

1.4-PROPIEDADES FOTOFUNCIONALES DEL TiO_2 y ZnO

Las propiedades del TiO_2 y ZnO que son objeto de estudio en esta tesis atienden a sus cualidades como materiales fotoactivos, es decir, teniendo en cuenta su respuesta cuando estos materiales interaccionan con luz dentro del rango del espectro ultravioleta-visible.

Los óxidos semiconductores de banda ancha ZnO y TiO_2, son buenos candidatos a ser usados en aplicaciones fotofuncionales debido a su gran estabilidad química en los entornos de trabajo y a la posibilidad de ser procesados de forma adecuada para la aplicación buscada.[43-44]

Las propiedades fotofuncionales de estos semiconductores se basan en los procesos de excitación de electrones desde la banda de valencia hasta la banda de conducción cuando sobre el material incide un f otón con energía superior al ancho de banda prohibida. Este proceso genera un par electrón-hueco, como ilustra la figura 1.12. La principal diferencia de cómo se ha abordado en esta tesis el estudio de las propiedades fotofuncionales del TiO_2 y ZnO radica en el modo en que se utiliza este par e^-/h^+.

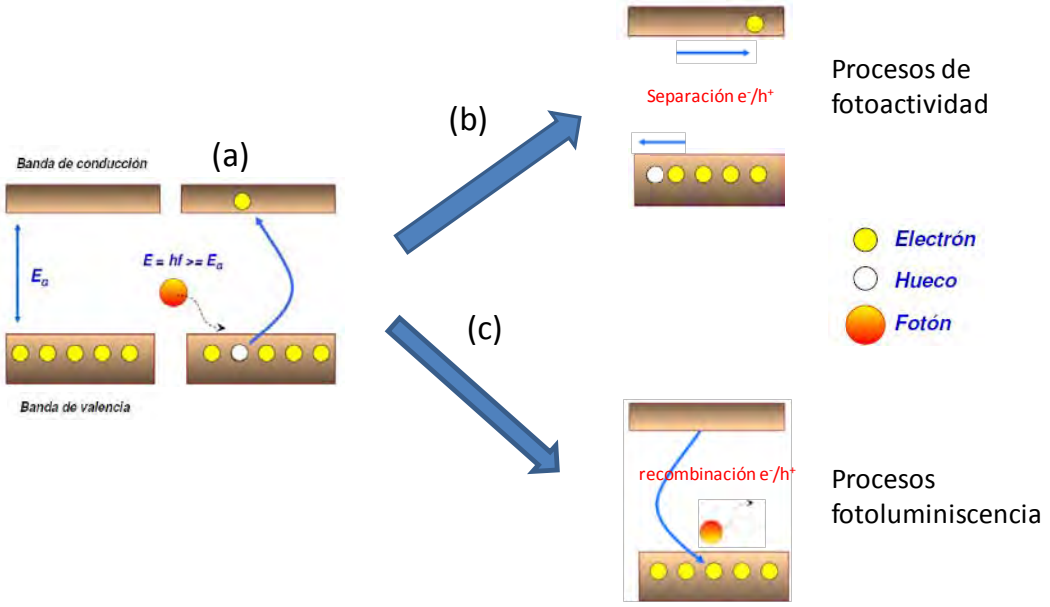

Figura 1.12. Esquema de procesos de fotoactivación de semiconductores de banda ancha. (a) proceso de fotoexcitación del semiconductor. (b) proceso de separación del par e^-/h^+ en TiO_2. (c) proceso de recombinación e^-/h^+ y la correspondiente emisión de un fotón debido a la recombinación del excitón en el caso del ZnO.

Los procesos de fotoactividad que involucran al TiO_2 se fundamentan en la separación de los portadores de carga de forma que se hacen reaccionar por separado al e^- y al h^+ en la superficie. Los procesos de fotoluminiscencia estudiados referidos al ZnO se fundamentan en la desexcitación del par e^-/h^+ por recombinación, proceso que genera un fotón.

1.4.1- Fotoactividad del TiO_2

El TiO_2 ha sido ampliamente estudiado debido a la fotoactividad que presenta cuando se ilumina con luz en el rango del ultravioleta. Típicamente, este tipo de estudios se han realizado con vistas a sus aplicaciones en fotocatálisis, usando este material en forma de polvo. En estos estudios se ha demostrado que la fotoactividad generada es extraordinariamente dependiente de la estructura y microestructura de TiO_2.[45]

Los estudios sobre la fotoactividad del TiO_2 en forma de lámina delgada son menos numerosos, aunque durante los últimos años han experimentado una progresión creciente. Una aplicación específica se refiere a los cambios de capacidad de mojado superficial bajo irradiación,[6] además de ampliar las posibilidades dentro del campo de la fotocatálisis.[46]

Para la mejora de la fotoactividad del TiO_2 es necesario tener en cuenta los siguientes aspectos:

Absorción de luz

En semiconductores intrínsecos, como es el caso del TiO_2, la energía umbral que resulta efectiva en generar pares e^-/h^+ coincide con la banda de energía prohibida del semiconductor (ver figura 1.12). Los semiconductores extrínsecos, como es el caso del TiO_2 dopado con Nitrógeno,[47] pueden absorber luz a longitudes de onda mayores debido a la modificación del gap de absorción o debido a la formación de estados electrónicos discretos en la banda de energía prohibida. Ambos procesos son resultado de la acumulación de defectos de la red del semiconductor.

Un objetivo prioritario en el contexto de un aprovechamiento efectivo de la fotoactividad del TiO_2 es utilizar la radiación solar y no fuentes artificiales para su excitación. El espectro ultravioleta visible de la radiación solar en la superficie terrestre

tiene la forma que muestra la figura 1.13, donde se ha señalado la longitud de onda umbral que define la anchura de banda prohibida del TiO_2, aproximadamente en el límite entre las zonas de UV y visible del espectro electromagnético. Ello significa que para todas las fases cristalinas del TiO_2 sólo se aprovecha el 5 % de la radiación total,[27] siendo un punto importante a abordar en esta tesis el aumento de dicha capacidad de absorción de radiación solar.

Una introducción crítica más detallada sobre este punto se recoge en la sección 1.4.3

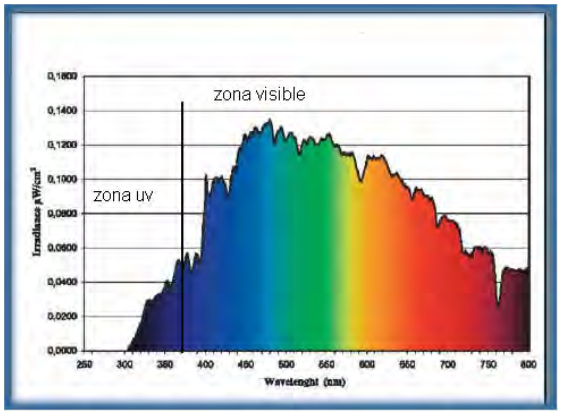

Figura 1.13. Espectro ultravioleta visible de la radiación solar en la superficie terrestre.

Atendiendo a estas premisas generales, históricamente, se ha investigado este fotocatalizador en forma de polvo debido a su fácil obtención mediante síntesis convencionales y la posibilidad de modificar su porosidad y otros parámetros capaces de exaltar su respuesta fotocatalítica.[48] Actualmente se ha desarrollado la utilización de este material en forma de capa delgada soportada, fácilmente separable del medio de reacción.[49] Esta forma de sintetizar materiales, puede ser usada para otros problemas que utilizan la luz solar como fuente de energía, como son las celdas solares, producción de hidrógeno en celdas fotoelectroquímicas etc. [50-51]

La fabricación del fotocatalizador TiO_2 en forma de lámina delgada se ha desarrollado usando diversas técnicas, como son sol-gel,[46] técnicas de deposición desde fase vapor tanto físicas[52-54] como químicas[52,55] etc. Recientemente se está aclarando cómo los diferentes parámetros estructurales y microestructurales de las películas crecidas, controlan la fotoactividad del material. Parámetros importantes en este sentido son el espesor,[56] porosidad[52] o microestructura de la muestra.[52]

Conviene también resaltar que para el TiO_2, la zona de energía prohibida depende de su fase cristalina, siendo 3.2 eV para la Anatasa,[57] 3.05 eV para el rutilo[58] y 3.4 eV para el material en forma amorfa.[27]

Otro factor muy importante a tener en cuenta es la influencia de la fase cristalina del material en la fotoactividad. En este sentido, la fase cristalina Anatasa ha demostrado ser la fase más activa del TiO_2,[59] aunque en la actualidad numerosos estudios están intentando comprender por qué la mezcla de fases rutilo-anatasa muestra una mejora en la fotoactividad del óxido.[60] Explicar esta sinergia es uno de los objetivos de esta tesis como se pondrá de manifiesto en el apartado 1.4.2.

Migración y recombinación de portadores

En teoría de semiconductores, se consideran portadores de carga a los electrones y huecos que pueden moverse por la red. Para producir procesos fotocatalíticos es necesario que los portadores de carga lleguen a la superficie de contacto del material con el medio. La movilidad de los electrones depende de la red cristalina por la que se transporta. Para la mayoría de procesos fotocatalíticos que involucran el transporte de estos portadores de carga, es fundamental conocer y evitar las posibles elimininaciones de estos portadores de carga mediante su recombinación con huecos.[61] Para ello, en primer lugar, se debe evitar que el semiconductor tenga centros de recombinación que produzcan dichas desexcitaciones.[61] Para el caso del TiO_2, se consideran centros efectivos de recombinación los defectos de red, la presencia de impurezas y otros defectos estructurales.

Para que se produzca la difusión de portadores hasta la superficie es necesario tener un campo eléctrico que favorezca el movimiento de los mismos desde el interior del semiconductor a la superficie. Este campo eléctrico puede ser generado mediante un campo eléctrico aplicado externamente o ser el resultado de una diferencia entre los potenciales químicos de las especies del medio y el nivel de Fermi del semiconductor. Esta diferencia de potenciales produce una transferencia de carga del semiconductor al medio o viceversa, dando origen a la formación de una barrera de Schottky en la intercara.

Formación de una barrera de Schottky en la superficie

La estructura electrónica del TiO_2 como la de otros semiconductores óxido se puede describir en primera aproximación como formada por una banda de valencia totalmente llena y una de conducción totalmente vacía, separadas por una zona de energías prohibidas. Si en el semiconductor hay un cierto grado de dopado tipo **n** como resultado por ejemplo de una pequeña pérdida de estequiometría, el nivel de Fermi del sistema se coloca entre los niveles discretos de los defectos y la banda de conducción. Un esquema de esta situación se presenta en la Figura 1.14 Esta sería la situación de un semiconductor másico que no estuviera limitado por el medio.

Figura 1.14. Esquema de bandas de semiconductor tipo n.

En la superficie de los sistemas reales, este esquema de bandas se puede ver drásticamente modificado si en contacto con el material se coloca alguna especie química, denominada aquí genéricamente como A, con un potencial electroquímico con menor energía que el valor correspondiente al del nivel de Fermi (Figura 1.15(a)). Si se da esta circunstancia se darían procesos de transferencia de carga desde el semiconductor a las especies A, convirtiéndose estas en especies de tipo A^-. Como consecuencia de ello, se genera un espacio de carga positivo dentro del material que induce un campo eléctrico que, como consecuencia, produce un doblado de las bandas en la superficie, tal y como se representa en la Figura 1.15(b). Ese doblado de las bandas prosigue hasta que el nivel de Fermi coincide con el nivel del potencial electroquímico del sistema A/A^-. De esta forma se produce lo que se denomina una barrera de potencial, denominada "barrera de Schottky" en la superficie.[62] La zona de carga positiva y, en consecuencia la longitud de la barrera de Schottky se puede extender varios cientos de nanómetros, dependiendo de la conductividad eléctrica del material. Su altura depende del potencial electroquímico del sistema A/A^-.

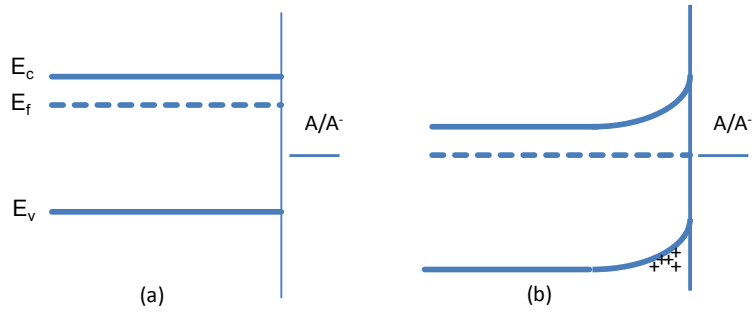

Figura 1.15. Esquema de formación de la barrera de Schottky.

La importancia de la formación de una barrera de Schottky en la superficie para el control de los procesos de foto-activación es extraordinaria. Ella es la que propicia que los foto-huecos, generados en la banda de valencia mediante la irradiación del material con fotones de energías capaces de excitar electrones desde la banda de valencia a la de conducción (figura 1.16), salgan hasta la superficie donde reaccionan con las especies adsorbidas sobre la misma (tener en cuenta que los foto-huecos tienen tendencia a ocupar los niveles más altos en los diagramas de energía definidos para los electrones con carga negativa). La etapa controlante de los procesos foto-químicos en TiO_2 y otros semiconductores inorgánicos es en consecuencia la migración de foto-huecos hasta la superficie, proceso que se ve favorecido si la altura y la pendiente de la barrera de Schottky son más elevadas. Estos conceptos se usarán de forma sistemática a lo largo de este trabajo de tesis y más concretamente en el capítulo 4 dedicado al estudio de la foto-actividad de bicapas rutilo-anatasa.

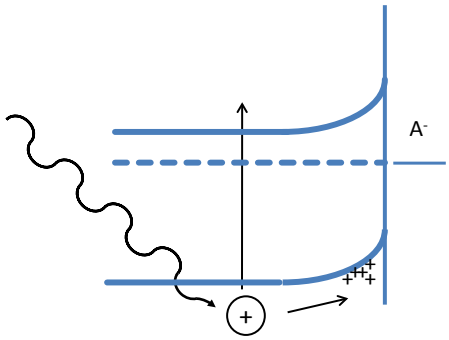

Figura 1.16. Esquema de proceso degeneración y migración del par e^-/h^+.

1.4.1.1-Control del mojado superficial

El ángulo de contacto se define como el ángulo que forma la superficie de un líquido al entrar en contacto con un sólido. El valor del ángulo depende principalmente del equilibrio entre las fuerzas adhesivas líquido-sólido y las fuerzas cohesivas del líquido como se muestra la figura 1.17.

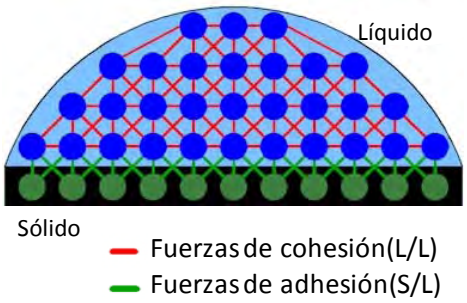

Figura 1.17. Esquema representativo del equilibrio de fuerzas cohesivas-adhesivas.

En la figura 1.17 se muestran de forma simplificada los átomos/moléculas del sólido y del líquido. Las fuerzas de cohesión involucran al átomo/molécula que están en la fase líquida y sus vecinos más cercanos, siempre que formen parte de la fase líquida. Las fuerzas de adhesión involucran a los átomos/moléculas que están en fase líquida con los átomos/moléculas del sólido.

El ángulo de contacto depende de las energías intersuperficiales en juego. Si denotamos la energía de la intercara sólido-gas como γ_S, energía sólido-líquido como γ_{SL}, la presión de vapor del líquido sobre el sólido como π_e y la energía líquido-vapor como γ_{LV} (véase figura 1.18) se obtiene la ecuación de Young modificada[1],[63] (ecu. 1.1) que satisface la condición de equilibrio:

$$\gamma_S - \gamma_{SL} - \pi_e = \gamma_{LV} \cos\theta \text{ (ecu. 1.1)}$$

[1] La ecuación de Young original relaciona las fuerzas en la intercara según el esquema de la figura 1.18. Sin embargo ha sido una práctica frecuente usar una expresión modificada en forma de energías superficiales y presiones.

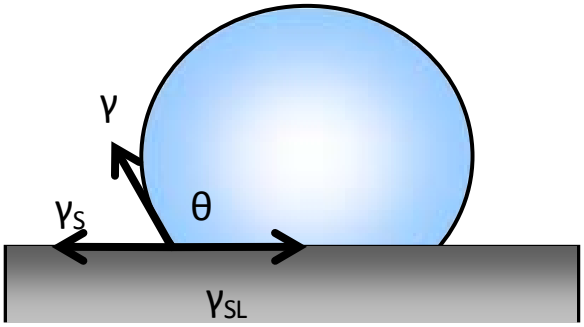

Figura 1.18. Esquema de las energías intersuperficiales gota-superficie.

donde θ es el ángulo de contacto en el equilibrio.

Para el caso particular de que el líquido utilizado sea agua, si el valor del ángulo de contacto es inferior a 90º, se dice que la superficie tiene un comportamiento hidrofílico. Por el contrario, cuando este ángulo supera ese valor se trata de una superficie hidrofóbica.

Esta propiedad puede ser utilizada para evidenciar la actividad de las muestras de TiO_2 bajo irradiación. Desde el trabajo de Wang,[6] que observó cómo el TiO_2 cambia su carácter hidrofóbico a hidrofílico cuando es iluminado con luz en el rango del ultravioleta, son muchos los trabajos que han estudiado esta propiedad.[64-66] De todos ellos, sólo algunos trabajos han puesto de manifiesto una cierta actividad bajo irradiación en el visible correspondiendo a muestras de TiO_2 modificadas mediante distintos elementos.[67] Desde un punto de vista conceptual, este ensayo tiene carácter superficial sin estar del todo claro los parámetros de los que depende.[52] Es por ello que el estudio de la actividad en el visible de las muestras puede ayudar a conocerlos.

Cabe asimismo señalar que esta propiedad del TiO_2 puede ser interesante desde un punto de vista tecnológico, ya que con este material se pretende preparar superficies autolimpiables. Esta aplicación tecnológica se relaciona con la formación de gotas de rocío en superficies que se encuentran a la intemperie. La irradiación solar y el consiguiente cambio de la superficie a superhidrofílica, provoca que este agua se extienda sobre la superficie y arrastre la suciedad acumulada en la superficie del material.[68]

1.4.1.2-Procesos fotocatalíticos

El TiO_2 es un fotocatalizador típico debido a la fotoactividad que presenta cuando se irradia con luz UV, además de poseer una buena estabilidad química.[69-70]

Como ya se ha adelantado anteriormente, los procesos fotocatalíticos se basan en la excitación del semiconductor mediante luz y la posterior separación en la superficie del par e^-/h^+ cómo ilustra la figura 1.12. Las reacciones de reducción y oxidación que involucran a este par se producen en la superficie del sólido excitado, sin que el catalizador sufra cambios químicos.

La fotocatálisis depende fuertemente de parámetros del medio como pH, temperatura y concentración de contaminantes, así como la intensidad de la radiación. Para poder utilizar este proceso como test de fotoactividad se deben fijar los parámetros anteriormente expuestos.

En esta tesis se ha investigado la actividad fotocatalítica donde el fotocatalizador consiste en una lámina delgada de TiO_2. Un punto muy importante en este caso es que la fotoactividad del TiO_2 se induce por luz UV lo que se considera insuficiente si se quiere excitar el TiO_2 con luz solar. Por ello, se están realizando modificaciones del óxido para aprovechar la luz en el rango del visible.[47,71] Las aproximaciones desarrolladas para ello se explican con más detalle en apartado 1.4.3.

Las muestras utilizadas durante el transcurso de esta tesis se prepararon en forma de lámina delgada. Una ventaja que presentan dichas muestras frente a las muestras crecidas en forma de polvo es su fácil extracción de la fase liquida una vez realizada la fotocatálisis, consiguiéndose así que el fotocatalizador no sea un residuo de la fase líquida.[72]

1.4.2-El problema de las intercaras anatasa-rutilo

De todas las fases puras del TiO_2, se ha demostrado que la fase Anatasa es la más activa si se utiliza este óxido como fotocatalizador.[59] Sin embargo, en la bibliografía, sobre todo para muestras en polvo, se ha demostrado que una mezcla de las fases anatasa-rutilo produce una mejora de la fotoactividad de la muestra. De hecho, la muestra

comercial más utilizada es el P-25 de Degussa, consistente en una mezcla de las fases anatasa y rutilo en las proporciones 80% y 20% respectivamente.

Recientemente se están intentando comprender las causas de este efecto sinérgico entre las dos fases y, más concretamente, cuál es el tipo de fenómeno que se produce en la intercara entre ambas fases cristalinas. Estudios realizados, por un lado Kawahara[73] y por otro lado, por Zhang[60] utilizando sistemas cuyas intercaras están en contacto con el medio problema, consiguieron observar una mejora en la fotoactividad de las muestras, siendo la existencia de estas intercaras las causantes de dicha mejora. En ese contexto se acuñó el término "hot spot" para referirse a los puntos de esas intercaras, que en contacto con el medio, serian responsables de la exaltación de la fotoactividad.

Sin embargo, este tipo de sistemas en forma de polvo, no son ideales desde un punto de vista estructural y microestructural, ya que las muestras no tienen un tamaño de grano bien definido ni una microestructura controlada.

Una alternativa a este tipo de sistemas para comprender las causas del efecto sinérgico anatasa-rutilo es el estudio de sistemas formados por una bicapa de estas dos fases. En esta tesis se plantea el estudio de bicapas anatasa-rutilo formadas por dos capas, crecidas una sobre de la otra, como ilustra la figura 1.19. La primera capa crecida sobre el sustrato, consiste en una capa de TiO_2-rutilo, mientras que la otra consiste en una capa de TiO_2-Anatasa crecida sobre la capa previa de rutilo. En este sistema se pueden tener bien definidos parámetros tales como tamaños de grano, microestructura, etc. por lo que puede servir para estudiar si existe alguna sinergia atribuible a la interacción electrónica entre ambas capas.

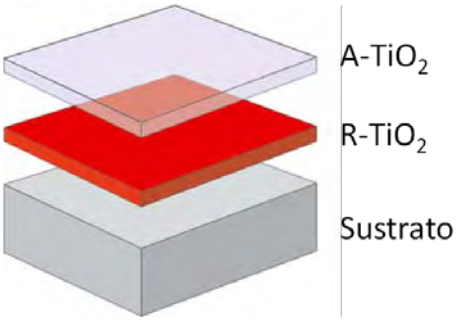

Figura 1.19. Esquema de una bicapa de TiO_2 crecida sobre el sustrato. A-TiO_2 se refiere a una capa Anatasa y R-TiO_2 se refiere a una capa de Rutilo.

En paralelo al estudio de la fotoactividad catalítica de este tipo de muestras, se propone en esta tesis el estudio de la evolución del ángulo de contacto de la muestra cuando se ilumina con luz UV. Dado que esta propiedad del TiO_2 tiene un marcado carácter superficial,[52] cabría pensar que este tipo de procesos no depende del espesor u otras características másicas de la bicapa, sino del estado superficial de la capa más externa expuesta al medio de reacción.

Los resultados obtenidos se presentan en el capítulo 5 de esta tesis correspondientes a un trabajo publicado en la revista ChemPhysChem, 2010.

1.4.3-Sensibilización del TiO_2 con luz visible

El principal problema que hay que resolver si se quiere maximizar el rendimiento energético del TiO_2 usando radiación solar es lograr su sensibilización con luz visible.[47] El TiO_2 sólo aprovecha el rango del ultravioleta del espectro solar que, como se ha dicho anteriormente, sólo es el 5% de la luz solar total que llega a la tierra.[57] Como el aprovechamiento solar referido al rango del UV es pequeño, la extensión del rango de absorción hasta el visible es un problema crítico en la actualidad para una gran cantidad de aplicaciones

Para ello, se ha propuesto modificar la estructura de bandas del semiconductor consiguiendo una mayor absorción de luz en el rango visible. Esta estrategia se plantea desde una doble vertiente. La primera persigue la disminución de la banda de energía prohibida ("band gap") del óxido. La segunda se basa en la generación de estados electrónicos discretos dentro del gap, utilizando dichos estados para los procesos de excitación. Ambas aproximaciones deben producir un aumento en la absorción de la luz solar en el visible ampliando el rango de absorción.

El objetivo de cambiar la capacidad de absorción ha dado lugar a un gran número de publicaciones.[74-75] Con el propósito de cambiar las características electrónicas del óxido se ha abordado la incorporación a la red de cationes de la serie de transición que se intercambiarían por el catión titanio.[76-78] Se han utilizado elementos de la serie de transición como son Mn, Cr, V, Co etc. En primera aproximación, parecería que la introducción de estos cationes en la red del TiO_2 produce los cambios necesarios en su estructura de bandas que se traducen en un aumento de la absorción de la luz visible y

de poder realizar procesos fotocatalíticos con esta luz.[79] Sin embargo, fenómenos de segregación de los óxidos componentes y/o la exaltación de los procesos de recombinación e^-/h^+ dan como resultado que tal estrategia se haya descartado casi por completo en la actualidad. Otra aproximación es la modificación de la estructura electrónica del óxido utilizando aniones. Se ha postulado para ello el uso de N, F, S, P etc.[47,75,80-81] Desde el trabajo de Asahi,[47] sobre TiO_2 modificado con N (N-TiO_2 en lo sucesivo), que puso de manifiesto la estabilidad química que presenta dicho material modificado y su actividad fotocatalítica con luz visible, el estudio de los sistemas N-TiO_2 ha experimentado un impulso extraordinario.[74-75,82]

Un punto de gran interés en este contexto es determinar las causas que hacen que el TiO_2 con Nitrógeno presente fotoactividad en el visible. Uno de los problemas principales reside en determinar cuál es la especie de nitrógeno que realmente induce esta actividad y cómo la misma modifica la estructura de bandas del semiconductor. En la bibliografía hay una gran confusión en este sentido con diversas propuestas, a veces contradictorias. Este problema se ha abordado de diferentes puntos de vista mediante la utilización de diferentes técnicas de caracterización como EPR,[83] XPS,[71] RAMAN,[84] Elipsometría[85] etc. así como utilizando cálculos cuánticos.[57] A lo largo de esta tesis se han utilizado diferentes técnicas de caracterización con este fin.

Los resultados obtenidos se presentan en el capítulo 4 de esta tesis correspondientes a un trabajo publicado en la revista "*The Journal of Physical Chemistry C*" (2009, Volumen 113, páginas 13341–13351).

1.4.4-Fotoluminiscencia del ZnO

En general, la emisión de luminiscencia del ZnO depende directamente de cómo se excita el material, así como del método de síntesis utilizado para su preparación, ya que las propiedades electrónicas se ven por lo general muy afectadas por el método de fabricación. Para semiconductores óxidos tales como el ZnO, la energía de la radiación de excitación tiene que ser mayor que la energía del gap del semiconductor.[7] La luminiscencia del ZnO se caracteriza por dos emisiones, una en el rango del ultravioleta próximo y otra en el visible (Fig Foto izq). La primera emisión está relacionada con la formación de un excitón (par electrón-hueco) en el material. La segunda emisión está

relacionada con la recombinación de pares electrón-hueco que involucran a los estados electrónicos dentro del gap formados por los defectos del material.[7] La naturaleza y origen de ambas emisiones se ilustran en el esquema de bandas de la figura 1.20.

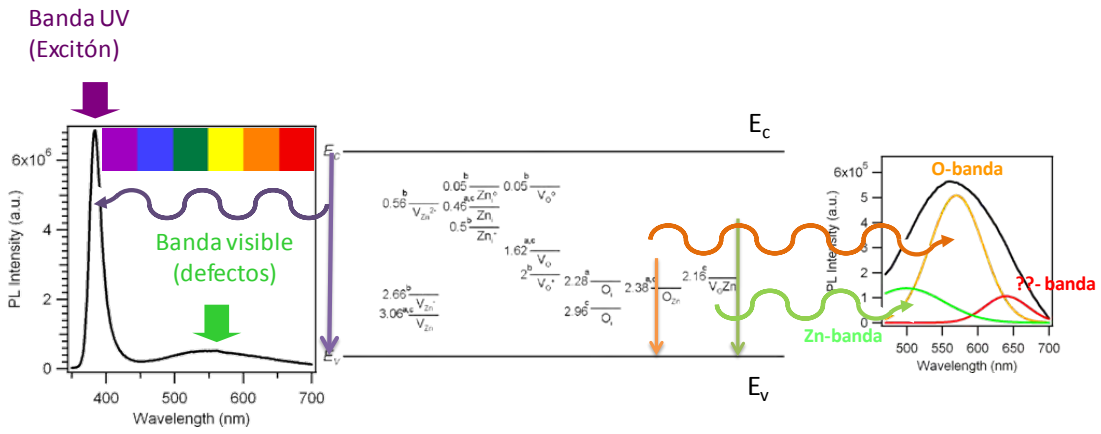

Figura 1.20. Procesos de desexcitación por emisión del semiconductor ZnO. A la izquierda se muestran las dos emisiones encontradas al registrar el espectro uv-vis. En el centro se muestra un esquema de bandas simplificado, con la posición de todos los estados electrónicos en el gap designados teóricamente con la notación de Kröger-Vink. A la derecha se presenta la deconvolución de la banda de emisión en el visible de ZnO asociada a defectos de oxígeno y Zinc.

En la parte central de la figura se presenta un esquema simplificado de la estructura de bandas del ZnO, en el cual se muestran las bandas de valencia y de conducción, además de una gran cantidad de estados electrónicos en el gap del semiconductor asociados a defectos en la red del material. Las flechas indican posibles desexcitaciones del material produciendo la emisión de fotones de diferentes longitudes de onda. El espectro que se obtiene se caracteriza por presentar una banda extensa atribuida a la desexcitación del excitón del material y por otro lado una serie de emisiones de luminiscencia asociadas a defectos de Zinc para longitudes de onda relativamente menores (más energía) y defectos asociados al Oxígeno a longitudes de onda mayores (menor energía). Existe otra banda a menores longitudes de onda la cual no ha sido asociada a ningún defecto electrónico del material.[7]

La luz emitida por el ZnO puede utilizarse para diferentes aplicaciones como el desarrollo de sensores de gases fotónicos,[8] laseres de ultravioleta[10] o diodos electroluminiscentes.[9] Para todas estas aplicaciones es necesario tener un buen conocimiento del material depositado y, en lo posible, exaltar el rendimiento de emisión

en el rango de energía deseado. En general, se sabe que el rendimiento de fotoluminiscencia depende estrechamente de su estado superficial, cristalinidad, microestructura, defectos del material etc.

El trabajo que se expone en esta tesis se enmarca dentro del contexto del desarrollo de sensores fotónicos de gases. Sin embargo, en esta memoria no se ha incorporado ningún resultado al respecto ya que los mismos están incluidos en un documento de patente que en la actualidad está en fase de redacción.

El trabajo que puede comentarse aquí se refiere al crecimiento de diferentes nanoestructuras de ZnO (nanocolumnas, fibras, etc.), centrando el estudio especialmente en la relación entre la emisión de fotoluminiscencia del material y su nanoestructura. Para ello, durante el transcurso de esta tesis se han fabricado capas finas de ZnO crecidas mediante la técnica de deposición PECVD mediante la cual se ha perseguido tener un control estricto sobre sus características estructurales y microestructurales, relacionando dichas características con las propiedades fotónicas del material.

Los resultados obtenidos se presentan en el capítulo 6 de esta tesis correspondientes a un trabajo publicado en la revista "*The Journal of Physical Chemistry C*" (DOI. 0.1021/jp103902u, año 2010).

1.5-CONSIDERACIONES METODOLÓGICAS

1.5.1- Fotodegradación de colorantes

Para verificar la foto-actividad de las capas de TiO_2 se ha seguido la degradación del colorante naranja de metilo en disolución (10^{-5} M) bajo irradiación UV o visible. Para este estudio se ha medido la evolución del espectro de absorción de las disoluciones en función del tiempo de irradiación. Un ejemplo de la evolución se ejemplifica en la figura 1.21(c). En ella, se observa cómo evoluciona la banda de absorción del colorante del espectro de UV-visible, tomando una medida cada 5 min.

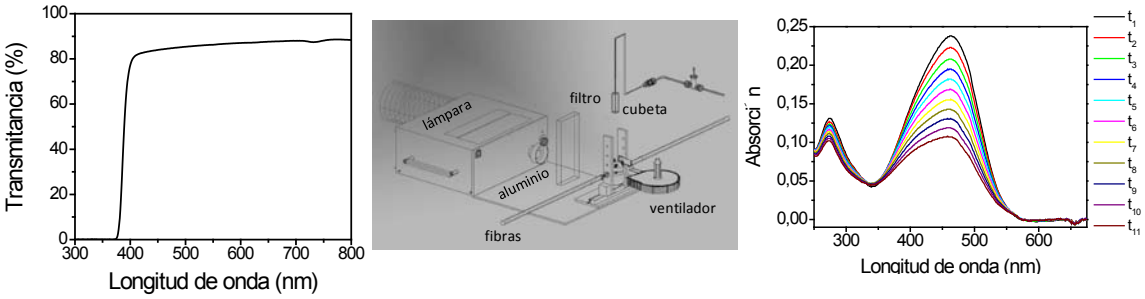

Figura 1.21. Ensayo de fotodegradación de colorante. A la izquierda se muestra el espectro UV-visible del metacrilato para justificar su uso como filtro del UV. En el centro un esquema de el experimento utilizado. A la derecha la evolución del pico de absorción del naranja de metilo durante los experimentos realizados.

Para estos experimentos se utiliza una muestra de TiO_2 en forma de capa fina, cuya superficie es 1×0.9 cm^2. Para realizar los ensayos de forma correcta se debe tener en cuenta la distancia de la fuente a la disolución de colorante, la estabilidad de la fuente y la cantidad y concentración de colorante, además del contenido de oxígeno en la disolución. El sistema experimental utilizado se muestra en la parte central de la figura 1.21.

El dispositivo que se muestra en la parte central de la figura 1.21 consta de una lámpara de Xenón de gran intensidad como emisor de fotones, una base de Aluminio que sirve como bancada óptica que permite mantener las distancias fijas de la fuente a la muestra, opcionalmente un filtro de ultravioleta que consiste en un paralelepípedo de metacrilato cuyo espectro de transmisión se muestra en la figura 1.21(a), una cubeta de cuarzo para contener el colorante así como a la lámina y dos fibras ópticas conectadas a una fuente de ultravioleta-visible y la otra a un detector. Además, el sistema consta de un sistema de burbujeo, que mantiene la disolución saturada en oxígeno y un ventilador para evitar que el sistema se caliente.

Para determinar el grado de degradación fotocatalíticia del colorante proporcionado por cada muestra, experimentada por el colorante, se calculó la integral del pico de absorción del colorante en el visible dividiéndolo por la absorción inicial del colorante, obteniéndose el grado de degradación del colorante como muestra la figura 1.21(b). La intensidad del pico de absorción está directamente relacionada con la concentración del colorante utilizado. Para hallar la constante cinética de la reacción, asumiendo un proceso de primer orden, se aproxima la evolución de intensidades a la

ecuación $I = I_0 e^{-\frac{t}{k}}$, donde I_0 corresponde a la intensidad de la absorción del colorante en el momento inicial, I intensidad de la absorción del colorante en el tiempo t y k es la constante de la reacción, cuyas unidades son $[t^{-1}]$.[43]

1.5.2-Ángulo de contacto bajo irradiación

Este ensayo basado en el método de Young[63] consiste en la observación de cambio del ángulo que forma una gota de agua de pH controlado sobre la superficie de la muestra. En nuestro ensayo, este ángulo de contacto se mide en función del tiempo de iluminación cuando sobre la muestra se incide con luz. Para verificar la fotoactividad de las muestras se realiza el ensayo en tres partes. La primera parte corresponde a la evolución del ángulo de contacto con el tiempo cuando la muestra está bajo irradiación visible observándose si la muestra evoluciona hacia una superficie con carácter hidrofílico. En la segunda parte se irradia la muestra con luz UV observándose la evolución de la muestra a una superficie con carácter hidrofílico. Por último, en la tercera parte se estudia la recuperación de la muestra en la oscuridad hasta recuperar una situación de carácter hidrofóbico.

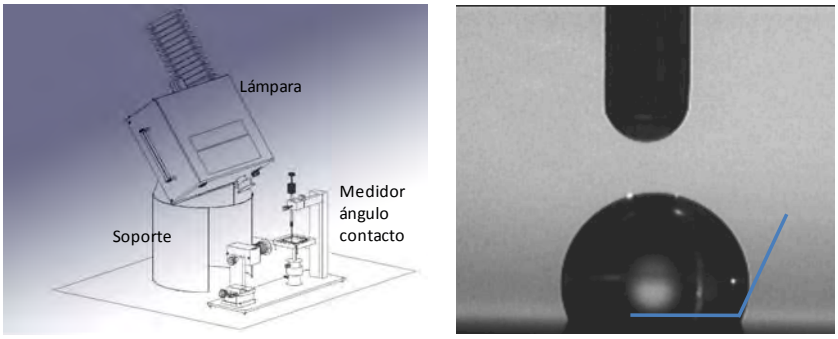

Figura 1.22. Imagen del dispositivo experimental utilizado (a) y de la geometría de una gota depositada sobre una capa de TiO_2 (b).

El instrumento de medida está formado por una cámara conectada a un ordenador, además de una jeringa para depositar las gotas sobre la superficie.

El dispositivo experimental utilizado se muestra en la figura 1.22. El dispositivo está compuesto por una lámpara de Xenon, soporte de la lámpara, cámara y el sistema dosificador de gotas de agua. Además se representa una imagen típica de una gota depositada sobre la superficie del TiO_2. El ángulo de contacto sobreimpreso sobre la imagen de la gota presentada en una figura se determina mediante un software disponible dentro del sistema de control del aparato.

1.5.3-Deposición de películas delgadas de N-TiO_2 mediante plasma

Dispositivo experimental y condiciones de preparación.

En la Figura 1.23 se presenta un esquema de la cámara de deposición de películas delgadas PECVD que se ha utilizado en este trabajo. El sistema experimental consta de las siguientes partes:

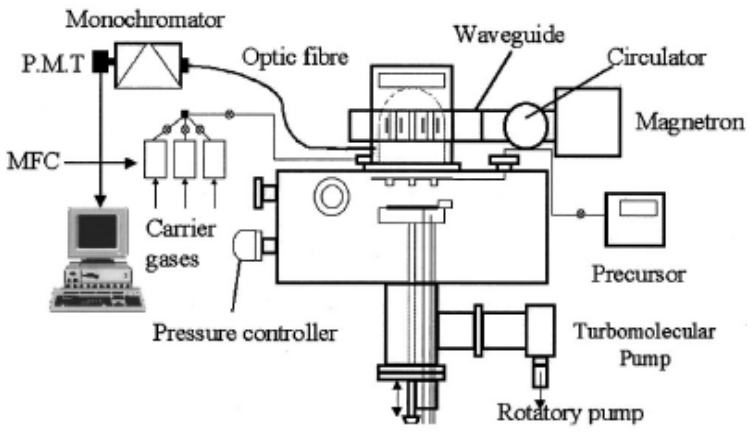

Figura 1.23. Esquema sistema de deposición de películas delgadas PECVD.

Sistema de generación del plasma.

Para la generación del plasma se ha utilizado una fuente comercial SLAN I de la casa Plasma Consult, GMBh, Alemania. El mismo integra un sistema de acoplo de las microondas al vaso de cuarzo donde se genera la descarga. Para cerrar el circuito eléctrico y evitar que alguna potencia de microonda llegue al sustrato, se colocó una rejilla entre el vaso y el portamuestras que eléctricamente está conectada a tierra.

Este sistema de deposición lleva acoplado un conjunto de imanes de 875 Gauss que consigue que la descarga se pueda mantener a presiones del orden de 10^{-4} torr (condiciones ECR).

La potencia máxima que puede alcanzar la fuente de microondas es 2000 W, pero durante el transcurso de esta tesis se fabricaron las muestras con 400 W de potencia

Sistemas de inyección de precursores.

Para la deposición de las películas de TiO_2 y ZnO se han utilizado cuatro precursores diferentes. Los precursores utilizados son Tetrakis isopropoxido de titanio (TTIP), cuya fórmula química es $[(CH_3)_2CHO]_4Ti$; Tetrakis dietil amino de Titanio (TDEAT), cuya fórmula es $[(CH_3CH_2)_2N]_4Ti$; Tetrakis dimetil amino de Titanio (TDMAT), cuya fórmula es $[(CH_3)_2N]_4$ Ti. Para preparar las capas de ZnO se usó el precursor Dietil Zinc cuya fórmula es $(CH_3CH_2)_2Zn$. Un esquema de los precursores de Ti se muestra en la figura 1.24.

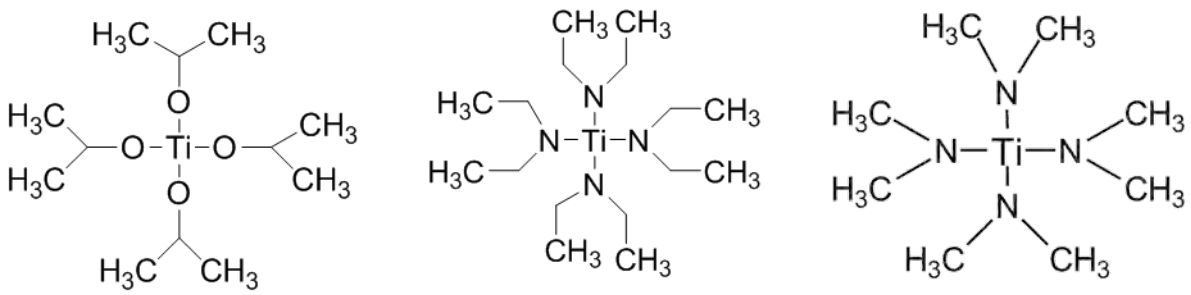

TTIP **TDEAT** **TDMAT**

Figura 1.24. Precursores de Titanio utilizados para el crecimiento de las películas N-TiO_2. (a) TTIP, (B) TDEAT, (C) TDMAT.

Estos precursores se eligieron debido a que el TTIP es un precursor que conteniendo Titanio y Oxígeno tiene una presión de vapor relativamente alta y no es corrosivo. Los precursores TDMAT y TDEAT se utilizaron porque contienen Titanio y Nitrógeno en su estructura y el precursor Et_2Zn se utilizó debido a que es un precursor de Zinc volátil comercial con poco contenido de Carbono.

Para la dosificación de precursores dentro de la cámara se tuvo en cuenta la presión de vapor de los mismos. Para los precursores TTIP y TDEAT se escogió un sistema de burbujeo de gas inerte como muestra la Figura 1.25. El precursor TDMAT tiene una presión de vapor adecuada en las condiciones de trabajo, por lo que solamente hubo que conectarlo a la cámara sin tener ninguna consideración adicional. Por otro lado el precursor de Zinc, al tener una elevada presión de vapor, se dosifica mediante un controlador de flujo másico regulable de 5 sccm.

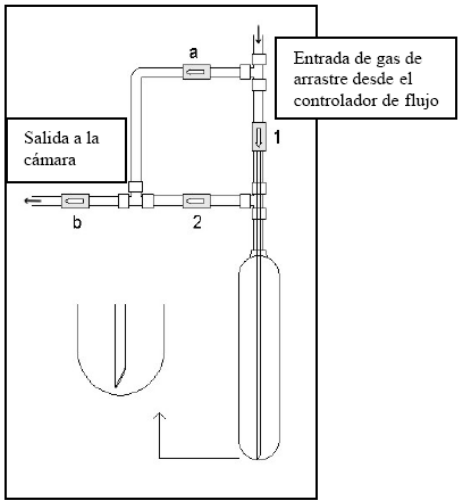

Figura 1.25. Esquema del sistema de burbujeo para precursores de baja presión de vapor.

Condiciones experimentales.

Los parámetros que se variaron fueron los siguientes:

A- composición del plasma cambiando la relación N_2/O_2 gradualmente. Se consideró además la incorporación de Ar y H_2 en el plasma.

B- Temperatura de los sustratos: 300 K, 410 K, 473 K, 523 K y 573 K.

C- Presión de la cámara. Se prepararon muestras en condiciones estándar (3-4 x 10^{-3} Torr) y en condiciones ECR (5-6 x10^{-5} Torr).

El espesor de la muestra varía según la aplicación, estando todas ellas en el rango 10-2000 nm.

Los sustratos utilizados fueron: Sílice fundida, Silicio intrínseco (100), Silicio extrínseco (100), osciladores de cuarzo, Titanio metálico.

1.5.4- Diagnosis de plasma

Para la diagnosis de plasma se han utilizado tanto la sonda de Langmuir como la espectroscopia óptica de emisión.

La sonda de Langmuir se basa en la introducción de un hilo conductor dentro del plasma, al cual se le aplica un potencial eléctrico para producir una corriente de

electrones o iones respecto a ese potencial. El uso de la sonda de Langmuir es probablemente la forma más simple de caracterizar el plasma. Esta técnica, a diferencia de la espectroscopia de emisión óptica, es una técnica perturbativa; por ello, el hilo conductor que se introduce debe estar diseñado cuidadosamente para que no perturbe o interfiera con el plasma. A pesar de todo, la interpretación de la curva corriente-voltaje que se mide no es trivial y desde los tiempos de Langmuir (1927) no han dejado de aparecer teorías que intentan mejorar esta técnica. La medida del flujo de partículas es esencialmente local pudiendo ser utilizada para caracterizar el plasma en la zona de depósito de las películas. Con la sonda de Langmuir se puede medir densidades electrónicas (n_e) e iónicas (n_i), temperatura electrónica (T_e), la función de distribución de los electrones (f_e) y tiempo de vida de las especies en el plasma. Para caracterizar el plasma, una vez obtenida la curva característica corriente-voltaje, se utilizó la técnica propuesta por F.F.chen basada en la cuidadosa determinación del potencial flotante.[86]

Por otro lado, la OES se basa en registrar la radiación electromagnética proveniente del decaimiento de las especies excitadas del plasma, las cuales emiten a una longitud de onda característica debido a su estructura atómica o molecular. La principal ventaja de la técnica OES es que es capaz de discernir las especies radiativas existentes en el plasma, aunque también es capaz de medir temperaturas electrónicas en ciertos casos. Para reconocer las especies existentes en el plasma se utilizan bases de datos. La base de datos más utilizada para la diagnosis de los plasma es la NIST Atomic Spectra Database.[87]

En la figura 1.23 se muestra la posición de la fibra óptica utilizada para las medidas de OES. Como se muestra en dicha figura los espectros adquiridos se obtienen directamente de la descarga luminosa. La punta de la sonda de Langmuir se coloca en la misma posición que el centro del portasustratos.

Los resultados obtenidos utilizando estas técnicas se presentan en el capítulo 3 de esta tesis correspondientes a un trabajo publicado en la capítulo del libro "Industrial Plasma Technology " (WILEY-VCH, Weinheim, Alemania, 2010, pags. 349-355).

1.5.5- Métodos de implantación iónica y nanoestructuración superficial

Como se ha explicado previamente, la técnica de implantación de iones es una técnica de modificación superficial de materiales basada en hacer incidir sobre una muestra, un haz de iones previamente acelerados mediante campos eléctricos. El perfil de implantación de los iones depende directamente de la energía utilizada para la implantación y del ángulo de incidencia. En el caso que aborda esta tesis, se utilizaron energías que están en el orden de las decenas o centenas de Kiloelectronvoltios y ángulos de incidencia de 0 ó 45 grados para las distintas energías. Los iones utilizados fueron N_2^+, B^+, S^+, F^+. Las muestras se obtuvieron en un acelerador de media energía de configuración lineal. Los iones utilizados fueron escogidos debido a la diferencia de afinidad química que tienen con la matriz de TiO_2, lo que, en principio puede hacer pensar en la obtención de diferentes microestructuras debido a los defectos generados en la red del TiO_2. El rango de energía utilizado permite obtener perfiles de implantación dentro de un espesor comprendido entre las decenas o centenas de nanómetros. Todos los perfiles de implantación se calcularon de forma teórica, utilizando el programa de cálculo SRIM (www.srim.org). Para conseguir implantar a 45 grados se diseño un portamuestras calentable para tal efecto como muestra la figura 1.26.

Figura 1.26. Portamuestras del acelerador de partículas para implantar a 45º.

Este sistema experimental propuesto consiste en una lámina de acero formando un ángulo de 45º con el haz incidente, pudiéndose calentar durante el proceso mediante una resistencia interna. El proceso es compatible con las condiciones de vacío y temperatura requeridas, además de los requisitos tanto de conductividad eléctrica como de conductividad térmica.

La técnica de implantación iónica se considera una técnica de postratamiento, ya que su utilidad es modificar la composición/estructura de la superficie del material que previamente ha sido crecida. En nuestro caso se trata de capas de TiO_2 preparadas mediante PECVD.

Condiciones experimentales del acelerador.

La irradiación se llevó a cabo en el acelerador High current ion implanter DANFYS 1090-200 (DANFYSIK A/S, Jyllinge Denmark) en the Institute of Ion Beam Physics and Materials Research (Forschungszentrum Dresden-Rossendorf, Germany). Se escogió este acelerador debido a que es capaz de variar sus parámetros experimentales dentro del orden que se requería para el tipo de estudio propuesto.

En la figura 1.27 se muestra un e squema de un i mplantador iónico utilizado. Básicamente está compuesto por los siguientes elementos:

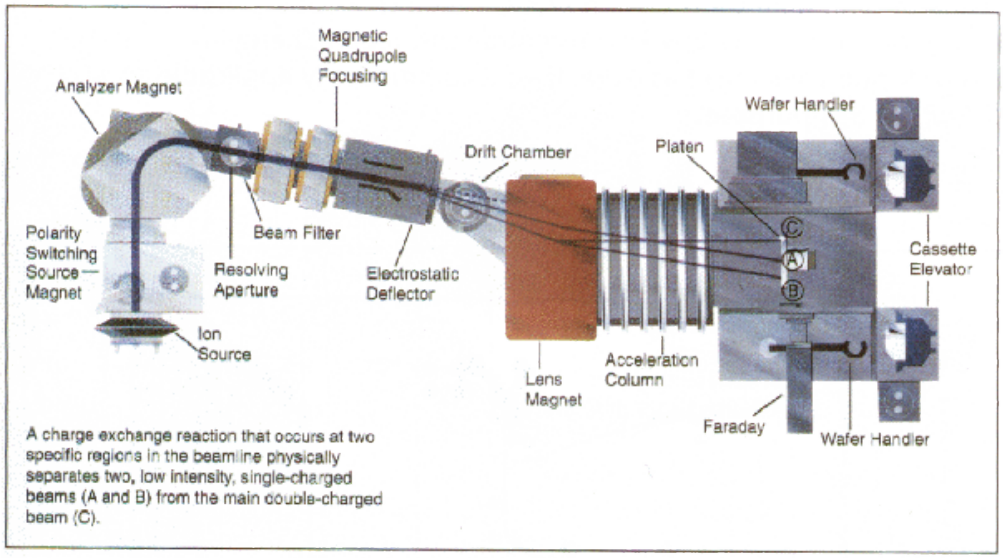

Figura 1.27. Esquema de un implantador iónico[88].

1- Sistema de generación de iones.

Para generar los iones, se parte de una cámara de ionización con electrodos que pueden aplicar un potencial alto. Una válvula regula el flujo de gas que entra en la fuente de iones. En esta se genera un plasma de partículas entre las que se encuentran

aquellas que se quiere implantar. La ionización del gas se produce a partir de los choques de las moléculas del gas contra los electrones emitidos por un cátodo y viene controlada por un campo magnético. Los iones se extraen a través de una rendija próxima al filamento usando un electrodo a potencial negativo respecto a la cámara puesta a tierra.

2- Analizador de iones.

El gas extraído de la fuente de iones contiene tanto los iones que se desean implantar como otros elementos que no se desean implantar, provenientes del plasma (isotopos, iones con distinta carga etc.). Para seleccionar los iones deseados, se coloca un campo magnético perpendicular a la trayectoria de los iones. Cada partícula realiza una trayectoria circular, cuyo radio viene relacionado con la relación carga/masa, de acuerdo con la ecuación (ecu 1.2)

$$R = \frac{\sqrt{2\,V\left(\frac{M}{q}\right)}}{B} \text{ (ecu 1.2)}$$

donde V es la tensión aplicada, B es el campo aplicado y M / q es la relación masa/carga del ion. Una rendija a la salida del analizador permite elegir las partículas.

3- Tubo de aceleración.

Los iones extraídos se aceleran mediante un tubo de aceleración formado por anillos que van incrementando paulatinamente el potencial. Para el acelerador utilizado, el rango de potencial varía entre 10-200 KeV.

4- Sistema de deflexión del haz.

Para eliminar los iones que han sido neutralizados por colisión con los átomos del gas residual, se utiliza un sistema de deflexión del haz. Este sistema tiene una doble funcionalidad, ya que sirve también para barrer la superficie de la muestra donde se desea realizar la implantación.

5- Cámara de implantación.

En la cámara de implantación se colocan las muestras a implantar, así como los sistemas de medida de la dosis, calefactores etc. Los materiales a implantar deben de tener un contacto eléctrico y térmico apropiado. Para neutralizar la carga de los iones que llegan

a la muestra, se impone un circuito eléctrico externo que además, sirve para medir la dosis implantada.

En el proceso de implantación puede existir un problema de falseo de la medida de la dosis debido a que la colisión ion-blanco puede producir electrones de baja energía. Para evitar este falseo de la medida, se coloca una caja de Faraday con una tensión alta respecto de la muestra.

1.5.6 Cálculos de la estructura electrónica

Para el cálculo de las estructuras de bandas del TiO_2 modificado con diferentes especies de Nitrógeno se han utilizado cálculos mecanicocuánticos. Los cálculos se realizaron en colaboración con el Dr. Said Hamad Gómez de la Universidad Pablo de Olavides. Los cálculos computacionales se basan en la resolución de la ecuación de Schrödinger independiente del tiempo $H\Psi = E\Psi$.

El hamiltoniano del sistema incluye las interacciones entre todos los electrones, por lo que esta ecuación es extraordinariamente complicada de resolver. Por ello, se hace necesario el uso de aproximaciones con las que podamos simplificar el tratamiento matemático, sin llegar a pe rder aspectos importantes de la física del sistema. Concretamente los más utilizados son los métodos Hartree-Fock y los basados en la Teoría del Funcional de la Densidad (más conocida por sus siglas en ingés, DFT), los cuales parten de la aproximación de electrones no interactuantes, para a continuación, introducir correcciones que incluyan las interacciones interelectrónicas.

Método Hartree-Fock, HF. El método Hartree-Fock es un método variacional, en el cual se parte de una solución a la ecuación de Schrödinger del sistema sin tener en cuenta las interacciones electrónicas, por lo que el hamiltoniano del sistema se puede considerar que viene dado por la suma de los hamiltonianos monoelectrónicos (h_i). Es decir:

$$H = -\sum_{i=1}^{n} h_i, \text{ donde } h_i = \sum_{i=1}^{n}\left(-\frac{1}{2}\nabla_{\mathrm{i}}^2 - \sum_{I=1}^{N}\frac{Z_I}{r_{Ii}}\right),$$

siendo N el número de núcleos atómicos que hay en el sistema. La interacción interelectrónica se introduce de un modo promediado, consistente en que si conocemos

los espín-orbitales (Φ, que son el producto de una función orbital espacial, φ, por una función de espín, σ), de los N-1 electrones que actúan sobre un determinado electrón, se puede conocer el efecto promedio que ejerce sobre él. Como los espín-orbitales son soluciones de la ecuación de Schrödinger, se parte de la aproximación de orden cero que normalmente es la solución de electrones no interactuantes. La interacción promedio de un electrón con los demás electrones (calculada usando este conjunto inicial de espín-orbitales) se introduce en el hamiltoniano. Este hamiltoniano se usa para escribir una nueva ecuación de Schrödinger. Al resolver esta nueva ecuación de Schrödinger obtenemos una nueva serie de espín-orbitales. Con estos nuevos espín-orbitales calculamos entonces de nuevo la interacción promedio sobre cada electrón, y se inicia un nuevo ciclo. Este ciclo se para cuando la diferencia (por ejemplo en la energía del sistema) que se obtiene al realizar nuevos ciclos está por debajo de un nivel umbral que consideramos aceptable. Si se continúan realizando ciclos no se observarán cambios apreciables en las funciones de onda. Por esta razón, esté método se denomina método del campo autoconsistente (o por sus siglas en inglés, SCF, de Self-Consistent Field). Para realizar los cálculos de forma computacionalmente eficiente cada espín-orbital se suele escribir como una combinación de funciones base gausianas, las cuales, aunque no forman un conjunto completo de la solución se acercan a dicho conjunto completo (En 1951, Clemens C.J. Roothaan1 y George Garfield Hall), y se obtiene así una descripción bastante precisa del sistema en un tiempo adecuado.

Teoría del Funcional de la Densidad, DFT: El método Hartree-Fock es poco preciso para la química del estado sólido, ya que no incluye los efectos de correlación electrónica. Para introducir dichos efectos de modo adecuado, a la vez que evitando incrementar significativamente el tiempo de cálculo, se suele recurrir a la Teoría de Funcional de la Densidad, o DFT. La DFT se basa en el denominado "primer teorema de Hohenberg y Kohn":

"cualquier observable de un sistema puede escribirse como un funcional de la densidad electrónica del estado fundamental".

Es decir, que si conociéramos la densidad electrónica de un sistema podríamos conocer de forma exacta la función de onda del sistema ya que ambos, están biunívocamente relacionadas. Todos los observables del sistema se pueden escribir entonces como función de la densidad electrónica (de ahí viene su nombre). Pero este

primer teorema sólo nos prueba que podemos obtener toda la información que queramos de un sistema, conociendo sólo su densidad electrónica. No nos dice cómo podemos calcular dicha densidad electrónica. Para ello necesitamos un segundo teorema, también de Hohenberg y Kohn, que dice:

"si se aplica una densidad electrónica de prueba al funcional de la densidad siempre se obtendrá una energía igual o mayor que la energía exacta del estado fundamental".

Es decir, que si calculamos la energía del sistema como función de la densidad electrónica, el valor mínimo de energía lo obtendremos cuando la densidad electrónica sea efectivamente la del sistema real. Cualquier otra densidad electrónica que usemos dará un valor de energía mayor. Tenemos por tanto ya la herramienta necesaria, se puede seguir un método autoconsistente como el mencionado anteriormente, donde ahora se empezaría con una densidad electrónica de prueba, con la cual calculamos la energía. Con esa energía calculamos una nueva función de prueba, hasta que lleguemos a una situación autoconsistente, en la cual la realización de nuevos ciclos no disminuye apreciablemente la energía del sistema. Todo este proceso se basa en escribir la energía del sistema en función de la densidad electrónica, y ahí precisamente estriba la principal dificultad de los métodos DFT, que no se conoce cuál es la relación funcional exacta entre la densidad electrónica y la energía del sistema. Hay una serie de potenciales de intercambio-correlación, que permiten calcular las energías de intercambio (debidas al principio de exclusión de Pauli) y de correlación (debidas a las interacciones coulómbicas entre los electrones), de forma aproximada. Se han conseguido potenciales de intercambio-correlación bastante precisos, aunque la búsqueda del potencial "exacto" (en caso de existir) aún sigue abierta.

Desde un punto de vista computacional, la aproximación DFT no describe adecuadamente sistemas con enlaces débiles (como las interacciones de Van der Waals) ni complejos por transferencia de carga. En estos casos se suelen emplear métodos post-HF, tales como MP2 o Coupled Cluster. Tampoco hay mucha experiencia en el tratamiento de estados excitados, aunque se están realizando grandes progresos en este campo últimamente. Donde más ampliamente se están empleando los métodos DFT es en el estudio de sistemas periódicos (cristales y superficies), debido a que con ellos se consigue describir los sistemas, incluyendo la correlación electrónica, y con unos tiempos de cálculos aceptables (órdenes de magnitud menores de lo que se necesitaría

para realizar cálculos post-HF). Debido a que en esta tesis se realizan estudios de estructuras electrónicas de sistemas N-TiO_2 se hace necesaria la utilización de métodos DFT frente a otros basados en Hartree-fock. Todos los cálculos los hemos realizado usando el programa VASP,[89] en el cual las funciones de onda se expresan como combinaciones de ondas planas, en vez de combinaciones de gausianas.

1.6.- ESTRUCTURA DE LOS RESULTADOS DEL TRABAJO DE TESIS

La presentación de los resultados obtenidos e investigaciones realizadas se acoge a la modalidad de "trabajo de investigación" aprobada por el departamento de Química Inorgánica de la Universidad de Sevilla. Según este esquema los capítulos 2, 3, 4, 5 y 6 se corresponden con trabajos de investigación publicados en revistas científicas, en las cuales el doctorando ha sido el investigador que ha realizado la mayor parte del trabajo experimental y realizado la primera interpretación de resultado.

Dado el carácter parcelado que, necesariamente, tienen los trabajos publicados en revistas científicas, se ha considerado oportuno establecer en esta sección las relaciones que existen entre ellos y que confieren a este trabajo de tesis una estructura común. Tales relaciones se ilustran en el esquema de la Figura 1.28.

La figura 1.28 presenta un esquema de la estructura general de la tesis. En este esquema se define un primer nivel de integración referido al método utilizado. Se compone de dos bloques representativos que dependen del método utilizado para el crecimiento de la nanoestructura superficial. El primer bloque estudia la utilización de aceleradores de partículas para generar la nanoestructura. El segundo bloque estudia la utilización de la técnica PECVD con el mismo fin. Un segundo nivel de integración contempla aspectos concretos de las propiedades de las capas sintetizadas y otros aspectos relevantes de su síntesis. Este segundo nivel se corresponde con los capítulos en los que se ha agrupado el trabajo realizado. Así en el capítulo 2 se estudia esta forma de nanoestructuración para el caso del TiO_2. Por otro lado, la nanoestructuración mediante la técnica de deposición PECVD de los sistemas basados en ZnO o TiO_2 y su estudio como material fotofuncional se han estudiado en los capítulos 3, 4, 5 y 6. A continuación se explica más en detalle este último bloque. En primer lugar, se estudian las características del plasma y cómo influyen en el crecimiento de los nanomateriales. De ello se encarga el

capitulo 3, que está dedicado al estudio de las condiciones del plasma óptimas para el crecimiento de las películas N-TiO_2. Además, en el capítulo 6, se realiza un inciso que relaciona algunas condiciones del plasma con las nanoestructuras del ZnO obtenidas. El siguiente paso, es el crecimiento de la nanoestructura. De ello, se encargan el capítulo 6 para el ZnO y el capitulo 4 para el TiO_2. El siguiente paso, fue estudiar las propiedades fotofuncionales de las muestras N-TiO_2 y ZnO. De ello se encargan los capítulos 4 y 6 respectivamente. Por último, estrechamente relacionado con la propiedad fotofuncional de las muestras N-TiO_2, se estudia la fotoactividad del sistema TiO_2 rutilo-anatasa en el capítulo 5.

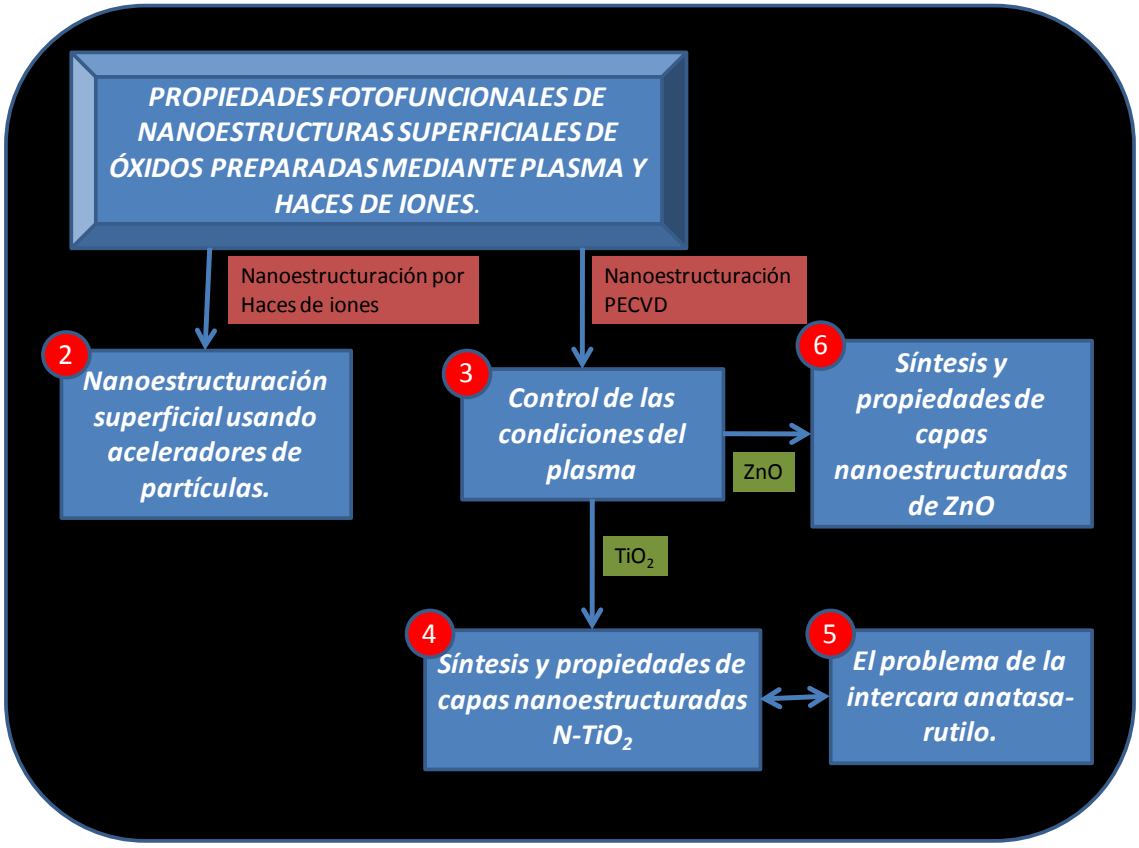

Figura 1.28. Esquema general de la tesis.

1.7.- BIBLIOGRAFÍA.

(1) Dai, Z. R.; Pan, Z. W.; Wang, Z. L. *Advanced Functional Materials* **2003**, *13*, 9.

(2) Tian, Y.; Tatsuma, T. *Journal of the American Chemical Society* **2005**, *127*, 7632.

(3) Pearton, S. J.; Abernathy, C. R.; Overberg, M. E.; Thaler, G. T.; Norton, D. P.; Theodoropoulou, N.; Hebard, A. F.; Park, Y. D.; Ren, F.; Kim, J.; Boatner, L. A. *Journal of Applied Physics* **2003**, *93*, 1.

(4) Pyun, M. W.; Kim, E. J.; Yoo, D. H.; Hahn, S. H. *Applied Surface Science* **2010**, *257*, 1149.

(5) Watanabe, T.; Nakajima, A.; Wang, R.; Minabe, M.; Koizumi, S.; Fujishima, A.; Hashimoto, K. *Thin Solid Films* **1999**, *351*, 260.

(6) Wang, R.; Hashimoto, K.; Fujishima, A.; Chikuni, M.; Kojima, E.; Kitamura, A.; Shimohigoshi, M.; Watanabe, T. *Nature* **1997**, *388*, 431.

(7) Djurisic, A. B.; Leung, Y. H. *Small* **2006**, *2*, 944.

(8) Wang, Z. L. *Materials Science & Engineering R-Reports* **2009**, *64*, 33.

(9) Konenkamp, R.; Word, R. C.; Godinez, M. *Nano Letters* **2005**, *5*, 2005.

(10) Han, X. H.; Wang, G. Z.; Wang, Q. T.; Cao, L.; Liu, R. B.; Zou, B. S.; Hou, J. G. *Applied Physics Letters* **2005**, *86*.

(11) Borras, A.; Cotrino, J.; Gonzalez-Elipe, A. R. *Journal of the Electrochemical Society* **2007**, *154*, P152.

(12) Myers, S. M.; Follstaedt, D. M.; Petersen, G. A.; Seager, C. H.; Stein, H. J.; Wampler, W. R. *Nuclear Instruments & Methods in Physics Research Section B-Beam Interactions with Materials and Atoms* **1995**, *106*, 379.

(13) Li, Y.; Sasaki, T.; Shimizu, Y.; Koshizaki, N. *Journal of the American Chemical Society* **2008**, *130*, 14755.

(14) Gonzalez-Garcia, L.; Lozano, G.; Barranco, A.; Miguez, H.; Gonzalez-Elipe, A. R. *Journal of Materials Chemistry* **2010**, *20*, 6408.

(15) Meyyappan, M.; Delzeit, L.; Cassell, A.; Hash, D. *Plasma Sources Science & Technology* **2003**, *12*, 205.

(16) Nitta, N.; Taniwaki, M.; Hayashi, Y.; Yoshiie, T. *Journal of Applied Physics* **2002**, *92*, 1799.

(17) Nitta, N.; Taniwaki, M.; Hayashi, Y.; Yoshiie, T. *Physica B-Condensed Matter* **2006**, *376*, 881.

(18) Ruck, B. J.; Koo, A.; Lanke, U. D.; Budde, F.; Granville, S.; Trodahl, H. J.; Bittar, A.; Metson, J. B.; Kennedy, V. J.; Markwitz, A. *Physical Review B* **2004**, *70*.

(19) Borras, A.; Barranco, A.; Espinos, J. P.; Cotrino, J.; Holgado, J. P.; Gonzalez-Elipe, A. R. *Plasma Processes and Polymers* **2007**, *4*, 515.

(20) Mangas, J. M. H., Universidad de Valladolid, 2000.

(21) Reyntjens, S.; Puers, R. *Journal of Micromechanics and Microengineering* **2001**, *11*, 287.

(22) Bala, K.; Hoepfner, J.; Tanimoto, H.; Takedai, S.; Sugiura, S.; ElKareh, B. *Ion Implantation Technology - 96* **1997**, 49.

(23) Frabboni, S.; Corni, F.; Nobili, C.; Tonini, R.; Ottaviani, G. *Physical Review B* **2004**, *69*.

(24) Perez-Bergquist, A.; Zhu, S.; Sun, K.; Xiang, X.; Zhang, Y.; Wang, L. M. *Small* **2008**, *4*, 1119.

(25) Kucheyev, S. O.; Williams, J. S.; Jagadish, C.; Zou, J.; Craig, V. S. J.; Li, G. *Applied Physics Letters* **2000**, *77*, 1455.

(26) Martinet, C.; Paillard, V.; Gagnaire, A.; Joseph, J. *Journal of Non-Crystalline Solids* **1997**, *216*, 77.

(27) Martinu, L.; Poitras, D. *Journal of Vacuum Science & Technology A* **2000**, *18*, 2619.

(28) Palmero, A.; Cotrino, J.; Barranco, A.; Gonzalez-Elipe, A. R. *Physics of Plasmas* **2002**, *9*, 358.

(29) Ohgushi, T.; Okamoto, T.; Watanabe, S.; Okamoto, Y. *Applied Surface Science* **2001**, *169*, 593.

(30) Guo, L. H.; Kondo, M.; Fukawa, M.; Saitoh, K.; Matsuda, A. *Japanese Journal of Applied Physics Part 2-Letters* **1998**, *37*, L1116.

(31) Malyshev, M. V.; Donnelly, V. M. *Physical Review E* **1999**, *60*, 6016.

(32) Borras, A.; Yanguas-Gil, A.; Barranco, A.; Cotrino, J.; Gonzalez-Elipe, A. R. *Physical Review B* **2007**, *76*.

(33) Ryu, Y. R.; Zhu, S.; Look, D. C.; Wrobel, J. M.; Jeong, H. M.; White, H. W. *Journal of Crystal Growth* **2000**, *216*, 330.

(34) Kim, J. P.; Bae, J. S.; Hong, T. E.; Won, M. S.; Yoon, J. H.; Lee, B. S.; Lee, H. J. *Thin Solid Films* **2010**, *518*, 6179.

(35) Li, Y.; Meng, G. W.; Zhang, L. D.; Phillipp, F. *Applied Physics Letters* **2000**, *76*, 2011.

(36) Laudise, R. A.; Ballman, A. A. *Journal of Physical Chemistry* **1960**, *64*, 688.

(37) Joo, J.; Kwon, S. G.; Yu, J. H.; Hyeon, T. *Advanced Materials* **2005**, *17*, 1873.

(38) Greene, L. E.; Law, M.; Tan, D. H.; Montano, M.; Goldberger, J.; Somorjai, G.; Yang, P. D. *Nano Letters* **2005**, *5*, 1231.

(39) Kong, X. Y.; Wang, Z. L. *Nano Letters* **2003**, *3*, 1625.

(40) Bekermann, D.; Gasparotto, A.; Barreca, D.; Bovo, L.; Devi, A.; Fischer, R. A.; Lebedev, O. I.; Maccato, C.; Tondello, E.; Van Tendeloo, G. *Crystal Growth & Design* **2010**, *10*, 2011.

(41) Djurisic, A. B.; Choy, W. C. H.; Roy, V. A. L.; Leung, Y. H.; Kwong, C. Y.; Cheah, K. W.; Rao, T. K. G.; Chan, W. K.; Lui, H. T.; Surya, C. *Advanced Functional Materials* **2004**, *14*, 856.

(42) Martin, A.; Espinos, J. P.; Justo, A.; Holgado, J. P.; Yubero, F.; Gonzalez-Elipe, A. R. *Surface & Coatings Technology* **2002**, *151*, 289.

(43) Hoffmann, M. R.; Martin, S. T.; Choi, W. Y.; Bahnemann, D. W. *Chemical Reviews* **1995**, *95*, 69.

(44) Ozgur, U.; Alivov, Y. I.; Liu, C.; Teke, A.; Reshchikov, M. A.; Dogan, S.; Avrutin, V.; Cho, S. J.; Morkoc, H. *Journal of Applied Physics* **2005**, *98*.

(45) Nakaoka, Y.; Nosaka, Y. *Journal of Photochemistry and Photobiology a-Chemistry* **1997**, *110*, 299.

(46) Carp, O.; Huisman, C. L.; Reller, A. *Prog. Solid State Chem.* **2004**, *32*, 33.

(47) Asahi, R.; Morikawa, T.; Ohwaki, T.; Aoki, K.; Taga, Y. *Science* **2001**, *293*, 269.

(48) Okamoto, K.; Yamamoto, Y.; Tanaka, H.; Tanaka, M.; Itaya, A. *Bulletin of the Chemical Society of Japan* **1985**, *58*, 2015.

(49) Sopyan, I.; Watanabe, M.; Murasawa, S.; Hashimoto, K.; Fujishima, A. *Journal of Photochemistry and Photobiology a-Chemistry* **1996**, *98*, 79.

(50) Mor, G. K.; Varghese, O. K.; Paulose, M.; Shankar, K.; Grimes, C. A. *Solar Energy Materials and Solar Cells* **2006**, *90*, 2011.

(51) Li, Y.; Zhang, J. Z. *Laser & Photonics Reviews* **2010**, *4*, 517.

(52) Rico, V.; Romero, P.; Hueso, J. L.; Espinos, J. P.; Gonzalez-Elipe, A. R. *Catalysis Today* **2009**, *143*, 347.

(53) Nakano, Y.; Morikawa, T.; Ohwaki, T.; Taga, Y. *Applied Physics Letters* **2005**, *86*.

(54) Mwabora, J. M.; Lindgren, T.; Avendano, E.; Jaramillo, T. F.; Lu, J.; Lindquist, S. E.; Granqvist, C. G. *Journal of Physical Chemistry B* **2004**, *108*, 20193.

(55) Maeda, M.; Watanabe, T. *Journal of the Electrochemical Society* **2006**, *153*, C186.

(56) Takahashi, M.; Tsukigi, K.; Uchino, T.; Yoko, T. *Thin Solid Films* **2001**, *388*, 231.

(57) Serpone, N. *Journal of Physical Chemistry B* **2006**, *110*, 24287.

(58) Bendavid, A.; Martin, P. J.; Jamting, A.; Takikawa, H. *Thin Solid Films* **1999**, *355*, 6.

(59) Ovenstone, J.; Yanagisawa, K. *Chemistry of Materials* **1999**, *11*, 2770.

(60) Zhang, J.; Xu, Q.; Feng, Z.; Li, M.; Li, C. *Angewandte Chemie-International Edition* **2008**, *47*, 1766.

(61) Fujishima, A.; Zhang, X.; Tryk, D. *TiO2 photocatalysis and related surface phenomena*, 2008.

(62) Morrison, S. R. *THE CHEMICAL PHYSICS OF SURFACE* MENLO PARK, 1977.

(63) Young, T.; Philos *the Royal Society of London* **1805**, *95*, 65.

(64) Cebeci, F. C.; Wu, Z. Z.; Zhai, L.; Cohen, R. E.; Rubner, M. F. *Langmuir* **2006**, *22*, 2856.

(65) Kamei, M.; Mitsuhashi, T. *Surface Science* **2000**, *463*, L609.

(66) Miyauchi, M.; Kieda, N.; Hishita, S.; Mitsuhashi, T.; Nakajima, A.; Watanabe, T.; Hashimoto, K. *Surface Science* **2002**, *511*, 401.

(67) A. Borras; C. Lopez; V. Rico; F. Gracia; A. R. Gonzalez-Elipe; E. Richter; G. Battiston; R. Gerbasi; N. McSporran; G. Sauthier; E. Gyorgy; Figueras, A. *J. Phys. Chem. C* **2007**, *111*, 1801.

(68) Fujishima, A.; Hashimoto, K.; Watanabe, T. *BKC Tokyo* **1999**.

(69) Heller, A. *Acc. Chem. Res* **1995**, *28*, 503.

(70) Hadjiivanov, K. J.; Klissurski, D. K. *Chem. Soc. Rev.* **1996**, *25*, 61.

(71) Tseng, Y. H.; Kuo, C. S.; Huang, C. H.; Li, Y. Y. *Zeitschrift Fur Physikalische Chemie-International Journal of Research in Physical Chemistry & Chemical Physics* **2010**, *224*, 843.

(72) Rico, V., Tesis Doctoral. US-CSIC, 2010.

(73) Kawahara, T.; Konishi, Y.; Tada, H.; Tohge, N.; Nishii, J.; Ito, S. *Angewandte Chemie-International Edition* **2002**, *41*, 2811.

(74) Li, Y. X.; Jiang, Y. A.; Peng, S. Q.; Jiang, F. Y. *Journal of Hazardous Materials* **2010**, *182*, 90.

(75) Liu, S. W.; Yu, J. G.; Wang, W. G. *Physical Chemistry Chemical Physics* **2010**, *12*, 12308.

(76) Gracia, F.; Holgado, J. P.; Caballero, A.; Gonzalez-Elipe, A. R. *Journal of Physical Chemistry B* **2004**, *108*, 17466.

(77) Li, X. Z.; Li, F. B.; Yang, C. L.; Ge, W. K. *Journal of Photochemistry and Photobiology a-Chemistry* **2001**, *141*, 209.

(78) Dvoranova, D.; Brezova, V.; Mazur, M.; Malati, M. A. *Applied Catalysis B-Environmental* **2002**, *37*, 91.

(79) Wang, M. C.; Lin, H. J.; Yang, T. S. *Journal of Alloys and Compounds* **2009**, *473*, 394.

(80) Ang, T. P.; Law, J. Y.; Han, Y. F. *Catalysis Letters* **2010**, *139*, 77.

(81) Han, T.; Fan, T. X.; Chow, S. K.; Zhang, D. *Bioresource Technology* **2010**, *101*, 6829.

(82) Zhang, X. R.; Lin, Y. H.; Zhang, J. F.; He, D. Q.; Wang, D. J. *Acta Physico-Chimica Sinica* **2010**, *26*, 2733.

(83) Konstantinova, E. A.; Kokorin, A. I.; Lips, K.; Sakthivel, S.; Kisch, H. *Applied Magnetic Resonance* **2009**, *35*, 421.

(84) Senthilnathan, J.; Philip, L. *Chemical Engineering Journal* **2010**, *161*, 83.

(85) Farkas, B.; Budai, J.; Kabalci, I.; Heszler, P.; Geretovszky, Z. *Applied Surface Science* **2008**, *254*, 3484.

(86) Chen, F. F. *Physics of Plasmas* **2001**, *8*, 3029.

(87) http://physics.nist.gov/PhysRefData/ASD/lines_form.html.

(88) Daryanani, S.; Jillson, J.; Eddy, R. *III-Vs review,* **1997**, *10(2)*, 26.

(89) Kresse, G.; Furthmüller, J. *Phys. Rev. B* **1996**, *54*, 11169.

Capítulo 2

Nanoestructuración superficial usando aceleradores de partículas

PHYSICAL REVIEW B 82, 115420 (**2010**)

Surface nanostructuring of TiO_2 Thin Films by High Energy Ion Irradiation

P. Romero-Gomez[a], A. Palmero[a,1], T. Ben[b], J.G. Lozano[b], S.I. Molina[b], A.R. González-Elipe[a]

a) Instituto de Ciencia de Materiales de Sevilla (CSIC/Universidad de Sevilla), c/ Américo Vespucio 49, 41092 Sevilla (Spain)

b) Departamento de Ciencia de los Materiales e I.M. y Q.I., Facultad de Ciencias, Universidad de Cádiz, Campus Río San Pedro, s/n, 11510 Puerto Real, Cádiz, Spain

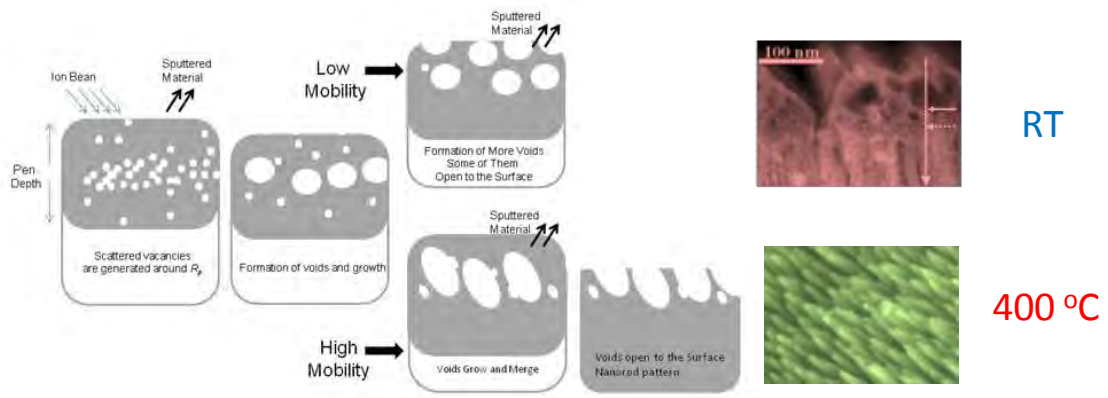

Title: Surface nanostructuring of TiO_2 Thin Films by High Energy Ion Irradiation.

Authors: **P. Romero-Gomez**, A. Palmero, T. Ben, J.G. Lozano, S.I. Molina, A.R. González-Elipe

Source: Physical Review B 82, 115420 (2010)

D.O.I. 10.1103/PhysRevB.82.115420

Surface nanostructuring of TiO_2 Thin Films by High Energy Ion Irradiation

P. Romero-Gomez[a], A. Palmero[a,1], T. Ben[b], J.G. Lozano[b], S.I. Molina[b], A.R. González-Elipe[a]

a) Instituto de Ciencia de Materiales de Sevilla (CSIC/Universidad de Sevilla), c/ Américo Vespucio 49, 41092 Sevilla (Spain)

b) Departamento de Ciencia de los Materiales e I.M. y Q.I., Facultad de Ciencias, Universidad de Cádiz, Campus Río San Pedro, s/n, 11510 Puerto Real, Cádiz, Spain

Abstract

The effects of a high ion dose irradiation on TiO_2 thin films under different conditions of temperature and ion nature are discussed. We have shown that anatase TiO_2 thin films irradiated with N^+ ion at room temperature develop a typical microstructure with mounds and voids open to the surface, whereas irradiations at 700 K generate a surface pattern of well-ordered nanorods aligned with the ion beam. The formation of these patterns is caused by the simultaneous effect of ion irradiation near the film surface and a film temperature favoring the structural mobilization of the defective network of the material. To explain these phenomena a qualitative model has been proposed and further tested by irradiating the TiO_2 thin films with F^+ and S^+ ions under different conditions. The obtained results demonstrate that ion irradiation techniques enable the formation of tilted nanorod surface patterns with lengths of about 100 nm on anatase TiO_2 thin films.

1) E-mail: alberto.palmero@icmse.csic.es

I. Introduction

Titanium dioxide (TiO_2) is a wideband semiconductor with numerous applications in science and technology. Its excellent optical transmittance, high refractive index and chemical stability make this material good candidate for antireflection coatings, solar cells, capacitor for high bit DRAM (dynamic random access memory), anodic electrochromic materials, etc.[1-4]. Furthermore, photoactive properties of this oxide under light irradiation has fostered new and interesting applications in the field of photo-catalysis, self-cleaning materials or photo-voltaic cells, all of them actively investigated during the last years[5]. For these applications, it was found that the anatase crystalline phase is especially adequate to optimize many of the previous properties, and that its performance clearly improves when the film surface is nanostructured[6] and/or when it is doped with nitrogen to shift its spectral response from the ultraviolet towards the visible light spectrum[7-8].

The development of reliable techniques for surface nanostructuring of thin films is nowadays a key issue that has been approached by different physical and chemical methods[9]. In particular, considerable efforts have been devoted during the last years to the preparation of mesostructured[10] and one dimension TiO_2 structures (nanorods, nanowires, nanotubes)[11-12] which have depicted unprecedented results as hydrogen sensors, self-cleaning surfaces under ultraviolet light exposure, or dye sensitized heterojunction solar cells[13-15]. In this latter case, the presence of highly ordered one-dimensional TiO_2 arrays improves the photogenated charge carrier lifetimes by more than one order of magnitude in comparison with nanoparticulate systems (see for instance ref.[16] and references therein).

In a recent publication we showed that anatase TiO_2 thin films under the irradiation of a high energy ion beam caused important structural and chemical changes in the material, such as the decrease of crystallinity of the films and the depletion of oxygen in the upmost surface layers due to its preferential sputtering[17]. Although these phenomena have extensively been reported in the literature for this oxide material subjected to different thermal and ion beam treatments (see for instance ref. 18 and references therein), in ref. 17 we also showed the existence of additional processes affecting the nanostructure and surface topography. For instance, we found that when a TiO_2 anatase

thin film was irradiated at room temperature with a high dose of N^+ ions, with energies around 50 KeV, a porous layer appeared at a depth similar to the ion projected range (R_p). Furthermore, by reducing the ion irradiation energy, and thus R_p, various surface morphologies were obtained, such as cellular defect structures or nanorods surface patterns aligned with the angle of incidence of the beam. These results suggested a strong link between pore formation mechanisms in the material and the development of nanorods at the surface. An interesting aspect of this proposed technique in comparison with other methods is the possible customization of the nanorod surface patterns. In references[19-20], for instance, a technique that involves a femtosecond laser irradiation of the film in water was proposed. As a result, a nanorod surface pattern consisting of quasiperiodic sharp conical spikes, about 50 nm wide and with length in the micrometer range, perpendicular to the substrate, was found. These results, together with those in ref.[17], suggest that by tuning the operational parameters, the size, length and tilt angle of the nanorods could be controlled while further research must be carried out in order to understand the surface nanostructuring of thin films.

The formation of pores after ion irradiation has been recently reported for crystalline silicon irradiated with helium ions[21]. In this case, the very small momentum transferred during the collision, as well as the low solubility of the implanted species in the material, produced many localized point defects in the network that formed pores in the bulk of the material through segregation and precipitation mechanisms[21]. Pore formation after ion irradiation has also been intensively studied for GaN thin films[22-24], where a stoichiometric imbalance of N and Ga in the network induced the formation of multiple N_2 molecules that, scattered in the material, generate the pores. Similar results were also obtained for materials such as Ge, GaSb or InSb, where the long-range migration of atoms through the bulk and the short range movement of point defects during irradiation were responsible for the so-called anomalous swelling and the formation of pores[25-27]. In our previous work, we tentatively proposed that this latter mechanism could be responsible for the formation of pores in the TiO_2 thin films since they also develop when the material is irradiated with boron or sulfur, two elements that in no way could form gaseous molecules within the material. In the present work, we present a more thorough and detailed study of the changes occurring in TiO_2 thin films after irradiation under several conditions. The obtained results have enabled us to propose a general mechanism accounting for the formation of either pores in the interior

of TiO_2 or ordered nanorods at its surface, depending on the conditions of the experiment. We think that the proposed model can be extended to account for the formation of voids in other oxides where generation of point and other structural defects are particularly favored. Another outcome of this investigation is the demonstration that, by fine tuning of the experimental conditions, it is possible to tailor the generation of ordered nanorod patterns on the surface of ion beam irradiated oxides.

II. Experimental

TiO_2 thin films with a thickness comprised between 300 and 500 nm were deposited at 523 K using the plasma enhanced chemical vapor deposition technique. The films, depicting the anatase structure, showed a high degree of crystallinity and a clear columnar microstructure perpendicular to the substrate. The details of the as-deposited material, as well as the description of the deposition technique, appear in ref. 28. The ion irradiations were carried out at the Institute of Ion Beam Physics and Materials Research (Forschungszentrum Dresden-Rossendorf, Germany) under the conditions that appear in Table 2.I. It is worth noting that in the cases where the ion irradiation was carried out at room temperature, the ion current was specifically set low enough to keep the film temperature below 70º C (340 K). Other irradiation experiments were carried out at 700 K, a temperature at which no excessive oxygen depletion in the material due to desorption from the film surface is expected. Finally, the value of R_p was estimated through the SRIM software[29]. From now forth we will refer to each irradiation condition with the corresponding label '#' defined in Table 2.I which, to provide a better reading of the paper, is accompanied by the following data: value of R_p-ion used for the irradiation-value of the film temperature.

Sample	*Ion*	*Dose (ion/cm^2)*	*Flux (ion/cm^2 s)*	*Energy (KeV)*	*Angle (º)*	*R_p(nm)*	*T (K)*	*Resistivity (Ω cm)*
#1	N^+	2.4 10^{17}	2.0 10^{13}	60	45	~100	RT	3.20
#2	O^+	2.4 10^{17}	2.0 10^{13}	65	45	~100	RT	0.83
#3	N^+	2.4 10^{17}	2.6 10^{13}	15	45	~50	RT	1.90
#4	N^+	2.4 10^{17}	2.0 10^{13}	15	45	~50	700	0.078
#5	F^+	2.4 10^{17}	1.3 10^{13}	50	45	~50	RT	180
#6	F^+	2.4 10^{17}	1.3 10^{13}	50	45	~50	700	0.019
#7	S^+	5 10^{16}	1.3 10^{13}	45	45	~50	700	0.005

Table 2.I. Irradiation conditions for each sample along with the measured resistivity of the films.

Films were characterized by X-ray diffraction in a Siemens D5000 Spectrometer working in the Bragg-Brentano configuration and using the Cu Kα radiation as excitation source. Cross-sectional and top view SEM micrographs were obtained using a Hitachi S5200 field emission microscope working at 5.0 KeV for thin films grown on a silicon wafer. XPS spectra of the films were recorded in an ESCALAB 210 spectrometer working under energy transmission constant conditions. The Mg Kα line was used for excitation spectra. They were calibrated in binding energy by referencing to the C1s peak taken at 284.6 eV. Quantification was done by calculating the area of the peaks and by correcting these areas with the sensitivity factor of each element/electronic level. The transmittance spectra of the samples were determined by UV-vis absorption spectroscopy (Perkin-Elmer Lambda 12 Spectrometer) for samples prepared on fused silica. Measurement of the surface electrical conductivity of the samples was done by using the four point probe test. A Keithley 617 electrometer and a Hewlett-Packard 34401 A voltammeter were used for the measurements. These consisted of applying a voltage ranging between -0.25 and 0.25 V to the two external probe electrodes. The intensity was then measured within the two internal probes. High angle annular dark field scanning transmission electron microscopy (HAADF-STEM) and electron energy loss spectroscopy (EELS) studies were carried out at 200 KV in a JEOL 2010F microscope equipped with a GIF camera providing an energy resolution of about 1.6 eV, with a collection angle of 24 mrad.

III. Results and discussion

N^+ and O^+ ion beam bombardment

In figure 2.1a, we show the cross-sectional view of a SEM micrograph taken for sample #1 (100- N^+-RT). Here, N^+ ions are implanted far from the surface, a process that in agreement with ref. 17 results in both the formation of a porous layer at a depth about R_p and pore diameters comprised between 5 and 10 nm, and in the removal of the intrinsic columnar structure within the implanted region. The thickness of the sputtered region removed from the film due to the ion irradiation is estimated to be around 30-40 nm. In figure 2.1b, we show the cross-sectional SEM image of sample #2 (100-O^+-RT). In this case, we have used O^+ instead of N^+ ions and an ion energy chosen to have a penetration depth similar to that in sample #1(100- N^+-RT). Again, it seems clear that a porous layer appears in the material at about the same ion penetration depth, although this time the concentration and size of the pores are appreciably smaller. The columnar structure was also removed in the implantation region where, in addition to the pores, a glassy homogenous layer was formed. Regarding the similar microstructural modifications observed in figures 2.1a-b, it is possible to conclude that pore formation is controlled by similar mechanisms in both cases, no matter whether the irradiation is done using N^+ or O^+ ions. Furthermore, surface conductivity measurements of samples #1 (100-N^+-RT) and #2 (100-O^+-RT), reported in Table 2.I, indicate that in both cases ion bombardment has induced a considerable concentration of free electrons in the conduction band that must be associated to the formation of oxygen vacancies and Ti^{3+} species in the lattice[30].

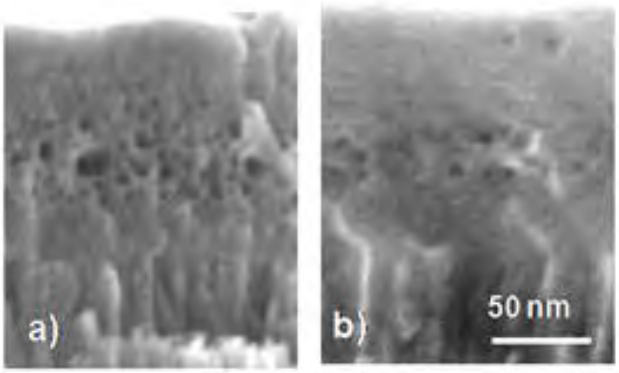

Figure 2.1. Cross-sectional SEM micrographs of irradiated anatase thin films: a) sample #1 (100-N^+-RT) in Table 2.I, b) sample #2 (100-O^+-RT) in Table 2.I.

In figure 2.2(a) we show the top view SEM micrograph of a TiO_2 anatase thin film irradiated at room temperature with N^+ ions which, according to the SRIM calculations, are implanted near the surface (sample #3, (50-N^+-RT)). This micrograph displays a surface with irregular motives and open pores. In figures 2.2(b) and 2.2(c), we show the top and cross-sectional SEM micrographs of the same sample annealed at 700 K after its irradiation. Comparing figures 2.2(b)-(c) with 2.2(a), we find that the annealing process induces the opening of some voids buried near the surface, thus leading to the formation of a porous surface. In parallel, voids located deeper into the material remain closed but change their shape, appearing now as large ellipsoidal voids (figure 2.2c). It is likely that these large and not-spherical voids are caused by the merging of nearby smaller voids located underneath the surface. In figure 2.2(d), we depict the top SEM view of sample #4 (50- N^+-700): now the irradiation conditions are equal to those of sample #3 but imposing a film temperature of 700 K *during the irradiation*. In this case, the surface topography, quite different to that depicted in figures 2.2(a) and 2.2(b), is characterized by a homogenous surface pattern made of nanorods of 20-30 nm diameter aligned with the angle of incidence of the ion beam. This result suggests that the obtained morphology in figure 2.2(d) is the consequence of the *simultaneous* action of both, the ion irradiation and some thermally activated processes.

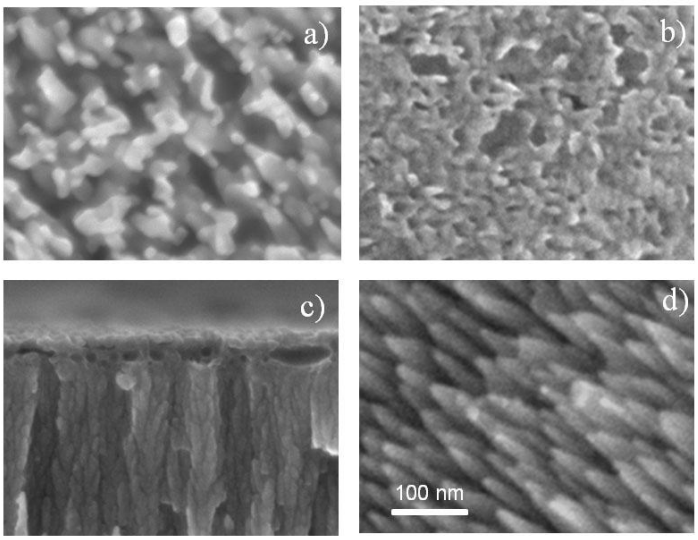

Figure 2.2. SEM micrographs of irradiated anatase thin films: a) top view of sample #3 (50-N^+-RT) in Table 2.I, b) top view of sample #3 (50-N^+-RT) after its annealing at 700 K, and c) cross-sectional image of sample #3 (50-N^+-RT) after its annealing at 700 K, and d) top view of sample #4 (50-N^+-700) in Table 2.I.

Structural and chemical characterization of the implanted layer

Due to the relevance of irradiations under conditions #3 (50-N^+-RT) and #4 (50-N^+-700) in relation with the formation of surface patterns, we have studied the structural and chemical modifications induced in the samples after their irradiation with nitrogen. In figure 2.3(a), we show the XRD diagram of both samples along with some reference data. The label 'REF' in figure 2.3(a) corresponds to an as-deposited nonirradiated sample and the corresponding diagram depicts the typical peaks and intensities of randomly oriented TiO_2 anatase in powder form ('pattern anatase' labeled curve in figure 2.3(a)). Furthermore, sample #3 (50-N^+-RT) depicts no clear diffraction peak, a feature that indicates a significant structural damage of the material and the loss of crystallinity. Finally, sample #4 (50-N^+-700) presents a XRD spectrum typical of an anatase polycrystalline network with a preferential orientation according to the (004) plane. Since a similar diagram is also found for as-deposited non-irradiated thin films annealed at 700 K (result not shown), this preferential texturing must be solely attributed to an effect of the temperature during irradiation.

Figure 2.3(b) shows the N1s photoemission spectra of samples #3 (50-N^+-RT) and #4 (50-N^+-700). In both cases, the spectra are dominated by a main peak at 396.3 eV and a tail extending to higher binding energies that suggests some additional contributions in an energy range going up to 401 eV. Previous studies in literature have attributed different N1s peaks in N-doped TiO_2 to nitride and oxinitride species of the type: Ti-N (396.3 eV), Ti-ON (399.3 eV) and Ti-NO (400.7 eV)[8]. According to these previous assignments, the spectra in figure 2.3(b) support the formation of a high concentration of Ti-N species in the implanted samples. Figure 2.3(c) shows the UV-vis absorption spectra of the as-deposited sample (labeled as 'REF'), along with those of samples #3(50-N^+-RT) and #4(50-N^+-700). These spectra depict the typical oscillations caused by the interferences observed when a transparent or partially transparent thin film with high refraction index is deposited on a low refraction index substrate. In addition, the spectra of samples #3 (50-N^+-RT) and #4 (50-N^+-700) evidence a progressive decrease in the transmittance within the whole visible spectral range. Broad absorption features extending from the blue to the red regions of the spectrum have been attributed in literature to N-doped TiO_2 and oxygen-deficient TiO_2, respectively[31]. The comparison between the magnitudes of these absorptions for the two implanted samples indicates that temperature plays an important role in the optical properties of the films inducing an additional loss of transmittance in the sample #4 (50-N^+-700) irradiated at 700 K. This feature agrees with its relatively higher electrical conductivity (see Table 2.I) and suggests a higher reduction degree of this sample. In this regard, since loss of oxygen due to the preferential surface sputtering mechanism mainly affects to the upmost surface layer of the film, migration of oxygen through the whole implantation region must be assumed to compensate this high oxygen concentration gradient from the surface and the formation of a relatively homogeneous $TiO_x(N)$ composition.

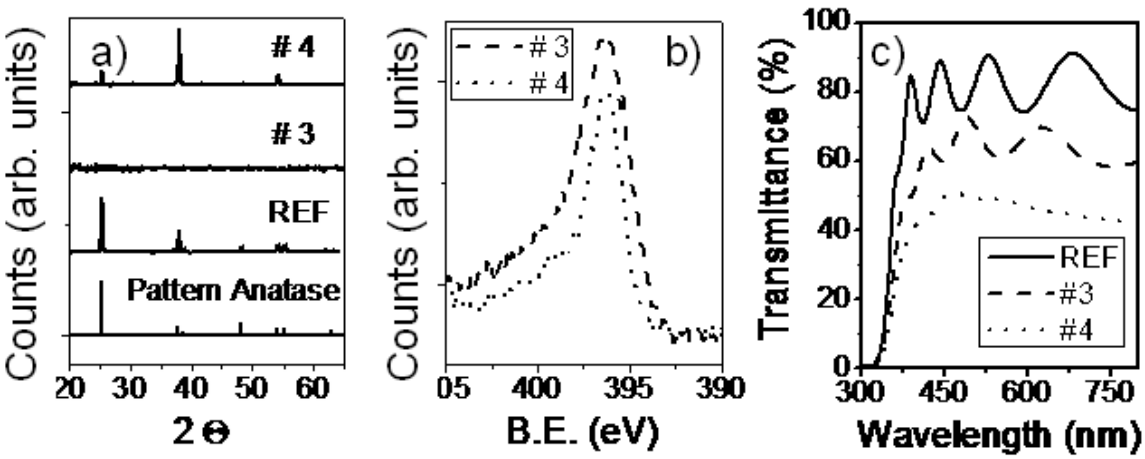

Figure 2.3. Characterization results of samples #3 (50-N^+-RT) and #4 (50-N^+-700) in Table 2.I: a) X-ray difraction diagrams of an as-deposited TiO_2 thin film along with those of samples #3 (50-N^+-RT) and #4 (50-N^+-700) in Table 2.I, and a reference spectrum. b) N1s photoemission spectra of samples #3 (50-N^+-RT) and #4 (50-N^+-700), and c) Transmission spectra of samples #3 (50-N^+-RT) and #4 (50-N^+-700) along with that of a reference sample.

Figure 2.4 reports a series of characterization studies by HAADF-STEM and EELS of sample #3 (50-N^+-RT). Figure 2.4(b) shows a HAADF image of the cross-section of the topmost layers of this sample. Images recorded by this technique offers brightness contrast associated with the concentration and atomic number of constituent elements. Figure 2.4(b) shows that the topmost surface regions consist of mounds and open pores, with a high density of large voids in the region just below R_p, i.e. below 50 nm, that become smaller in size as we go deeper into the material. These small voids disappear at a depth of about 170 nm, where we find the original columnar structure of the film. Chemical information along this altered layer formed in sample #3 (50-N^+-RT) can be gathered through a sequence of EELS spectra, each taken at a particular position crossing the surface region. Spectra were recorded in spectrum-imaging mode in regularly spaced localizations with 3 nm steps along the vertical arrow displayed in figure 2.4(b), with an acquisition time of 4 s. Nitrogen intensity profiles, extracted from the individual spectra (using the normal background subtraction method[32]) are displayed in figure 2.4(a), whose vertical axis is scaled with figure 2.4(b). This profile shows that a maximum concentration of implanted nitrogen exists at a depth of approximately 100 nm, with a shoulder at around 60 nm. Furthermore, two of these spatially resolved spectra for determined depths (marked by the horizontal arrows) centered in energy

range around the N K edge are shown in Figure 2.4(c), where they have also been scaled in order to compare their shapes. The species of nitrogen at a depth similar to that of the maximum concentration in figure 2.4(a) is characterized by a strong main peak at about 401 eV, which is attributed to molecular nitrogen embedded into the material[33]. In regions closer to the surface (above R_p), corresponding to the region with larger voids in figure 2.4(b), a smaller relative concentration of molecular nitrogen is detected: in this case the N signal is characterized by two peaks at around 398 and 409 eV, indicating the existence of nitride species[34]. This analysis provides evidence that N_2 gas has mostly desorbed from the outer region of the implanted layer whereas it remains trapped in the material below this region. The maximum concentration of nitrogen is found at a depth below R_p, i.e. at about 100 nm from the sample surface, in the region immediately below the largest voids. The nitrogen concentration decreases to disappear for a depth of 170 nm, i.e., at distances from the surface higher than the implantation depth. The electron diffraction patterns (result not shown) indicates that below 170 nm, the film keeps the crystalline planes of anatase whereas for depths above 170 nm the material is much less crystalline, in agreement with its XRD spectrum depicted in Figure 2.3(a).

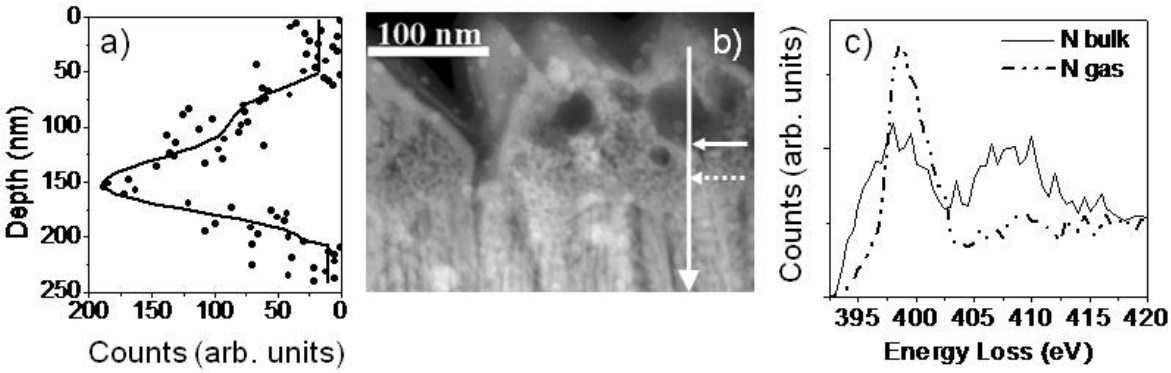

Figure 2.4. Chemical analysis of sample #3 (50-N^+-RT) in Table 2.I. a) Nitrogen intensity profiles obtained through the EELS spectra, b) cross-sectional HAADF image of the surface scaled with figure 2.4a, and c) EELS spectra for the positions given by the horizontal arrows in figure 2.4b (slashed and continuum curves correspond to the slashed and continuum arrows).

Figure 2.5 shows a similar HAADF-STEM and EELS analysis for sample #4 (50-N^+-700). In particular, Figure 2.5(b) shows a HAADF-STEM cross-sectional image of the sample, where the existence of surface nanorods, aligned with the direction of the ion beam, and with a length of about 100 nm are clearly visible. In comparison with figure 2.4(a) (sample #3 (50-N^+-RT)), Figure 2.5(a) shows a shift in the maximum of the nitrogen depth profile towards the surface. This means that the mobility of N implanted in the material has increased and that thermal diffusion processes have induced a certain migration of nitrogen atoms towards the surface. Furthermore, figure 2.5(b) does not reveal any sign of voids near the surface, indicating that in sample #4 (50-N^+-700) there is a different balance between the mechanisms governing the evolution of the microstructure of the implanted layer. In agreement with that, figure 2.5c shows an intense EELS spectrum at the depth indicated by the horizontal arrow, showing two peaks at 398 and 409 eV. Thus, despite the fact that some contribution of molecular nitrogen cannot be discarded, this spectral shape can be reasonably attributed to nitride species[34]. The depth profile in figure 2.5(a) indicates that, just below the nanorods, the amount of nitrogen incorporated to the network increases and reaches a maximum at a depth around 50 nm (i.e., at a depth where large voids were found in Figure 2.3(b)). Then, for deeper zones of the implanted layer, the nitrogen concentration drastically diminishes to practically disappear at around 150 nm. It is also important to mention that electron diffraction analysis of the implanted region revealed that from the tip of the nanorods to the zone below the implantation region, the whole material possesses an anatase structure with good crystallinity (result not shown). This re-crystallization observed in sample #4 (50-N^+-700) must be attributed to the high temperature of the film during irradiation.

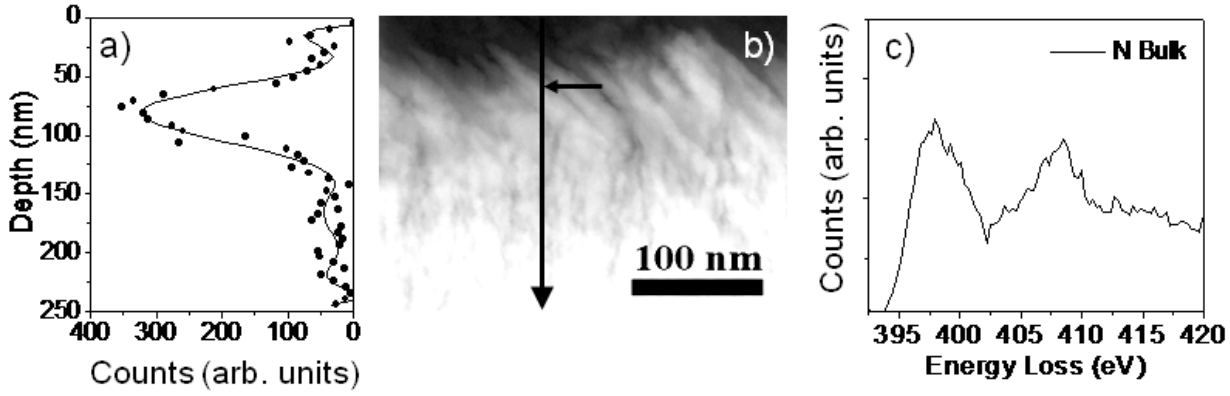

Figure 2.5. Chemical analysis of sample #4 (50-N^+-700) in Table 2.I. a) Nitrogen intensity profiles obtained through the EELS spectra, b) cross-sectional HAADF image of the surface scaled with figure 2.5a, and c) EELS spectra for the positions given by the horizontal arrows in figure 2.5b (slashed and continuum curves correspond to the slashed and continuum arrows).

Surface nanostructuring of irradiated TiO_2

Ion-implantation generated point defects are known to be responsible for the formation of pores under the film surface in different materials. For GaSb irradiated at room temperature with different ions it is known that, in an initial stage, voids of a few nanometres of diameter are formed by the aggregation of migrating vacancies formed as a result of the primary implantation events. This process continues if additionally created vacancies migrate towards the voids, enlarging them or forming new ones, ending up with the formation of sponge-like structures at high implantation doses[25-26]. Under low defect mobility conditions (e.g., at low temperatures), vacancies do not aggregate easily and remain scattered in the material. For increasing ion doses under these conditions, it is known that vacancy generation goes on until their concentration reaches a critical value which is typically determined by the elastic properties of the material. At that point, voids are abruptly formed at a depth about the ion projected range. In this way, new vacancies are absorbed by the voids which grow, forming a typical cellular structure[26,35]. In these experiments for GaSb, typical ion doses were between 10^{14} and 10^{15} $ions/cm^2$, whereas for TiO_2 we found cavities for doses as large as 2.4×10^{17} $ions/cm^2$, i.e. two-three orders of magnitude above. Interestingly, for both materials similar structures consisting of voids, cellular structures or nanorod surface

patterns have been observed. For GaSb irradiated with 30 KeV Ga^+ ions, A. Perez-Bergquist et al. 27 found that for low doses ($1.3\times10^{15}\ ions/cm^2$) the first layers of the material breached, exposing a thin porous regions to the surface. By contrast, at higher doses ($6.5\times10^{15}\ ions/cm^2$), the pores grew outwards developing a typical nanorod surface pattern. It is also important to stress that for GaSb the mobility of vacancies in the material has a strong dependence on the irradiation temperature, becoming quite important when defining the void formation and growth. Likewise, helium-implanted single crystal silicon also develops voids whose structural evolution follows a common pattern for increasing doses: for low doses platelike clusters of highly pressurized helium bubbles are formed, whereas for higher doses, helium in these bubbles effuses from the surface leaving empty nanovoids[21]. This evolution has been found to be strongly conditioned by the film temperature, and caused by segregation and precipitation phenomena of helium in the material. The similarities between the abovementioned irradiated materials suggest that similar mechanisms are responsible for the formation of the observed nanostructures in TiO_2. However, we must insist in that in our case a much higher ion dose must be employed in order to achieve the required vacancy concentration.

By considering the previous evidences reported for GaSb[27], He implanted Si[21] and the results presented in this paper for TiO_2, we propose the mechanism schematized in figure 2.6 for the formation of surface patterns in anatase TiO_2. In an initial stage, ions are implanted at a depth about the ion projected range, forming atom vacancies which are scattered in the material. Because of the high dose employed in the irradiation, the defect concentration reaches a critical value and the material collapses forming small voids. It is worthy to mention, that we expect that not only the ion dose but also the ion flux may play a relevant role in the void formation and growth due to the different typical times associated to vacancy formation and migration kinetics in the material. Once voids are formed in the material, they grow in size in a preferential direction defined by the ion beam due to the ion induced damage in the material (in the same way as explained in ref. 25 for Sn ion-implantation of GaSb thin films). The migration of vacancies and atoms in the material is controlled by the film temperature during irradiation: when the mobility of vacancies in the material is high enough, nearby voids merge, being brought towards the surface due to the sputtering removal of the first layers. This abovementioned nanostructuring processes are responsible for generating a

nanorod surface pattern aligned with the angle of incidence of the ion beam as illustrated in figure 2.6. By contrast, when the mobility of single vacancies is low enough, most voids remain isolated from each other, and only a small fraction of them open to the surface. Overall, we have found that high values of the dose and a high temperature enhance the growth of the voids in the material (whenever the ion dose is high enough to reach the critical density of point defects to make the material collapse). As mentioned above, another important variable is the ion flux: preliminary experiments carried out to check the influence of this quantity have shown that it plays a certain role in determining the formation of voids. However, at the present stage we have not been able to find the critical threshold values of ion dose and flux leading to void formation.

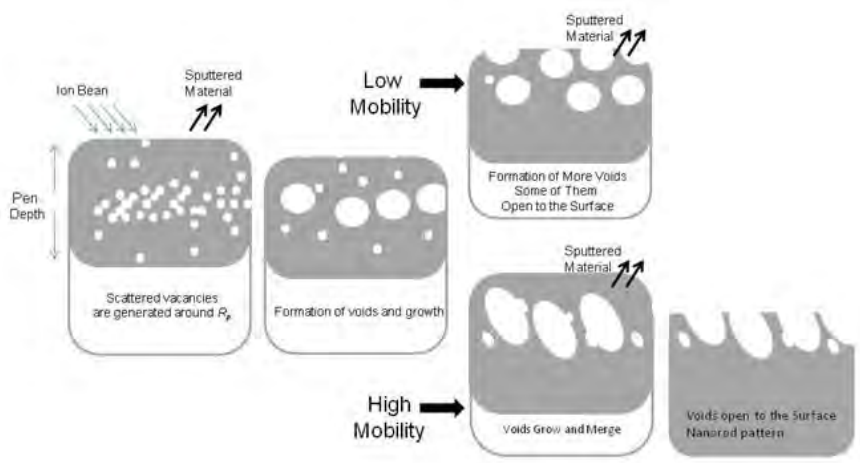

Figure 2.6. Proposed model for the void production, growth, coarsening and opening to the surface to explain the different surface nanostructures formed during ion implantation.

In our model, a key parameter is the mobility of the vacancies in the partially reduced titanium oxide. This mobility is enhanced by the fact that the implanted region consists of a defective $TiO_x(N)$ material with a significant loss of stoichiometry due to the preferential release by sputtering of oxygen from the topmost surface layers and the thermally activated migration of oxygen towards the surface responsible for the homogenization of the oxygen concentration in the implanted region. In fact, Rutherford backscattering spectroscopy (RBS) characterization of the implanted layers shows an excess of Ti over the TiO_2 stoichiometry (result not shown). Defective titanium oxides are known for having a high lattice mobility and structural plasticity (a typical case is

that of the so-called Magnelli phases, well known for their easy rearrangement at moderate temperatures[36]), a feature that must be the main factor responsible for the surface nanostructuring processes undergone by the implanted and heated samples. Thus, film temperature during irradiation governs two cumulative processes that contribute to void growth: on the one hand film temperature directly controls the atoms and vacancies mobility in the network, and, on the other hand, it also contribute to homogenize the oxygen concentration in the implanted region, a feature that also enhances to the overall mobility in the material.

General character of the surface patterning processes with other ions

Vacancy formation and loss of stoichiometry during ion implantation must depend not only on temperature, but also on the reactivity of the implanted ion species. To check to which extent the basic guidelines of the model in figure 2.6 comply with the results, we have carried out equivalent irradiations using F^+ and S^+ as implantation ions. In comparison with N and O, F and S atoms cannot be released so easily in the form of gaseous molecules and it can be expected that they will become incorporated more efficiently to the TiO_x network. This means that their use as irradiation ions should favor the removal of point defects and lower down their production rate. Figure 2.7 shows the SEM micrographs corresponding to samples #5 (50-F^+-RT), #6 (50-F^+-700) and #7 (50-S^+-700). Figure 2.7(a) shows the cross-sectional view of sample #5 (50-F^+-RT) irradiated at room temperature. Since no trace of voids is appreciable in the image, we can conclude that either they do not form under the used irradiation conditions or they are too small to be detected. Furthermore, the surface electrical resistivity of this sample (see values in Table 2.I) is higher than that for samples #3 (50-N^+-RT) and #4 (50-N^+-700), thus suggesting a lower defect concentration in the fluorine implanted region. By contrast, if the ion irradiation takes place at 700 K we found a different behavior as evidenced by the normal view SEM micrograph in figure 2.7(b) showing that the microstructure of this sample is similar to that of sample #4 (50-N^+-700).

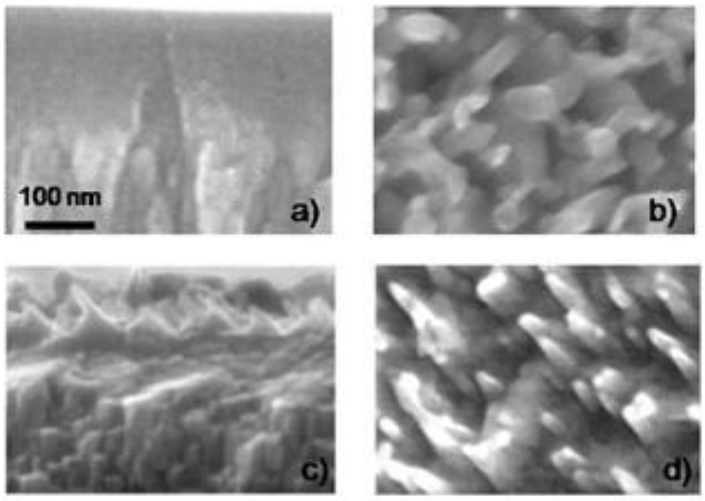

Figure 2.7. SEM micrographs of TiO_2 anatase thin films: a) cross-sectional view of sample #5 (50-F^+-RT) in Table 2.I, b) top view of sample #6 (50-F^+-700), c) cross-sectional view of sample #7 (50-S^+-700), and d) top view of sample #7 (50-S^+-700).

The abovementioned results suggest that, at room temperature, the growth of voids is completely inhibited due to the low mobility and/or low production rate of point defects, caused by the incorporation of fluorine to the material's network. However, the increase of the implantation temperature up to 700 K enhances the mobility of the vacancies and atoms in the material contributing to the migration of oxygen and therefore to the survival of point defects not saturated by fluorine. This is corroborated by the value of the resistivity of the film, which by increasing several orders of magnitude (see results for sample #6 (50-F^+-700) in Table 2.I) indicates a significant loss of stoichiometry and the accumulation of defects in the implanted layer. This highly defective surface state evolves towards the development of a surface pattern as that schematized by the low mobility case in figure 2.6. According to our model, an even higher substrate temperature would be necessary in order to enhance the surface mobility required to generate a nanorod surface pattern. Unfortunately, experimental limitations in our setup impeded us to verify this model hypothesis.

To confirm the general character of the aforementioned phenomena and, therefore, support the premises of our model, TiO_2 thin films have been irradiated with less electronegative species under the assumption that they will present a lesser tendency than O, N or F to become incorporated into the material's network. The corresponding

experiment consisted of the irradiation with a half ion dose of S^+ ions, the other conditions remaining similar to those used for sample #4 (50-N^+-700). The lower dose used in this experiment is intended to limit the magnitude of the network damage induced by this higher atomic mass ion. Even though, the cross-sectional and top view SEM micrographs of sample #7 (50-S^+-700) reported in figures 2.7(c) and 2.7(d) show that the open voids appearing at the surface are deformed in the direction of the ion beam and become open to the surface shaping a structure consisting of ellipsoidal voids and tilted nanorods. The resistivity measurements for this sample reported in Table 2.I show that it is more conductive than sample #4 (50-N^+-700), probably because it contains a larger number of defects and vacancies in its structure. All these features agree with the formation of a surface pattern as that schematized by the high mobility cartoon in figure 2.6. The previous results confirm that the formation of surface nanorods in irradiated TiO_2 thin films can be achieved by using a wide variety of ions and experimental conditions (ion dose and temperature) provided that a critical concentration of oxygen vacancies is reached in the implanted layer.

IV. Conclusions

In this paper we have discussed the effects of a high ion dose irradiation on TiO_2 thin films under different conditions of temperature and ion nature. We have found three different microstructures depending on the type of ion and the degree of mobility in the network, this latter depending on temperature and the degree of nonstoichiometry of the implanted samples. We have shown that at room temperature N^+ irradiated TiO_2 anatase thin films develop a typical microstructure with mounds and voids open to the surface. Meanwhile, irradiations at 700 K generate a surface pattern consisting of ordered nanorods aligned with the ion beam. The formation of these patterns is caused by the simultaneous effect of ion irradiation and film temperature that favors the structural mobilization of the defective lattice of the irradiated titanium oxide. A qualitative model has been proposed to account for the void formation, their growth and merging within the ion penetration depth, as well as their opening towards the surface. This model takes into account the generation of ion induced point defects and the mobility and the coarsening of the vacancies in the material. The general character of these phenomena has been tested by using F^+ ions as projectiles. With these experiments we have shown

that temperature plays a crucial role during irradiation finding an almost flat surface at low temperatures and a porous surface pattern at 700 K. A similar experiments with S^+ ions confirm that the reported procedure can be considered as a common method for the surface nanoestructuring of TiO_2 anatase thin films. Finally, our results confirm the validity of the ion irradiation methodology for the production of tilted nanorod patterns that depend on the irradiation beam characteristics. This technique may have a great impact for multiple applications and, very likely, for the surface nanoestructuring of other materials with different functionalities.

Acknowledgements

Financial support from the Spanish Ministry of Innovation (projects MAT 2007-65764, CONSOLIDER INGENIO 2010-CSD2008-00023 and PIE 200960I132) and the Junta de Andalucía (projects TEP2275 and P07-FQM-03298) is acknowledged. We would also like to acknowledge a grant of the EU to carry out the implantation experiments in the Forschungzentrum of Rossendorf (Germany).

References

(1) O. Carp. C.L. Huisman, A. Reller, Prog. Sol. Stat. Chem. **32**, 33 (2004)

(2) A. Fujishima, T.N. Rao, D.A. Tryk, J. Photochem. Photobiol. C: Photochem. Rev. **1**, 1 (2000).

(3) M.R. Hoffman, S.T. Martin, D.W. Choi, D.W. Bahnemann, Chem. Rev. **95**, 69 (1995).

(4) M. Fujihira, Y. Satoh, T. Osa, Nature **293**, 206 (1981).

(5) U. Diebold, Surf. Sci. Reports **48**(5-8), 53 (2003).

(6) V. Rico, P. Romero, J.L. Hueso, J.P. Espinós, A.R. González-Elipe, Catalysis Today **143**, 347 (2009).

(7) R. Asahi, T. Morikawa, T. Ohwaki, K. Aoki, Y. Taga, Science **293**, 269 (2001).

(8) P. Romero-Gomez, V.Rico, A.Borras. J. Phys. Chem. C **113**, 13341 (2009).

(9) D. V. Bavykin, J. M. Friedrich, F. C. Walsh, Advance Materials **18**(21), 2807 (2006).

(10) M. Zukalová, A. Zukal, L. Kavan, M.K. Nazeeruddin, P. Liska, M. Gratzel, Nano Lett. **5**, 1789 (2005).

(11) M. Adachi, Y. Murata, J. Takao, J. Jiu, M. Sakamoto, F. Wang, J. Am. Chem. Soc. **126**, 14943 (2004).

(12) M. Law, L. E. Greene, J.C. Johnson, R. Saykally, P.D. Yang, Nat. Mater. **4**, 455 (2005).

(13) M. Paulose, O.K.Varghese, G.K. Mor, C.A. Grimes, K.G. Ong, Nanotechnology **17**, 398 (2006).

(14) G.K.Mor, K. Shankar, M. Paulose, O.K. Varghese and C.A. Grimes, Nano Lett. **6**, 215 (2006).

(15) K. Shankar, G.K.Mor, H.E. Prakasam, S. Yoriya, M. Paulose, O.K.Varghese, C.A. Grimes, Nanotechnology **18**, 065707 (2007).

(16) C.A. Grimes, J. Mater. Chem. **17**, 1451 (2007).

(17) P. Romero-Gomez, A. Palmero, F. Yubero, M. Vinnichenko, A. Kolitsch, A.R. Gonzalez-Elipe, Scripta Materialia **60**, 574 (2009) .

(18) S. Nakao, T. Nonami, P. Jin, Y. Miyagawa, S. Miyagawa Surf. Coat. Technol. **128-129**, 446 (2000).

(19) T.-H. Her, R. J. Finlay, C. Wu, S. Deliwala, Appl. Phys. Lett. **73**(12), 1673 (1998).

(20) M. Shen, J.E. Carey, C.H. Crouch, M. Kandyla, H.A. Stone, E. Mazur, Nanoletters **8**(7), 2087 (2008).

(21) S. Frabboni, F. Corni, C. Nobili, R. Tonini, G. Ottaviani, Phys. Rev. B **69**, 165209 (2004).

(22) S.O. Kucheyev, J.S. Williams, C. Jagadish, J. Zhou, V.S. J. Craig, G. Li, Appl. Phys. Lett. **77**(10), 1455 (2000).

(23) S.O. Kucheyev, J.S. Williams, J. Zhou, C. Jagadish, G. Li, Appl. Phys. Lett. **77**(22), 3577 (2000).

(24) S.O, Kucheyev, J. E. Bradby, C.P. Li, S. Ruffell, T. van Buuren, T.E. Felter, Appl. Phys. Lett. **91**, 261905 (2007).

(25) N. Nitta, M. Taniwaki, Y. Hayashi, T. Yoshiiem J. Appl. Phys, **92**(4), 1799 (2002).

(26) N. Nitta, M. Taniwaki, Y. Hayashi, T. Yoshiiem, Physica B **376**, 881 (2006).

(27) A. Perez-Bergquist, S. Zhu, Kai Sun, X. Xiang, Y. Zhang, L. Wang, small **8**, 1119 (2008).

(28) A. Borras, C. Lopez, V. Rico, F. Gracia, A.R. Gonzalez-Elipe, J. Phys. Chem. C **111,** 1801 (2007).

(29) http://www.srim.org/

(30) T. Le Mercier, J.-M. Mariot, P. Parent, M.-F. Fontaine, C.F. Hague, M. Quarton, Applied Surface Science **86**, 382 (1995).

(31) Z. Lin, A. Orlov, R. M. Lambert, M.C. Oayne J. Phys. Chem. B **109**, 20948 (2005).

(32) R.F. Egerton, Electron Energy-Loss Spectroscopy in the Electron Microscope (Plenum Press, New York, 1996), p. 245.

(33) R. McLaren, S.A.C. Clark, I. Ishii, A. P. Hitchcock, Phys. Rev. A 36, 1683 (1987).

(34) S. Trasobares, O. Stephan, C. Colliex, Eur. Phys. J. B **22**, 117 (2001)

(35) F.H. Eisen, Physical Review **123**, 736 (1961).

(36) L. Liborio and N. Harrison, Phys. Rev. B **77**(10), 104104 (2008).

Capítulo 3

Control de las condiciones del plasma

Plasma Deposition of N-TiO_2 thin films

P. Romero- Gómez, A. Barranco, J. Cotrino, J.P. Espinós, F. Yubero, A.R. González-Elipe

Instituto de Ciencia de Materiales de Sevilla (CSIC-Univ. Sevilla). Avda. Américo Vespucio 49. 41092 Sevilla (Spain). http://www.sincaf-icmse.es/

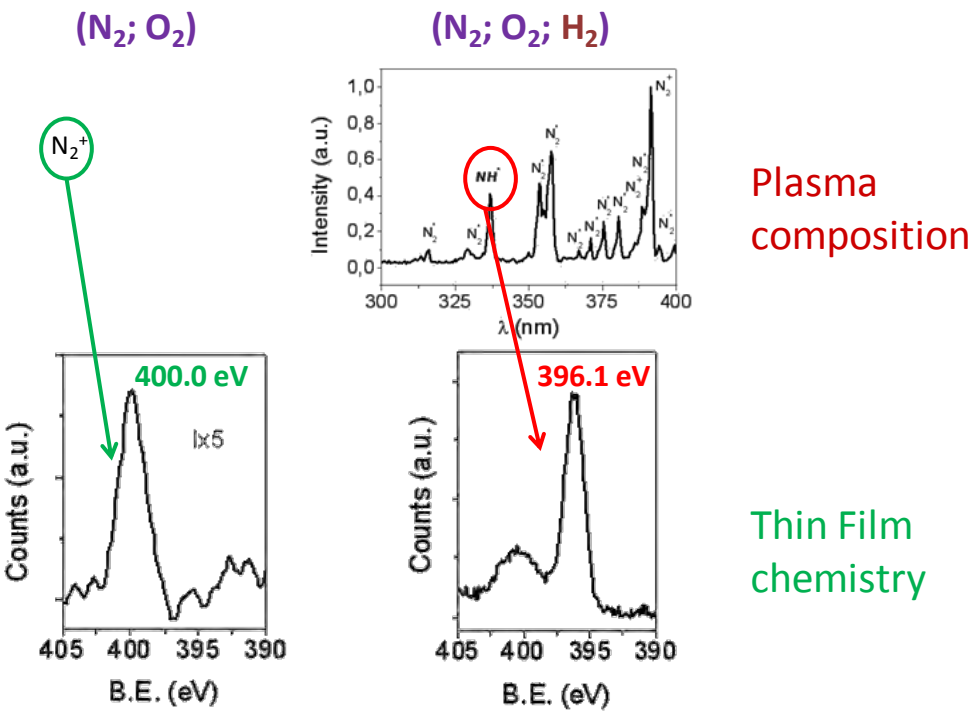

Title: Plasma Deposition of N-TiO_2 thin films.

Authors**: P. Romero- Gómez**, A. Barranco, J. Cotrino, J.P. Espinós, F. Yubero, A.R. González-Elipe

Edited by: Y.Kawai, H.Ikegami, N.Sato, A. Matsuda, K. Uchino, M. Kuzuya, A. Mizuno

Source. WILEY-VCH, Weinheim, Alemania, 2010, pags. 349-355

Plasma Deposition of N-TiO_2 thin films

P. Romero- Gómez, A. Barranco, J. Cotrino, J.P. Espinós, F. Yubero, A.R. González-Elipe

Instituto de Ciencia de Materiales de Sevilla (CSIC-Univ. Sevilla). Avda. Américo Vespucio 49. 41092 Sevilla (Spain). http://www.sincaf-icmse.es/

Abstract

The properties of the nitrogen plasmas used for the preparation of N-doped TiO_2 thin films are characterized by means of a single Langmuir probe placed in the downstream region of a 2.45 GHz microwave plasma source. Results are compared for plasmas of N_2 + O_2 + H_2 mixtures in different proportions. Optical emission spectra (OES) have been recorded to characterize the intermediate species of the plasmas and the evolution of their spectral intensities with the plasma composition. The obtained results are related with the efficiency of these plasmas to prepare N-doped titanium oxide thin films under the different conditions of preparation as determined by X-ray photoemission spectroscopy (XPS).

1.Introduction

Plasmas containing N_2 and H_2 are extensively studied because of their widespread applications for the processing of materials[1]. Despite their extensive use, only limited information is available on the role of the different nitrogen species of the plasma in the nitridation processes[2]. Thus, for example, although it is known that NHx radicals play an important role as intermediate precursor of N and H atoms in plasma driven reactions[3], little is known about the plasma-surface interactions involving this kind of species.

This situation is clearly exemplified by the studies aiming at preparing N-doped TiO_2 thin films. The quest for N-doped TiO_2 thin films and powders has been fostered by the discovery that this doped titanium dioxide may present photoactivity in the visible region[4-6]. At present there is a vivid controversy about the reasons of this photo-activity[7, 8] and how it is mediated by the amount of nitrogen incorporated into the films, its chemical state and other characteristics of the samples such as their structure, microstructure, optical properties and so on. Several methods, including magnetron sputtering using nitrogen gas[9] or plasma enhanced chemical vapor deposition (PECVD)[10], have been reported for the preparation of N-doped TiO_2 films. However, in most cases, the plasma conditions used by these preparations are not well described and the reproducibility of the results is not always straightforward.

The present paper presents characterization of data of a series of plasmas used for the synthesis of N-doped TiO_2 thin films by PECVD. For this purpose, the composition (i.e. nitrogen or hydrogen content) and other characteristics of the plasma used for decomposition of the titanium precursor have been systematically changed. The plasma characteristics have been analyzed by Optical Emission Spectroscopy (OES) and Langmuir probe measurements. These plasma characteristics have been correlated with the amount of nitrogen incorporated within the structure of the film, a key issue for the control of the visible photoactivity of this oxide.

2.Experimental setup and diagnostic techniques

N-doped TiO_2 thin films were prepared by PECVD in a plasma reactor with a remote configuration. The system, supplied with a microwave plasma source (SLAN, from Plasma Consult, GMBh, Germany) has been described in previous works[11, 12]. The plasma source is powered by a 2.45 GHz microwave generator working at 400 W and was separated from the reaction chamber by a grid to avoid the microwave heating of the substrates.

Titanium tetra isopropoxide (TTIP) was used as titanium precursor. For dosing the TTIP in a controlled way, the precursor was placed in a stainless steel recipient through which oxygen was bubbled while heating at 305 K. Both the bubbling line and the shower-type dispenser used to dose the precursor into the chamber were heated at 373 K to prevent any condensation in the tube walls. The plasma source was operated with a mixtures of gases containing nitrogen, basically N_2, N_2+H_2, N_2 +O_2 and N_2 + H_2 + O_2. During deposition, oxygen was always present as a carrier gas of the precursor. By other plasma characterization experiments (e.g., Langmuir probe measurements) neither oxygen nor TTIP were fed into the discharge. During operation, N_2, H_2 and O_2 gas flows and total pressure in the chamber were controlled by using mass flow controllers and a throttle valve, respectively. Total pressure during deposition and the other plasma characterization experiments was $4x10^{-3}$ Torr. A detailed description of this experimental set-up can be found in a previous publication[13].

The emission spectrum was analyzed using a 0.5 m CVI/Digikrom DK480 monochromator (CVI Laser Corporation, Albuquerque, NM) with a 1200 grooves/mm grating, spectra resolution of 0.2 nm and spectral sensitivity ranging from 200 to 900 nm (Hamamatsu R928). The light was collected by an optical fiber which was fixed to the monochromator and positioned 4 cm downstream from the source center. The light was collected through a hole in the air cooling ring. It should be noted that the spectroscopic intensities are integrated over the line of sight, so preventing any spatial resolution of the measurements.

The plasma parameters were assessed by a single Langmuir probe movable along the vacuum chamber diameter at an axial distance of about 8 cm from the grid that avoid the microwave heating of the substrates. The probe tip was made of tungsten, had a radius of 0.125 mm and a length of 7 mm. The non-active part of the probe wire was protected from the plasma by a coaxial ceramic tube of length 10 cm. The stainless steel

walls of the vacuum chamber were used as a reference electrode. The measurements were performed by a computer-controlled probe system which has been described in detail elsewhere[14]. Briefly, the system offers the possibility of single and floating double probe measurements. The algorithm to derive the ion density from the single probe characteristics is described in detail in[14]. Langmuir's orbital-motion limited (OML) theory is used to analyze the results[15,16]. We found a total standard uncertainty of the ion density of 25%, which results from the uncertainty of the probe surface area (systematic error ±8%) and of the statistical uncertainty of 17% when running the discharge at different times under identical conditions of the process parameters.

TiO_2 thin films were prepared at two substrate temperatures, 298 and 523 K. Nitrogen incorporation into the TiO_2 thin films was assessed by X-ray photoemission spectroscopy (XPS). XP spectra were recorded on an ESCALAB 210 spectrometer working under energy transmission constant conditions. The Mg Kα line was used for excitation of the spectra. They were calibrated in binding energy (BE) by referencing to the C1s peak taken at 284.6 eV due to the surface contamination. Quantification was done by calculating the area of the peaks and by correcting then with the sensitivity factor of each element/electronic level.

3.Results and Discussion

Table 3.1 summarizes the values of the ion density, electron temperature and plasma potential determined with the Langmuir probe for plasmas of pure N_2, H_2 and a mixture (50%) of hydrogen plus nitrogen. The analysis of the radial dependence of these magnitudes showed that their values decrease for measurements made far from the central position (i.e. about 15 cm) of the chamber where the deposition experiments were carried out. The values reported in Table 3.1 correspond to this central position where the plasma characteristics were homogeneous. A significant difference is that, for all radial positions, the ion density follows the order N_2+H_2 > H_2 > N_2, while the plasma potential has an opposite trend and the electron temperature is minimum for the N_2+H_2 plasma (cf. Table 3.1). The enhancement of the ion density for the N_2+H_2 mixture can be attributed to an increase in the intensity in the tail of the electron energy distribution function[17] and the lower ionization energy of H_2 with respect to N_2. Besides this observation, it is also worthy of note the high ion density values characteristic of these plasmas. These conditions ensure a high reactivity and the total decomposition of the TTIP precursor used for the deposition of the films.

Table 3.1: Ion density, electron temperature and plasma potential of different plasmas used in the present work.

Plasma Composition	**Ion density (m^{-3})**	**Electron Temperature (eV)**	**Plasma Potential (V)**
N_2	$6x10^{16}$	5.6	28
H_2	$9.5x10^{16}$	5.6	27
$N_2 + H_2$	$10.5x10^{16}$	5.0	25

Fig. 3.1 shows, as examples, OES spectra corresponding to $O_2/N_2/H_2$ (i.e., 65%/12%/23% in volume) and O_2/N_2 (88%, 12% in volume) plasmas. In this figure it is possible to detect the presence of N_2^*, NH^* and N_2^+ species. It is important to remark that no NH* species are detected in the absence of hydrogen in the plasma. Similar spectra were also recorded for other spectral regions under these and other plasma compositions, with and without the TTIP precursor. A full account of the species detected under these different working conditions is reported in Table 3.2 where we also include the wavelengths of these peaks/bands used for assignation according to previous works from literature and data basis[18-20]. It is important to note that the type of species detected did not change when the precursor was added to the plasma (i.e., under deposition conditions), although the intensity of the bands attributed to O* in the plasmas of mixtures O_2/N_2 decreased or disappeared and that of the bands/peaks due to H* significantly increased. It is also worthy of note that although no O* species were detected in the plasma of mixtures $O_2/N_2/H_2$, this does not mean that no oxygen reactive species are formed. The formation of (N-doped, see below) titanium oxide under these conditions proves the reactivity of the precursor with active species of oxygen in the plasma.

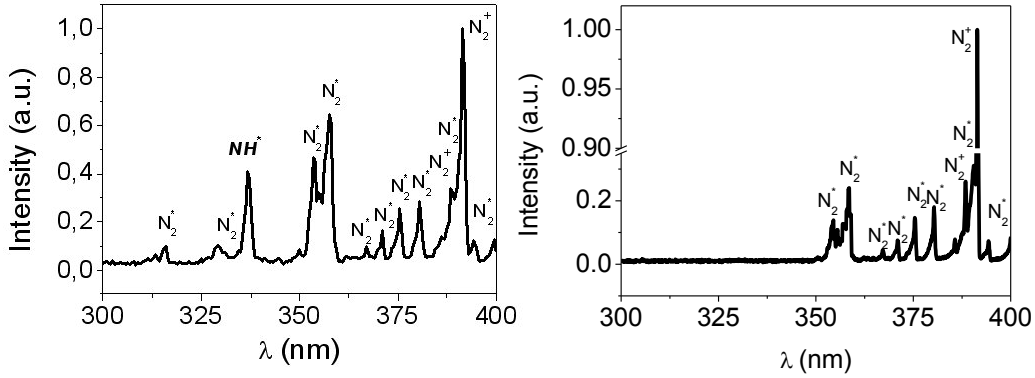

Figure 3.1. OES spectrum recorded in the region from 300 to 400 nm for a $N_2/O_2/H_2$ (65, 12, 23 %) and N_2/O_2 plasmas.

An important evidence from the data in Table 3.2 for the purpose of incorporating nitrogen within the TiO_2 lattice is the detection of N_2^* and N_2^+ species for mixtures of $N_2 + O_2$ as plasma gas. The observed bands correspond to the bands of the second positive (i.e., $C^3\Pi_u - B^3\Pi_g$) and the first positive (i.e., $B^3\Pi_g - A^3\Sigma_u^+$) systems of molecular nitrogen and to the first positive systems of N_2^+ molecular ion (i.e., $B^2\Sigma_u^+$ - $X^2\Sigma_g^+$). It is also noticeable the development of a series of peaks attributed to NH* species and the detection of the hydrogen Balmer α (656 nm) and Balmer β (486 nm) lines in the $N_2 + H_2 + O_2$ mixtures. From the work of Dood et al.[21] the formation of NH* species can be accounted for by the reaction $N(^2D) + H_2 \rightarrow NH + H$, which implies an important $N(^2D)$ state population.

Table 3.2: Plasma species detected by OES.

Plasma composition ($\%N_2$, $\%O_2$, $\%H_2$)	**Species**	**Wavelength (s)(nm)**	**Transition(s)**
(88,12,0)	N_2^*	250-500 600-900	Molecular bands SPS[a] ($C^3\Pi$, v→$B^3\Pi$, v') FPS[b] ($B^3\Pi$, v→$A^3\Sigma$, v')
	N_2^+	391.4- [d]	Molecular bands FNS[c] ($B^2\Sigma$, v→$X^2\Sigma$, v')
(17,83,0)	N_2^*	250-500 600-900	Molecular bands SPS[a] ($C^3\Pi$, v→$B^3\Pi$, v') FPS[b] ($B^3\Pi$, v→$A^3\Sigma$, v')
	N_2^+	391- [d]	Molecular bands FNS[c] ($B^2\Sigma$, v→$X^2\Sigma$, v')
	O*	436.8, 532.9, 615.6, 645.6, 777.4, 844.6	Atomic lines involving the 3s and 3p states
(65,12,23)	H*	656, 486	H_α 2p-3d; H_β 2p-4d
	NH*	337.0	Molecular band (1,1) ($^3\Pi$, v→$^3\Sigma$, v')
	N_2^*	250-500 600-900	Molecular bands SPS[a] ($C^3\Pi$, v→$B^3\Pi$, v') FPS[b] ($B^3\Pi$, v→$A^3\Sigma$, v')
	N_2^+	391- [d]	Molecular bands FNS[c] ($B^2\Sigma$, v→$X^2\Sigma$, v')
	H[e]	H_α(656 nm) H_β (486 nm)	*2p - 6d* ; *2p - 5d;* *2p - 4d* ; *2p - 3d*

a)SPS, second positive system; b)FPS, first positive system; c) FNS, first negative system; d) Only the band at 391 nm is clearly visible in the spectra, the other bands overlaps with hose due to the N_2 SPS; e) Visible when the precursor is added to the plasma even for gas mixtures without hydrogen

To examine the influence of hydrogen in the characteristics of the plasma, different mixtures of nitrogen and hydrogen with increasing amounts of this latter gas were also analyzed. We found that the intensities of the lines of atomic hydrogen, H_α and H_β located at 656.3 nm and 486.1 nm, increased and that of the head bands N_2 (0→2) and N_2^+ (0→0) decreased with the amount of hydrogen in the plasmas. It was also found that the increase in the H_2 flow rate had a strong impact on the intensity of the emission lines of the radical NH which relatively increased with the proportion of this gas. The fact that the maximum incorporation of nitrogen into the TiO_2 is reached for plasmas containing hydrogen (see table 3.3) proves that the incorporation of nitrogen into the titanium oxide lattice is favored under chemically reduction conditions and, very likely, the presence of NH* species in the plasma.

The TiO_2 thin films prepared under the different conditions of work were characterized by XPS, with the purpose of estimating both the amount of nitrogen incorporated into the films and its chemical state. Table 3.3 summarizes the value of the N/Ti ratios determined by XPS for a series of thin films prepared by changing the plasma conditions and substrate temperature. It is apparent from this table that the amount of nitrogen incorporated into the films increases for the plasmas containing hydrogen or when the deposition was carried out at room temperature.

To get a deeper insight into the characteristics of the incorporated nitrogen, we have looked in more detail the shape of the N1s spectra. Fig. 3.2 shows two examples corresponding to the films obtained with the N_2/O_2 and $N_2/O_2/H_2$ plasmas. Besides the quite different intensity of the two spectra (note the multiplication factor in the spectrum of the sample prepared with the N_2/O_2 plasmas), the most noticeable difference is that the peaks in the two cases appear at quite different BEs, that is, at 400.0 and 396.1 eV. According to the literature the second peak can be attributed to nitrogen species bonded to titanium and forming a kind of nitride species[22]. The attribution of the first peak is less straightforward, although it has been tentatively assigned to nitrogen species interacting simultaneously with titanium and oxygen atoms in interstitial position[23].

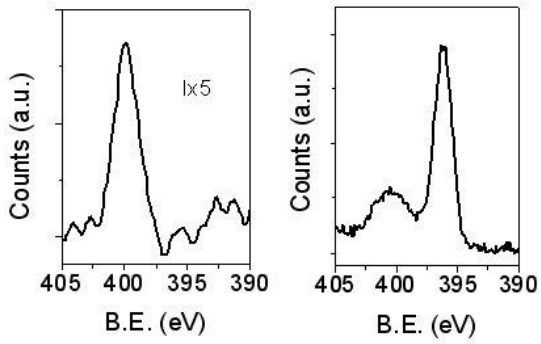

Figure 3.2. N1s photoemission spectra recorded for two N-doped TiO_2 thin films prepared with (left) a N_2/O_2 (12, 88 %) and (right) a $N_2/O_2/H_2$ (65,12,23%) plasma at 523 K.

Preparation conditions (N_2,O_2,H_2 in %) and (T Substrate in K)	**N/Ti**	**$N_{400\ eV}$ (%)**	**$N_{396\ eV}$ (%)**
(12,88,0)(523)	0.01	100	0
(65,12,23)(523)	0.11	28	72
(88,12,0)(523)	0.04	67	33
(88,12,0)(298)	0.11	100	0

Table 3.3. Ratio N/Ti and percentage of the two types of nitrogen species detected in N-doped TiO_2 thin films prepared with different plasmas and substrate temperatures.

An overall assessment of the data in Fig. 3.2 and Table 3.3 in relation with the plasma characteristics shows that formation of the nitrogen species at 400.0 eV is favored when no hydrogen has been added to the plasma or when performing the deposition at room temperature. By contrast a majority 396.1 eV peak is formed with plasmas containing hydrogen and/or when working at 523 K. It is likely that the presence of NH* species detected in the plasma under these conditions plays a favorable role in the doping processes of the films. Under more oxidant conditions as those existing in the N_2/O_2 plasmas or by decreasing the temperature of deposition less nitrogen is incorporated within the films. In this case, the nitrogen is characterized by a BE of 400.0 eV. Although the attribution of these species is still controversial in the literature, recent papers attribute the photoactivity in the visible of the N-doped TiO_2 to its presence as a doping species[23]. Additional work is being carried out in our laboratory to clearly establish a correlation between the detection of these species and the visible photoactivity of N-doped TiO_2.

In conclusion, our work has shown that it is possible to incorporate nitrogen into the structure of anatase prepared by PECVD and that the characteristics of this nitrogen incorporation depend on the plasma conditions for mixtures N_2+O_2+H_2. The analysis of the plasma by OES has provided important clues to understand this phenomenology.

4.Acknowledgments

We thank the Ministry of Science and Education of Spain (projects MAT 2007 65764/NAN2004-09317, and the CONSOLIDER INGENIO 2010-CSD2008-00023) and the Junta de Andalucía (projectsTEP2275 and P07-FQM-03298) for financial support. Part of this work has been carried out within the EU project NATAMA (contract nº 032583).

5.References

(1) J.L. Hueso, J.P. Espinós, A. Caballero, J. Cotrino, A.R. González-Elipe. *Carbon* **2007,** *45*, 89.

(2) K.S. Suraj, P. Bharathi, V. Prahlad, S. Mukherjee, *Surf. Coatings Tech.* **2007**,*202*, 301.

(3) B. Gordiets, C.M. Ferreira, MJ Pinheiro, A. Ricard, *Plasma Source Sci. Technol*. **1998,** 7, 363 .

(4) R. Asahi, T. Morikawa, T. Ohwaki, K. Aoki, Y. Taga, *Science* **2001** 293, 269 .

(5) S. Sakthivel, M. Janczarek, H. Kirsch, *J. Phys. Chem. B* **2004,** 108, 19384.

(6) H.M. Yates, M.G. Nolan, D.W. Sheel, M.E. Pemble, *J. Photochem. Photobiol. A:Chemistry* **2006,** 179, 223.

(7) S. Livraghi, M.C. Paganini, E. Giamello, A. Selloni, C.D. Valentin, G. Pacchioni, J.

Am. Chem. Soc. **2006,**128, 15666.

(8) J.-Y. Lee, J. Park, J.-H. Cho, *Appl. Phys. Lett*. **2005,** 87, 011904.

(9) Ming-Show Wong, Hung Pang Chou, Tien-Syh Yang, Thin Solid Film, **2005**, 494, 244.

(10) M. Maeda, T. Watanabe, *J. Electrochem. Soc*. **2006,** 153, C186

(11) A. Borrás, J. Cotrino, A. R. González-Elipe, *J. Electrochem. Soc*., **2007,** 154, 152.

(12) F. Gracia, J.P. Holgado, A.R. González-Elipe, Langmuir, **2004,** 20, 1688.

(13) J.Cotrino, A Palmero, V. Rico, J. Vac. Sci. Technol. B, **2001**, 19, 1071.

(14) Brockhaus A, Borchardt A and Engeman J Plasma Sources Sci. Technol., **1994,** 3**,** 539.

(15) J. H. van Helden, P. J. van den Oever, W. M. M. Kessels, M. C. M. van de Sanden, D. C. Schram, and R. Engeln, J. Phys. Chem. A **2007,** 111**,** 11460-11472.

(16) J L Jauberteau and I Jauberteau, Plasma Source Sci. Technol., **2008,** 17, 015019.

(17) J Loureiro and A Ricard, J. Phys. D: Appl. Phys. **1993**, 26, 163

(18) R. W. B. Pearse and A. G. Gaydon, *The Identification of Molecular Spectra* Wiley,New York, **1963.**

(19) W. L. Wiese, M. W. Smith, and B. M. Glennon, *Atomic Transition Probabilities,National Bureau of Standards, Gaithersburg, MD*, **1966.**

(20) M K Boudam, B Saoudi M Moisan and A Ricard, *J. Phys. D: Appl. Phys.* **2007**,*40*, 1694.

(21) J.A.Dood, S.J.Lipson, D.J.Flanagan, W.A.M.Blumberg, J.C.Person and B.O.Green, *J. Chem.Phys.,* **1991, 94**, 4301.

(22) X. Qiu, Y. Zhao, C. Burda, *Adv. Mater*., **2007,** 19, 3995.

(23) R. Asahi, T. Morikawa, H. Hazama, M. Matsubara, *J. Phys.: Condens. Matter* **2008,** 20,064227.

(24) Y. Cong, J. Zhang, F. Chen, M. Anpo, *J. Phys. Chem. C,* **2007,** 111, 6976.

Capítulo 4

Síntesis y propiedades de capas nanoestructradas N-TiO_2

Band gap narrowing vs. formation of electronic states in the gap in N-TiO_2 thin films

P. Romero-Gómez[1], Said Hamad[3], J.C. González[1], A. Barranco[1], J.P. Espinós[1], J. Cotrino[1,2], A.R. González-Elipe[1*]

1. Instituto de Ciencia de Materiales de Sevilla (CSIC-Univ. Sevilla). Avda. Américo Vespucio 49. 41092 Sevilla (Spain). http://www.sincaf-icmse.es

2. Departamento de Física Atómica, Molecular y Nuclear. Universidad de Sevilla. Avda. Reina Mercedes 49, 41012 Sevilla. Spain.

3. Department of Physical, Chemical and Natural Sciences. Universidad Pablo de Olavide. Carretera de Utrera, km 1. Sevilla. Spain

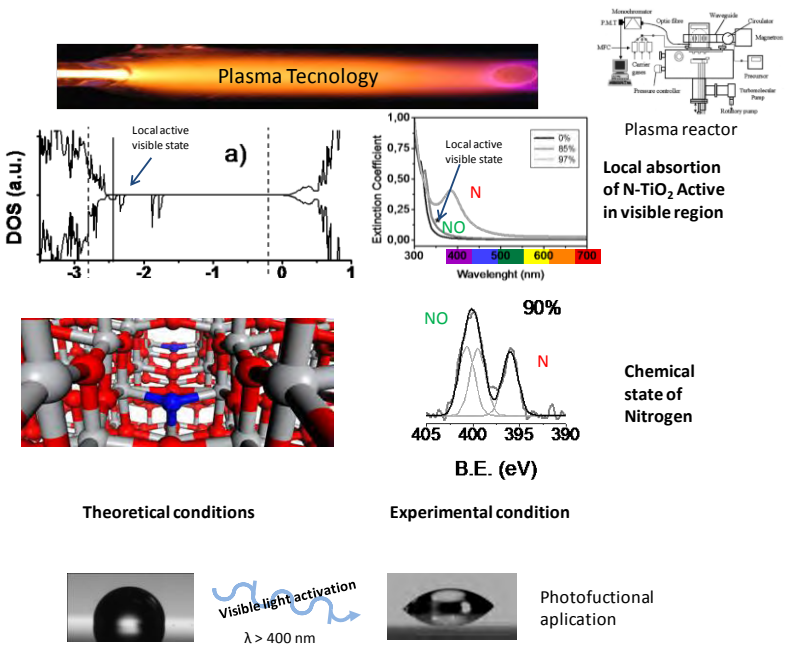

Title: Band gap narrowing vs. formation of electronic states in the gap in N-TiO_2 thin films

Authors **P. Romero-Gómez**, Said Hamad, J.C. González, A. Barranco, J.P. Espinós, J. Cotrino, A.R. González-Elipe.

Source: (*J. Phys. Chem. C*, Article ASAP)

D.O.I. 10.1021/jp104634j

Band gap narrowing vs. formation of electronic states in the gap in N-TiO_2 thin films

P. Romero-Gómez[1], Said Hamad[3], J.C. González[1], A. Barranco[1], J.P. Espinós[1], J. Cotrino[1,2], A.R. González-Elipe[1*]

1. Instituto de Ciencia de Materiales de Sevilla (CSIC-Univ. Sevilla). Avda. Américo Vespucio 49. 41092 Sevilla (Spain). http://www.sincaf-icmse.es

2. Departamento de Física Atómica, Molecular y Nuclear. Universidad de Sevilla. Avda. Reina Mercedes 49, 41012 Sevilla. Spain.

3. Department of Physical, Chemical and Natural Sciences. Universidad Pablo de Olavide. Carretera de Utrera, km 1. Sevilla. Spain

*arge@icmse.csic.es

Abstract

N-containing TiO_2 thin films with different amounts of nitrogen have been prepared by plasma enhanced chemical vapor deposition (PECVD) by using different titanium precursors without (titanium isopropoxide, TTIP) and with (tetrakis diethyl amino titanium, TDEAT and tetrakis dimethyl amino titanium, TDMAT) nitrogen in their structures and different N_2/O_2 ratios as plasma gas. For low/high content of nitrogen, Ti-NO and/or Ti-N like species have been detected in the films by X-ray photoelectron spectroscopy (XPS). Their optical behavior is characterized by a red shift of their absorption edge when Ti-N species are a majority, and by an unmodified edge with localized absorption states in the gap when only Ti-NO like species are present in the film. The experimental results have been interpreted by calculating the density of states of model systems consisting of a 2x2x3 repetition of the anatase unit cell. This basic structure incorporates nitrogen defects in either substitutional or interstitial lattice positions that are considered equivalent to the Ti-N and Ti-NO like species detected by XPS. To simulate the effect of, respectively, a low or a high concentration of nitrogen, calculations have been carried out by placing two nitrogen defects either in separated or in nearby positions of the anatase structure. The computational analysis reveals that the defects have different stabilization energies and confirm that an edge shift of the valence band is induced by the substitutional nitrogen centers, as observed when a high

concentration of Ti-N species becomes incorporated into the films. In agreement with the experimental results, when only Ti-NO like species are detected by XPS, no band gap narrowing is obtained by the calculations that predict the appearance of localized electronic states in the gap. The fact that only these latter films present water wetting angle photo-activity when irradiated with visible light supports that the presence of Ti-NO like species is a required condition for visible light photoactivity.

Keywords: N-modified TiO_2; plasma deposition; optical properties; visible photo-activity; electronic structure; N species

1. Introduction

N-modified TiO_2 materials have been widely studied during the last years because of the possibility of making them photo-catalytically active under visible light illumination. Since the seminal work of Asahi et al,[1] many papers have appeared in the literature trying to unravel the reasons that sustain this behavior.[2-10] Of particular relevance in this regard are the recent works by Di Valentin et al[11-15] where, by combining theory and experiments mainly by EPR, they show that the species responsible for the visible photoactivity of N-containing TiO_2 consist of N atoms located in interstitial lattice positions where it bonds to Ti atoms and interacts with a nearby O ion of the lattice (i.e., a kind of Ti-NO species). This model contrasts with more traditional views linking the visible photoactivity of N-doped TiO_2 with the formation of substitution nitrogen species (i.e., a kind of Ti-N species).[1, 5,16] Another related aspect that has generated much discussion within this topic is the influence of the incorporated nitrogen on the optical properties of the materials, namely in the changes in light absorption due to possible modifications of the band gap of the titanium oxide.[17-21] The appearance of absorption features in the visible region of the spectra of N-containing TiO_2 is generally taken as a required but not sufficient condition for visible photoactivity.[22] However, the physical causes of this visible absorption are also controversial, with some authors supporting that the effect of the nitrogen species is to shift the band gap of the titanium oxide towards the visible[17-20] and others claiming that these species do not modify the band gap of the oxide but induce some electronic states

in the band gap region that give rise to localized absorption features close to the absorption edge of the titanium oxide.[11-15, 22-24]

In a recent work on N-doped TiO_2 thin films prepared by plasma and evaporation methods, we have shown that while Ti-NO species are able to induce some visible light decrease of the wetting angle of the surface,[22] Ti-N species do not induce any kind of visible light activation. However, for the samples to present photocatalytic activity towards the photodegradation of dyes it was required that besides Ti-NO species, the films were crystalline with a mixture of anatase and rutile. In this previous investigation we already noted that the absorption spectra of films with a high content of nitrogen depicted some absorption features in the visible, although no correlation could be established between the nitrogen content and the characteristics of the ultraviolet-visible (UV-vis) absorption spectra.

As a continuation of this previous work, herein we primarily aim at determining whether each kind of nitrogen species (i.e. Ti-NO or Ti-N) has a specific effect on the physical causes (i.e., gap narrowing or development of localized states in the gap) determining the changes in the absorption spectra of N containing titanium oxide thin films (in the following, named in general as N-TiO_2 although changes in the Ti/O ratio may occur as a consequence of the development of oxygen vacancies whose formation is related with the incorporation of Ti-N species of nitrogen[25]). We approach this problem firstly by investigating experimentally a series of N-TiO_2 thin films where we have systematically changed the type and concentration of nitrogen species. To get such an ample set of samples with different concentrations of nitrogen species, we have employed the plasma enhanced chemical vapor deposition (PECVD) procedure and systematically modified the plasma conditions and other working parameters like the type of precursor and temperature of the substrate. Such an experimental approach has hitherto not been widely used for the preparation of photoactive N-TiO_2 thin films, although the preparation of photoactive nanoparticles by atmospheric plasma deposition has been reported.[26] The most common titanium precursor used for the PECVD synthesis of TiO_2 thin films is titanium isopropoxide (TTIP).[23, 27-30] Tetrakis dimethyl amino titanium (TDMAT) and tetrakis(diethylamido) titanium (TDEAT)[31-33] are other two precursors that are commonly used in methods of preparation of optical thin films. Therefore, another innovative approach of our work is the use of three titanium precursors (TTIP, TDEAT and TDMAT) with the idea that the presence of direct Ti-N

bonds in the structure of two of them and, very likely, their different reactivity, permit one to tune the state of nitrogen in the films and to control film properties such as UV-vis absorption spectra and photo-activity.

To account for the different experimental findings and particularly for the changes in the absorption spectra depending on the type and concentration of nitrogen species in the prepared N-TiO_2 thin films, we have theoretically modeled the electronic structure of these materials by calculating the density of states (DOS) of N-modified anatase for three different types of N defects incorporated in its structure. Modeling the Ti-NO (and Ti-ON as a possible alternative) defect states is done by assuming that N occupies an interstitial position and interacts with both oxygen and titanium ions of the lattice. This species, with nitrogen bearing a formal charge of -1 (i.e., NO^{3-} like species), could be described as a $(NO)_O^t$ defect centre according to the Kröger-Vink notation of defect states in oxides. To simulate the Ti-N species, nitrogen replaces substitutionally replace an oxygen of the lattice and bonds directly to titanium in a kind of nitride species (i.e. N^{3-} species or N_O^t according to the Kröger-Vink notation). Similar calculations simulating the effect of Ti-N and Ti-NO like species can be found in the works by Di Valentin et al.[11,15] and Graciani et al.[25,34] Herein, besides studying the stability of Ti-ON like species, we have simulated the effect on the optical properties of N-TiO_2 materials of the concentration of Ti-N or Ti-NO species, an aspect that had not been addressed in these previous theoretical works. For this purpose, calculations have been carried out by placing two defect states quite separated (i.e., simulating a low concentration of nitrogen) or in nearby positions of the structure (i.e., simulating a high concentration of nitrogen), in this latter case making it possible that the two defect states interact between them as it would be the case in samples with a high concentration of nitrogen species. The DOS calculations and particularly the analysis of the partial DOS plots of N, Ti and O have confirmed the experimental findings and show that the incorporation of a high concentration of Ti-N species induces a red shift in the absorption gap of the material. Meanwhile Ti-NO species do not significantly modify the magnitude of the gap between the valence and conduction bands, but induce the formation of new localized states in the band gap zone of the oxide.

Finally, all these experimental and theoretical results are critically discussed in relation with the actual photoactivity of N-TiO_2 materials by analyzing the superhydrophilic conversion of the surface state of the prepared films under visible light irradiation.

2. Experimental

2.1 Thin film preparation

TiO_2 and N-TiO_2 thin films have been prepared by PECVD in a plasma reactor with a remote configuration. The system, supplied with a microwave plasma source (SLAN, from Plasma Consult, GMBh, Germany) has been described in previous works.[27, 28, 35] It consists of an external 2.45 GHz microwave electron cyclotron resonance (MW-ECR) plasma source coupled to the reaction chamber and separated from it by a grid to avoid the microwave heating of the substrates. Under normal conditions of operation, the grid confines the plasma out of the reaction chamber (remote plasma conditions) where the substrate and the precursor dispenser are located. Titanium tetra-isopropoxide (TTIP), Tetrakis(diethylamido)titanium(IV)(TDEAT) and Tetrakis(dimethylamido)titanium(IV) (TDMAT) were used as titanium precursors. In Figure 4.1 we show a schematic representation of the structure of these three precursors, showing that four direct Ti-N bonds exist in TDEAT and TDMAT. It is likely that some of them can be preserved during the plasma processing of the N-TiO_2 thin films.

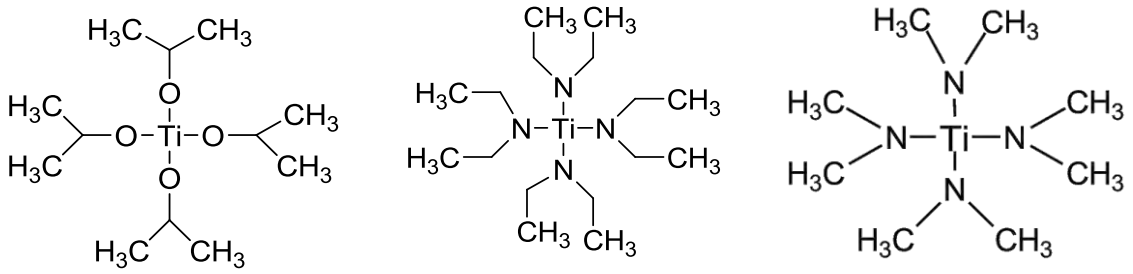

TTIP **TDEAT** **TDMAT**

TTIP: titanium tetrakis isopropoxide

TDEAT: tetrakis diethyl amino titanium

TDMAT: tetrakis dimethyl amino titanium

Fig. 4.1. Schematic representation of the Ti precursors utilized for the synthesis of the N-TiO_2 thin films by plasma deposition.

The plasma source was operated with a power of 400 W with either pure O_2 or mixtures N_2+O_2 at different proportions of nitrogen from 0 % to 97%. The synthesis of the films was carried out either at 298 K or 523 K, although most reported data corresponds to this latter temperature. Controlled dosing of the precursors was achieved by placing

them in a stainless steel recipient heated to 305 K, while oxygen or a N_2/O_2 mixture was bubbled through it. Both the bubbling line and the shower-type dispenser used to dose the precursor into the chamber were heated to 373K to prevent any condensation in the tube walls. The total pressure during deposition was $4x10^{-3}$ Torr (normal operation conditions). A deposition rate of approximately 2.5 nm min^{-1} was estimated by means of a quartz crystal monitor for the samples grown at room temperature.

The different plasmas used for deposition of the films were characterized by Optical Emission Spectroscopy (OES). The emission spectrum was analyzed using a 0.5 m CVI/Digikrom DK480 monochromator (CVI Laser Corporation, Albuquerque, NM) with a 1200 grooves/mm grating, spectra resolution of 0.2 nm, and spectral sensitivity ranging from 200 to 900 nm (Hamamatsu R928). The light is collected by a fiber optic, which is fixed to the monochromator and positioned 4 cm downstream from the source center. The light was collected through a hole in the air cooling ring. It should be noted that the spectroscopic intensities are integrated over the line of sight, thus limiting the spatial resolution.

All the films were deposited simultaneously on a silicon wafer and on quartz plates. The thickness of the prepared samples was estimated by measuring the mass thickness of the films by X-ray fluorescence (XRF) and Rutherford Back Scattering (RBS) or directly from cross section views in the electron microscope (note that for a given sample these two values do not coincide except for completely compact thin films). Most experiments were carried out with films with a thickness of some hundreds of nanometers.

2.2 Methods of characterization

The optical properties of the samples were primarily determined by UV-vis absorption spectroscopy (Perkin-Elmer Lambda 12 Spectrometer) for samples prepared on fused silica. The ellipsometric characterization of the N-TiO_2 films was carried out in a J.A. Woollam VASE (variable angle spectroscopic ellipsometry) spectroscopic ellipsometer. Values of Ψ and Δ were obtained over the spectral range comprised between 300 and 1000 nm, at 5nm resolution. To check the consistency of the data, they were collected at three angles of incidence: 65º, 70º, and 75º. Optical modeling and parameters fitting were carried out with the WASE32© program (J.A. Woollam Co.,Inc.). To model the ellipsometric spectra we fixed the thickness (thickness values were obtained by

transversal SEM images) and applied non-ideal model options such as film thickness non-uniformity and angular spread of the beam entering the detector. Some fitting parameters were coupled among them and their range limited within defined values. Non partial polarization or monochromator bandwidth effects were considered. Quality assessment of the fit data was performed by using the mean-squared error (MSE) value. A small MSE implies that the assumed model was appropriate. In our case, the MSE was below 5 units in the absorbing region and below 2 units in the transparent region. The used optical model consists of two layers deposited on the Si (1 mm) substrate: an external region and an EMA (effective medium approximation) layer with a harmonic oscillator. In this layer a Cauchy dispersion (with Urbach absorption)) and a classic harmonic oscillator model were implemented in a single material layer. The Cauchy dispersion equation was used in the transparent region ($\lambda > 700$nm). No dispersion of refractive index and in the extinction coefficient were considered for $700<\lambda< 1000$nm. For $\lambda < 700$nm one or two harmonic oscillators were added to the Urbach absorption of the Cauchy model. Finally, a certain surface roughness consisting of 50% of film material and 50% of voids was assumed to describe the external layer.

X-ray photoelectron spectroscopy (XPS) spectra of the films were recorded on an ESCALAB 210 spectrometer working under energy transmission constant conditions. The Mg Kα line was used for excitation of the spectra. They were calibrated in binding energy (BE) by referencing the different peaks to the C1s signal due to contamination taken at 284.6 eV. Quantification was done by calculating the area of the peaks and by correcting then with the sensitivity factor of each element/electronic level. To check the effect of surface impurities, the films were subjected to a gentle sputtering with Ar^+ ions of 2.5 keV. A current density of about 10 $\mu A\ cm^{-2}$ for a sputtering time of 2 min was used for these treatments. No significant changes in peak shape or in element ratio (except for the removal of most of the contaminating carbon) were found after this cleaning treatment. Fitting analysis of the N1s peak was carried out by using elemental bands of gaussian/lorentzian shape after background subtraction of the spectra with a Shirley-type curve.

SEM cross section and normal images were measured in a Hitachi S5200 field emission microscope for thin films grown on a silicon wafer.

Structural characterization of the thin films was done by X-ray Diffraction in a Siemens D5000 difractometer working in the Bragg-Brentano configuration and using the Cu Kα line as excitation source.

Measurement of the surface electrical conductivity of the samples was carried out with the typical four point probe test. A Keithley 617 Electrometer and a Hewlett-Packard 34401 A Voltammeter were used for the measurements. These consisted of applying a voltage ranging between -0.25 and 0.25 V to the two external probes and the measurement of the current flowing between the two internal probes.

Measurement of water contact angles was carried out by the Young method by dosing small droplets of deionized and bidistilled water on the surface of the illuminated samples. In the experiments where the contact angle variation was determined as a function of the illumination time, a metal foil acting as a shutter was used to close and open the lamp output. All wetting angle measurements within a given experiment were taken after illumination for successive periods of time. Therefore, the time scale in the plots refers to the accumulative illumination of the samples. The maximum uncertainty in the determination of the water contact angle is about 10º depending on the sample position. In the course of this investigation it was noticed that the "as-prepared" thin films were more hydrophilic than the same samples some time after their preparation. Therefore, the reported results correspond to samples that were stored in desiccators for at least two months before testing their photo-activity. Illumination of the samples was carried out with a Xe discharge lamp with photon intensity at the position of the samples of 2 Wcm^{-2} for the complete spectrum. For simplicity we will refer this situation in the text and figures as UV illumination. Other experiments consisted of the illumination with the same lamp by placing an UV filter (i.e., $\lambda > 400$ nm) between the lamp and the sample. The light intensity at the sample position was then 1.6 Wcm^{-2}. In all cases an infrared filter (i.e., a water bath) was kept between the lamp and the samples to prevent any possible heating by the infrared radiation.

2.3 Computational details

All the calculations were performed using the Vienna Ab-initio Simulation Package (VASP) 4.6 code,[36-38]. Inner core electrons were described by the projector-augmented-

wave method[41] (PAW) and a 500 eV cut-off energy. The Ti (3s, 3p, 3d, 4s), O (2s, 2p) and N (2s, 2p) electrons were treated as valence states, while the remaining electrons were kept frozen as core states. The optimisation of the structures was performed via a conjugated gradient technique, which utilises the total energy and the Hellmann-Feynman forces on the atoms (and stresses on the unit cell). The Brillouin-zone integrations were performed using Monkhorst-Pack grids,[42] using a (2x2x1) mesh, with which convergence in energy was achieved. The simulation cell is formed by a 2×2×3 repetition of the anatase unit cell, in which there are 72 Ti atoms and 144 O atoms. We have employed a LDA+U approach, as described by Dudarev et al,[43-45] with a value of U of 4.5 eV. Calzado et al.[46] found that this value of U yields a correct description of the gap states in periodic LDA+U calculations. All calculations have been carried out in the Finis Terrae supercomputer, in Santiago de Compostela, Spain.

3. Results

3.1 State and concentration of nitrogen in N-TiO_2 thin films

The amount of nitrogen incorporated in the film varied by changing the precursor and the plasma process parameters. Adjusting the plasma gas composition by using different O_2+N_2 mixtures as plasma gas was very important for this purpose. The OES spectra of the plasmas of these mixtures for N_2 concentration higher than 80% were characterized by a series of peaks and bands attributed to N_2* and N_2^+ species (see supporting information S1).[47,48] These nitrogen bands substitute those attributed to O_2* and O* that characterize the spectra recorded in our experimental system when pure oxygen is used as plasma gas.[27] A summary of the main species and spectral features detected as a function of the O_2/N_2 ratio are reported in the supporting information S1 and in a previous contribution of our group.[49] From this analysis it is important to realize that although nitrogen excited species detected by OES are majority in the N_2/O_2 plasmas, this does not necessarily preclude the formation of activated oxygen species, but just indicates that the average life time of these latter species is short as compared with that of the nitrogen species. The high reactivity of the oxygen species accounts for the formation of a titanium oxide film and enables the release of the carbon and hydrogen atoms of the precursors in the form of volatile oxidized compounds. Simultaneously, the presence of active species of nitrogen in the plasma provides a mechanism for the

incorporation of nitrogen in the film by the reaction with the partially decomposed precursor molecules in the plasma phase or on the surface of the growing film. We will show later that the amount and type of incorporated nitrogen depends on the ratio between nitrogen and oxygen in the plasma gas.

Plasma deposition of TiO_2 thin films has been typically carried out by using TTIP as titanium precursor. The use of other precursors like TDMAT and TDEAT offers the possibility to incorporate some nitrogen within the structure even if no molecular nitrogen is added to the plasma gas, provided that some of the Ti-N bonds existing in the precursor molecules are preserved in the films. To verify this possibility we have analyzed by XPS a series of films prepared with a plasma of pure oxygen but using TTIP, TDMAT and TDEAT as precursors and 523 and 298 K as substrates temperatures. It was found that small amounts of nitrogen became incorporated in the films prepared with TDMAT and TDEAT precursors (see supporting information S2). The incorporation was more favorable at 298 K. For all samples the O1s and Ti2p spectra were similar to those amply reported in the literature for TiO_2.[50] The N/Ti ratios deduced from the quantitative analysis of the spectra of the N-TiO_2 films prepared at 523 K and O_2 as the sole plasma gas were 0.037, 0.017 and 0.0 for the TDEAT, TDMAT and the TTIP precursors, respectively. The N1s spectra of the two former films were characterized by a broad peak at around 400 eV (see supporting information S2) which is commonly attributed to interstitial nitrogen species bonded to titanium and oxygen (i.e., a kind of Ti-N-O species[12, 22]). Similar spectra were obtained when the deposition was carried out with a substrate temperature of 298 K, although the intensity of the N1s signal was approximately twice higher in this case. It is also important to mention that the width of this N1s peak was also higher at 523 K (i.e., a half width at half-maximum HWHM of 2.8 eV) than at 298 K (i.e., a HWHM of 1.8 eV). This difference suggests that the nitrogen signal at 523 K is a convolution of different species of nitrogen. N1s spectra with more than one component at around 400 eV have been reported by several authors.[51-53] Their development in our case would indicate that at 523 K there are nitrogen species with slightly different geometries and bonding arrangements.

The concentration and type of nitrogen species in the N-TiO_2 thin films changed when O_2+N_2 mixtures were used as plasma gas. Under these conditions the main parameter controlling the incorporation of nitrogen into the films was the concentration of nitrogen

in the gas mixture. Figure 4.2 shows a series of N1s spectra taken for films prepared at 523 K by using TDMAT as titanium precursor and increasing concentrations of N_2 in the plasma gas. Similar spectra were obtained for the other precursors. It is found that for percentages of N_2 higher than 85%, a new nitrogen species at around 396 eV appears in the spectrum. This species becomes dominant for higher percentages of nitrogen in the plasma gas. Similar results were obtained for the two other precursors, thus sustaining that the plasma gas composition and not the type of precursor is the main variable controlling the amount of nitrogen incorporated into these films. This new form of nitrogen has been attributed on the basis of XPS studies to nitride species in substitutional positions of the titanium oxide lattice (i.e., a Ti-N species[1, 7, 10 53-55]). The combined XPS, near-edge X-ray absorption fine structure (NEXAFS) and Rietveld analysis made recently by H. Chen et al[55] for ammonia treated titania have quite unequivocally supported this attribution. It is also worthy of note that for most investigated films the shape of the O1s and Ti2p spectra is similar to that reported for TiO_2, thus indicating that the upmost surface layers of the films have become oxidized by exposure to the air. Nevertheless, the shape of the Ti2p spectrum of the films prepared with a 97% of nitrogen in the plasma gas slightly changed with the development of a shoulder at lower binding energy, evidencing that some Ti^{n+} species (n<4) remain in the surface of this sample even after its handling in air.

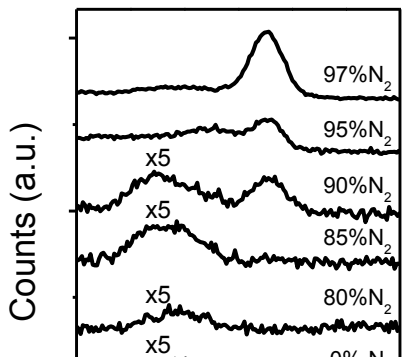

Fig. 4.2. N1s spectra recorded for a series of N-TiO_2 thin films prepared with the TDMAT precursor and different percentages of N_2 in the plasma as indicated. Note that some spectra are affected by a multiplication factor to bring them into a common scale.

A deeper insight into these spectra can be obtained by fitting. Fig. 4.3 shows such an analysis for some selected case examples taken from Fig. 4.2 and others corresponding to thin films prepared with TTIP as precursor. The two sets of samples were synthesized with relative N_2 contents in the plasma gas of 0, 90 and 97%. In the case of the TDMAT samples, the spectra can be properly fitted with four bands located at 396.1, 399.3, 400.7 and 401.7 eV, the three latter accounting for the broad peak at around 400 eV. Meanwhile, a reasonable fitting could be obtained for the spectra of the TTIP samples by using just three bands at 396.1, 399.3 and 400.7 eV. A variety of peaks with N1s BEs comprised between 399 and 402 eV were already found in the early work of Saha et al.[56] dealing with the thermal oxidation of titanium nitride. Because of the similarities of the preparation techniques, it is also worth mentioning a recent publication by Chen et al.[26] where they investigated by XPS the type of nitrogen species incorporated into N-TiO_2 powder samples prepared by an atmospheric plasma procedure and posterior annealing. These authors found different components in the N1s photoelectron spectra, which they attributed to Ti-N (395.8-397.8 eV), Ti-NO (398.8-401.2 eV) and Ti-NO_2 (402.0-403.0 eV) species, in good agreement with our own results. Another relevant result of that work was the verification that the latter species was inactive in inducing any visible photocatalytic activity. Similarly, Dunnill et al.,[57] using a thermal chemical vapor deposition process at 500 ºC for the preparation of N-TiO_2 thin films, found that in the majority of cases a peak at 400 eV was the only species detected and that these samples presented photocatalytic activity in the visible. On the basis of these and many other recent studies,[1, 7, 10, 12, 22, 51-55] we attribute the different features to Ti-N (i.e., band at 396.3 eV assigned to nitrogen triple bonded to titanium) and to nitrogen in a titanium oxinitride local environment (399.3 and 400.7 eV), where nitrogen simultaneously bonds to oxygen and to titanium in a defective lattice site (i.e., in a kind of Ti-N-O or Ti-O-N local structure). Meanwhile, the fourth band at 401.7 eV, observed in samples prepared with the TDMAT and TDEAT precursors, must be attributed to N bonded to a less electropositive environment or, alternatively, to a large number of oxygen atoms. Therefore, we attribute tentatively this band to Ti-NO_2 species (i.e. a nitrogen atom bonding simultaneously to one titanium and two oxide ions of the lattice [26]). A similar attribution has been made recently by Asahi et al[53] based on first principles calculations for a peak with a BE higher than that of the band used here for fitting. For simplicity, in the rest of the paper we will refer to Ti-N and Ti-NO species (this latter including the species that we have designed as Ti-

ON), even if different environments, and therefore BEs, can be expected for the different interstitial species of nitrogen. Theoretical calculations have been performed for Ti-N (i.e., N_s according to the notation used with the calculations with the model systems), Ti-NO (i.e. N_i) and Ti-ON (i.e. N_{si}) species in *section 3.3*.

Figure 4.3. Fitted (gray line) and experimental (black line) N1s normalized spectra of selected N-TiO_2 thin films prepared at 523 K with the TDMAT (left) and the TTIP (right) precursors and different percentages of N_2 in the plasma gas. Elemental bands used for fitting are plotted in gray.

XPS has been also used to quantitatively estimate the concentration of nitrogen in the films as a function of the plasma deposition conditions. Figure 4.4 shows a plot of the N/Ti ratio as a function of the relative concentration of nitrogen in the plasma gas determined by XPS for an ample series of thin films prepared at 523 K. In this plot we make no distinction according to the precursor used for their synthesis, as the plasma gas composition is the main parameter controlling the nitrogen content. It is also important to mention that at 298 K the amount of incorporated nitrogen was always

slightly higher than at 523 K for N_2/O_2 ratios higher than 50% (data not shown). The plot in Fig. 4.4 shows that the concentration of nitrogen in the film remains relatively constant up to N_2 percentages of 80-85%. Above these values, the concentration of nitrogen in the films sharply increases, reaching N/Ti ratios of ca. 0.5 when a 97% nitrogen plasma was used for the synthesis. As mentioned previously, for this sample the shape of the Ti2p spectrum broadens towards lower BEs, pointing to certain reduction of the titanium cations and the formation of oxygen vacancies within the lattice. The incorporation of nitrogen, particularly in the form of Ti-N species, and its relationship with the formation/elimination of oxide vacancies within the lattice has been addressed previously in the literature both experimentally and theoretically. [25, 34, 54, 55] In relation with these previous works dealing with an already formed TiO_2 network where nitrogen is added either by ion implantation or upon annealing in ammonia, our experimental conditions are different because the N-TiO_2 materials are created directly by the deposition and/or reaction of/with plasma species. However, the fact that the maximum concentration of Ti-N species appears when the oxide is defective suggests that the incorporation of this nitrogen species becomes favored in partially reduced titanium oxide networks.

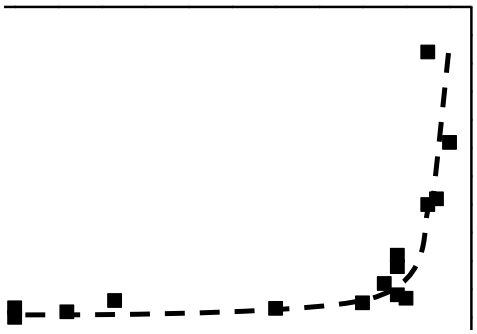

Figure 4.4. N/Ti ratio determined from the intensities of the N1s and Ti2p photoelectron peaks as a function of the percentage of nitrogen in the O_2+N_2 mixture used as plasma gas. The dashed line is included to guide the eyes.

3.2 Optical and electrical properties of N-doped titanium oxide films

Figure 4.5. Set of absorption spectra recorded for a series of N-TiO_2 thin films prepared at 523 K with the TDMAT precursor and different percentages of nitrogen in the plasma gas as indicated in each particular panel. The gray color spectrum included for comparison in each panel corresponds to the absorption spectrum of a pure TiO_2 thin film.

The progressive incorporation of nitrogen into the films, particularly in the form of Ti-N species, induces significant changes in their optical behavior. Fig. 4.5 shows a series of UV-vis absorption spectra recorded for selected thin films prepared with TDMAT as precursor and 85%, 90%, 95% and 97% N_2 in the plasma gas. It is important to note that the three latter samples have incorporated a considerable amount of nitrogen (cf. Figs. 4.3 and 4.4). These spectra are compared with the spectrum of a film prepared with 0% N_2 taken as a reference. All the curves are characterized by the typical oscillatory behavior found when a high refraction index (**n**) material is deposited on a transparent substrate with smaller **n.** These oscillations are originated by the interference of the partially reflected beams at the film/air and film/substrate interfaces.[58] Besides these oscillations, another quite remarkable effect is the shift of the absorption threshold to lower wavelengths for thin films prepared with percentages of nitrogen higher than 85%. Usually, this shift has been recognized in the literature as a hint of visible

photoactivity in doped TiO_2, [17-20] although this correlation has been claimed as a necessary but not sufficient condition.[22-24, 59] It is also important to remark in this figure that the minima of the oscillations recorded for the sample prepared with 97% N_2 appear quite above the curve of the reference TiO_2, which indicates a significant absorption in the visible region (i.e., for λ>500 nm). For percentages of N_2 in the plasma smaller than 85%, for which the amount of incorporated nitrogen is still small (c.f. Fig.s 4.3 and 4.4.a), the shape of the curves, except for the oscillatory behavior in the transparent region that depends on the film thickness, was similar to that corresponding to the film prepared with 0% N_2 and did not depict any clear hint of a shifted absorption edge. Similar sets of curves were obtained when using either TTIP or TDEAT as titanium precursor. For the whole set of investigated samples, we have calculated the value of the absorption threshold by assuming a Tauc model for the evaluation of the band gap of TiO_2 (i.e., $A(h\nu)^{1/2}$).[60] The obtained values are represented in Fig. 4.6. The shape of the curve defined by the different points is the reverse of that in Fig. 4.5, this latter corresponding to the relative concentration of nitrogen incorporated into the films. Consequently, a representation of the absorption threshold values against the N/Ti ratio in the films follows a linear tendency (see supporting information S3). This behavior indicates that the absorption threshold of the N-TiO_2 films is controlled by the amount and perhaps the type of incorporated nitrogen. For the samples prepared with N_2 percentages higher than 85% the Ti-N species is the most abundance species, as evidenced by the shape of the XPS spectra in Figs. 4.2 and 4.3. These samples present a clear shift in the absorption threshold whose magnitude is correlated with the amount of nitrogen within the lattice (cf. Figs. 4.5 and 4.6). By contrast, samples prepared with 85% or a lesser amount of nitrogen in the plasma, incorporate a limited amount of nitrogen in the form of Ti-NO species. These samples do not present a clear shift in the absorption threshold, although a clear determination is difficult with absorption spectra such as those in Fig. 4.5, where the presence of interference oscillations may mask changes at the edge spectral region.

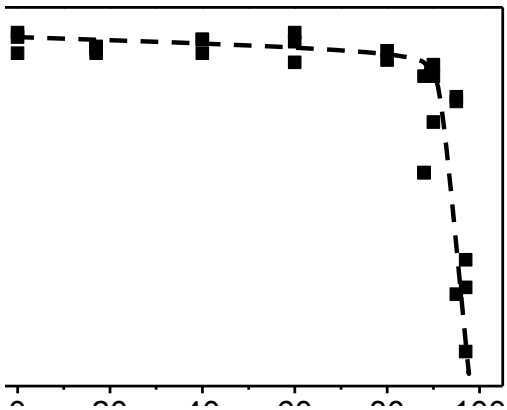

Figure 4.6. Values of the absorption threshold plotted against the percentage of nitrogen in the plasma gas for N-TiO_2 thin films prepared with the TTIP, TDMAT and TDMAT precursors at 523 K. The dashed line is included to guide the eyes.

Electrical characterization of the films prepared with a high concentration of N_2 in the plasma gas showed that they present a certain sheet conductivity (see supported information S4) which is indicative of some reduction of the titanium ions and the presence of a certain concentration of oxygen vacancies within the lattice.[61] The broad absorption feature extending through all the visible region of the spectra (i.e., λ>500 nm) found for the samples prepared with 97% N_2 can therefore be associated with the lost of stoichiometry in these samples.[21] This confirms our evidences based on the analysis of the Ti2p XPS spectra and supports the already commented relationship between the incorporation of Ti-N species and the formation of oxygen vacancies within the lattice. [25, 34, 54, 55]

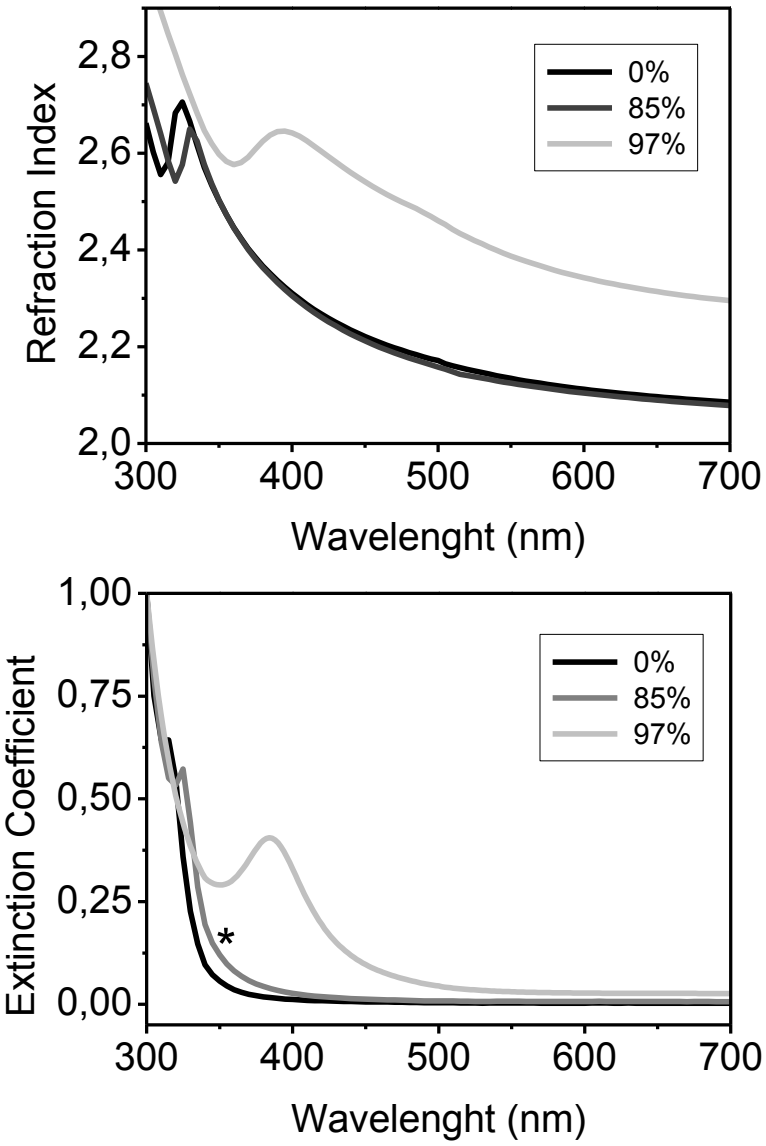

Figure 4.7.Top) Refraction index and bottom) Extinction coefficient curves determined for N-TiO_2 thin films prepared at 523 K by using TDMAT as a precursor and different percentages of N_2 in the mixture used as plasma gas as indicated. The star points to the region whose reproduction is only possible by admitting an oscillator around 375 nm.

Owing to the oscillatory behavior of the UV-visible transmission spectra, it is difficult to ascertain whether real absorption features close to the absorption threshold superimpose in the spectra of the films prepared with percentages of N_2 lower or equal than 85%, where only Ti-NO species have been determined by XPS. In order to check this point, we employed ellipsometry to determine the extinction coefficient (**k**) and refraction index (**n**) functions of selected films for $\lambda > 300$ nm. The corresponding plots are shown in Fig. 4.7 for three thin films prepared at 523 K with TDMAT as the

precursor and percentages of N_2 in the plasma gas of 0%, 85% and 97%. For the whole spectral region, the refraction indices of the 97% N_2 film was higher than those of the other two samples (e.g., at λ=550 nm, the measured values were 2.38 and 2.12, respectively), in agreement with its UV-vis absorption spectrum (Fig. 4.5) and its extinction coefficient curve plotted in the bottom panel of Fig. 4.6. This latter curve is characterized by a broad and intense maximum at around 400 nm that defines a shifted absorption threshold of 2.11 eV, extending through the whole visible region of the spectrum. By contrast, the extinction coefficient curve of the film prepared with 85% nitrogen does not present this broad absorption and its edge jump defines an absorption threshold of 3.19 eV, quite similar to that of the film prepared with pure oxygen as plasma gas. The main difference between the curves of the samples prepared with 0% and 85% N_2 consists of a small but well defined absorption feature at around 375 nm in the extinction coefficient curve of the latter (indicated by a star in the figure). An absorption feature in this position was indeed needed to extract a reasonable extinction coefficient curve from the ellipsometric data recorded for this film.

3.3. Density of states calculations for model N-TiO2 systems

The three model systems used to calculate the DOS of the different N-TiO_2 thin films are shown in Fig. 4.8. They represent the substitutional, N_s, interstitial, N_i and substitutional-interstital, N_{si} defect states. In this latter type of defect state, N occupies the same position as in the case of the N_s defect, but there is also an O atom occupying an interstitial site. We will assume that these states of nitrogen correspond to the XPS bands attributed in section 3.1, and attributed to Ti-N, Ti-NO and Ti-ON species. Calculations based on structures similar to those of the two former types of defects have been previously carried out by Di Valentin et al [12,13, 15] to account for modifications of the band structure in N-doped TiO_2. These authors have also considered either the effect of Ti-N[12,13, 15] or Ti-NO[12, 13] like species, although they employed smaller simulation cells (with 96 and 72 atoms for the anatase and rutile supercells respectively). Herein, besides studying the effect of another type of species (i.e., Ti-ON), we address systematically the possible influence in the electronic structure of the concentration of incorporated nitrogen for both the Ti-N and Ti-NO species in a larger supercell, with 216 atoms. To simulate the influence of the concentration of nitrogen in real samples,

we have considered two different simulation cells for each system, one containing one defect, and another containing two defects. In addition, in this latter case we have used two different arrangements for the two defect states, placing them in either two nearby or in quite separated positions within the lattice. These two geometries are employed to represent the electronic structure of N-TiO_2 systems with, respectively, a high and a low concentration of nitrogen. The most relevant geometrical parameters of the studied defect configurations are reported in Table 4.1.

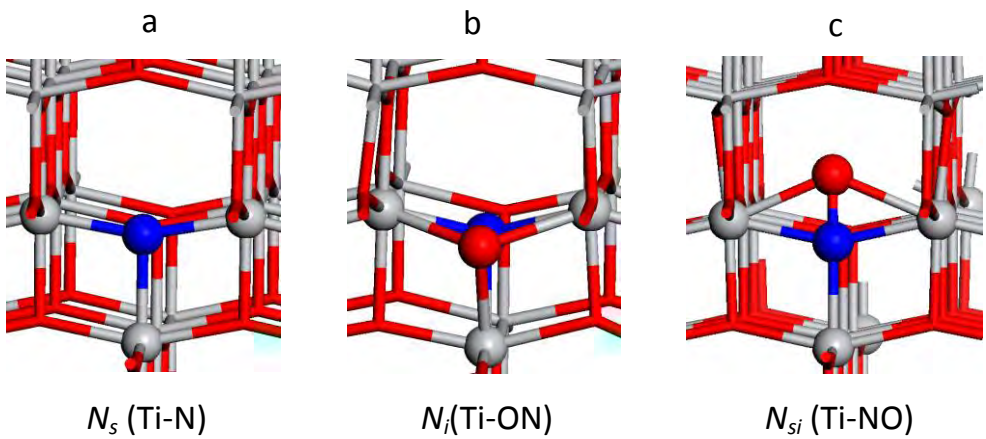

Figure 4.8. Structures of the three type of N centers studied. a) Substitutional defect, N_s , in which a N atom replaces a O atom. b) Interstitial defect, N_i, in which the N atom is located in an interstitial place, and the O atom is also displaced from its original site. c) Substitutional-interstitial defect, N_{si}, in which the N atom occupies the same position as in the case of the N_s defect, and the O atom occupies an interstitial place.

We also performed calculations on a different type of defect, in which the O atom was initially placed at its equilibrium lattice location, and the N atom is in an interstitial site above the O atom at a distance of 1.35 Å along the z axis. We studied two systems with one and two defects of this kind. Upon energy minimization, the cells underwent large geometrical rearrangements, leading in the two cases to final configurations equivalent to that of the N_i defects. This suggests that this initial configuration is not stable and that minimization of the energy is accomplished by a displacement of the O atoms from their initial location and their substitution by nitrogen. This also means that the assumed

detection by XPS of these species in some of our samples (i.e., band at 401.7 eV of BE, cf. Fig. 4.3) is likely related with the fact that the plasma deposition process utilized for the synthesis of the N-TiO_2 films is an out of equilibrium procedure.

Table 4.1: Relevant distances (in Å) involved in the three types of defects studied: N_i, N_s and N_{si}. The distance between the two defects in the unit cell is taken into account by labeling with C and S the structures in which the N atoms are close and separated respectively.

Species	**O-Ti**	**N-O**	**N-Ti**
***N_i*-C**	2.06, 2.06, 2.01	1.48	1.95, 1.98, 2.05
***N_i*-S**	2.13, 2.13, 2.28	1.36	2.06, 2.06, 2.28
***N_S*-C**			1.98, 2.00, 2.07
***N_S*-S**			2.00, 2.00, 2.09
***N_{Si}*-C**	2.09, 2.17, 3.33	1.29	1.98, 2.02, 2.04
***N_{Si}*-S**	2.17, 2.17, 3.30	1.28	2.02, 2.03, 2.03

The calculations also provided interesting information regarding the energy of the different studied systems. Thus, when TiO_2 is modified with N_S defects, the energy of the system where the two defect states are in nearby positions is 29.1 kJ/mol higher than the energy of the system in which the two defects are far away. When considering N_i defects, this energy difference is much smaller, just -1.1 kJ/mol, which means that there is no strong energetic driving force preventing the aggregation of N_i defects. In the case of N_{Si} defects, this energy difference is 14.0 kJ/mol, indicating that it is energetically favourable to keep N_{Si} defects as far away as possible within the lattice. On the other hand, to determine the relative stability of the N_{Si} and N_i defect states we can compare directly the energies of the corresponding systems, as they have the same number of atoms. For the systems modelling low nitrogen concentrations (with defects far away from each other), we find that N_i defects are 8.3 kJ/mol more stable than N_{Si} defects. Meanwhile, for the systems modelling a high concentration of nitrogen, the N_i defects

are 29.0 kJ/mol more stable than N_{Si} defects, a result which suggests that TiO_2 materials with a high concentration of nitrogen will tend to have N_S and N_i defects and that the formation of N_{Si} defects would not be favoured.

The total DOS calculations for pure TiO_2 (shown in the Supporting Information S6) predict a gap between the valence and conduction bands of 2.7 eV. This value is smaller than the experimental band gap of anatase TiO_2 (i.e., 3.2 eV[62]), a difference that is due to the well known underestimation of the band gap in DFT calculations.[63] The value of the Hubbard parameter U that we used is 4.5 eV, which provides a good description of the gap states in periodic LDA+U calculations of TiO_2 and, at the same time, predicts a reasonably good value for the band gap (i.e., 2.7 eV).[46] A similar result has been also obtained by Di Valentin et al.[11] when modeling N-TiO_2 systems.

The total DOS of the six studied N-TiO_2 systems are shown in Fig. 4.9. The reported results indicate that the N-TiO_2 systems have developed new electronic states in the band gap close to the valence states of titanium dioxide. A similar result has been obtained by other authors simulating the electronic structure of N-TiO_2 systems, [11-15, 25, 34] although in these previous works smaller supercells were employed in the calculations. Particularly interesting with regard to the optical properties of N-TiO_2 is the difference observed in Fig. 4.9 between the shape of the gap states corresponding to the N_s and the N_i and N_{si} defects around the highest occupied molecular orbital (HOMO) level (marked with a continuous line in the figure). In the former case (i.e. DOS curves a and b) the extra states due to the incorporation of N appear as a continuous prolongation of the valence band states of pure TiO_2 (marked with a dashed line in the figure). By contrast, for the case of N_i and N_{si} defect states, the N-related gap states appear as well defined discrete peaks separated from the valence band of TiO_2 (i.e. DOS curves c)-f)). Phenomenologically, this difference is equivalent to say that the N_s defects have induced a shift of the valence band edge, producing a decrease in the gap of the system, while the N_s and N_{si} states do not modify the valence band of TiO_2 but introduce new electronic states in the gap. This point has been previously discussed based on both experimental[54] and theoretical[11-15] studies. Thus, Diebold et al.[54] studied by XPS and valence band photoemission N-implanted anatase and rutile, and concluded that localized states rather than a band gap narrowing develop upon nitrogen implantation and the subsequent formation of N^{3-} (i.e., Ti-N) species. Theoretically, studying the anatase polymorph, Di Valentin et al[11-12] concluded that substitutional

nitrogen states (i.e., Ti-N) lie just above the valence band, while interstitial nitrogen states (i.e., Ti-NO) lie higher in the gap. These authors also found that Ti-N species in rutile might produce a certain increase of the gap with the N-associated states close to the valence band maximum.[15] The main difference between these previous studies and our calculations reside in the fact that we deal with more than one nitrogen species and define two different scenarios for them depending on whether they are located in separated or close positions of the lattice. When N atoms are close, as in the DOS curves a, c and e, the number of gap states is higher and appear more scattered along the band gap, as if there is a splitting of peaks due to the electronic interaction between defects. By contrast, when the N atoms are separated within the lattice, as in DOS curves b, d and f, there is a smaller number of peaks in the gap, and they tend to be more concentrated around certain energy values in the band gap (i.e., more localized states). In particular, for the N_s species located in nearby lattice positions, it appears that the TiO_2 valence band maximum extends continuously to higher energies. From an experimental point of view, this is equivalent to saying that there has been a narrowing of the gap. This would be in fact the situation for our samples prepared with nitrogen percentages in the plasma higher than 85% (cf. Figs. 4.4 and 4.5).

As shown in the partial DOS plots in Fig. 4.10, the new states developed in the gap have a mixed titanium-nitrogen-oxygen character and show slightly different features depending on the kind of nitrogen defect considered in each case. This figure represents in an enlarged scale the gap zone to clearly depict the new states appearing in the N-TiO_2 systems. The plots represent the titanium, oxygen and nitrogen projected states of the DOS curves in the regions around the HOMO lines in each system (note that the HOMO lines appear at different energies in each case). For oxygen, they are represented both the states corresponding to the oxygen atoms close to nitrogen and those located in separated positions. This distinction is important since for the N_i and N_{si} states nitrogen is directly bonded to an oxygen atom whose contribution to the DOS of the new states is expected to be quite substantial. The first conclusion we could draw from these plots is that all the defect states have a mixed character with contributions from the oxygen, nitrogen and titanium atoms.

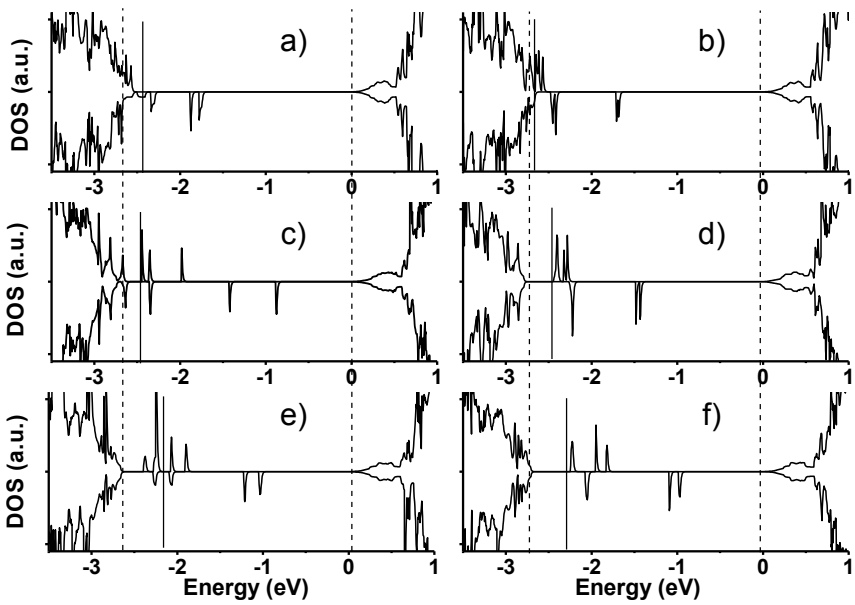

Figure 4.9. Density of states plots of the six N-TiO_2 systems studied, showing the two spin components separately. **a** and **b** correspond to the two systems with substitutional N doping (N_s), with 2 N atoms located at close and separated positions, respectively. **c** and **d** correspond to the two systems with interstitial N doping (N_i), with 2 N atoms located at close and separated positions, respectively, respectively. **e** and **f** correspond to the two substitutional-interstitial N configurations (N_{si}), with 2 N atoms located at close and separated positions, respectively, respectively. The bands are plotted in such a way that the origin of the energy (0 eV) is placed at the bottom of the conduction band. The two vertical dashed lines are placed to indicate HOMO-LUMO gap in TiO_2. The vertical solid line indicate the highest occupied orbital of the system, which in the case of N-TiO_2 corresponds to new gap states generated by the presence of nitrogen in the lattice.

However, a closer look to these curves also reveals that in the N_s defects the nitrogen contribution to the gap states is relatively higher than that of the close oxygen atoms, while for the N_i and N_{si} defects the nitrogen and close oxygen contributions are rather similar, thus supporting the importance of these oxygen atoms in determining the electronic properties of the system. This closer look to the new states around the HOMO line also suggests that the DOS curves of the N_s defects, particularly for the case with the two nitrogen atoms located in nearby positions, are a continuous extension of the valence band. The fact that the nitrogen contribution to these states extends through the entire DOS region, both bellow and above the HOMO line, supports our view in the sense that a narrowing of the valence band has occurred in this case. By contrast, for the N_i and N_{si} defects, the nitrogen contribution to the new states appears quite concentrated in localized levels that do not form a continuum with the valence band

states. This result suggests that even for N-TiO_2 systems with a high concentration of Ti-NO species, their electronic structure can be described by the appearance of localized states in the gap.

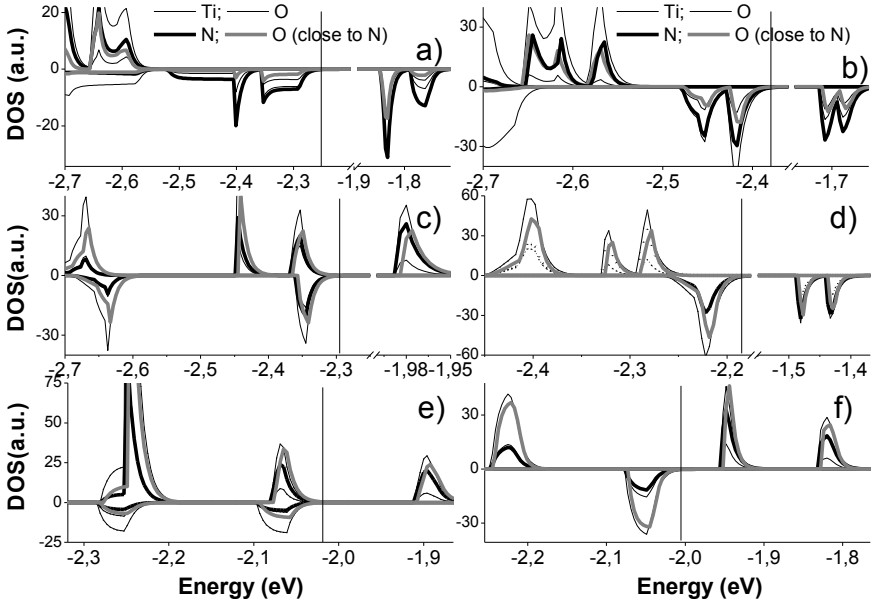

Figure 4.10. Partial density of states plots of N, Ti and O in the gap states for the six studied N-TiO_2 systems with the labelling a)-f) being the same than in Fig. 4.9. The oxygen contribution is differentiated for the oxygen atoms close to the nitrogen and the rest of oxygen atoms of the lattice. The total densities of states plotted in Figure 4.9 are calculated as the sum of these partial densities of states. The vertical solid line indicates the highest occupied orbital of the system.

3.4 Wetting angle photo-activity of N-TiO_2 thin films

The photoactivity of N-TiO_2 thin films has been the subject of a large debate during the last years.[1-14] In recent publications we have shown that transformation of the surface state of N-TiO_2 from partially hydrophobic (i.e., wetting contact angles around 80º) into hydrophilic can be induced by visible light in samples containing Ti-NO species, regardless of whether they were amorphous or crystalline. By contrast, visible photocatalytic activity towards, for example, the photodegradation of dyes seems to constitute a more demanding process, which requires titanium oxide to be in crystalline phase, forming a mixture composed mainly by anatase and a small amount of rutile.[22]

In agreement with previous studies with PECVD TiO_2 thin films using TTIP as volatile precursor of titanium and pure oxygen as plasma gas[25]), we have found that amorphous TiO_2 is obtained for deposition temperatures lower than 523 K and that the anatase phase of this oxide is obtained for T ≥ 523 K. By contrast, most N-TiO_2 thin films prepared at this temperature with TDMAT and TDEAT as precursors were amorphous, as shown by their XRD spectra (see supporting information S7). Since no photocatalytic activity was found for any of the N-TiO_2 thin films when illuminated with visible light and very little when using UV light, to check the possible role of the different nitrogen species in controlling the visible photoactivity of these materials we have looked for changes in wetting contact angle under visible and UV light illumination. Fig. 4.11 presents some selected results showing that for samples containing Ti-NO species (i.e., a sample prepared with 85% N_2) the wetting angle decreases by almost 50º when illuminated with visible light, while for the films with a high concentration of Ti-N species (i.e. sample prepared with 97% N_2) no visible light effect was observed. This different behavior according to the type of nitrogen species was common for the rest of N-TiO_2 thin films. When after the visible illumination the samples were irradiated with UV light, we found that all of them became superhydrophilic (i.e., wetting angle lower than 10º), which is the typical behavior of UV-illuminated TiO_2 thin films. Even if wetting induced changes and photocatalytic processes are not equivalent tests of TiO_2 photoactivity,[22, 64] the reported results in Fig. 4.11 clearly prove that Ti-N species are unable to induce visible light photoactivity and that the presence of Ti-NO species in the films is a requisite for promoting visible light activation of N-TiO_2 thin films, at least for a partial hydrophilic conversion of their surface.

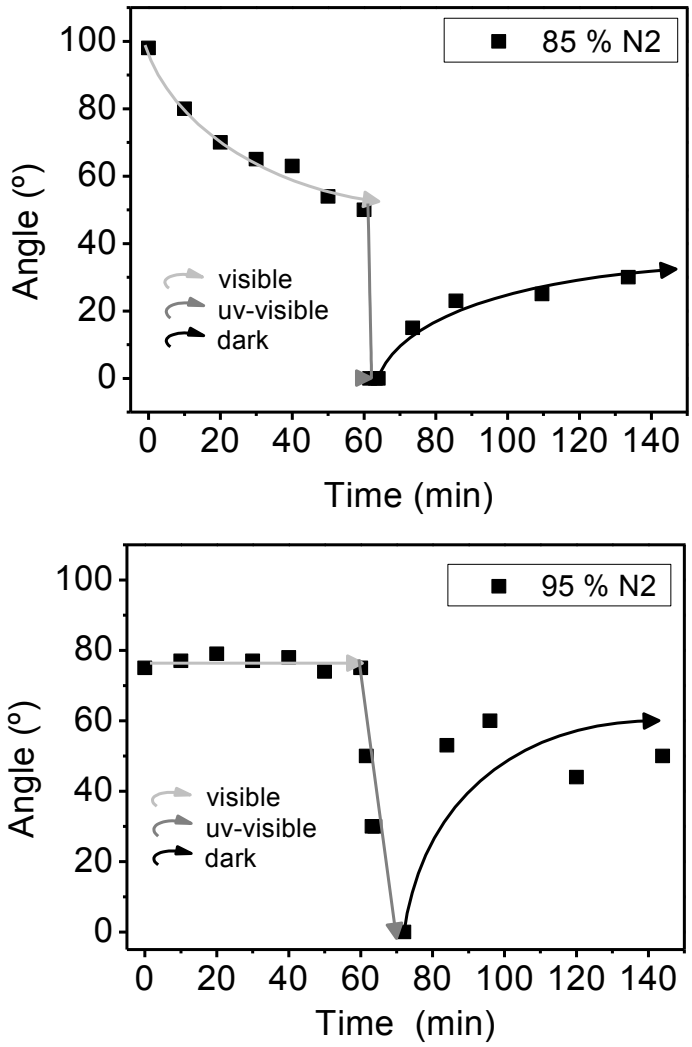

Figure 4.11. Evolution of the wetting angle as a function of the illumination time with visible and UV lights and then left in the dark for N-TiO_2 samples prepared with 85% (top) and 97% (bottom) of N_2 in the plasma gas. The lines are plotted to guide the eyes.

4. Discussion

The previous results on N-TiO_2 thin films prepared by PECVD have provided information about both the influence of the incorporated nitrogen on both the optical properties of TiO_2 and on the characteristics of the nitrogen species incorporated within the structure of the oxide according to the different conditions of preparation. In relation to this latter aspect, we have also described theoretically how the different species of nitrogen may affect the electronic structure of the prepared materials. The influence of these species of nitrogen on the photo-activity of N-TiO_2 is finally discussed in relation with visible-light hydrophilic conversion of the surface of the prepared films.

4.1.-Type and concentration of nitrogen species and band gap narrowing in N-TiO_2 thin films

The previous XPS results have shown that the incorporation of small amounts of nitrogen in the form of Ti-NO species (i.e., N_i defects according to the notation used for the DOS calculations) occurs when using TDMAT or TDEAT as precursors or when the films are deposited with a O_2+N_2 plasma mixture with less than 90% of nitrogen. We have proposed that the existence of four Ti-N bonds in the two latter precursor molecules may account for the presence of Ti-NO species in these films, even if no nitrogen gas has been added to the plasma. For 90% or higher concentration of nitrogen a progressive incorporation of Ti-N species takes place. For all experimental conditions used for the synthesis of the N-TiO_2 films we have also found that the amount of incorporated nitrogen species (Ti-N and Ti-NO) was higher at low (i.e., 298 K) than at high (523 K) temperatures. The stability of Ti-N implanted in rutile and anatase polymorphs of TiO_2 has been addressed in previous articles,[34, 54] where a certain desorption upon annealing has been observed only for the case of anatase[54] and an extra stabilization is achieved when gold is deposited onto the surface.[34] These results have been interpreted in terms of the interaction of the implanted nitrogen (and deposited gold particles) with oxygen vacancies in the lattice.[25,34, 54] Although most of our films were amorphous and a comparison with literature data is therefore not straightforward, we must stress that our results point to a certain relationship between the formation of Ti-N species and the existence of oxygen vacancies within the lattice. The aforementioned dependence of the Ti-N concentration on the temperature of the PECVD process and the fact that the maximum concentration of this species is found for defective and high conductive samples support such dependence.

Ti-N and Ti-NO species of nitrogen have been previously detected and discussed in literature,[1, 12, 22, 51-57] although no complete agreement exists on their specific role in altering the electronic and optical properties of N-TiO_2 materials. In fact, during the last years there has been a vivid discussion on whether modifying the TiO_2 with nitrogen produces a shift in the absorption edge or just the development of absorption centers close to an unmodified gap. Our experimental results indicate that both localized band states and band gap narrowing may occur depending on the type and concentration of

nitrogen species incorporated within the films. Thus, we have found experimentally that the incorporation of a relatively low concentration of interstitial nitrogen (i.e. Ti-NO species) does not modify substantially the band gap structure of the oxide, but induces the formation of some localized electronic states in the gap (cf. Figs. 4.5 and 4.7). A similar situation has been claimed in the theoretical works of Di Valentin et al.[11-15] By contrast, our data suggest that a narrowing of the band gap due to a shift in the valence band edge may occur when substitutional nitrogen (i.e. Ti-N species) is incorporated within the lattice. We have also found that the magnitude of this shift is directly related with the amount of incorporated Ti-N species that we control by changing the relative amount of nitrogen in the plasma. In recent experimental [54] and theoretical[11-15] studies on titanium oxide with incorporated Ti-N species such a narrowing has not been detected, a difference that might be related with the fact that in these experiments a lower concentration of nitrogen species was actually incorporated within the lattice and because only the effect of isolated nitrogen species was theoretically modeled.

The films with a high concentration of nitrogen in the form of Ti-N species (i.e., those prepared with a N_2 percentage of 95% or above) present a loss in transmission that has been associated with the formation of oxygen vacancies (associated with Ti^{n+} species, n<4, detected by XPS) that would be responsible for a wide absorption extending over a large zone of the visible spectrum.[21, 61] The decrease in the resistivity of these films (cf. supporting information S7) confirms that these films are oxygen defective, again suggesting that incorporation of Ti-N species becomes favored by the presence of oxygen vacancies. [25, 34, 54]

4.2. Density of states and electronic structure in N-TiO_2

The DOS calculations reported in *section 3.4* account for the different phenomenological behaviors found for N-TiO_2 thin films depending on the type and concentration of the nitrogen species incorporated into the lattice. We have shown that the N_i and N_{si} defects, associated to the Ti-NO and Ti-ON species detected by XPS, give rise to localized electronic states in the gap above the valence band edge of the oxide. In previous works, Di Valentin et al[11,13, 15] reached a similar conclusion by simulating the electronic structure of isolated N_i defect states. We have investigated the influence of interdefect distances on the electronic properties, in larger supercells. For a two-defect

model simulating the incorporation of a high concentration of N_i species within the lattice (cf. Figs. 4.9 and 4.10), we have also proved that the gap states do not become extensively mixed with the valence band levels of the oxide and keep a localized character. This theoretical result supports the experimental findings by ellipsometry and UV-vis spectroscopy for the 85% N_2 sample (cf. Fig. 4.7), where the presence of a localized harmonic oscillator at around 375 nm is required for a good fitting of the experimental curves. Unfortunately, our experimental protocol does not enable the incorporation of a high concentration of Ti-NO species without Ti-N species being also formed. This limitation might be explained by the calculated energies of formation of the different defect states (*section 3.4*). Even though, the good agreement between experimental and theoretical results supports the development of isolated states in the gap rather than a band gap narrowing in the samples prepared with 85% or a lower concentration of N_2 in the plasma gas.

A direct comparison between our experimental and theoretical results is possible when dealing with the N_s defect states (i.e., Ti-N species according to the notation used by the XPS analysis) where, particularly for the structures simulating a high concentration of this species, a substantial mixing between the valence band states and those pertaining to the nitrogen can be deduced from the calculated partial density of state curves (c.f. Fig. 4.10). As an overall effect, it can be interpreted that this mixing produces a shift towards the visible of the valence band edge, in agreement with our experimental observations for the samples prepared with nitrogen rich plasmas. As discussed in *section 4.1*, the different interpretation regarding the modifications of the gap that was outlined in previous theoretical[11-15] and experimental[54] works, might be connected with the fact that they simulate or interpret experiments with more separated Ti-N species. In this way, our description of the optical and electronic properties of N-TiO_2 systems with a high concentration of Ti-N species would be in a better agreement with the original suggestions of Asahi et al.[1] of a band gap narrowing than with those of these more recent works.

4.3. Wetting photo-activity of N-doped TiO_2

Visible photo-activity of N-doped TiO_2 thin films is a very elusive effect with somehow contradictory results in the literature, where the red shift of the valence band edge has

been taken sometimes as a sufficient evidence warranting reactivity under visible illumination.[16] In recent works, it has been pointed out that although visible absorption is a required condition, it is not sufficient to assure visible photo-activity of N-TiO_2. Moreover, different conditions seem to be required for photocatalysis and for light induced wetting angle changes over flat surfaces of this material.[64] The former is a much more demanding process that, besides the presence of nitrogen species, requires that the nitrogen modified titania is crystalline and complies with some additional structural conditions, such as the simultaneous presence of both anatase and rutile polymorphs in the photoactive material.[22] Since most N-TiO_2 thin films prepared in the present work were amorphous, we have investigated the effectiveness of either Ti-N or Ti-NO species in inducing some kind of visible photoactivity by following the changes in wetting angle upon illumination with visible light. The experiments carried out with the N-TiO_2 thin films have shown that samples with a high concentration of Ti-N species do not show visible photo-activity and keep their original wetting angle even after a prolonged illumination with visible photons (cf. Fig. 4.11). By contrast, films containing Ti-NO species do present some visible photoactivity, which was evidenced by a partial and progressive decrease in the water contact angle of ca. 50º from an original wetting angle of 98º to a wetting angle of 52 º after 60 min illumination. This behavior, even if occurring with a slow rate, indicates that in the presence of this species visible light is capable of photoactivating the surface of these titanium oxide samples. A thorough discussion of this kind of partial hydrophilic transformation of N-TiO_2 surfaces upon visible light irradiation can be found in reference 24.

Our theoretical and experimental results have shown that a small concentration of Ti-NO species in the films do not modify significantly the band gap of the oxide but induces some localized electronic states close to the band edge. Visible light excitation up to the conduction band of the electrons associated to these electronic states in the gap should render a conduction band electron and a localized hole in the gap state. We believe that precise localized character of this photohole is the factor precluding a continuous operation of these films as a photocatalyst as the mobility of these photoholes induced with visible light is rather limited.[15] Indeed, for a continuous photocatalytic process to take place, the migration of both electrons and holes towards the surface, as it usually happens in undoped TiO_2 illuminated with UV light. In N-TiO_2 systems, migration towards the surface of the photoholes generated in the illuminated

layer (i.e. in the order of the micron) can only take place if a continuous band-like state forms in the gap. This is not certainly the case in our samples with a low concentration of incorporated Ti-NO species. However, as previously discussed by us,[24] visible-light partial conversion of the surface hydrophilicity occurs by just activating the utmost atomic layers whereby only surface electron-hole pairs are involved in the transformation. Therefore, the point to be stressed here is that while Ti-NO species are able to induce this visible-light transformation, Ti-N species are not. This finding contrasts with the original proposal of Asahi et al.[1] and thereafter of other authors [5, 16] attributing to the Ti-N species the visible photo-activity of N-TiO_2 materials. However, it complies with more recent results stressing that for visible photoactivity to occur, Ti-NO like species must be present. [26, 56]

5.-Conclusions

The previous results have shown that by using the PECVD technique it is possible to obtain a large set of N-TiO_2 thin films where the amount and type of nitrogen can be tuned by controlling the working parameters during the deposition of the films. Thus, Ti-NO species are the only type of incorporated nitrogen species when the films were prepared with a relatively low concentration of nitrogen in the plasma gas. On the other hand, a high concentration of Ti-N species becomes incorporated into the films for nitrogen rich plasmas.

DOS calculations of differently doped anatase model systems have provided a detailed description of the influence of the N states, Ti-N and Ti-NO (and the related one Ti-ON), on the electronic structure of N-TiO_2. It is found that in anatase with a relatively high concentration of Ti-N species the valence band edge shifts upwards because of the mixing of the N atomic levels with the levels of the lattice atoms. Consequently, the absorption edge of the UV-vis absorption spectra is red shifted as found experimentally. On the contrary, for the Ti-NO species the electronic levels of the interstitial nitrogen species remain localized, and no band gap narrowing occurs. Experimentally, this situation yields spectra whose absorption edge are not shifted but present a separated absorption oscillator close to it.

Films containing Ti-N species are not photoactive with visible light even if they present a red-shifted absorption edge. Visible light wetting photoactivity is only observed in N-TiO_2 films with Ti-NO defect states. This observation has been related with the surface excitation of the electronic states associated to these species, which appear in the gap close to a virtually un-modified valence band edge.

6.-Acknowlegdments.- We thank the Ministry of Science and Education of Spain (projects MAT 2007-65764 and the CONSOLIDER INGENIO 2010-CSD2008-00023) and the Junta de Andalucía (projects TEP2275/P09-TEP-5283/CTS-5189) for financial support. This work has been carried out within the EU project NATAMA (contract no. 032583)

Supporting Information Available.

Some additional information referred in the text as S1-S8 is available free of charge via the Internet at http://pubs.acs.org.

References

(1) Asahi, R.; Morikawa, T.; Ohwaki, T.; Aoki, K.; Taga, Y., Science **2001**, 293, 269.

(2) Diwald, O.; Thompson, T. L.; Zubkov, T.; Goralski, E. G.; Walck, S.D.; Yates, J.T., *J. Phys. Chem. B,* **2004**, 108, 6004.

(3) Nakano, Y.; Morikawa, T.; Ohwaki, T.; Taga, Y., *Appl. Phys. Lett.* **2005**, 86, 132104.

(4) Diwald, O.; Thompson, T.L.; Goralski, E.G.; Walck, S.D.; Yates, J.T., *J. Phys. Chem. B* **2004**, 108, 52.

(5) Yates, H.M.; Nolan, M.G.; Sheel, D.W.; Pemble, M.E., *J. Photochem. Photobiol. A: Chemistry* **2006**, 179, 223.

(6) Thompson, T.L.; Yates, J.T., *Chem. Rev.* **2006**, 106, 4428.

(7) Emeline, A.V.; Kuznetsov, V.N.; Rybchuk, V.K.; Serpone, N., *Int. J. Photoener.* **2008** Art. ID 258394

(8) Mitoraj, D.; Kisch, H., *Angew. Chem. Int. Ed.* **2008**, 47, 9975.

(9) Trenczek-Zajac, A.; Kowalski, K.; Zakrzewska, K.; Radecka, M., *Mater. Res. Bull.* **2009**, 44, 1547.

(10) Oropeza, F.E.; Harmer, J.; Egdell, R.G.; Palgrave, R.G., *Phys. Chem. Phys.* **2010**, 12, 960.

(11) Di Valentin, C.; Pacchioni, G.; Selloni, A.; Livraghi, S.; Giamello, E., *J. Phys. Chem. B* **2005**, 109, 11414.

(12) Livraghi, S.; Paganini, M.C.; Giamello, E.; Selloni, A.; Di Valentin, C.; Pacchioni, G., *J. Am. Chem. Soc.* **2006**, 128, 15666.

(13) Di Valentin, C.; Finazzi, E.; Pacchioni, G.; Selloni, A.; Livraghi, S.; Paganini, M.C.; Giamello, E., *Chem. Phys.* **2007**, 339, 44.

(14) Napoli, F.; Chiesa, M.; Livraghi, S.; Giamello, E.; Agnoli, S.; Granozzi, G.; Pacchioni, G.; Di Valentin, C., *Chem. Phys. Lett*. **2009**, 477, 135.

(15) Di Valentin, C. ; Pacchioni, G. ; Selloni A., *Phys. Rev. B* **2004**, 70, 085116

(16) Chen, X.; Burda, C., *J. Phys. Chem. B*, **2004**, 108, 15446

(17) Vyacheslav, N.; Kuznetsov, N.; Serpone, N., *J. Phys. Chem. B* **2006**, 110, 25203.

(18) Lei, Z.; Ma, G.; Liu, M.; You, W.; Yan, H.; Wu, G.; Takata, T.; Hara, M.; Domen, K.; Li, C.*; J. Catal.* **2006**, 237, 322

(19) Umebayashi, T.; Yamaki, T.; Itoh, H.; Asai, K., *Appl. Phys. Lett.* **2002**, 81, 554.

(20) Liu, B.; Wen, L.; Zhao, X. Solar Energy Mater.&Solar cells **2008**, 92, 1

(21) lin, Z.; Orlov, A.; Lambert, R.M.; Payne, M.C., *J. Phys. Chem. B*, **2005**, 109, 20948

(22) Romero-Gómez, P.; Rico, V.; Borrás, A.; Barranco, A.; Espinós, J.P.; Cotrino, J.; González-Elipe, A.R., *J. Phys. Chem. C* **2009**, 113, 13341.

(23) Nakamura, R.; Tanaka, T.; Nakato, Y., *J. Phys. Chem. B* **2004**, 108, 10617

(24) Borrás, A.; López, C.; Rico, V.; Gracia, F.; González-Elipe, A.R.; Richter, E.; Battiston, G.; Gerbasi, R.; McSporran, N.; Sauthier, G.; Gyorgy, E.; Figueras, A., *J. Phys. Chem. C* **2007**, 111, 1801.

(25) Graciani, J.; Alvarez, L.J.; Rodríguez, J.A.; Fernández-Sanz, J., *J. Phys. Chem. C* 2008, 112, 2624

(26) Chen, C.; Bai, H.; Chang, Ch., *J. Phys. Chem. C* **2007**, 111, 15228

(27) Borrás, A.; Cotrino, J.; González-Elipe, A. R., *J. Electrochem. Soc.,* **2007**, 154, 152

(28) Gracia, F.; Holgado, J.P.; González-Elipe, A.R., *Langmuir* **2004**, 20, 1688.

(29) Ahn, K.-H.; Park, Y.-B.; Park, D.-W., *Surf. Coat. Technol*. **2003,** 171, 198

(30) Nakamura, M.; Kato, S.; Aoki, T.; Sirghi, L.; Hatanaka, Y. *Thin Sol. Films* **2001**, 401, 138

(31) Song, XM,; Gopireddy, G.; Takoudis, C.G., *Thin Sold Films* **2008**, 516, 6330

(32) Song, XM; Takoudis, C.G., *J. Vac. Sci. Technol. A* **2007**, 25, 360

(33) Xie, Q.; Yiang, Y.L.; Detavernier, C.; Deduytsche, D.; Van Meirhaeghe, R.L.; Ru, G.P.; Li, B.Z.; Qu, X.P., *J. Appl. Phys.* **2007,** 102, art. N. 083521

(34) Graciani, J.; Nambu, A.; Evans, J.; Rodriguez, J.A.; Fernández-Sanz, J., *J. Am. Chem. Soc*. **2008**, 130, 12056

(35) Barranco, A.; Cotrino, J.; Yubero, F.; Espinós, J.P.; Clerc, C.; Gonzalez-Elipe, A.R., *Thin Solid Films* **2001,** *401*, 150

(36) Kresse G.; Hafner, J. *Physical Review B*, **1993**, 47, 558-561.

(37) Kresse G.; Furthmuller, J. *Physical Review B*, **1996**, 54, 11169-11186.

(38) Kresse G.; Furthmuller, J. *Comput. Mater. Sci.*, **1996**, 6, 15-50.

(39) Wang Y.; Perdew, J. P. *Phys. Rev. B*, **1991**, 44, 298.

(40) Perdew, J. P.; Chevary, J. A.; Vosko, S. H.; Jackson, K. A.; Pederson, M. R.; Singh, D. J.; Fiolhais, C. *Physical Review B*, **1992**, 46, 6671.

(41) Kresse G.; Joubert, J. *Physical Review B*, **1999**, 59, 1758.

(42) Monkhorst, H. J.; Pack, J. D. *Physical Review B*, **1976**, 13, 5188-5192.

(43) Solovyev, I. V.; Anisimov, V. I.; Dederichs, P. H. *Phys. Rev. B*, **1994**, 50, 16861-16871.

(44) Anisimov, V. I.; Aryasetiawan, F.; Lichtenstein, A. I. *Journal of Physics:*

Condensed Matter, **1997**, 9, 767.

(45) Dudarev, S. L.; Botton, G. A.; Savrasov, S. Y.; Humphreys, C. J.; Sutton, A. P.,

Phys. Rev. B, **1998**, 57, 1505.

(46) Calzado, C. J.; Hernández, N. C.; Fernández-Sanz, J. ; *Phys. Rev. B*, **2008**, 77, 045118.

(47) Pearse, RWB; Gaydon, AG, *The identification of molecular spectra*, Chapman & Hall Ltd, London **1950**.

(48) Suraj, KS; Bharathi, P; Prahlad, V.; Mukherjee, S., *Surf. Coat. Technol.* **2007**, 202, 301.

(49) Romero-Gómez, P.; Barranco, A.; Cotrino, J.; Espinós, J.P.; Yubero, F.; González-Elipe, A.R., *Plasma Deposition of N-TiO_2 thin Films, i*n "Industrial Plasma Technology. Applications from Environmental to Energy Technologies". Y. Kawai, Y.; Ikegami, H.; Sato, N.; Matsuda, A.; Uchino, K.; Kuzuya, M.; Mizuno, A., edts.; Wiley. Weinhaim **2010**. pag.349

(50) G. Lassaletta, G.; Fernández, A.; Espinós, J.P.; González-Elipe, A.R., *J. Phys. Chem*. **1995**, *99*, 1484

(51) Cong, Y.; Zhang, J.; Anpo, M. J. Phys. Chem. C **2007,** 111, 6979

(52) López-Luke, T.; Wolcott, A.; Xu, L-p.; Chen, Sh.; Wen, Z.; Li, J.; de la Rosa, E.; Zhang, J.Z., *J. Phys. Chem. C* **2008,** 112, 1282.

(53) Asahi, R.; Morikawa, T.; Hazama, H.; Matsubara, M., *J. Phys. Condens. Matter* **2008,** 20, 064227

(54) Batzill, M; Morales, E.H.; Diebold, U., *Phys. Rev. Lett.,* **2006**, 96, 026103

(55) Chen, H.; Nambu, A.; Wen, W.; Graciani, J.; Zhong, Z.; Hanson, J.C.; Fujita, E.; Rodriguez, J.A., *J. Phys. Chem. C* **2007**, 111, 1366

(56) Dunnill, C.W.H.; Aiken, Z.A.; Pratten, J.; Wilson, M.; Morgan, D.J.; Parkin, I.P., *J. Photochem. Photobiol. A. Chemistry,* **2009**, 207, 244

(57) Saha, N.C.; Tompkins, H.G., *J. Appl. Phys.,***1992**, 72, 3072

(58) Swanepoel, R. *J. Phys. E* 1983, 16, 1213.

(59) Irie, H.; Washizuka, S.; Watanabe, Y.; Kako, T.; Hashimoto, K. *J. Electrochem. Soc.* **2005,** 152 , E351

(60) Serpone, N.; Lawless, D.; Khairutdinov, R. *J. Phys. Chem.* **1995,** 99, 16646.

(61) Martin, N.; Besnard, A.; Sthal, F.; Vaz, F.; Nouveau, C. *Appl. Phys. Lett*. **2008**, 93, 064102.

(62) Zhu, J.; Ren J.; Huo Y.; Bian Z., *J. Phys. Chem C.* **2007**, 111, 18965.

(63) Finazzi, E.; di Valentin, C.; Pacchioni, G.; Selloni, A.; J. Chem. Phys. **2008**, 129, 154113

(64) Rico, V.; Romero-Gomez, P.; J.L.Hueso, J.L.; J.P.Espinós, J.P.; González-Elipe, A.R., *Catal. Today* **2009**, 143, 347

Supporting information

Band gap narrowing vs. formation of electronic states in the gap in N-TiO_2 thin films

*P. Romero-Gómez[1], Said Hamad[3], J.C. González[1], A. Barranco[1], J.P. Espinós[1], J. Cotrino[1,2], A.R. González-Elipe[1]**

1. Instituto de Ciencia de Materiales de Sevilla (CSIC-Univ. Sevilla). Avda. Américo Vespucio 49. 41092 Sevilla (Spain). http://www.sincaf-icmse.es

2. Departamento de Física Atómica, Molecular y Nuclear. Universidad de Sevilla. Avda. Reina Mercedes 49, 41012 Sevilla. Spain.

3. Department of Physical, Chemical and Natural Sciences. Universidad Pablo de Olavide. Carretera de Utrera, km 1. Sevilla. Spain

Supporting information S1.- OES spectrum recorded for a plasma of a mixture of O_2+N_2 with 88% of nitrogen.

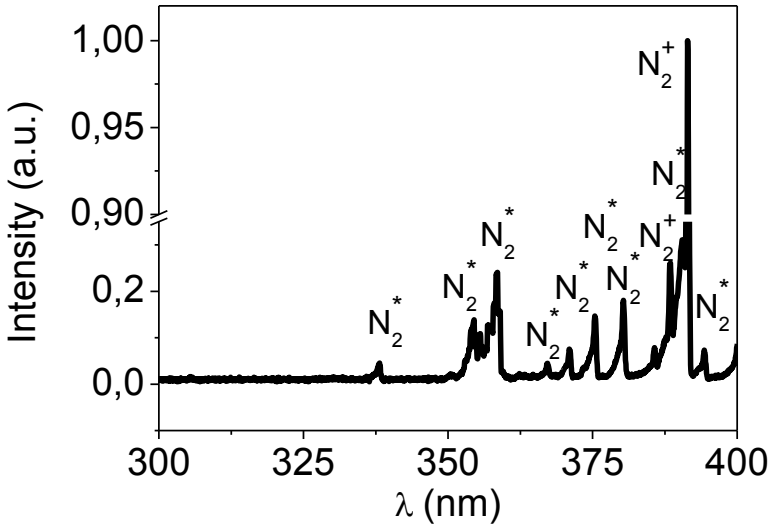

Attribution of the bands and lines detected in the OES spectra to different intermediate species:

Plasma composition (%N_2, %O_2, %H_2)	**Species**	**Wavelength (s)(nm)**	**Transition(s)**
(88,12,0)	N_2^*	250-500 600-900	Molecular bands SPS[a] ($C^3\Pi$, v→B^3 Π, v') FPS[b] ($B^3\Pi$, v→A^3 Σ, v')
	N_2^+	391.4- [d]	Molecular bands FNS[c] (B^2 Σ, v→X^2 Σ, v')
(17,83,0)	N_2^*	250-500 600-900	Molecular bands SPS[a] ($C^3\Pi$, v→B^3 Π, v') FPS[b] ($B^3\Pi$, v→A^3 Σ, v')
	N_2^+	391- [d]	Molecular bands FNS[c] (B^2 Σ, v→X^2 Σ, v')
	O*	436.8, 532.9, 615.6, 645.6, 777.4, 844.6	Atomic lines involving the 3s and 3p states

Supporting information S2

N1s spectra recorded for N-TiO_2 thin films prepared at 523 K (left) and 298 K (right) by PECVD with a plasma of pure oxygen in the plasma gas and TTIP, TDMAT and TDEAT as precursors.

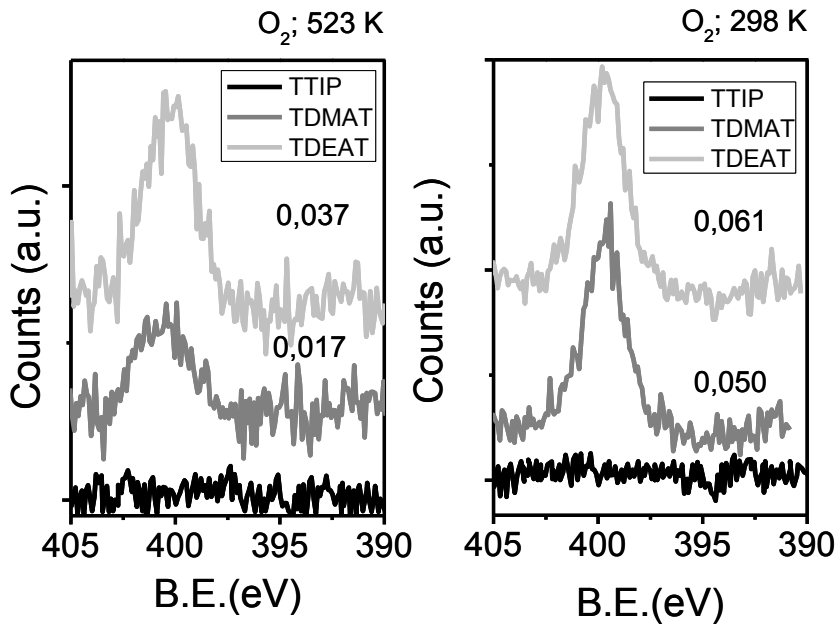

Supporting information S3.

Representation of the band gap of the different thin films plotted against the amount of nitrogen in the films expreseed as the N/Ti ratio.

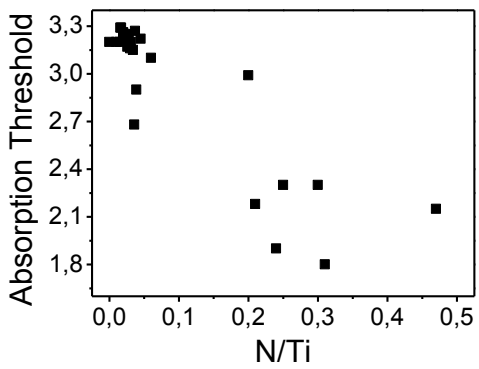

Supporting information S4

Selected conductivity values determined for N-TiO_2 thin films prepared under different plasma deposition conditions.

Plasma Condition (% N_2)	***Resistivity (Ω·cm)***
0%	*Infinity*
80%	*Infinity*
85%	*Infinity*
90%	*Infinity*
95%	*Infinity*
97%	1.3×10^5

Supporting information S5

XRD of N-TiO_2 thin films prepared by PECVD at 523 K with the TTIP, TDMAT and TDEAT precursors and 90.% N_2 in the plasma gas mixture. Amorphous structures by this technique are also found for the films prepared with percentages of N_2 higher than90 % (left). These films crystallized into the anatase structure after their annealing at 673 K (right)

Supporting information S6.- DOS curves determined for the pure TiO_2 model system.

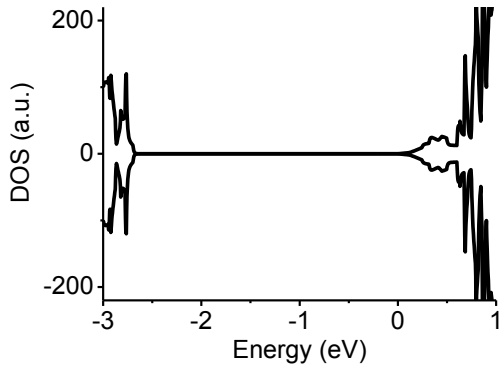

Supporting information S7.- XRD diagrams of N-doped thin films prepared by PECVD at 523 K by using pure O_2 (left) or mixtures O_2/N_2 with 90 % of N_2 (right) as plasma gas

J. Phys. Chem. C **2009,** *113,* 13341–13351

Chemical state of nitrogen and visible surface and Schottky barrier driven photoactivities of N-doped TiO_2 thin films

P. Romero- Gómez[1], V. Rico[1], A. Borrás, A. Barranco[1], J.P. Espinós[1], J. Cotrino[1,2], A.R. González-Elipe[1*]

1. Instituto de Ciencia de Materiales de Sevilla (CSIC-Univ. Sevilla). Avda. Américo Vespucio 49. 41092 Sevilla (Spain). http://www.sincaf-icmse.es

2. Departamento de Física Atómica, Molecular y Nuclear. Universidad de Sevilla. Avda. Reina Mercedes 49, 41012 Sevilla. Spain.

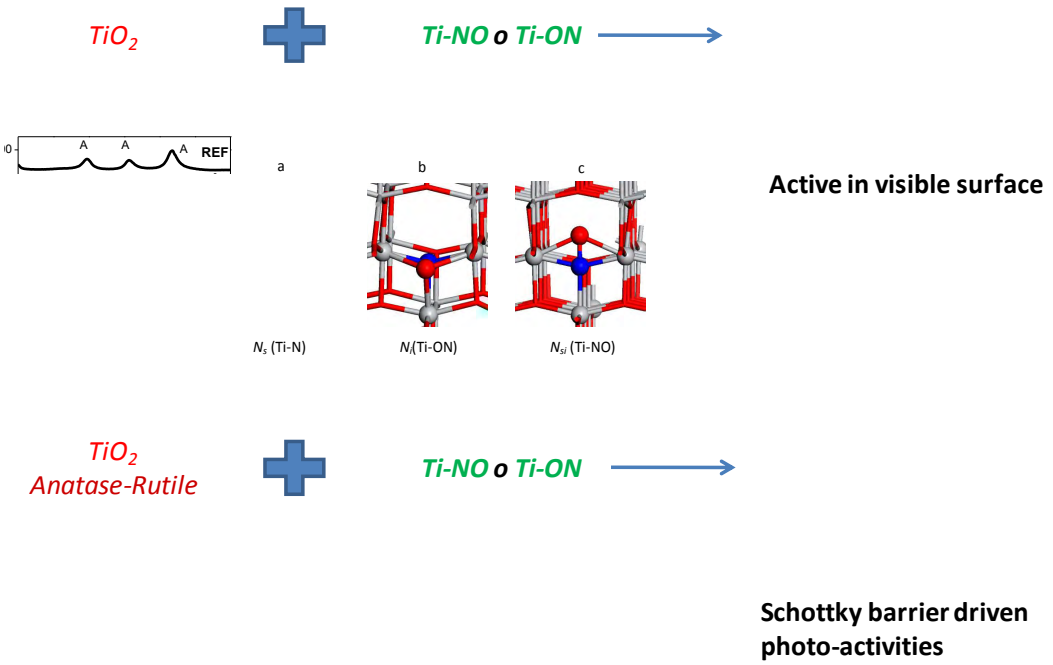

Title: Chemical state of nitrogen and visible surface and Schottky barrier driven photo-activities of N-doped TiO2 thin films.

Authors ***P. Romero- Gómez****, V. Rico, A. Borrás, A. Barranco, J.P. Espinós, J. Cotrino, A.R. González-Elipe.*

Source: J. Phys. Chem. C, Vol. 113, No. 30, 2009

D.O.I. 10.1021/jp9024816

Chemical state of nitrogen and visible surface and Schottky barrier driven photoactivities of N-doped TiO_2 thin films

P. Romero- Gómez[1], V. Rico[1], A. Borrás, A. Barranco[1], J.P. Espinós[1], J. Cotrino[1,2], A.R. González-Elipe[1*]

1. Instituto de Ciencia de Materiales de Sevilla (CSIC-Univ. Sevilla). Avda. Américo Vespucio 49. 41092 Sevilla (Spain). http://www.sincaf-icmse.es

2. Departamento de Física Atómica, Molecular y Nuclear. Universidad de Sevilla. Avda. Reina Mercedes 49, 41012 Sevilla. Spain.

*arge@icmse.csic.es

Abstract

N-doped TiO_2 thin films have been prepared by plasma enhanced chemical vapor deposition (PECVD) and by physical vapor deposition (PVD) by adding nitrogen or ammonia to the gas phase. Different sets of N-doped TiO_2 thin films have been obtained by changing the preparation conditions during the deposition. The samples have been characterized by X-ray diffraction (XRD), Raman, UV-vis spectroscopy and X-ray photoemission spectroscopy (XPS). By changing the preparation conditions, different structures, microstructures, and degrees and types of doping have been obtained and some relationships established between these film properties and their visible light photoactivity. The N1s XP spectra of the samples is characterized by three main features, one tentatively attributed to Ti-N (i.e., nitride with a binding energy (BE) of 396.1 eV) and two others with BEs of 399.3 and 400.7 eV, tentatively attributed to nitrogen bonded simultaneously to titanium and oxygen atoms (i.e., Ti-N-O like species). By controlling the deposition conditions it is possible to prepare samples with only one of these species as majority component. It has been shown that only the samples with Ti-N-O like species show surface photoactivity being able to change its wetting angle when they are illuminated with visible light. The presence of these species and an additional complex structure formed by a mixture of anatase and rutile

phases is an additional condition that is fulfilled by the thin films that also present photocatalytic activity with visible light (i.e., surface and Schottky barrier driven photoactivities). The relationships existing between the reduction state of the samples and the formation of Ti-N or Ti-N-O like species are also discussed.

1. Introduction

The quest for N-doped TiO_2 thin films and powders was fostered by the discovery of Asahi et al.[1] that titanium dioxide may become photoactive when irradiated with visible light. Since the publication of this seminal work, much effort has been dedicated to both the development of different experimental strategies of doping[2-7] and the understanding of the reasons that make this material photoactive in the visible when appropriately doped.[8,9] However, none of these two questions has yet a clear answer and some controversy exists because the obtained results are not always reproducible. This situation is well reflected in recent reviews dealing with this subject.[10,11]

From an experimental point of view, X-ray photoemission spectroscopy (XPS) has been the most widely used technique to check the state of nitrogen in N-doped TiO_2 materials. Already Asahi et al.[1] pointed out that there were at least two types of nitrogen species in their N-doped TiO_2. A first one was characterized by a binding energy (BE) of about 396 eV (hereafter called α) and another one by a BE of about 400 eV (hereafter called β). These two species have been determined by XPS with different total and relative intensities in other N-doped TiO_2 materials.[1, 6, 7, 12-16] However, no agreement exists about the assignment of these nitrogen species that have been alternatively attributed to nitride, [1, 7, 12] NH,[7] molecular nitrogen[7, 16] or NO[7, 14] species, either in substitutional or interstitial locations of the TiO_2 lattice.

N-doped TiO_2 has been prepared in the form of powder or as thin films. In this latter case magnetron sputtering,[5,17,18] electron beam evaporation,[19] ion beam assisted deposition (IBAD) [20] or plasma enhanced chemical vapor deposition (PECVD) [21] have been utilized. The photoactivity of N-doped TiO_2 thin films can be checked by looking to its photocatalytic ability to produce chemical reactions under the action of light and/or by following the evolution of the wetting angle of water or other liquids on its surface as a function of the irradiation time. As justified in the discussion, we will refer

to these two types of photoactivity as "*surface*" and "*Schottky barrier driven*" photoactivities, respectively. In some works in the literature, the two effects have been implicitly taken as equivalent. However, this assumption must be considered critically as even for un-doped TiO_2 it has been demonstrated that the efficiencies for photocatalytic degradation of dyes and the change in wetting angle upon UV light irradiation can be quite different.[22] In this line, we have recently shown that TiO_2 thin films doped by nitrogen ion beam implantation become partially hydrophilic when irradiated with visible light, even if no photocatalytic activity was observed for these samples.[23]

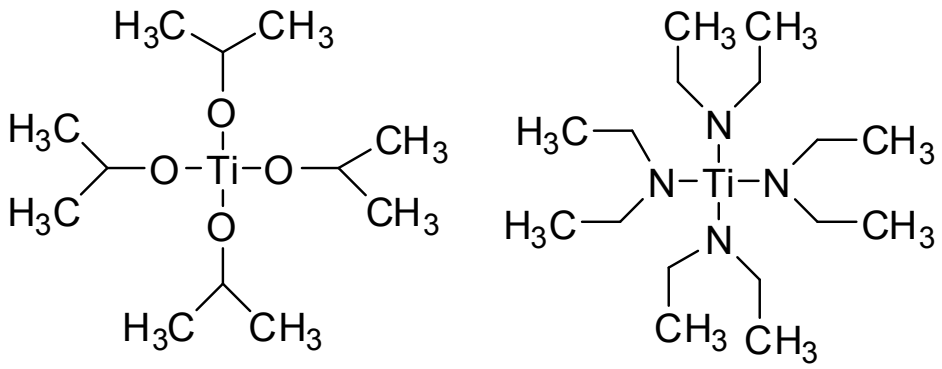

Scheme 4.1. Representation of the structure of the TTIP and TDEAT precursors of Ti used for the PECVD of N-doped TiO_2 thin films

The present paper addresses some of the aforementioned open issues by studying the synthesis and analyzing the properties of N-doped TiO_2 thin films prepared by PECVD and physical vapor deposition (PVD) at glancing angle evaporation. The plasma and evaporation conditions have been changed in order to control the doping state, the type of species present in the samples, and other properties of the films. In particular, we have tried to correlate the type of species formed in each case with the observed *surface* and *Schottky barrier driven* photoactivities of the samples. This latter has been checked by following the photocatalytic degradation of dyes in aqueous solutions. For the purpose of controlling the state and amount of nitrogen into the films, the composition (i.e. nitrogen, oxygen or hydrogen content) and other characteristics of the plasma used for decomposition of the precursors during PECVD have been systematically changed. In addition, the performance of films from a N-containing precursor (i.e., with Ti-N

bonds present in the precursor molecule) is compared with that of films deposited from an standard isopropoxide precursor typically used for the fabrication of TiO_2 optical thin films by PECVD. In this latter case, N-doping of samples is produced by reaction with nitrogen species of the plasma discharge. By PVD, the residual gas during evaporation and the temperature of the substrate have been critical parameters to get thin films with *Schottky barrier driven* photoactivity in the visible. The films have been characterized by Scanning Electron Microscopy (SEM), X-ray photoemission spectroscopy (XPS), Raman spectroscopy, X-ray diffraction (XRD) and UV-visible absorption spectroscopy. A critical evaluation of the different results obtained has enabled a first assessment of the influence of the state of nitrogen and other thin film characteristics as their structure and microstructure for the visible activation of N-doped TiO_2.

2.Experimental Section

2.1 Thin film preparation and selected samples.

A series of TiO_2 and N-doped TiO_2 thin films were prepared by PECVD in a plasma reactor with a remote configuration. The system, supplied with a microwave plasma source (SLAN, from Plasma Consult, GMBh, Germany) has been described in previous works. 24, 25 It consists of an external 2.45 GHz microwave electron cyclotron resonance (MW-ECR) plasma source coupled to the reaction chamber and separated from it by a grid to avoid the microwave heating of the substrates. Under normal conditions of operation, the grid confines the plasma out of the reaction chamber (remote plasma conditions) where the substrate and the precursor dispenser are located. Ion bombardment effects on the growing sample can be enhanced by externally applying a voltage bias to the substrate or by decreasing the operation pressure of the plasma. Control of this effect has demonstrated to be quite effective in modifying the samples characteristics (structure, microstructure), even if the plasma composition remains the same. Titanium tetra-isopropoxide (TTIP) was used as titanium precursor. For comparison, some experiments were also carried out with the nitrogen- containing Tetrakis(diethylamido)titanium(IV) (TDEAT) precursor. Scheme 4.1 shows a representation of the two precursors used in this work. It is worth noting the four direct Ti-N bonds existing in the TDEAT.

The plasma source was operated with a power of 400 W with either pure O_2, O_2 + Ar or mixtures of gases containing nitrogen, basically N_2+O_2 and N_2+H_2+O_2. The synthesis of the films was carried out at variable temperatures between room temperature and 523 K, although only results at 298 and 523 K are reported. For dosing TTIP or TDEAT in a controlled way they were placed in a stainless steel recipient through which oxygen was bubbled while heating at 305 K. Both the bubbling line and the shower-type dispenser used to dose the precursor into the chamber were heated at 373K to prevent any condensation in the tube walls. Total pressure during deposition was $4x10^{-3}$ Torr (normal operation conditions). Another series of samples was prepared at a much lower pressure ($4x10^{-4}$ Torr) with N_2 +O_2 as plasma gas. In this latter case, the system was working under the typical ECR conditions characterized by a higher ion density than at higher pressures. [26] A deposition rate of approximately 2.5 nm min^{-1} was estimated by means of a quartz crystal monitor for the samples grown at room temperature.

Although we prepared a large number of PECVD samples by changing synthesis parameters such as temperature of substrate, pressure, voltage bias applied to the substrate and mixture of plasma gases, we have summarized the results by referring to the type of nitrogen species detected by XPS. Some basic properties of the set of samples selected for this analysis have been gathered in Table 4.2, where details about some relevant parameters of the procedure of synthesis are indicated for samples prepared with TTIP as precursor. Occasionally, comments are also made in the text to samples prepared by modifying the preparation parameters reported in Table 4.2. The order A-E defined in this table has been established after the relative N/Ti ratio determined by XPS as reported in the next section. It can be realized that the thin films were prepared at 298 K (samples C) or 523 K (samples A, B, D, E), by using mixtures of O_2+N_2 that can be rich either in O_2 (samples A) or in N_2 (samples B, C and E) or also contain H_2 (samples D). A bias voltage of 150 V was applied to the substrate for the majority of the preparations reported in Table 4.2 (samples B-E). In one case, ECR low pressure conditions were also used for the deposition of the films (sample E). An un-doped TiO_2 sample (sample REF), intended as a reference, was prepared with pure oxygen as plasma gas. A fully account of the characteristics of this reference thin film can be found in previous publications. [24, 25] From these previous works, an important feature of the un-doped TiO_2 thin films prepared by PECVD is that they are amorphous when prepared at T<523 K, but become crystalline when prepared at 523 K as temperature of the substrate.

Another series of N-doped TiO_2 thin films were prepared by PVD at glancing angles (i.e., GAPVD). [27-29] The films studied in the present paper were prepared by electron evaporation of TiO_2 as target material and an evaporation angle of 85º between the substrate and the evaporation source. During evaporation, the substrate was kept at 673 K, while a 50% mixture of NH_3+O_2 at a pressure of 10^{-4} torr was dosed in the evaporation chamber. This type of thin films is labelled as sample F. Some of its basic properties are also summarized in Table 4.2. It is important to indicate that, in a similar way than the PECVD samples, other films prepared by PVD using different deposition conditions with nitrogen as the sole residual gas only showed *surface* photo-activity and will not be considered specifically here.

Table 4.2. Summary of main properties of samples

PARAMETER OF SYNTHESIS				**STRUCTURAL AND OPTICAL PROPERTIES**		
Sample	**T(K)**	**Plasma composition (N_2%, O_2%, H_2%)**	**Pressure (Torr)**	**Structure[1] and crystal size (nm)**	**Absorption edge**	**N/Ti**
A	523	(17,83,0)	$4\cdot10^{-3}$	A (84.2)	3.14 eV	0.01
B	523	(88,12,0)	$4\cdot10^{-3}$	A (85.0)	2.8 eV	0.04
C	298	(88,12,0)	$4\cdot10^{-3}$	Amor.	3.32 eV	0.11
D	523	(65,12,23)	$4\cdot10^{-3}$	Amor.	2.75 eV	0.11
E	523	(88,12,0)	$4\cdot10^{-4}$	Amor.	2.4 eV	0.24
F	673	PVD	10^{-4}	A(22.6)+ R(9.0)	2,92 eV	0,01
REF	523	(0,100,0)	$4\cdot10^{-3}$	A (89.2)	3.22 eV	0

1) A: anatase; R: rutile; amor. amorphous

All the films were deposited simultaneously on a silicon wafer and on quartz plates. Thickness of the prepared samples was estimated by measuring the mass thickness of the films by both X-ray fluorescence (XRF) and Rutherford Back Scattering (RBS). Note that the mass thickness is different than the actual thickness of the films determined by Scanning Electron Microscopy and/or by optical methods. Typical (optical) thicknesses of the thin films prepared on silicon or on fused silica substrates were in the order of 300 nm. However, for SEM cross section views, thicker films were prepared on silicon substrates.

2.2 Methods of characterization

The optical properties of the samples were determined by UV-vis absorption spectroscopy (Perkin-Elmer Lambda 12 Spectrometer) for samples prepared on fused silica. Typical thickness of the samples used for optical characterization was around 350 nm.

XPS spectra of the films were recorded on an ESCALAB 210 spectrometer working under energy transmission constant conditions. The Mg Kα line was used for excitation of the spectra. They were calibrated in binding energy (BE) by referencing to the C1s peak due to contamination taken at 284.6 eV. Quantification was done by calculating the area of the peaks and by correcting then with the sensitivity factor of each element/electronic level. To remove the carbon and other contamination from the surface of the films, they were subjected to a gentle sputtering with Ar^+ ions of 2.5 keV. A current density of about 10 μA cm^{-2} for a sputtering time of 5 min was used in these treatments. Fitting analysis of the N1s peak was carried out by using elemental bands of gaussian/lorentzian shape after background subtraction of the spectra with a Shirley-type curve.

SEM cross section and normal images were measured in a Hitachi S5200 field emission microscope for thin films grown on a silicon wafer. The thickness of the samples for SEM analysis was generally higher than for the other characterization experiments.

Structural characterization of the thin films was done by X-ray Diffraction in a Siemens D5000 difractometer.

Raman spectra were collected in a LabRAM HR High Resolution 800 UV Confocal Raman Microscope. For the measurements a green laser (He-Ne 532.14 mn), 600 line/mm, 100X objective, 20 mW and 100µ pinhole, was used.

Measurement of the surface electrical conductivity of the samples was carried out with the typical four point probe test. A Keithley 617 Electrometer and a Hewlett-Packard 34401 A Voltammeter were used for the measurements. These consisted of applying a voltage ranging between -0.25 and 0.25 V to the two external probes and the measurement of the current flowing between the two internal probes.

Measurement of contact angle was carried out by the Young method by dosing small droplets of deionized and bidistilled water on the surface of the illuminated samples. In the experiments where the contact angle variation was determined as a function of the illumination time, a metal foil acting as a shutter was used to close and open the lamp output. All wetting angle measurements within a given experiment were taken after illumination for successive periods of time. Therefore, the time scale in the plots refers to the accumulative illumination of the samples. The maximum uncertainty in the determination of the water contact angle is about 10º depending on the sample position. In the course of this investigation it was noticed that the "as-prepared" thin films were more hydrophilic than the same samples a given time after their preparation. Therefore, the reported results correspond to samples that were stored in a desicator, at least for two months, before testing their photo-activity.

Illumination of the samples was carried out with a Xe discharge lamp with a photon intensity at the position of the samples of 2 Wcm^{-2} for the complete spectrum of the lamp. For simplicity we will refer this situation in the text and figures as UV illumination. Other experiments consisted of the illumination with the same lamp by placing an UV filter (i.e., λ> 400 nm) between the lamp and the sample. The light intensity was then 1.6 Wcm^{-2} at the sample position. In all cases an infrared filter (i.e., a water bath) was kept between the lamp and the samples to prevent any possible heating by the infrared radiation.

Photocatalytic tests were carried out in a specially constructed experimental setup. It consisted of a small cell made of quartz (total volume 3 cm^3) where 2 cm^3 of a $3.5x10^{-5}$ M solution of methyl orange dye was placed together with a piece of a silicon substrate (1x0.8 cm^2) with the thin film deposited on its surface. The films, deposited on a silicon

wafer, were irradiated from a frontal position while spectra of the solution were simultaneously recorded with the help of two optical fibres connected to an UV-visible spectrometer and placed in opposite sides of the vessel. The solution was bubbled with oxygen and the vessel closed with a Teflon cover to avoid the evaporation of the liquid. The whole set-up was refrigerated with a fan placed behind the vessel. This experimental set-up permitted the automatic recording of the spectra from the solution while the films are irradiated. Blank experiments were also carried by placing a piece of a silicon wafer without any TiO_2 thin film deposited on its surface. The intensity of the UV+vis radiation at the position of the cell was 1.8 W (i.e., approximately 0.3 Wcm^{-2} for photons with $\lambda < 380$ nm). Visible illumination was carried out by placing a filter (i.e., $\lambda > 380$ nm) between the Xe discharge lamp and the reaction vessel. The intensity of the visible radiation at the cell position was 160 mW cm^{-2}. Since the illumination area of the samples was defined with a slit of 1 cm^2 and was always the same for all the experiments, their results can be properly compared. The curves reported in the paper to show the evolution of the concentration of dye versus illumination time have been obtained after dividing the curves obtained with the thin films by the curve of the blank experiment. We must stress that placing a silicon wafer in the blank experiment is critical for a proper correction of the results. In fact, in the absence of any reflecting surface in the cell, the effect of the reflected light through the solution is not considered in the blank experiment and flaw final results are obtained.

3. Results

3.1.Microstructure and structure of the thin films

Fig. 4.12 shows a series of SEM micrographs corresponding to samples A-F and to the reference sample. It is apparent from this figure that the films prepared at 298 K (i.e. sample C) or at 523 K under ECR conditions (i.e., sample E, the image of this latter not shown) present a homogenous microstructure where no columns or crystals can be seen. A similar microstructure was always obtained under normal pressure conditions of PECVD by applying a high bias voltage to the substrate (i.e., voltages of the order of 300V, image not shown). This result and the homogenous microstructure of sample E support that an enhancement of the ion bombardment effects during the film growth favor the surface mobility of the ad-species during growth and, as a result, a

homogeneization of the microstructure. This contrasts with the microstructure of the films prepared under "normal" PECVD conditions (i.e., samples A,B and D) at 523 K as substrate temperature and 150 V as bias voltage, all of them presenting a columnar microstructure formed by the agglomeration of small grains and/or crystallites quite similar to those of the reference sample. The microstructure of sample F prepared by PVD at glancing angles was characterized by tilted columns that leave large open pores between them. This microstructure is typical of this kind of thin films. [29] A rough estimation of the porosity of these films based on the assessment of their refraction indices yields values of the order of 40% of void spaces.

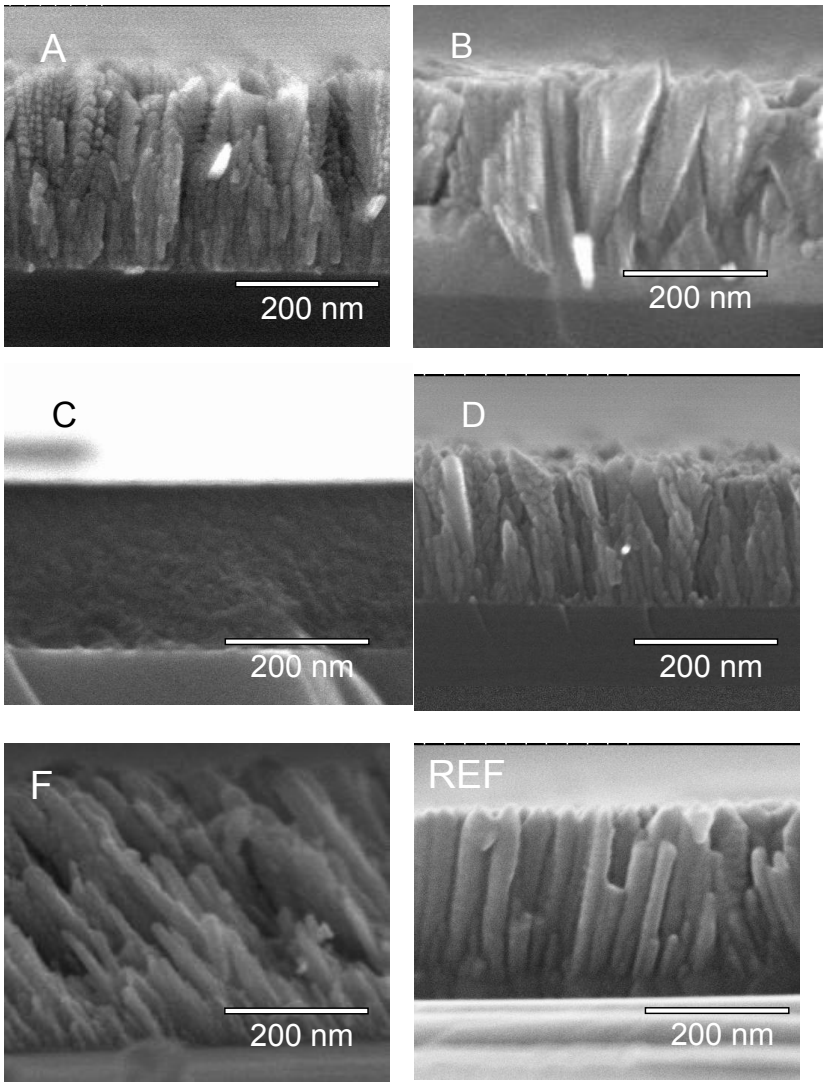

Fig. 4.12. Cross section views of thin films A-F and that of the REF sample. Sample E has a microstructure very similar to that of sample C.

The structure of the films was analyzed by XRD. The films prepared at 298 K (i.e., samples C) were all amorphous, while those prepared by PECVD at T>523 K (i.e.,

samples A, B, D and E) were amorphous or crystalline depending on the particular experimental protocol used in each case. Fig. 4.13 reports a series of diffraction diagrams recorded for various samples. The diagrams in this plot corresponding to samples A and B are typical of the anatase structure of TiO_2 although the relative intensity of the different peaks of the diagram slightly differs from that of a polycrystalline sample where the crystals are randomly oriented (see the patterns of anatase an rutile included in the figure for comparison). The crystal size determined by the Scherrer method for the set of samples A and B yielded values of 84.2 and 85.0 nm, respectively. From the (101) peak of the anatase phase of the REF sample, a crystal size of 89.2 nm could be also determined. Samples C, D and E were amorphous, at least as determined by XRD. This result was quite surprising since samples D and E were prepared by PECVD at 523 K, the temperature at which anatase films are obtained by this method when using an oxygen plasma. [24] Some of these sample characteristics are collected in Table 4.2. It is also worth noting that a thin film prepared under conditions similar to those of thin films B, but by biasing the substrate with a voltage of 300 V, was also amorphous.

The diagram of samples F prepared by GAPVD, also reported in Fig. 4.13, was characterized by a rich structure where peaks of anatase and rutile can be detected. The crystal size of the anatase phase was estimated in 22.6 nm and that of rutile in 9 nm.

A deeper insight into the structure of the films can be obtained by Raman spectroscopy. Fig. 4.14 (top) shows the Raman spectra of samples A-F compared with the spectrum of the reference sample in the region comprised between 210 and 800 cm^{-1}. These spectra are characterized by a series of peaks with different intensities located at 395, 515 and 638 cm^{-1}.[30,31] Samples C and E have a very poor crystallinity as no resolved peaks of anatase can be detected in this region of the spectra.

Fig. 4.13. XRD of samples A-F and that of the REF sample included for comparison.

Peaks due to the anatase and rutile phases are indicated in the form of patterns.

The Raman spectrum of samples F shows a more complex pattern where, in agreement with literature,[32] peaks at the positions of the anatase and rutile phases of TiO_2 can be detected. This spectrum confirms the detection by XRD of these two phases.

It is worth stressing that no clear hints of an oxinitride phase could be found in the previous spectra. The formation of this phase in N-doped TiO_2 thin films has been claimed by some authors[33] from the fitting analysis of Raman spectra very similar to those of samples A or B in Fig. 4.14. Recently, other authors [34, 35] have attributed the background features appearing at around 328, 585, 680 and 815 cm^{-1} to defective titanium oxide. For the case of thin films F, we think that the peaks in Fig. 4.14 (top) around these positions are due to spectral features of the rutile phase detected by XRD.

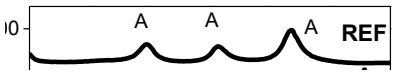

Figure 4.14. (Top) Raman spectra in the zone between 200 and 800 cm^{-1} for samples A-F compared with that of the reference anatase sample; the peaks attributed to the rutile phase are indicated. (Bottom) Raman spectra in the zone of the main peak of anatase at around 150 cm^{-1}.

Fig. 4.14 (bottom) shows an enlarged view around the region of the main peak of the Raman spectrum of anatase attributed to the E_g vibration mode.[30,31] For samples A, B and F and even more pronounced for sample D, the position of the main mode at around 150 cm^{-1} is shifted from 143.2 cm^{-1} in the reference anatase to around 150.0 cm^{-1} and beyond in samples A, B, F and D. In these four cases, the peak also broadens with respect to the peak of the reference sample. It is important to remark that for sample D no well resolved diffraction peaks could be observed by XRD, thus sustaining that Raman can be a more sensitive technique to detect first crystallization stages in thin films. Frequency shift and line width broadening of the main mode have been attributed to crystalline size effects[33-35] and/or to the accumulation of structural defects and/or lack of stoichiometry of the oxide.[36] Since the cristal size determined by XRD is not much

smaller in samples A and B (although it is smaller in sample and F) than in the sample REF we must conclude that accumulation of structural defects and/or some chemical reduction with a loose of stoichiometry are likely the main reasons for the observed Raman shift in these samples.

3.2. UV-vis spectra and reduction degree of the films

A first assessment of the reduction state of the oxide thin films was obtained by measuring their surface conductivity. Samples A, B, C and F present a high surface resistivity and no reliable final data on sheet resistance could be obtained with the used technique. However, surface conductivity in the dark could be measured for samples D and E. Sample E was the most conductive one with an estimated resistivity of 1.5×10^{-1} (cm Ω). The measured values were dependent on the time elapsed since the preparation of the samples with the conductivity slightly decreasing for the sample stored for long periods of time. Surface conductivity in titanium oxide thin films is associated with the presence of vacancies and other structural defects within a layer of several tenths of nanometer, indicating a certain lost of stoichiometry (i.e., formation of Ti^{3+} species). [37,38]

Fig. 4.15 shows the UV-vis absorption spectra of samples A-F, together with the spectrum of the anatase thin film taken as a reference. The value of the absorption edges, obtained by the Tauc method by extrapolating to zero the function $A(h\nu)^{1/2}$, [39] is reported in Table 4.2. The obtained data indicate that samples A and C present absorption edges that are very close to that of the reference anatase film, while samples B, D, E and F present absorption edges which are shifted to smaller energies. In addition, samples B, D, E and F present some specific absorption features in the blue region of the spectra that are clearly distinguishable from the typical interference oscillations presented by high refraction index thin films deposited on a quartz substrate. For samples B, D and F, this first absorption feature is located around 420 nm. In samples E, besides an absorption around this wavelength, there is also a broad absorption extending through the whole range of wavelengths and centered at λ=500 nm. Very likely this broad absorption is related with the existence of a high

concentration of structural defects and/or Ti^{3+} species as it can be deduced from the relatively high surface conductivity of this sample.

The absorption spectra of N-doped titanium oxide has conceited much interest in literature because absorption features in the visible have been taken as a hint of visible photoactivity of this material and because of a vivid controversy about the effect of doping in narrowing the band gap of TiO_2.[10, 11] According to Serpone et al.[40] absorption features appearing in the visible in anion doped titanium oxide originate from color centers associated with the reduction of the titanium oxide rather than with a narrowing of the band gap as claimed by others. [41-43] Meanwhile, Lin et al., [44] combining theoretical calculations with the analysis of UV-visible spectra, concluded that the optical absorption of N-doped TiO_2 is primarily located between 400 and 500 nm, while that of oxygen-deficient TiO_2 appears above 500 nm. These authors coincide in that no narrowing of the band gap of TiO_2 occurs as an effect of the incorporation of nitrogen into the structure of the oxide. In relation with our results, we can tentatively assume that samples E, depicting a broad absorption at λ= 500 nm and showing a measurable surface conductivity, is chemically reduced and presents a considerable concentration of oxygen vacancies and other defects in its structure. Meanwhile, the absorption features at around 430 nm found in samples B, D and F are likely related with absorption centers associated to nitrogen incorporated within the structure of the titanium oxide.

Fig. 4.15.UV-vis absorption spectra of samples A-F compared with that of the reference thin film. The asterisk in some of the plots indicates the presence of a specific absorption feature.

3.3 XPS analysis and chemical state of nitrogen

XPS has been used to check whether nitrogen has been incorporated within the structure of the titanium oxide films. This technique also provides information about the actual chemical state of nitrogen in the different samples. Fig. 4.16 shows N1s fitted photoemission spectra recorded for samples A-F. The spectra are represented by applying different multiplication factors to bring all the spectra to a similar height. The

N/Ti ratios determined for these samples are reported in Table 4.2. The obtained data show that samples C, D and E have a high content of N, while in samples A and B this amount approximately decreases by one order of magnitude. Sample F presents a spectrum that is similar to that of sample A. To a first approximation, the N1s spectra in Fig. 4.17 can be considered as the contribution of three main components, a first one centered around 396 eV (species α) and two others centered around 400 eV (species β and β´). Photoemission spectra of the O1s, C1s and Ti2p levels were also recorded. The O1s and Ti2p spectral shapes were quite similar in all cases and equivalent to the reported spectra of TiO_2 (i.e., attributed to $O^{=}$ and Ti^{4+} species[45]). The corresponding spectra are reported in the supporting information S1. The C1s spectra was characterized by a main peak at 284.6 eV, taken as a reference for the BE scale. In some cases a small shoulder at about 290 eV could be observed in the spectra. This peak is normally attributed to carbonate species,[46] while the main peak is ascribed to carbonaceous rests contaminating the surface of the samples. For the PECVD samples, another source of this spurious carbon can be some adsorbed rests of the organic parts of the titanium precursor. The amount of contaminating carbon (i.e., around 15% atomic) was similar to that detected in other oxide thin films handled in air. Its surface character was confirmed by subjecting the examined thin films to a mild sputtering treatment for 5 min (see the Experimental Section). After this treatment, the carbon content in the samples decreased to less than 7 % atomic in all cases. This contrasts with the fact that the N/Ti ratios measured for the sputtered films remained almost unmodified after that treatment. This supports that nitrogen is distributed homogenously through all the films. Apart from a broadening in the spectral shape, the form of the N1s spectra in the different samples was not modified significantly after that treatment (see supporting information S8). This indicates that the different species identified in the spectra of Fig. 4.16 distribute homogeneously through the first layers of the films. It is also interesting that in sample E subjected to the sputtering treatment, the Ti2p level depicted a shoulder at 456.5 eV that can be attributed to Ti^{3+} species. In the other samples, such a feature is not so clearly observed (note that TiO_2 is always reduced when subjected to Ar^{+} sputtering due to the preferential loss of oxygen[47]). This result sustains the previous evidences in section 3.2 in the sense that this sample is partially reduced.

Figure 4.16. N1s fitted photoemission spectra of samples A-F

In relation with the XPS analysis of samples, it is also important to remark that, particularly for samples D and E and to lesser extent B, the spectra underwent a certain evolution with time. This evolution is characterized by a relative decrease in the α band at 396 eV and an increase in the intensity of the β bands around 400 eV.

A deeper insight into the type of nitrogen species that become incorporated into samples A-F can be obtained by the fitting analysis of the spectra in Fig. 4.16. We have intended such an analysis under the assumption that all the spectral shapes can be well reproduced by the contribution of three bands centered at 396.1 (species α), 399.3 (species β) and 400.7 (species β') eV. The results of the fitting analysis are reported in Fig. 4.16. The fitting scheme used implies that around 396 eV there is only one type of

nitrogen species, while around 400 eV there is the contribution of two different bands. It is important to note that this fitting scheme based on the presence of three bands provides the minimum number of fitting bands with a similar width (i.e., between 1.7 and 1.4 eV) that would be common for the six analyzed spectra. However, we must stress that this analysis does not discard the presence of other possible species characterized by BEs similar to those of the three bands resulting from the fitting analysis.

The XPS analysis of the state of nitrogen in N-doped TiO_2 thin films has been widely addressed in the recent literature on the subject,[1,8,10-16,33,48-51] although no agreement exists neither about the attribution of the detected species nor about the species which is/are responsible for the visible light photoactivity of N-doped TiO_2. Of particular interest is the recent paper by Asahi et al.[51] who based on first-principles calculations using the projector argument wave method[52] has attributed the observed peaks in a series of N-doped TiO_2 photocatalysts to N (395.7 eV), NO (398.1 eV) and NO_2 (399.8 eV) species. Nitrogen species with BEs around these values have been detected during the oxidation of titanium nitride compounds[53,54] or by the nitrogen implantation in titanium and other metal oxides.[55,56] On the basis of these previous works, we tentatively ascribed the species detected in our films to nitride (396.3 eV) (i.e., nitrogen triple bonded to titanium) and to nitrogen in a titanium oxinitride local environment (399.3 eV and 400.7 eV) where nitrogen simultaneously bonds to oxygen and to titanium in a defective lattice site (i.e., in a kind of Ti-N-O local structure). Within this scheme, a different covalent character of the N-Ti bond would account for the differences in BE between the two β species (e.g., structures of the type: Ti-N-O$^{\cdots}$Ti or Ti-O-N$^{\cdots}$Ti). Basically, this tentative attribution assumes some kind of bonding between nitrogen and oxygen for the species yielding the peaks at around 400 eV. In line with some previous reports on this subject,[11] the latter attribution assumes that the nitrogen is also bonded to titanium. On the other hand, the need of bonding to an electrophilic atom is a requirement because species like NO^-, NO_2^- or NO_3^- where nitrogen is solely bonded to oxygen atoms are characterized by BEs larger than 402 eV[57] and molecular nitrogen species implanted in oxides are characterized by a BE of 403.4 eV.[56] In our case, the attribution of the nitrogen species at around 400 eV to a nitrogen atom simultaneously bonded to oxygen and titanium of the lattice was further sustained by the analysis of a N-doped TiO_2 sample prepared by PECVD using TDEAT

as precursor and a plasma of pure oxygen. In that case only a N1s broad band at around 400 eV, with a N/Ti ratio of 0.01, could be detected even if no nitrogen was present in the plasma (see supporting information S9). The fact that in the TDEAT precursor there are four nitrogen atoms directly bonded to the titanium supports that after extensive oxidation of the precursor during the plasma deposition process, some nitrogen may remain directly bonded to the Ti although also interacting with the oxide ions of the lattice.

3.4. Photoactivity of N-doped thin films.

A first way of probing the photoactivity of titanium oxide thin films is by measuring the wetting contact angle for samples exposed to illumination with UV, vis and/or UV+vis light. As indicated in the introduction we will refer to this experiment as *surface* photoactivity. Another way is by measuring the photocatalytic activity of the films.[58-61] These experiments will be denoted here as *Schottky barrier driven* photoactivity. In a recent publication on undoped TiO_2[22] we have pointed out that these two tests are not equivalent and that they may yield different information about the photoactivity of the studied systems. Here, we have tested the surface photoactivity of the different films by measuring the evolution of the wetting angle when they are illuminated with vis and UV+vis lights as a function of the irradiation time. *Schottky barrier driven* photoactivity tests consist of measuring the photocatalytic degradation of methyl orange dye in an aqueous solution.

Fig. 4.17 shows four experiments taken as examples of the *surface* photoactivity behavior of the different thin films when they are illuminated, first with visible light and then with UV light. The recovery of the wetting angle in the dark is also included. The behavior depicted by the REF thin film and sample E is typical of stoichiometric TiO_2 surfaces and consists of the transformation of the surface of this material from hydrophobic into superhydrophilic when illuminated with UV light.[62] When the film is left in the dark, it slowly recovers the initial wetting angle. These processes are very affected by the topography of the surfaces and large variation in wetting angles can be produced for nanostructured thin films in the form of fibres or similar nanostructures.[63] In our case, a similar behavior was also observed for samples C and D. The plots in the right side of Fig. 4.18, depict the behavior of samples A and F. Sample B also follows a

similar pattern. These plots are characterized by a partial and slow decrease in wetting angle for about 30-40 ºC when these thin films are illuminated with visible light and a subsequent sharp decrease when the films are illuminated with UV+vis light. In the dark, the films slightly recover the wetting angle reached upon visible light illumination. A similar behavior has been previously reported by us for N-doped TiO_2 and Ta_2O_5 thin films prepared by ion implantation[23, 29] or by other authors for thin films prepared by magnetron sputtering.[64] In other works from literature, complete transformation into the superhydrophilic state of the surface of N-doped TiO_2 thin films upon visible light irradiation has been also reported.[65]

Figure 4.17.- Evolution of the wetting angle for the REF and E thin films (left) and samples A and F (right) subjected sequentially to illumination with visible, UV+vis and then left in the dark. The curves are plotted to guide the eyes.

The *Schottky barrier driven* photoactivity of films A-F towards the degradation of the methyl orange dye was analyzed by illuminating with visible and with visible+UV light. We observed that none of A-E films presented a detectable activity in the visible, while samples A and B were active for photodegradation of the dye only when they were illuminated with UV+vis light; however, this activity was smaller than that of the reference sample. Meanwhile, thin films F were active with both visible and UV

irradiation. A comparison of the activity of the different films is reported in Fig. 4.18 for illumination with UV+vis and vis lights. The lack of *Schottky barrier driven* photoactivity in the visible for samples A-E is somehow contradictory with previous works in literature reporting the visible photodegradation of dye solutions with N-doped TiO_2 materials.[1,8,33,51,57-61] Differences in experimental conditions, such as the use of methylene blue (MB) as sacrificial dye in most of these previous works or the fact that we are working with nanometric thin films and not with powders might be reasons for this discrepancy. In fact, while the methyl orange solutions used in our case are stable under visible light irradiation (but not under UV irradiation), MB solutions are not stable either under UV or visible illumination. According to our experience, this and other factors generally not considered explicitly in the experimental parts of the papers, such as the control of both the concentration of oxygen and the temperature in the reaction vessel during illumination or the inner vessel reflectivity in the blank experiments are factors that, if not properly handled, may lead to flaw experiments and misleading results (e.g., uncontrolled direct light degradation of the dye in the solution).

Figure 4.18.- Evolution of the concentration of methyl orange dye in an illuminated solution of this molecule in the presence of the thin films. Curves corresponding to experiments with UV+vis (top) and

visible (bottom) illumination are reported. The curves upon UV+vis illumination have been corrected by the curve of a solution of the dye in the presence of a bare substrate of Si without thin film.

4. Discusión

The analysis of samples A-F has shown that they present different structures, microstructures and compositions. XRD and Raman analysis of samples (cf. Figs. 4.13 and 14) have shown that only samples A and B present well defined peaks attributed to the anatase structure. According to the Raman spectra in Fig. 4.14, samples D also present an incipient crystallinity. Meanwhile, F samples consist of a mixture of the anatase and rutile structures of TiO_2. The poor crystallinity or samples D must be related with the enhancement of ion bombardment effects during the preparation of the samples under ECR conditions.[24, 25] Meanwhile, the amorphous character of samples E, even if prepared at 523 K by PECVD, is likely related with the considerable reduction degree of these samples and/or with the high concentration of Ti-N species incorporated into their structure. On the other hand, comparison of the main peak of the Raman spectra of the reference sample and those of samples A, B and F indicates that these N-doped thin films present a considerable concentration of structural defects. We think that the incorporation of nitrogen within the structure of these samples is contributing to this effect.

The amount and chemical character of nitrogen incorporated in the structure of the films was also different depending on the sample. The concentration of nitrogen follows the order E>D=C>B>A=F (cf. Table 4.2) a similar trend than for the ratio α/(β+ β`) between the different kinds of nitrogen species. It is important to remark that samples E, characterized by the highest absolute and relative concentrations of both nitrogen and species α, respectively, present a high reduction degree. This result proves the existence of a link between the formation of Ti-N species of the α type and the reduction degree of titanium oxide.

Species β+β` are a majority in samples A, B and F with all of them prepared under mild oxidant conditions and, consequently, with little or no lattice reduction. Quite interesting is that only these samples present *surface* photoactivity in the visible. According to our tests, this means that species α with a BE around 396 eV (attributed to Ti-N) would be inactive for the visible photoactivation of N-doped TiO_2 and that the presence of species β and/or β` is a requirement for *surface* photoactivity in the visible.

Some hints in the recent literature on the subject[12,33,50] agree with this behavior of samples A-F. This finding is in apparent contradiction with previous reports in literature where the photoactivity of N-doped TiO_2 thin films has been associated with the presence of species α, [1, 62] although in most cases the two species, α and β, have been simultaneously detected. Without discarding other effects, a possibility is that in many previous experiments dealing with N-doped TiO_2 samples the distribution of nitrogen species is heterogeneous, so that the measured photoactivity in the visible responds exclusively to those parts of the samples with a majority concentration of β-β´ species. In powder materials this heterogeneity might correspond to a different distribution of nitrogen species in the individual grains of the specimens. In addition, in thin films, inhomogeneities in the depth distribution of nitrogen species might be an additional factor modifying the visible photoactivity of samples.

It has been generally considered that visible photoactivity of N-doped TiO_2 is linked with a shift in the position of the absorption edge. [10, 11] Without completely contradicting this view, our result with samples A-F introduce some nuances which deserve a specific consideration. Data in table 4.2 suggest a certain correlation between the concentration of nitrogen in the sample and the magnitude of the shift in the absorption edge. This means that those samples with a high concentration of the α species present a maximum shift in the absorption edge. This finding precludes an automatic use of the value of the absorption edge as a measurement of photoactivity since we have demonstrated that this species does not contribute to the visible photoactivity of the system. In this regard, it is worth noting that samples A, even presenting *surface* photoactivity in the visible attributed to the incorporation of species β/β´ in its structure (cf. Fig. 4.16), do not present any significant shift of the absorption edge. This suggests that other factors like lattice reduction or the presence of other defective sites associated to nitrogen must contribute to the shift in the absorption edge. A similar description has been proposed by Serpone et al.[11,40] to account for the edge shift in N-doped TiO_2.

From the three samples, A, B and F, that present *surface* photoactivity in the visible, only sample F presents *Schottky barrier driven* photoactivity. From the point of view of XPS this sample is very similar to sample A, although structurally sample F consists of a mixture of anatase and rutile and presents a shifted edge and some absorption band in the visible (cf. Table 4.2). This result suggests that the development of local electronic

heterojunctions between zones consisting of N-doped anatase and N-doped rutile could be a condition for the *Schottky barrier driven* photoactivity of this type of samples. It could be also possible that in these samples a minority oxinitride phase not detected in the Raman spectrum, is the responsible for the observed photocatalytic activity. At present, more experimental and theoretical work is being carried out to ascertain these hypotheses.

In any case, the photoactivity results found for samples A, B and F permits to establish that wetting angle variation and photocatalytic activity are two related but different manifestations of the photoactivity of N-doped TiO_2. The terms *surface* and *Schottky barrier driven* photoactivities used for convenience through all this manuscript deserve now a justification. Photocatalytic degradation of dye molecules is a complex process implying the migration of photoexcited electrons and holes from the irradiated solid up to its surface. The migration of UV induced photoholes through the valence band of TiO_2 is the rate controlling step of this process and is driven by the formation of a Schottky barrier at the surface.[10,11,66] A similar migration of photoholes produced by visible light should be expected in the case of N-doped TiO_2. However, such a migration from the bulk would only be possible is the electronic states associated to nitrogen forms a continuous band (or interband located between the valence and conduction band of TiO_2[8,9]). Although we have to explore further the reasons why samples F present *Schottky barrier driven* photoactivity, it is reasonable to think that the formation of anatase/rutile heterojunctions could contribute to favor the migration of photoholes from the interior of the material up to its surface. In this regard, it is worthy of mention a recent paper by Zhang et al.,[67] showing that in TiO_2 powders, consisting of rutile grains covered by small anatase nanoparticles, the photocatalytic reduction of ethanol or water towards the formation of H_2 is enhanced with regard to a sample consisting of pure anatase.

On the other hand, *surface* photoactivity, manifested as a change in the wetting angle by visible irradiation of the N-TiO_2 thin films, would be a less strict process if just the photoholes generated at the outmost surface layer(s) intervene in the photoinduced reaction. Since the number of photoholes required to induce the change in wetting angle is expected to be much smaller than for a sustained photocatalytic process, it is reasonable to assume that just photoexcitation processes affecting the top most layer of the sample may be enough to modify this surface property. Thus, although it seems that

in samples A and B there are no conditions for a *Schottky barrier driven* migration of photoholes generated with visible light, *surface* photoexcitation processes seem to be enough to induce the observed change in water contact angle. A scheme in this sense was proposed by us in a previous publication with N-doped TiO_2 samples prepared by nitrogen implantation where we also explained why the wetting angle does not necessarily yield the superhydrophobic state (i.e., wetting angle lower than 10º).[23]

5. Conclusions

In this paper we have prepared N-doped TiO_2 thin films by PECVD and GAPVD. We have been able to prepare samples that are amorphous (samples C and E), partially amorphous (samples D), samples with the anatase structure (samples A and B) and other set of samples (samples F) that consists of a mixture of anatase and rutile. Samples D and, particularly, E were partially reduced and presented a relative high absorption in the visible (λ=500 nm) that is not attributed to the incorporation of nitrogen within their structure.

Different nitrogen species have been detected in the samples by XPS. These species have been tentatively attributed to Ti-N and Ti-N-O species. The first one is majority in samples C-E and its formation in our films is associated with working conditions that induce a certain reduction of the titanium oxide lattice (i.e., some hydrogen in the plasma or deposition conditions where ion bombardment effects may have a considerable importance). Under partially oxidant conditions as those used for the preparation of samples A, B and F, Ti-N-O like species are majority. Samples A and B, both containing relatively low concentration of species Ti-N-O did not present photo-catalytic activity in the visible (i.e., *Schottky barrier driven* photoactivity) and were less efficient for the photocatalytic degradation of dye solutions under UV irradiation than the reference anatase sample. By contrast, the wetting contact angle on its surface decreased when irradiated with visible light (i.e., these samples presented visible *surface* photoactivity). This suggests that this kind of nitrogen species is the responsible of the visible photoactivity of N-doped TiO_2. It is also proposed that the wide and sometimes contradictory set of results in the literature relating photoactivity and type of nitrogen species can be the result of the heterogeneous distribution of the Ti-N and Ti-N-O species within the samples, in such a way that active zones or grains with the

required type and concentration of nitrogen species are the sole responsible for the visible activity of the whole specimen.

From our samples, only sample F presented both *surface* and *Schottky barrier driven* photoactivities in the visible. This sample only had Ti-N-O like species incorporated in its structure but consisted of a mixture of the anatase and rutile phases. This type of samples also presented some absorption features in the visible and a shifted position of the absorption edge. Further theoretical and experimental work is being undertaken to ascertain all the factors that are required for *Schottky barrier driven* photoactivity with visible light in N-doped TiO_2 systems.

6. Acknowledgments

We thank the Ministry of Science and Education of Spain (projects MAT 2007-65764/NAN2004-09317, and the CONSOLIDER INGENIO 2010-CSD2008-00023) and the Junta de Andalucia (projectsTEP2275 and P07-FQM-03298) for financial support. Part of this work has been carried out within the EU project NATAMA (contract nº 032583).

References

(1) R. Asahi, T. Morikawa, T. Ohwaki, K. Aoki, Y. Taga, Science 293, 269 (2001).

(2) S. Sakthivel, M. Janczarek, H. Kirsch, J. Phys. Chem. B 108, 19384 (2004) .

(3) O. Diwald, T. L. Thompson, T. Zubkov, E. G. Goralski, S.D. Walck, J.T. Yates, J. Phys. Chem. B, 108, 6004 (2004) .

(4) Y. Nosaka, M. Matsushita, J. Nasino, A. Y. Nosaka, Sci. technol. Adv. Mater. 6, 143 (2005).

(5) Y. Nakano, T. Morikawa, T. Ohwaki, Y. Taga, Appl. Phys. Let 86, 132104 (2005).

(6) O. Diwald, T.L. Thompson, E.G. Goralski, S.D. Walck, J.T. Yates, J. Phys. Chem. B 108, 52 (2004).

(7) H.M. Yates, M.G. Nolan, D.W. Sheel, M.E. Pemble, J. Photochem. Photobiol. A: Chemistry 179, 223 (2006).

(8) S. Livraghi, M.C. Paganini, E. Giamello, A. Selloni, C.D. Valentin, G. Pacchioni, J. Am. Chem. Soc. 128, 15666 (2006).

(9) J.-Y. Lee, J. Park, J.-H. Cho, Appl. Phys. Lett. 87, 011904 (2005).

(10) T.L. Thompson, J.T. Yates, Chem. Rev. 106, 4428 (2006).

(11) A.V. Emeline, V.N. Kuznetsov, V.K. Rybchuk, N. Serpone, Int. J. Photoener. (2008) Art. ID 258394.

(12) X. Chen, C. Burda, J. Phys. Chem. B108, 15446 (2004).

(13) S. Sato, R. Nakamura, S. Abe, Appl. Catal. A-Gen. 284, 131 (2005).

(14) C.S. Gopinath, J. Phys. Chem. B 110, 7079 (2006).

(15) R. Nakamura, T. Tanaka, Y. Nakato, J. Phys. Chem. B 108, 10617 (2004).

(16) R.P. Vitiello, J.M. Macak, A. Ghicov, H. Tsuchiya, L.F.P. Dick, P. Schmuki, Electrochem. Commun. 8, 544 (2006).

(17) J.M. Mwabora, T. Lindgren, E. Avendano, T.F. Jaramillo, J. Lu, S.E. Lindquist, C.G. Granqvist J. Phys. Chem. B 108, 20193 (2004).

(18) H. Irie, S. Washizuka, Y. Watanabe, T. Kako, K. Hashimoto, J. Electrochem. Soc. 152, E351 (2005).

(19) M.-Ch. Yang, T.-S. Yang, M.-Sh. Wong, Thin Sol. Films 469/470, 1 (2004).

(20) T.-S. Yang, M.-Ch. Yang, Ch.-B. Shiu, W.-K. Chang, M.-Sh. Wong, Appl. Surf. Sci. 252, 3729 (2006).

(21) M. Maeda, T. Watanabe, J. Electrochem. Soc. 153, C186 (2006).

(22) V. Rico, P. Romero, J.L. Hueso, J.P. Espinós, A.R. González-Elipe, Catal. Today, 143, 347.

(23) A. Borrás, C. López, V. Rico, F. Gracia, A. R. González-Elipe, E. Richter, G. Battiston, R. Gerbasi, N. McSporran, G. Sauthier, E. György, and A. Figueras, J. Phys. Chem. C; 111, 1801 (2007).

(24) A. Borrás, J. Cotrino, A. R. González-Elipe, J. Electrochem. Soc., 154, 152 (2007).

(25) F. Gracia, J.P. Holgado, A.R. González-Elipe, Langmuir 20, 1688 (2004).

(26) D. Korzec, F. Werner, R. Winter, J. Engemann, Plasm Sources Sci. Technol. 6, 216

(1996).

(27) A.C. van Popta, J. Cheng, J.C.Sit, M.J. Brett, J. Appl. Phys. 102, 013517 (2007).

(28) M. M. Hawkeye, M.J. Brett, J. Vac. Sci. Technol. A 25, 1317 (2007).

(29) V. Rico, A. Borrás, F. Yubero, J. P. Espinós, F. Frutos, A. R. González-Elipe J. Phys. Chem. C, 113, 3775.

(30) J.A.Dood, S.J.Lipson, D.J.Flanagan, W.A.M.Blumberg, J.C.Person, B.O.Green, J. Chem.Phys. **94**, 4301 (1991).

(31) T. Ohsaka, F. Izumi, Y. Fujiki, J. Raman Spectrosc., Vol. 7, NO 6(1978).

(32) J. Zhang, M. Li, Z. Feng, J. Chen, Can Li, J. Phys. Chem. B 110, 927 (2006).

(33) Y. Cong, J. Zhang, F. Chen, M. Anpo, J. Phys. Chem. C 111, 6976 (2007).

(34) A.I. Kontos, A. G. Kontos, D.S. Tsoukleris, G.D. Vlachos, P. Faralas, Thin Soil. Films, 515, 7370 (2007).

(35) A.I. Kontos, A. G. Kontos, Y.S. Raptis, P. Faralas, Phys. Stat. Soil. 2, 83 (2008).

(36) J.C. Parker and R.W. Siegel, Appl. Phys. Lett. **57, 943** (1990).

(37) E. Gyorgy, A. Pérez del Pino, P. Serra, J.L. Morenza, Appl. Surf. Sci. 186 (2002) 130.

(38) N. Martin, A. Besnard, F. Sthal, F. Vaz, C. Nouveau, Appl. Phys. Lett. 93, 064102 (2008).

(39) N. Serpone, D. Lawless, R. Khairutdinov, J. Phys. Chem. 99, 16646 (1995).

(40) N. Vyacheslav, N. Kuznetsov, N. Serpone, J. Phys. Chem. B 110, 25203 (2006).

(41) T. Umebayashi, T. Yamaki, H. Itoh, K. Asai, Appl. Phys. Lett. 81, 554 (2002).

(42) Z. Lei, G. Ma, M. Liu, W. You, H. Yan, G. Wu, T. Takata, M. Hara, K. Domen, C. Li, J. Catal. 237, 322 (2006).

(43) B. Liu, L. Wen, X. Zhao, Solar Energy Mater.&Solara cells 92, 1 (2008).

(44) Z. lin, A. Orlov, R.M. Lambert, M.C. Payne, J. Phys. Chem. B, 109, 20948 (2005).

(45) E.L. Bullock, L. Patthey, S.G. Steinemann, Surf. Sci. 532/534, 504 (1996).

(46) A.R.González-Elipe, J.P.Espinós, A.Fernández, G.Munuera, Appl. Surf. Science, 45, 103 (1990).

(47) D. Leinen, A. Fernández, J.P. Espinós, A.R. González-Elipe, Applied Physics A, 63, 237 (1996).

(48) Y. Zhao, X. Qiu, C. Burda, J. Phys. Chem. 20, 2629 (2008).

(49) S. Clouser, A.C.S. Samia, E. Navok, J. Alred, C. Burda, Top. Catal. 47, 42 (2008)

(50) X. Qiu, Y. Zhao, C. Burda, Adv. Mater. 19, 3995 (2007)

(51) R. Asahi, T. Morikawa, H. Hazama, M. Matsubara, J. Phys.: Condens. Matter 20, 064227 (2008)

(52) P.E. Blochl, Phys. Rev. B 50, 17953 (1994).

(53) R. Lahoz, J.P. Espinós, G.F. de la Fuente, A.R. González-Elipe, Surf. Coat. Technol. 2002, 1486 (2008).

(54) F. Esaka, K. Furuya, H. Shimada, M. Imamura, N. Matsubayashi, H. Sato, A. Nishijima, A. Kawana, H. Ichimura, T. Kikuchi, J. Vac. Sci. technol. A 15, 2521 (1997).

(55) I. Bertoti, R. Kelly, M. Mohai, A. Toth, Surf. Interf. Anal. 19, 291 (1992).

(56) A. Barranco, J.P. Holgado, F. Yubero, J.P. Espinós, A. Martín, A.R. González-Elipe, J. Vac. Sci. technol. 19, 1024 (2001).

(57) C.D. Batich, D.S. Donald, J Am Chem Soc 106, 2758 (1984).

(58) Y. Zhao, X. Qiu, C. Bruda, Chem. Mater. 20, 2629 (2008).

(59) M. Okada, Y. Yamada, P. Jin, M. Tazawa, K. Yoshimura, Appl. Surf. Sci. 254, 156 (2007).

(60) T-S. Yang, M.Ch. Yang, Ch.-B. Shiu, W.-K. Chang, M-Sh. Wong, Appl. Surf. Sci. 252, 3729 (2006).

(61) M-Ch. Yang, T.-S. Yang, M.-Sh. Wong, Thin Sol. Films, 469/470, 1 (2004).

(62) R. Wang, K. Hashimoto, A. Fujishima, M. Chikuni, E. Kojima, A.Kitamura, M.

Shimohigoshi, T. Watanabe, Nature 388, 431 (1997).

(63) A. Borrás, A. Barranco, A.R. González-Elipe, Langmuir 24, 8021 (2008).

(64) Q. Li, J.-K. Shang, J. Am. Chem. Soc. 91, 3167 (2008).

(65) J. Premkumar, Chem. Mater. 16, 3980 (2004).

(66) O. Carp, C.L. Huisman, A. Reller, Prog. Sol. State Chem. 32, 33 (2004).

(67) J. Zhang, Q. Xu, Z.Feng, M. Li, C. Li, Angew. Chem. Int. Ed. 47, 1766 (2008).

Supporting information

Chemical state of nitrogen and visible surface and Schottky barrier driven photo-activities of N-doped TiO2 thin films

*P. Romero- Gómez[1], V. Rico[1], A. Borrás,[1] A. Barranco[1], J.P. Espinós[1], J. Cotrino[1,2], A.R. González-Elipe[1]**

1. Instituto de Ciencia de Materiales de Sevilla (CSIC-Univ. Sevilla). Avda. Américo Vespucio 49. 41092 Sevilla (Spain). http://www.sincaf-icmse.es

2. Departamento de Física Atómica, Molecular y Nuclear. Universidad de Sevilla. Avda. Reina Mercedes 49, 41012 Sevilla. Spain.

Supporting information S8

A) Comparison of the N1s photoemission spectra of samples A-F, before and after being subjected to a mild Ar+ sputtering treatment. It is apparent that neither the shape nor the intensity of the curves change significantly after sputtering.

B) From left to right: Ti 2p, O1s and C1s photoemission spectra of samples A-F

Supporting information S9

Fitted N1s photoemission spectrum of a N-doped TiO_2 thin film prepared by PECVD with a plasma of oxygen and TDEAT as titanium precursor.

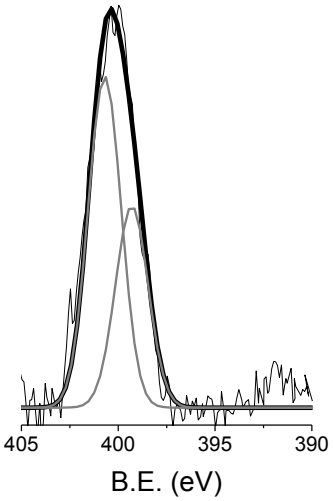

Capítulo 5

El problema de la intercara anatasa-rutilo

Enhanced Photoactivity in bilayer films with buried Rutile-Anatase heterojunctions

P.Romero-Gomez, A. Borras, A. Barranco, J.P. Espinos, A. R. Gonzalez-Elipe

Nanotechnology on Surfaces Laboratory. Materials Science Institute of Seville.

CSIC – University of Seville.

Avd. Américo Vespucio 49, 41092, Spain

Fax: (+)34954460665

E-mail: arge@icmse.csic.es

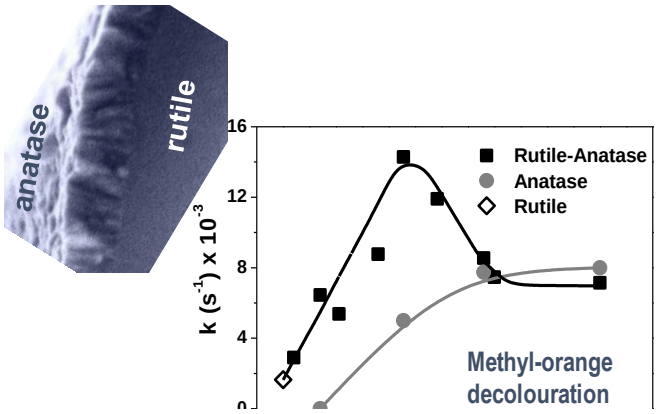

Title: Enhanced Photoactivity in bilayer films with buried Rutile-Anatase heterojunctions

Authors ***P. Romero-Gomez****, A. Borras, A. Barranco, J.P. Espinos, A. R. Gonzalez-Elipe*

Source: (will be filled in by the editorial staff)

D.O.I. *10.1002/cphc.201000734*

Enhanced Photoactivity in bilayer films with buried Rutile-Anatase heterojunctions

Pablo Romero-Gomez, Ana Borras, Angel Barranco, Juan P. Espinos and Agustin R. Gonzalez-Elipe*

Nanotechnology on Surfaces Laboratory. Materials Science Institute of Seville.

CSIC – University of Seville.

Avd. Américo Vespucio 49, 41092, Spain

Fax: (+)34954460665

E-mail: arge@icmse.csic.es

Herein, we study the photoactivity of anatase–rutile bilayer thin films consisting of an anatase overlayer of variable thickness from some tenths to some hundred nanometers deposited onto a rutile thin film. As references single anatase layers of equivalent thickness were deposited onto silicon. All the films were characterized by X-ray diffraction (XRD), scanning electron microscopy (SEM) and Raman spectroscopy. The photoactivity of the samples was assessed by following the evolution with the UV illumination time of both the wetting angle on the thin film surface and the decoloration of a dye in a water solution. While a similar efficiency is found for the first type of experiments irrespective of the anatase thickness, in the second type a maximum in the photoactivity is found for a thickness of the anatase layer of about 130 nm. This enhanced photoactivity in bilayer systems with a buried anatase–rutile heterojunction is related to the formation of different Schottky potential barriers in the anatase layer, depending on its thickness and the substrate (i.e. rutile or SiO_2) where it is deposited.

Introduction

Although the outstanding photoactivity properties of TiO_2 are known for more than forty years,[1] investigations in this area are still an active field of research because of the applications of this oxide as a photocatalyst for the removal of wastes, photo-anodes in photoelectrochemical cells, as self-cleaning coatings, for the development of hybrid photovoltaic cells, or as optical filters and optically active nanocomposites.[2] One of the most widely accepted issues for these applications is that the anatase phase of this oxide presents a higher photoactivity than the rutile.[3] It is also well known that powder materials consisting of a mixture of anatase and rutile (a classical reference material is the Degussa P25, a mixture of 20% rutile and 80% anatase[4]) depict higher photoactivities than those of pure anatase.[5] Recently, Zhang et al.[6] attributed the maximum photoactivity found for particulate systems formed by rutile core particles with anatase nanoparticles decorating their surface to the formation of surface-phase heterojunctions that would produce a spatial charge separation in the region in contact with the reaction medium. A different bilayer thin film system consisting of strips of anatase deposited on rutile with both fractions exposed to the reaction medium was studied by Kawahara et al.[7] The enhancement in photocatalytic activity found here was also attributed to the heterojunction formed between the two phases in contact with the reaction medium. However, in these previous studies the heterogeneity of the particle size distribution, the insufficient definition of the anatase/rutile interface contact areas or the effect of buried anatase/rutile interfaces may hamper a straightforward explanation of the photoactivity enhancement. Trying to unravel some of these open questions, herein we study the photo-activity of bilayer thin films formed by a thick rutile bottom layer with an anatase layer of variable thickness deposited on its surface. We investigated two different manifestations of the photo-activity of TiO_2. Firstly, we examine the efficiency for discoloring a dye solution where the illuminated thin film immersed in the solution is acting as the effective photoactive medium. Although the purpose of the present work is not carrying out a thorough study of the photo-catalytic activity of the bilayer films, a simple test of this kind should provide information about any difference in photo-activity related with the photon activation of the whole anatase layer. Secondly, we explore the efficiency for transforming the wetting properties of the surface of these double layer materials from partially hydrophobic into superhydrophilic when they are illuminated with UV light. This transformation,

originally discovered by Wang et al.,[2d,8] relates to photo-activity phenomena that are restricted to the utmost atomic layer of TiO_2 and that, consequently, should not be directly related with the thickness and electrical properties of the films.[9] Effectively, our results have shown that while the kinetics of wetting angle variations are little affected by the thickness of the anatase layer, an enhanced dye decoloration appears for the bilayer films with their buried rutile-anatase interface at a critical distance from the external surface of anatase. This different behaviour sustains that in anatase-rutile systems potential barrier effects may be involved in the control of the formation of electron-hole pairs in the interior of anatase and their migration to the surface.

Results and Discussion

Thin film characterization

To study how the thickness of the anatase layer ($d_{anatase}$) influences the photo-activity of the rutile-anatase bilayers (RABs), we varied such parameter in the range between some tenths and 350 nm. Single anatase layers (SALs) with a thickness varying within the same range were also studied for comparison. Figure 5.1 shows the microstructure of SALs deposited on Si(100) and of the anatase layers in a series of RABs for different anatase thicknesses. The SALs depicted a columnar morphology (c.f., Fig. 5.1 (left)) and a refractive index of about. 2.[10] The SEM micrographs of the RABs in Fig. 5.1 (right) show the formation of columnar anatase layers on a sharp interface with the rutile substrates.

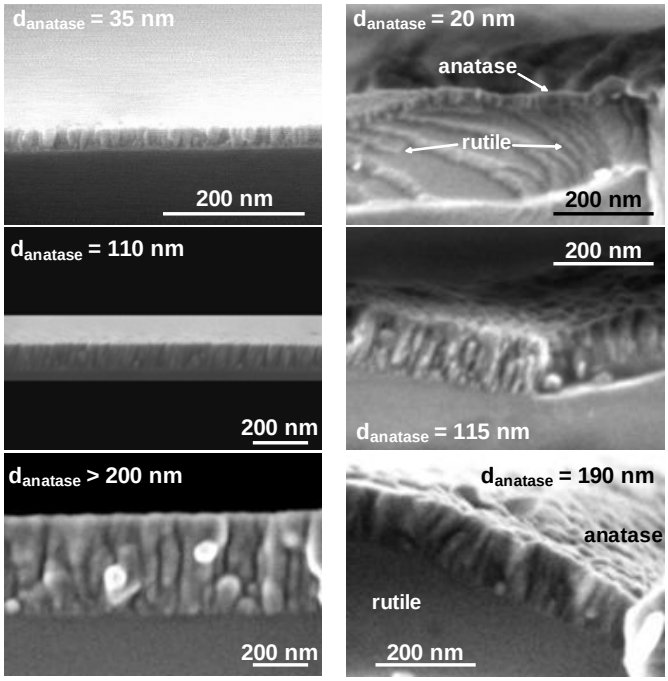

Figure 5.1. Cross section SEM micrographs of a series of anatase thin films deposited on Si(100) (left) and of the anatase layers in the rutile-anatase bilayer thin films (right). The thicknesses of the anatase layers are indicated by labels. Due to the high compactness and very low electrical conductivity of the rutile layer no details of its microstructure are observed.

The XRD diagrams corroborate that the crystal structure of the bilayers consists of the anatase and rutile phases of TiO_2. Figure 5.2 shows the X-ray diffraction diagrams of selected RABs and SALs for different thickness of the anatase layer. The diagrams of pure rutile and anatase ($d_{anatase}$ = 300 nm) thin films are included for comparison. The diagrams of the films with a thickness of the anatase comprised between 20 and 115 nm were recorded with the diffractometer working in a glancing angle configuration. Even if a quantitative evaluation of the peak intensities is not possible because of this recording configuration, it can be appreciated that the relative intensity of the anatase features increases with the nominal thickness of this phase as we have further analysed earlier.[10c] The crystallinity of the anatase layer has been also assessed by measuring the size of the crystal domains by means of the Sherrer formula applied to the (101) peak appearing at approximately 25º. We found that the size values of the crystalline domains of anatase increase with the thickness of this phase, particularly for the thinnest films where the approximate size of crystal domains was in the order of 20 nm or less. This size increases to reach values of the order of 100 nm for anatase layers thicker than 150 nm. No significant difference in crystallinity was found when comparing SAL and RAB

thin films with a similar thickness of the anatase layer, although differences in texture development[10c] can be appreciated when looking to the relative intensities of the peaks in the XRD diagrams in Figure 5.2 [see for example the relatively higher intensity of (004) (2θ ~ 37.8º) planes in the SAL thin films].

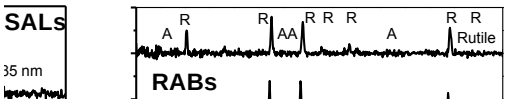

Figure 5.2. Selected XRD diagrams of a series of anatase thin films deposited on Si(100) (left) and of the anatase layers in the rutile-anatase bilayer thin films (right). The thicknesses of the anatase layers are indicated by labels. The pattern of a rutile thin film is also included for comparison.

Further evaluation of the structure of the RAB and SAL thin films was carried out by Raman spectroscopy. Figure 5.3 gathers the series of Raman spectra corresponding to selected films. For the RAB thin films it is apparent that with the nominal layer thickness of the anatase layer the relative intensity of the anatase peaks (i.e., 150, 395, 515 and 638 cm^{-1}) increases in detriment to those of rutile (i.e., 328, 585, 680 and 815 cm^{-1}).[11] All the SAL thin films present the typical spectrum of anatase, although small differences in relative intensity can be appreciated when comparing the different peaks of the spectra as a function of the layer thickness. Very likely, these small differences can be associated with the decrease in crystallilnity observed by XRD for the thinnest anatase layers. The RABs were also analyzed by XPS (data no shown). The surface composition, basically TiO_2 with the typical traces of contaminating carbon because of the handling of samples in air, was equivalent for all the samples irrespective of the anatase layer thickness.

SALs RABs

Figure 5.3. Selected Raman spectra of a series of anatase thin films deposited on Si(100) (left) and of the anatase layers in the rutile-anatase bilayer thin films (right). The thicknesses of the anatase layers are indicated by labels.

Photo-activity of anatase/rutile bilayer films

A first photo-activity test consisted of the photo-induced discoloration of a dye molecule. We must mention that although discoloration is not equivalent to full photo-catalytic degradation (i.e. mineralization), for the purposes of the present work we consider that bleaching of the solutions responds directly to the interaction of the reactant with electron-hole pairs produced by light excitation of the oxide. The experimental set-up was specially designed to verify the activity of thin film samples (further information in Experimental Section).[12] The dye decolouration under these conditions is usually taken as a semiquantitative measurement of the photo-catalytic activity of TiO_2 systems.[13] Figure 5.4, Top shows the results of the photo-activated decolouration process of methyl orange dye solutions as a function of irradiation time, corrected by the values in a blank experiment without TiO_2 thin films (see the original curves before correction and the equivalent corrected curves for single anatase layers in Figure 5.S1 in the Supporting Information). These curves reveal a strong dependence of the photoactivity of the films with the thickness of the anatase layer. Trying to quantify this dependence, and just for comparative purposes, we adjusted the decay curves to exponential functions of the type exp(-kt) (i.e. a pseudo first order kinetic typical of a Langmuir-Hinshelwood mechanism[13]). From the representations in Fig. 5.4, top plotting the natural logarithm of the corrected concentrations, the kinetic constants correspond to the slope of the fitting lines. The dependency of the kinetic constants k on the anatase thickness is represented in Fig. 5.4, Bottom. For the SALs a direct correlation is found between their thickness and k up to reach a steady-state value for $d_{anatase} \geq 200$ nm. Steady-state photoactivity around the same anatase thickness is also found for the

RABs. However, for $d_{anatase} < 200$nm, the activity profiles are different for the SALs and the RABs. In agreement with previous studies,[12,14] the photoactivity of the SALs increases with the thickness. By contrast, the series of RABs present a maximum photo-activity for a $d_{anatase} \approx 130$ nm, while the photoactivities for $d_{anatase} < 130$ nm are always higher for the RABs than for the SALs. Finally, the photoactivity of a rutile layer is comparatively negligible.

Figure 5.4. Top) Photo-activated decolouration curves of the methyl orange dye as a function of the illumination time for different anatase thickness in the RABs. Results for anatase (d > 200 nm) and rutile (d ~ 400 nm) films are shown as references. Bottom) Plot of the kinetic constant k as a function of the anatase thickness for the RAB, SAL and rutile thin films.

Another type of photo-activity tests refers to the study of the wetting angle as a function of the irradiation time. In previous studies we have shown that both amorphous and crystalline layers of TiO_2 are able to induce the transformation of its wetting properties under UV light irradiation[12] even if the former are completely inactive for decoloration of dye solutions or any other photo-catalytic reaction. Recently[9,12] we have shown that light induced wetting angle modification is a photo-induced process affecting to the utmost surface layers of the oxide and does not require the migration up to the surface of photo electrons and holes generated in the inner zones of the material. To differentiate these two TiO_2 mediated photo-activation processes we have coined the terms surface and Schottcky barrier driven photo-activities.[9] Recently, we have also shown that the surface crystallinity and roughness of anatase films may also have some

influence on the surface wetting transformation.[15] Wetting angle experiments carried out here with the SAL and RAB systems confirm a distinct behavior with respect to that found during the photodecoloration of dyes. Figure 5.5, top shows that the time evolution curves of the wetting angle of irradiated RAB thin films are quite similar, while that corresponding of pure rutile thin film indicates that this material possesses less surface photo-activity. A fitting of these curves and those measured with the set of SAL thin films (cf. Fig. 5.S2) with a first order kinetic function (i.e., $\exp(-k_2t)$) permits one to calculate a series of k_2 constant values for quantification of the surface photo-activity of the different analyzed thin films. The set of values reported in Figure 5.5, bottom shows that, except for the thinnest and less crystalline anatase layer in the RAB films, the photoefficiency for wetting angle variations is similar for all anatase surfaces, irrespective of its actual thickness (note that different initial constant wetting angles can be found for the different samples studied, a feature that we have explained by using surface roughness arguments[15]). This almost constant surface photoactivity contrasts with the tendencies found for the decoloration processes depicted in Fig. 5.4 where a maximum for d≈130 nm in RAB points out that the existence of a buried rutile-anatase heterojunction plays an important role in this process.

In powder systems,[4,5,16] and thin films with agglomerated crystallites of rutile and anatase,[17] an enhancement in photocatalytic activity has been usually related with the development of some junction points in contact with the reaction medium that would act as photocatalytic “hot spots”. It is likely that the behaviour of such “hot spots” is similar to that reported by Kawahara et al.[7] for strips of anatase deposited on rutile. Since in our RAB systems the buried rutile-anatase heterojunction is not exposed to the reaction medium, the enhancement in the dye decoloration photoactivity for $d_{anatase}$=130 nm must be accounted for by other grounds. The singular character of this behaviour, particularly in light of the rather constant surface photoactivity (i.e., wetting angle variations under irradiation) determined for all anatase terminated systems, supports that surface potential barrier factors should be taken into account to explain the difference decoloration efficiencies reported in Fig. 5.4. Before going into this discussion, it is pertinent to stress that in first instance and according to the observed phenomenology, wetting angle variation upon light illumination does not depend on the anatase layer thickness and that, in line with previous publications,[9,12] it is reasonable to assume that it is restricted to light excitation of the utmost atomic layers of samples.

Figure 5.5. Top) Evolution with the illumination time of the wetting angle measured on the surface of anatase surfaces in RABs thin films with different thickness of the anatase layer. Results for pure anatase (d > 200 nm) and rutile (d ~ 400 nm) thin films are included as references. Bottom) The kinetic constant k_2 as a function of the anatase thickness for the RAB, SAL and rutile thin films.

The decoloration of the dye solution, taken as representative of photocatalytic processes,[14] has been shown to be quite dependent on the anatase layer thickness and therefore seems to respond to a photoactivation process involving several few tenths of nanometer thickness (i.e., a Schottky barrier driven process as discussed earlier for thick TiO_2 thin films with incorporated nitrogen).[9a] Rutile and anatase are wide band gap semiconductors with, respectively, 3.0 and 3.2 eV gap energies and work functions of 4.9 and 5.1 eV.[14] It is also known that the Schottky potential barrier developed when TiO_2 is brought in contact with an external medium is higher and extends through a larger zone in anatase than in rutile where the photogenerated carriers also have shorter lifetimes.[18] These differences cause bulk recombination of electron and holes to be prevalent in rutile where photoactivity is usually smaller than in anatase (c.f., Figs. 5.4 and 5.5). In our case, the compact and resistive character of the rutile layer prepared by annealing at high temperatures must also contribute to decrease its photo-activity as evidenced in Fig. 5.4. To account for the evolution of decoloration photoactivity, we propose that the slope of the potential barrier formed at the anatase/liquid interface is

higher as the layer thickness decreases, making that the electrical field developed in the anatase layer contribute to mitigate the recombination of electron-hole pairs.

This would render a lower recombination rate of the excitons and, therefore, an increase in the photoactivity of the system as observed for a layer thickness of 130 nm. This positive effect would be progressively hampered for $d_{anatase} < 130$ nm due to the smaller thickness of the irradiated zone of anatase. A way to sustain the previous model would be to perform valence band photoemission experiments to ascertain the magnitude of the band bending of the system. Unfortunately, trying to carry out these experiments we realized that determination the work function of the system was hampered by the insulating character of the samples, which prevents any clear definition of the origin of binding energies.

It must be stressed that these arguments do not hold for the evolution of wetting angle, a surface photoactivity process, where just the electron-hole excitation of the utmost atomic layers would be sufficient to modify the surface character of the anatase and where the small differences in crystallinity (cf. Figs. 5.2 and 5.3) and/or an incomplete formation of a continuous anatase layer for the samples with the thinnest film of this phase would be a second order effect to be considered when trying to correlate this property with some film characteristics.

Conclusion

We have demonstrated that the dye decoloration photoactivity in rutile-anatase bilayer films with a buried rutile-anatase heterojunction reach a maximum for an anatase layer thickness of ~130 nm. This enhanced photoactivity has been explained by assuming a higher slope for the Schottky potential barrier formed at the external anatase layer. Similar effects must likely appear in powder systems, although in that case the contribution to the photoactivity of hot-spots at the surface and/or heterojuntion induced separation of photoelectrons and photoholes cannot be discarded.[6,7,16,17] Our results have also shown that buried rutile-anatase heterojunctions should be taken into account for designing highly photoactive TiO_2. This explanation scheme does not apply for the surface photoactivity phenomena as evidenced by the similar evolution of the wetting angles upon irradiation where the existence of a buried rutile-anatase heterojunction is irrelevant for the control of photo-activity.

Further experimental and more thorough theoretical calculations should contribute to describe accurately these effects.

Experimental Section

Anatase TiO_2 thin films with a thickness comprised between some tenths and 350 nm were prepared at 250 ºC by plasma enhanced chemical vapour deposition (PECVD)[10] in a plasma reactor with a remote configuration by using oxygen as plasma gas. Titanium tetra isopropoxide (TTIP) was used as precursor. Deposition was carried out either on silicon wafers (Si(100)) or on ~ 400 nm rutile films. The structure and microstructure of the single anatase layers (SALs), i.e. deposited on silicon wafers, and the rutile-anatase bilayers (RABs) films were analyzed by XRD, Raman and SEM. All the anatase films either deposited on silicon or on rutile, were annealed at 450 ºC for three hours before their analysis. This treatment aims at improving the electrical contact between the anatase and rutile phases and at minimizing any possible resistive losses. The silicon substrates were covered by a SiO_2 thin layer (i.e., approximately 20-30 nm forming a SiO_2/Si structure) that increased in thickness after deposition of the TiO_2 by plasma methods and the posterior annealing. The rutile layers were obtained by annealing in air at 1150 ºC for 3 hours amorphous TiO2 films prepared by PECVD. The resulting layers were quite compact and had a very high electrical resistivity.

The films were characterized by X-ray diffraction in a Siemens D5000 Spectrometer working either in the Bragg-Brentano or at glancing angle (at 0.5 º, for anatase layers thinner than 100 nm) configurations and using the Cu Kα radiation as excitation source. Cross sections views of the films were taken with a Hitachi S5200 field emission microscope working at 5.0 keV. Raman spectra were also used to characterize the single and bilayer films. Raman spectra were collected in a LabRAM HR High Resolution 800 UV Confocal Raman Microscope. For the measurements a green laser (He-Ne 532.14 nm), 600 line/mm, 100X objective, 20 mW and 100μ pinhole, was used.

The experimental set-up for the photo-activity test was specially designed to verify the activity of thin film samples[12] and consisted of a small cell made of quartz (total volume 3 cm^3) where 2 cm^3 of a 3.5 10^{-5} M solution of methyl orange dye (C14H14N3NaO3S purchased from Aldrich) was placed together with the thin film samples deposited on silicon (1 x 0.8 cm^2). It is important to remark that water solutions of this dye are stable

under visible light irradiation even in the presence of TiO_2. In our experiments we only observed decolouration when the UV lamp was switched on. For this purpose, the system was illuminated with a Xe lamp (150 W) supplying a total light intensity of 1.8 W cm^{-2} at the cell position, with approximately 0.3 W cm^{-2} for photons with $\lambda < 380$ nm. With this system, it was possible to monitor the spectra of the dye as a function of the irradiation time by means of two optical fibers located at the two sides of the cell. The maximum uncertainty in the determination of the dye concentration in this experiment is about $5x10^{-6}$ M. In Figure 5.4 we represent the ratio between the dye concentration for different irradiation times C corrected by the initial concentration of the dye, C0 and corrected, i.e. divided, by the same ratio for the blank experiment (C/C0)blank. The uncorrected curves are gathered in Figure 5.S1 in the Supporting Information.

Measurement of water contact angle was carried out by the Young method by dosing small droplets of deionized and bidistilled water on the surface of the illuminated samples. In the experiments where the contact angle variation was determined as a function of the illumination time, a metal foil acting as a shutter was used to close and open the lamp output. All wetting angle measurements within a given experiment were taken after illumination for successive periods of time. Therefore, the time scale in the plots refers to the accumulative illumination of the samples. The error bar in the determination of the water contact angle is about 10º depending on the sample position. In the course of this investigation it was noticed that the "as-prepared" bilayer and single layer anatase thin films were more hydrophilic than the same samples a given time after their preparation. Therefore, the reported results correspond to samples that were stored in dark in a desiccator, at least for two months, before testing their photo-activity. Illumination of the samples was carried out with a Xe discharge lamp with photon intensity at the position of the samples of 2 Wcm-2 for the complete spectrum. An infrared filter (i.e., a water bath) was kept between the lamp and the samples to prevent any possible heating by the infrared radiation.

XPS spectra of the films were recorded on a VG ESCALAB 210 spectrometer working under energy transmission constant conditions. The Mg Kα line was used for excitation of the spectra. They were calibrated in binding energy (BE) by referencing to the C1s peak due to contamination taken at 284.6 eV.

Acknowledgements

This work was funded by the EU (NMP3-CT-2006-032583) and the Spanish MICINN (MAT2010-21218, MAT2010-18447 and CONSOLIDER 2010-CSD2008-00023) and Junta de Andalucia (P09-TEP5283 and CTS-5189).

Keywords: Thin layers (inorg.) · Photocatalysis · Crystal growth · Surface · Raman spectroscopy

(1) a) A. Fujishima, K. Honda, *Nature* **1972**, *238*, 37; b) M. Fujihira, Y. Satoh, T. Osa *Nature* **1981**, *293*, 206; c) O. Carp, C. L. Huisman, A. Reller *Progress Solid State Chemistry* **2004**, *32*, 33; d) P.V. Komat *Chem. Rev.* **1993**, *93*, 267.

(2) a) O´Regan, M. Gratzel *Nature* **1991**, *353*, 737; b) Mills, A.; R. H. Davies, D. Worsley *Chem. Soc. Rev.* **1993**, *22*, 417; c) M. R. Hoffmann, S. T. Martin, W. Y. Choi, D. W. Bahnemann *Chem. Rev.* **1995**, *95*, 69; d) R. Wang, K. Hashimoto, A. Fujishima, M. Chikuni, E. Kojima, A. Kitamura, M. Shimohigoshi, T. Watanabe *Nature* **1997**, 388, 431; e) H. Tada, M. Tanaka *Langmuir* **1997**, *13,* 360; f) M. Gratzel *Nature* **2001**, *414*, 338; g) T. Bak, J. Nowotny, M. Rekas, C.C. Sorrell *Intern. J. Hydrogen Energy* **2002**, *27*, 991; h) S. In, A. Orlov, R. Berg, F. Garcia, S. Pedrosa-Jimenez, M.S. Tikhov, D.S. Wright, R.M. Lambert *J. Am. Chem. Soc.* **2007**, *129*, 13790; i) F. Parrino, A. Ramakrishnan, H. Kisch *Angew. Chem. Int. Ed.* **2008**, *47*, 7107; j) A. Borras, A. Barranco, A. R. Gonzalez-Elipe *Langmuir* **2008**, *24*, 8021; k) J. R. Sanchez-Valencia, A. Borras, A. Barranco, V. J. Rico, J. P. Espinos, A. R. Gonzalez-Elipe *Langmuir* **2008**, *24*, 9460; l) Y.Y. Lin, T.H. Chu, Ch-W. Chen, W.F. Su *Appl. Phys. Lett.* **2008**, *92*, 053312.

(3) a) J. J. Augustynski, *Electrochim. Acta* **1993**, *38*, 43; b) R. Ichikawa, R. Doi, *Thin Sol. Films* **1997**, *292*, 130; c) J. Ovenstone, K. Yanagisawa, *Chem. Mater.* **1999**, *11*, 2770; d) R. Molinari, L. Palmisano, M. Schiavello, *J. Phys. Chem. B* **2004**, *108*, 3303; e) J.F. Zhu, W. Zheng, B. He, J.L. Zhang, M. J. Anpo, *Mol. Catal. A* **2004**, *216*, 35.

(4) a) P.A.M. Hotsenpiller, J.D. Bolt, W.E. Farneth, J.B. Lowekamp, G.S. Rohrer *J. Phys. Chem. B* **1998**, *102*, 3216; b) D.C. Hurum, K.A. Gray, T. Rajh, M.C. Thurnauer *J. Phys. Chem. B* **2005**, *109*, 977.

(5) a) V. Loddo, G. Marci, C. Martin, L. Palmisano, V. Rives, A. Sciafani *Applied Catal. B. Environemental* **1999**, *20*, 29; b) A.L. Linsebigler, G. Lu, J.T. Yates *Chem Rev.* **1995**, *95*, 735; c) S. Bakardjieva, J. Subrt, V. Stengl, M.J. Dianez, M.J. Sayagues *Langmuir* **2005**, *58*, 193; d) S. Bakardjieva, V. Stengl, L. Szatmary, J. Subrt, J. Lukac, N. Murafa, D. Niznansky, K. Cizek, J. Jirkovsky, N. Petrova *J. Mater. Chem.* **2006**, *16*, 1709; e) L. Chen, M.E. Graham, G. Li, K. A. Gray *Thin Sol. Films* **2006**, *515*, 1176.

(6) J. Zhang, Q. Xu, Z. Feng, M. Li, C. Li *Angew. Chem. Int. Ed.* **2008**, *47*, 1766.

(7) T. Kawahara, Y. Konishi, H. Tada, N. Tohge, J. Nishii, S. Ito, *Angew. Chem. Int. Ed.* **2002**, *41*, 2811.

(8) a) R. Wang, K. Hashimoto, A. Fujishima, M. Chikuni, E. Kojima, A. Kitamura, M. Shimohigoshi, T. Watanabe *Adv. Mater.* **1998**, *10*, 135; b) M. Miyauchi, A. Nakajima, A. Fujishima, K. Hashimoto, T. Watanabe *Chem. Mater.* **2000**, *12*, 3.

(9) a) P. Romero-Gomez, V. Rico, A. Borras, A. Barranco, J. P. Espinos, J. Cotrino, A. R. Gonzalez-Elipe *J. Phys. Chem. C* **2009**, *113*, 13341; b) A. Borras, C. Lopez, V. Rico, F. Gracia, A. R. Gonzalez-Elipe, E. Richter, G. Battiston, R. Gerbasi, N. McSporran, G. Sauthier, E. Gyorgy, A. Figueras *J. Phys. Chem. C* **2007**, *111*, 1801.

(10) a) A. Borras, J. Cotrino, A.R. Gonzalez-Elipe *J. Electrochem. Soc.* **2007**, *154*, 152; b) F. Gracia, J.P. Holgado, A.R. González-Elipe *Langmuir* **2004**, *20*, 1688; c) A. Borras, J.R. Sanchez-Valencia, R. Widmer, V.J. Rico, A. Justo, A.R. Gonzalez-Elipe *Cryst. Growth Design* **2009**, *9*, 2868.

(11) a) J. A. Dood, S. J. Lipson, D. J. Flanagan, W. A. M. Blumberg, J. C. Person, B. O. J. Green *Chem. Phys.* **1991**, *94*, 4301, b) T. Ohsaka,; Izumi, F.; Fujiki, Y. J. *Raman Spectrosc.* **1978**, *7*, 6.

(12) V. Rico, P. Romero, J.L. Hueso, J.P. Espinos, A.R. Gonzalez-Elipe, *Catal. Today* **2009**, *143*, 347.

(13) M.R. Hoffmann, S.T. Martin, W. Choi, D.W. Bahnemann *Chem. Rev.* **1995**, *95*, 69.

(14) M. Takahashi, K. Tsukigi, T. Uchino, T. Yoko, *Thin Sol. Films* **2001**, *388*, 231.

(15) A. Borras, A. R. Gonzalez-Elipe *Langmuir* **2010**, *26*, 15875–15882

(16) a) D.C. Hurum, A.G. Agrios, K.A. Gray, T. Rajh, M.C. Thurnauer, *J. Phys. Chem. B* **2003**, *107*, 4545; b) D.C. Hurum, A.G. Agrios, S.E. Crist, K.A. Gray, T. Rajh, M.C. Thurnauer, *J. Electron. Spectrosc. Relat. Phenom.* **2006**, *150*, 155.

(17) G. Li, L. Chen, M.E. Graham, K.A. Gray, *J. Mol. Catal. A* **2007**, *275*, 30.

(18) a) C. Colbeau-Justin, M. Kunst, D. Huguenin, *J. Mater. Sci.* **2003**, *38*, 2429; b) G. Xiong, R. Shao, T.C. Droubay, A.G. Joly, K.M. Beck, S.A. Chambers, W.P. Hess *Adv. Funct. Mater.* **2007**, *17*, 2133.

(19) A.R. Gonzalez Elipe, G.Munuera, J.Soria, *J. Chem. Soc. Faraday I.* **1979**, *75*, 748.

Supporting information

Enhanced Photoactivity in bilayer films with buried Rutile-Anatase heterojunctions

*Pablo Romero-Gomez, Ana Borrás, Angel Barranco, Agustín R. González-Elipe**

Nanotechnology on Surfaces Lab.; Instituto de Ciencia de Materiales de Sevilla (CSIC-Univ. Sevilla). Avda. Américo Vespucio 49. 41092 Sevilla. Spain.

Figure 5.S1.

Representation of the concentration of methyl orange dye as a function of the illumination time for selected experiments with anatase thin films deposited on silicon wafers with the indicated layer thickness. Exponential fitting curves are included in the plot.

Figure 5.S2.

Evolution of the water contact angle measured for anatase thin films of different thickness under UV light irradiation. The results on pure anatase are also included for comparison.

Capítulo 6

Síntesis y propiedades de capas nanoestructuradas de ZnO

J. Phys. Chem. C, 2010, 114 (49), pp 20932–20940

Tunable Nanostructure and Photoluminescence of Columnar ZnO Films Grown by Plasma Deposition

Pablo Romero-Gómez[a], Johann Toudert[a],*, Juan R. Sánchez-Valencia[a], Ana Borrás[a], Angel Barranco[a] and Agustín R. Gonzalez-Elipe[a]

[a] Instituto de Ciencia de Materiales de Sevilla (CSIC-Universidad de Sevilla) c/ AmericoVespucio 49, 41092 Sevilla, Spain

*Author to whom all correspondence should be sent: johann.toudert@gmail.com

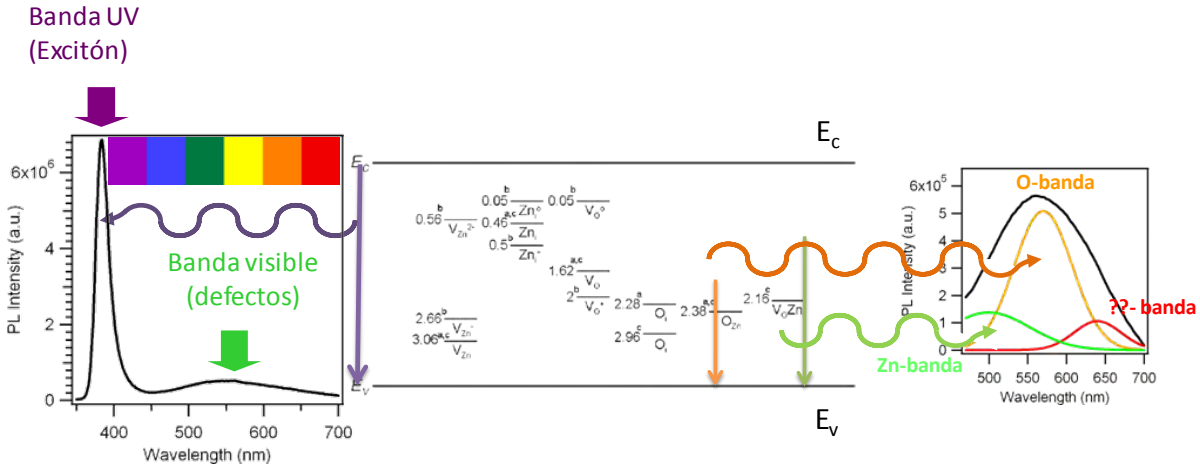

Title: Tunable Nanostructure and Photoluminescence of Columnar ZnO Films Grown by Plasma Deposition.

Authors **Pablo Romero-Gómez**, Johann Toudert, Juan R. Sánchez-Valencia, Ana Borrás, Angel Barranco and Agustín R. Gonzalez-Elipe

Source**:** *J. Phys. Chem. C*, 2010, 114 (49), pp 20932–20940
D.O.I. 10.1021/jp103902u

Tunable nanostructure and photoluminescence of columnar ZnO films grown by plasma deposition

Pablo Romero-Gómez[a], Johann Toudert[a,*], Juan R. Sánchez-Valencia[a], Ana Borrás[a], Angel Barranco[a] and Agustín R. Gonzalez-Elipe[a]

[a] *Instituto de Ciencia de Materiales de Sevilla (CSIC-Universidad de Sevilla) c/ Americo Vespucio 49, 41092 Sevilla, Spain*

**Author to whom all correspondence should be sent:* johann.toudert@gmail.com

Nanoporous ZnO thin films presenting a tunable nanostructure and photoluminescence (PL) were grown by plasma enhanced vapor deposition on surface oxidized Si substrates. These films consist of c-axis oriented wurtzite ZnO nanocolumns whose topology, crystallinity and PL can be tuned through the substrate temperature (varied in the 300 K – 573 K range) and nature of the plasma assistance (pure O_2, O_2/Ar, O_2/H_2 or O_2/N_2 mixture). In particular, these processing parameters influence the intensity of the UV and visible PL bands of the films, related to excitonic and defective radiative transitions respectively. Increasing the substrate temperature enhances the UV PL and rubs out the visible PL due to the increase of grain size and the removal of interstitial defects. Additional tuning of the intensity ratio between the UV and visible bands can be done by controlling the film thickness. A decrease of the UV PL is observed when the films go thicker, an effect that is likely to be linked to the microstructure of the films rather than to their crystallinity that is improved upon increasing of the film thickness, as seen from PL spectroscopy and XRD measurements. Indeed, a gradient of stress, decreasing from the substrate to the surface, is evidenced and related to a concentration gradient of interstitial defects. The drawbacks of the thickness effect, which prohibits growing thick films with a high optical quality, can be bypassed by growing the films in a O_2/H_2 plasma.

1. Introduction

Due to its wide band gap (~3.37 eV at room temperature) and high exciton energy (60 meV), ZnO presents an ultraviolet luminescence band[1] which is of prime interest for the realization of electroluminescent diods[2] or room temperature UV lasers[3]. In addition to the UV band related to excitonic radiative recombinations, other luminescence bands have been observed in the visible[1,4] and their existence has been ascribed to defect-related energy levels between the conduction and valence bands[4]. Depending on the fabrication conditions[5], native defects (such as oxygen or Zn vacancies[6] and interstitials[7] and oxygen antisites[8]) or extrinsic defects (such as nitrogen[9] or metal[10,11] heteroatoms) can be introduced into the network and thus lead to the control of the electronic structure of the material and consequently to the tailoring of its luminescence response in the visible range. Defects can be located in the volume or at the surface of the material in a proportion that is likely to be controlled by the synthesis process. Surface defects, which are sensitive to the chemical environment of the material[12], make ZnO a potential candidate for the realization of chemical[13] or gas[14] sensors converting chemical information into electrical[15] or optical signals[16]. Indeed, the existence of a correlation between the intensity of the visible and UV photoluminescence bands has been evidenced[17], thus suggesting the existence of a certain interaction between excitons and surface defects[18]. A particularly high chemical sensitivity is thus expected in the case of nanostructured materials, in which the surface-to-volume defect ratio may be high. Therefore, much attention has been paid in the last decades to the fabrication and structural characterization of ZnO nanostructures such as nanoparticles[19], nanoribbons[20], nanowires[21] and nanorods[22]. Nanorods can be grown perpendicularly to various substrates in the form of densely packed assemblies of nanostructures presenting a high aspect ratio that provides a high surface to volume ratio.

Among the chemical or physical fabrication routes used to grow ZnO, such as electrodeposition[23], pulsed laser deposition[24], hydrothermal[25], MOVPE[26] or VLS growth[27], chemical vapor deposition has allowed the catalyst-free growth of ZnO nanocolumnar films[28,29] and nanorods[30] presenting luminescence bands either in the ultraviolet or visible ranges. Alternatively, it has been shown that by choosing appropriate precursors and plasma conditions, the use of plasma assistance during

the growth of oxide materials by plasma-enhanced chemical vapour deposition (PECVD) is an efficient way to control their composition and nanostructure[31]. However, although some works have been devoted to the PECVD growth of nanocolumnar TiO_2[31,32] thin films, less has been done in this domain concerning ZnO[30,33,34]. Liu et al.[30] investigated the PECVD growth of ZnO nanorods on various crystalline substrates and presented a two-step method for growing ZnO nanorods perpendicular to sapphire substrates with a good optical quality. The growth was performed at 975 K in an O_2 plasma and the role of the bias voltage, oxygen pressure and duration of the first deposition step on the growth was underlined. Nevertheless, the influence of other important parameters such as the growth temperature or composition of the plasma has not been studied. In the case of ZnO films, the thickness of deposited material has also previously been shown to play an important role in controlling its structure and optical absorption[35,36], but its influence on the photoluminescence of CVD-grown ZnO films has not been investigated so far.

This paper reports a study of the influence of growth parameters during the PECVD deposition of nanocolumnar ZnO thin films on their nanostructure and optical response. By combining a microstructural and nanostructural characterization by scanning electron microscopy (SEM) and x-ray diffraction (XRD) with optical reflectance and photoluminescence (PL) measurements it is shown that oriented nanocolumnar ZnO films can be grown onto surface oxydized Si at temperature as low as 475 K, and that the nature of the plasma, the substrate temperature and the film thickness strongly influence the topology, crystallinity and defective state of the material.

2. Experimental details

ZnO thin films were grown onto surface oxidized Si (100) substrates by PECVD in a plasma reactor with a remote configuration[37] using Diethyl Zinc ($ZnEt_2$) as Zinc precursor. The dosed precursor was brought into the chamber by a dosing line equipped with a mass-flow controller, and sent onto the substrates through a shower-type dispenser located 3 cm above the sample holder. The dosing line and dispenser were heated at 375 K and the mass flow controller at 315 K to prevent any condensation in the line walls. A thermocouple was used to monitor the temperature

of the sample holder, which can be heated during the deposition using a halogen lamp. The microwave plasma source (SLAN, Plasma Consult GMbh) is coupled to the reaction chamber and separated from it by a grounded grid located 10 cm above the sample holder. This grid avoids the microwave heating of the substrates and minimizes ion bombardment effects[38]. Total pressure during deposition was 4.10^{-3} Torr. The plasma source was operated at a power of 400 W with either pure O_2 or O_2/H_2 (in a ratio 80%/20%), O_2/Ar (10%/90 %) or O_2/N_2 (10%/90%) mixtures as plasma gas. In all cases, the samples were treated with pure O_2 plasma in standard conditions of pressure, both before and after film deposition, in order to clean the substrates and the deposited films[39]. The synthesis of the films was carried out at a substrate temperature tuned between room temperature and 575 K. The thickness of the films was estimated ex-situ by fitting the optical reflectance spectra as measured in the 500 nm – 900 nm range at normal incidence with a Bruker spectrometer equipped with a confocal objective. Around forty samples were prepared to ascertain the influence of the nature of the plasma, substrate temperature and sample thickness on the nanostructure and optical response of the films. Since many of these samples present only a slightly different optical response, we focused the nanostructural and microstructural study on selected samples, whose preparation conditions and thickness are presented in table 6.1. The samples were labelled in order to present clearly the value of the three growth parameters that have been varied in this study. For instance, the sample grown with a mixture of O_2 and Ar, at a substrate temperature of 475 K and presenting a thickness of 700 nm, will be denoted as "O_2/Ar 475K 700nm".

The surface and in-depth microstructure of the films have been observed by plan-view and cross section SEM respectively, using a Hitachi S5200 field emission microscope operated at 5.0 keV. The crystal structure of the films has been studied by XRD in a Siemens D5000 Spectrometer operated in the θ-2θ configuration and using the Cu Kα radiation as excitation source. Continuous wave photoluminescence (PL) measurements were carried out at room temperature in the front face configuration using a Horiba Jobin Yvon Fluorolog3 fluorimeter equipped with a 450 W Xe lamp and two monochromators. The excitation monochromator, located between the source and the sample, was used to select the wavelength of the pumping beam, which was set at 280 nm. The light emitted by the sample was

collected by a PMT detector through the emission monochromator. PL measurements were performed by scanning the emission wavelength between 350 nm and 800 nm with a 5 nm monochromator step.

Table 6.1: Label, plasma conditions and substrate temperature during the growth of the ZnO films and thickness as determined by optical reflectance measurements. Due to the crudeness of the model used to fit the reflectance data, errors of a few tens of nanometers are expected in the determination of the thickness.

Sample's label	Plasma Conditions ($\%O_2$,$\%H_2$,%Ar,$\%N_2$)	Temperature T (K)	Thickness (nm)
O_2 300K 550nm	(100,0,0,0)	300	550
O_2 410K 450nm	(100,0,0,0)	410	450
O_2 475K 400nm	(100,0,0,0)	475	400
O_2 575K 500nm	(100,0,0,0)	575	500
O_2 410K 200nm	(100,0,0,0)	410	200
O_2 410K 870nm	(100,0,0,0)	410	870
O_2 410K 1270nm	(100,0,0,0)	410	1270
O_2 410K 1750nm	(100,0,0,0)	410	1750
O_2/H_2 475K 800nm	(80,20,0,0)	475	800
O_2/Ar 475K 700nm	(10,0,90,0)	475	700
O_2/N_2 475K 300nm	(10,0,0,90)	475	300

The system was equipped with filters in order to remove stray light effects, and the measured spectra were corrected from variations of the pumping intensity. All the samples were measured in identical experimental conditions in order to compare their PL intensities. Reflectance spectroscopy of the films of the "thickness" series was measured at room temperature with a Woollam VASE ellipsometer at a 25º incidence angle, with a S-polarized incident beam (i.e. close to the front face PL measurement conditions) in the [250-1000 nm] range with a 2 nm monochromator step.

3. Topology, crystal structure and optical response of the ZnO films

3.1. Influence of the growth temperature

Fig. 6.1 displays SEM cross-section views and plan views (insets) showing respectively the in-depth and surface topology of the films grown with a O_2 plasma at various substrate temperatures. It can be seen from the cross-section views that the films present a columnar microstructure whatever the substrate temperature. More precisely, they consist of nanocolumns oriented almost perpendicularly to the substrate, presenting rough lateral faces and whose apparent width increases from the interface with the substrate to the film surface. At a given distance from the substrate, the apparent width of the nanocolumns is shown to increase with the growth temperature. The growth temperature also influences the in-plane morphology of the material. Indeed, the in plane projected shape turns from elliptic without preferential orientation to almost circular when increasing the substrate temperature from 300 K to 475 K. The film grown at 575 K (micrograph not shown) presents a topology very similar to the one grown at 475 K.

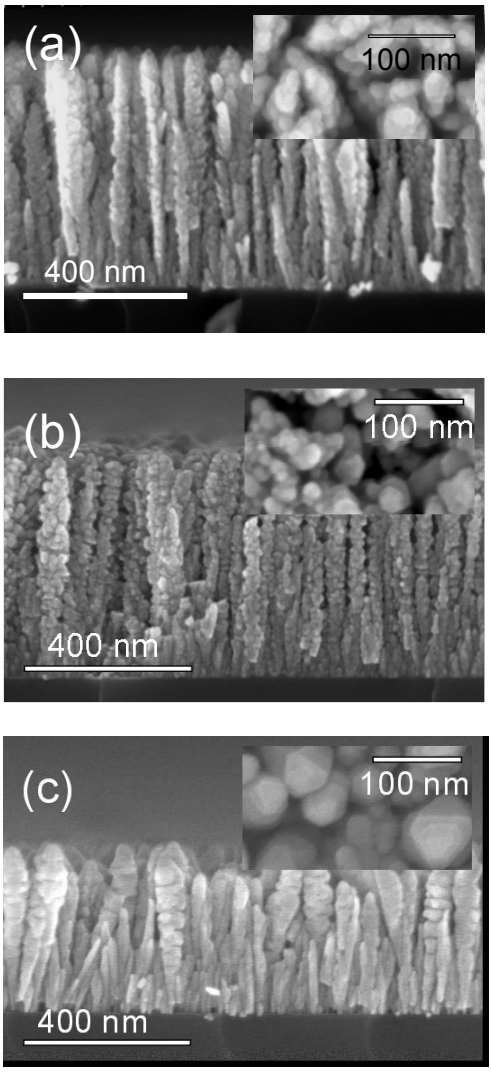

Figure 6.1. SEM cross section and plan view (insets) micrographs of the ZnO films grown with a O_2 plasma and at different substrate temperatures: (a) 300 K (O_2 300K 550nm), (b) 410 K (O_2 410K 450nm) and (c) 475 K (O_2 475K 400nm).

Fig. 6.2a shows the XRD patterns of the same film series, together with that of a ZnO wurtzite powder displaying three peaks located at 31.8º, 34.45º and 36.15º corresponding to the (100), (002) and (101) planes respectively of stress-free ZnO.

The presence of the three peaks in the XRD patterns of the film grown at 300 proves that this film consists of wurtzite ZnO. In contrast with the ZnO wurtzite powder, the most intense peak for this film is the one related to the (002) planes, testifying for a preferential crystal orientation with the c-axis of the hexagonal wurtzite elementary cell perpendicular to the substrate. The XRD patterns of the films grown at higher temperatures only display the (002) peak, showing that the preferential crystal orientation is improved upon increasing of the growth temperature. A

narrowing of the (002) peak is also observed as a result of a better crystallinity along the direction perpendicular to the substrate. Indeed, as shown in fig. 6.2b, the crystal domain size extracted from the full-width at half maximum of the (002) peak using the Scherrer equation increases from 42 to 100 nm when the temperature increases from 300 to 575 K. It can also be seen from the XRD patterns that the (002) peak shifts towards higher angle values when the temperature increases. This evolution is presented in fig 6.2c, where it can be seen that the (002) peak of the films grown at room temperature and 410 K (475 K and 575 K) appears at a lower (resp. higher) angle when compared to the stress-free ZnO powder. Similar changes have been observed upon annealing of ZnO films by Fang *et al.*[40] and attributed to a transition from a state of tensile stress to a state of compressive stress along the c-axis.

From the previous SEM and XRD results, it is apparent that ZnO nanocolumns with a preferential c-axis crystal orientation are formed at relatively low temperatures such as 300 K on silicon substrates presenting an amorphous oxidized surface. Such a c-axis oriented growth on surface oxydized silicon and other amorphous surfaces has been observed previously and discussed in terms of the minimization of the free energy of the growing crystals[41]. The existence of separated nanocolumns could result from the formation of c-axis oriented ZnO nuclei (following a Volmer-Weber like growth mechanism) in the early growth stages of the film[30]. These nuclei may act as seeds for the preferential growth of the columns that, additionally, may be influenced by shadowing and electric field effects[30]. The larger width and rounder in-plane projected shape of the nanocolumns as seen by SEM when the growth temperature is increased would thus reflect a faster diffusion of matter on the substrate during the early stages of growth. Indeed, the higher the temperature, the bigger and rounder will be ZnO nuclei. Increasing the substrate temperature has also been shown to improve the crystalline quality of the film through the increase of the grain size and to affect its stress state, which turns from tensile to compressive. Among the causes of stress of thin films, lattice mismatch[42] with the substrate and presence of interstitial defects are known to induce tensile stress.

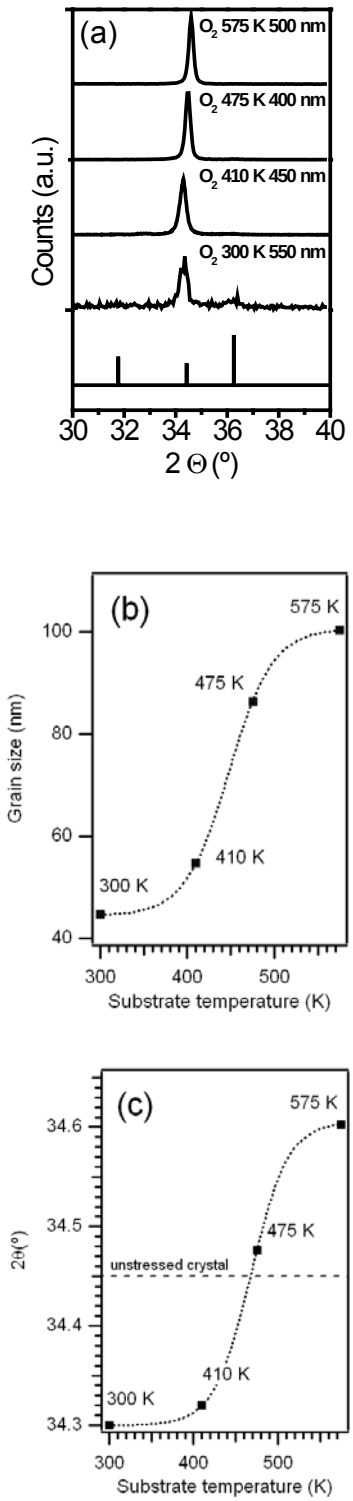

Figure 6.2. (a) θ–2θ x-ray diffraction spectra of the films grown with a O_2 plasma at various substrate temperatures , (b) evolution of the ZnO crystal size along the vertical axis determined from the (002) peak width, (c) evolution of the angular position of the (002) wurtzite diffraction peak as a function of the substrate temperature. The dotted lines in (b) and (c) are a guide for the eye. The dashed line in (c) represents the angular position of the (002) peak of a stress free ZnO wurtzite crystal, taken from JCPDS tables.

In our case, since the substrates are surface oxydized silicon, no epitaxial growth is expected and the tensile stress in the films that were grown at room temperature and 410 K should be due to the presence of interstitial defects. At a higher temperature, due to enhanced mobility of the atoms during the growth, these defects could be removed, thus minimizing tensile stress. The appearance of compressive stress in thin films that have a thermal expansion coefficient higher than that of the substrate (as occurs for the ZnO/Si system) is linked with the rapid cooling of the film/substrate system after the synthesis.[40]

The room temperature PL spectra of the films grown with a O_2 plasma at various substrate temperatures are gathered in figure 6.3a. It can be seen in this figure that the films present two photoluminescence bands, a narrow one in the UV range (peaking around 380 nm) and a broad one in the visible range (in the 500 nm – 700 nm range). The former is generally attributed to radiative excitonic recombinations[1,43] and the latter to radiative transitions involving defect-related energy levels located in the bandgap[1,4,44] (transition between two defect levels, between a defect level and the valence band, or between the valence band and a defect level). The PL spectrum is already dominated by the UV band at a growth temperature of 410 K, suggesting that films of excellent optical quality can be obtained in our PECVD system at relatively low temperatures. The intensity of the UV (visible) PL band increases (decreases) when the films are grown at higher temperature, thus inducing an increase of the “optical quality factor” (inset in figure 6.3a) defined in this paper as the ratio between the maximum of the UV peak and the intensity at 575 nm. Such an increase of the optical quality factor can be correlated to the improvement of the crystal quality as evidenced by SEM and XRD. Indeed, the elimination of the interstitial defects is known to produce a decrease of the intensity of the visible PL band. At the same time, the increase of the grain size [45,46] and thus the decrease of the surface to volume ratio, should contribute to the enhancement of the UV PL peak by decreasing the probability of non-radiative de-excitation processes at the surface of the grains.

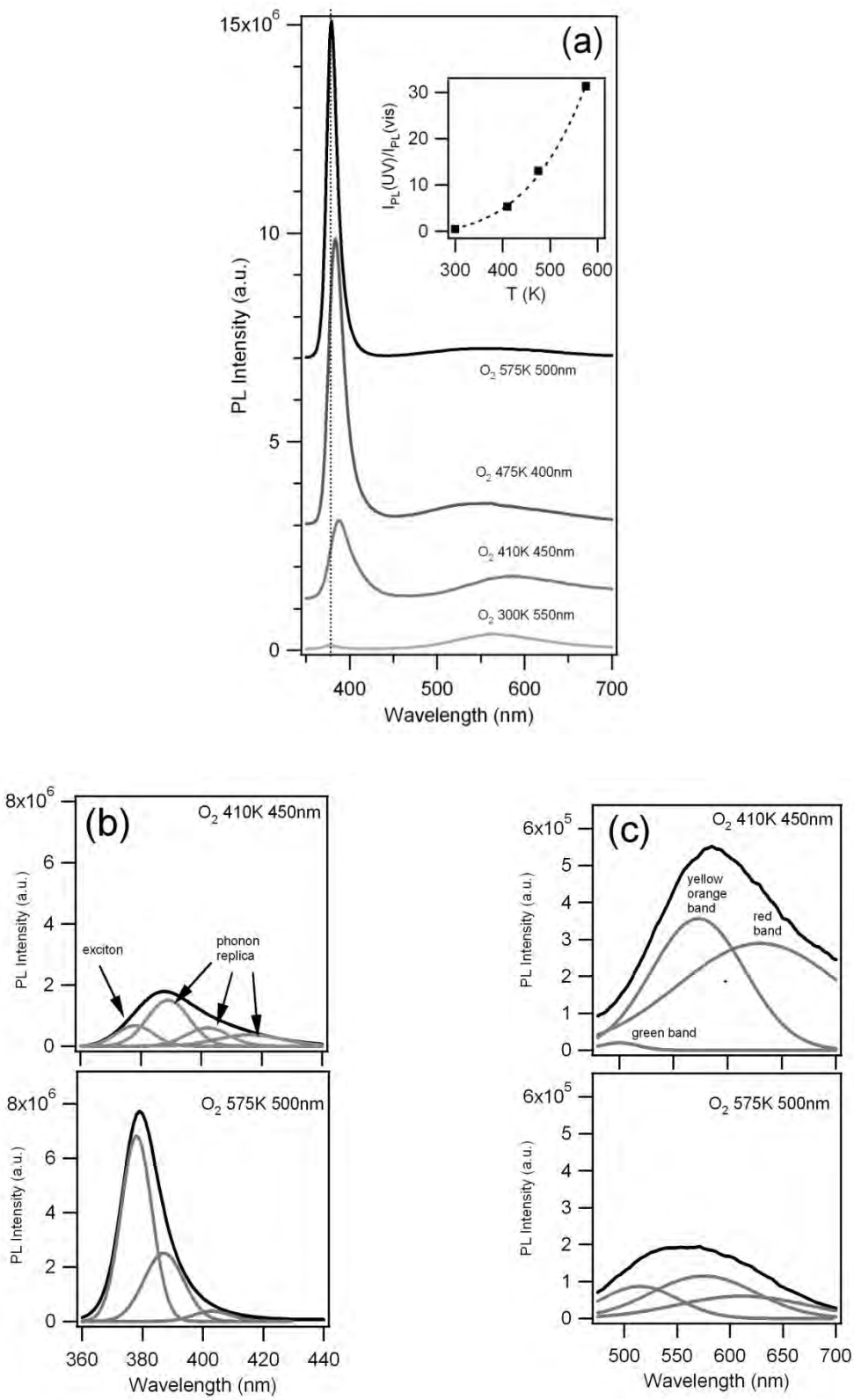

Figure 6.3. (a) Room temperature photoluminescence spectra of the thin films grown with a O_2 plasma at different substrate temperatures (The vertical dotted line representing the 378 nm wavelength has been drawn in each figure as a guide to the eye), (b) Spectra of the UV photoluminescence of two selected films and their corresponding Gaussian components. The peak at 378 nm is attributed to the recombination of free excitons and the others to phonon replicas. (c) Visible photoluminescence spectra of two selected films and their corresponding Gaussian components.

In addition to the intensity, it can be seen in figure 6.3a that the spectral position and shape of the UV and visible PL bands depend on the growth temperature. This dependence has been studied by performing a more accurate analysis of the PL spectra of two selected films: "O_2 410K 450nm", and "O_2 575K 500nm". The UV PL band is usually attributed to radiative excitonic recombinations[42]. When photoluminescence is measured at low temperature, peaks related to the recombination of free excitons followed by phonon replicas, bound excitons and even surface excitons can be resolved[41]. At room temperature, only subsist the contributions of the free exciton and phonon replicas that merge due to thermal damping. The UV PL band measured at room temperature is thus usually considered as the convolution of one peak related to the direct radiative recombination of the exciton and additional peaks linked to phonon replicas located at longer wavelengths. The relative weight of the exciton peak is usually affected by the crystal quality of the material. The PL band of a perfect crystal is governed by the exciton peak, whereas those of a defective and polycrystalline material will present stronger contributions from the phonon replicas[47]. In addition, in the case of confined structures such as nanorods, different waveguiding behaviors of the exciton and phonon replica luminescence may affect the emission pattern of the material[48]. In order to evaluate the weight of the different excitonic contributions in the spectra of the two films, their UV PL band was fitted with a sum of Gaussian functions, centered at 378 nm (free-excitonic contribution), 389 nm, 402 nm and 416 nm (phonon replicas). Figure 6.3b shows the UV PL bands of the two samples and in each case the corresponding Gaussian components. The phonon replicas dominate in the case of the "O_2 410K 450nm" film for which the excitonic contribution is almost absent. The weight of the free excitonic contribution increases with the growth temperature, inducing an apparent blue-shift of the UV PL band. These results are in agreement with XRD measurements showing that the crystal quality is improved (grain size increases) upon increasing the growth temperature.

The visible PL band is usually attributed to radiative recombination events involving defect levels located in the bandgap[1,4,42]. Due to the high number of possible defect levels, the visible PL bands generally present a complex spectral shape making the extraction of structural data from the spectra an uneasy task. Nevertheless, in the absence of trapped heteroatoms, it has been observed[49,50,51] that ZnO films

presenting a green luminescence band (peaking between 480 and 520 nm) are Zn-rich and that those presenting a yellow-orange luminescence band (peaking between 550 and 600 nm) are O-rich. Red or near Infra-Red luminescence bands whose origin remains unclear have also been reported. Fits of the visible PL bands of the two films have thus been performed with the sum of 3 Gaussian functions centered at around 520 nm, 580 nm and 650 nm. The experimental bands, which present significantly different spectral shapes are shown in figure 6.3c together with their corresponding 3 gaussian components. The visible band of the "O_2 410K 450nm" is dominated by the yellow band, suggesting that this film is O-rich. The absolute and relative intensity of this band are strongly reduced upon increasing the growth temperature. It can thus be proposed from these results and those of XRD, that the "O_2 410K 450nm" is under tensile stress due to the presence of interstitial oxygen in the crystal lattice. Additionally, the low intensity of the oxygen-linked band in the visible PL spectra of the "O_2 575K 500nm" film may reflect a lower amount of interstitial oxygen in this film.

3.2. Influence of the film thickness

Figure 6.4 shows the cross-section SEM micrograph of the thickest film of this study ("O_2 410K 1750nm"). Almost 1.5 microns-high, well defined and vertical columns can be seen, suggesting that the columnar growth is preserved even in the case of thick films. Moreover, the projected width of the columns increase from the substrate to the film surface, thus inducing a decrease of the porosity, whereas the lateral roughness of the columns increases.

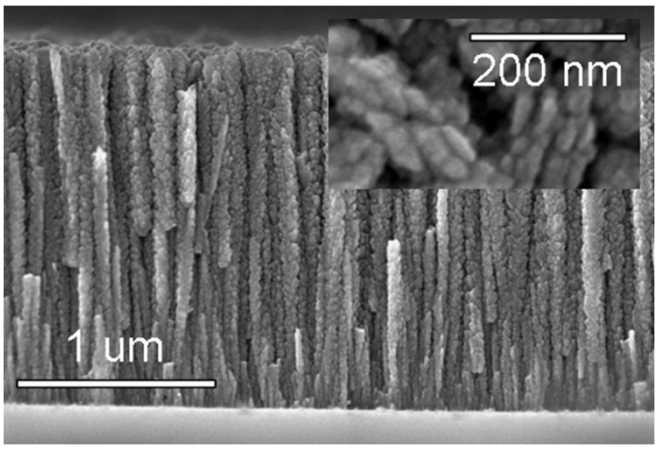

Figure 6.4. SEM cross-section view of the O_2 410K 1730nm film (inset : SEM surface view).

Figure 6.5a presents the XRD patterns of the samples grown at a 410 K temperature with a O_2 plasma presenting different thicknesses ranging from 200 nm to 1750 nm. All of them are dominated by the (002) peak, whose intensity increases with the thickness, showing that the material keeps growing with the c-axis perpendicular to the substrate whatever the deposited thickness. Moreover, it can be seen that the (002) peak shifts towards higher angles when the thickness is increased. It is centered at 34.28º for the 200 nm-thick film and at 34.41º for the 1750 nm-thick film, suggesting that the average stress state of the film turns from tensile to unstressed when the thickness increases. Looking more precisely at the (002) peaks, it can be seen that they are not symmetric, in contrast with the diffraction peaks of perfect crystals, and that their asymmetry increases with the film thickness. Fits of these peaks performed using a sum of Lorentz functions (see Supporting information S1) suggest that the ZnO films under study can be considered as a material with a vertically decreasing gradient of stress. As a typical example, the "O_2 410K 1750nm" film would present tensile stress close to the substrate and be almost unstressed close to the surface.

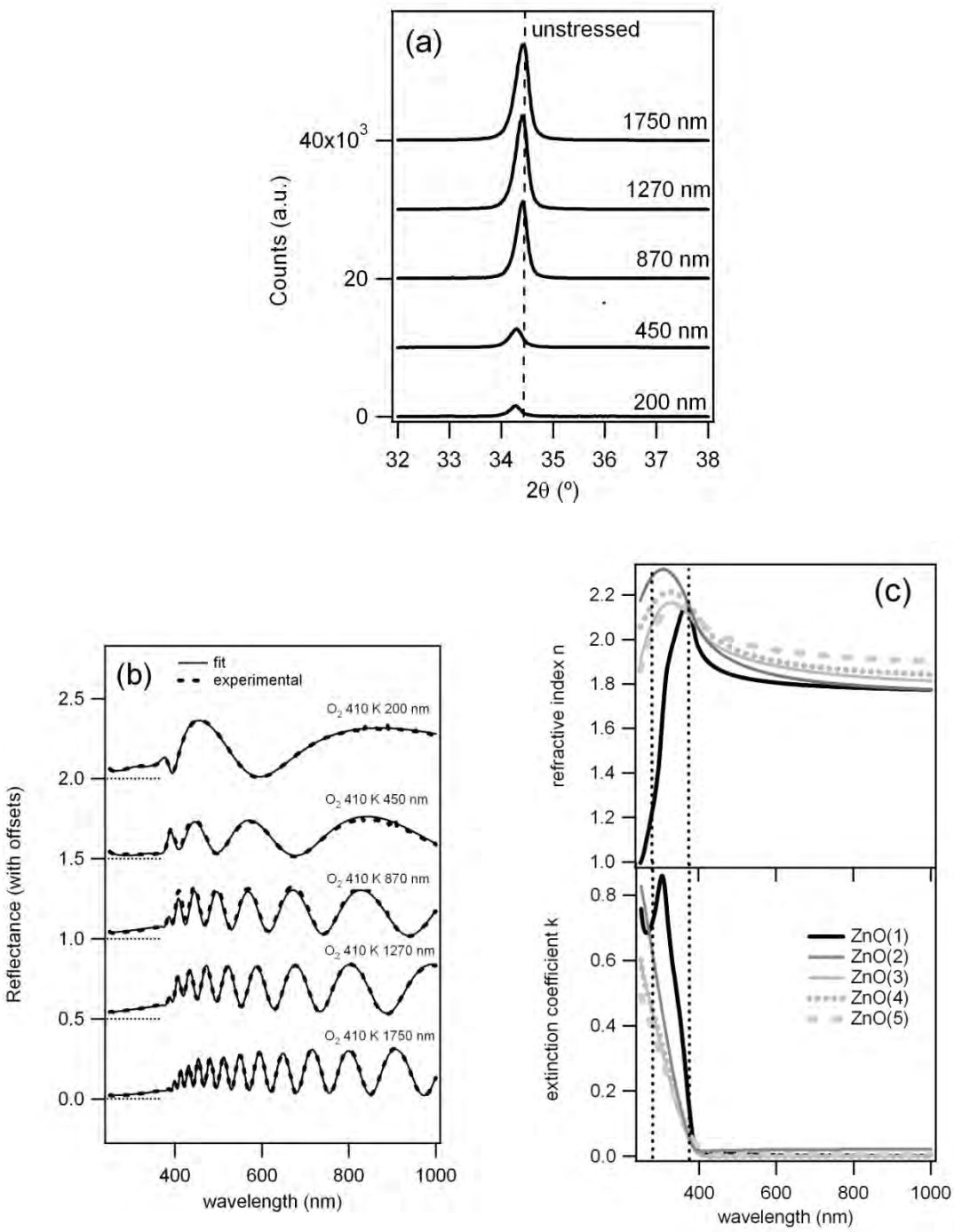

Figure 6.5. (a) θ–2θ x-ray diffraction spectra of films presenting different thicknesses grown with a O_2 plasma at a substrate temperature of 410 K. The vertical dashed line represents the angular position of the (002) peak of stress free ZnO wurtzite bulk crystal. (b) Reflectance spectra of the five films and corresponding best fits, (c) n and k spectra extracted for the five effective ZnO layers using the multilayer structures depicted in table 6.2. The vertical dotted lines correspond to wavelengths of 280 nm (excitation wavelength during PL experiments) and 375 nm (typical of the UV PL band).

Figure 6.5b presents the reflectance spectra of the films together with their corresponding best fit. Fitting was performed using the WVASE32 (Woollam) software. In order to account for a possible in-depth gradient of refractive index n and extinction coefficient k, each film was described as a stack of effective medium layers, the number of which increasing with the film thickness, as depicted on table 6.2. The top layer of each stack was an effective medium averaging the optical properties of void and the underlying material, in order to take the surface roughness into account. The n and k of the underlying layers were described as the sum of a Cauchy law with Urbach absorption tail and a Tauc-Lorentz oscillator. An excellent fit was obtained for thinnest film ("O_2 410K 200nm") considering it as a ZnO(1)/roughness bilayer (table 6.2). Fitting of the reflectance spectrum of the "O_2 410K 450nm" film was made using a [ZnO(1)/ZnO(2)/roughness] trilayer model, where the ZnO(1) layer had the same optical properties as that of the "O_2 410K 200nm" film. For the "O_2 410K 870nm", "O_2 410K 1270nm" and "O_2 410K 1750nm" films, fitting was performed with 4, 5 and 6 layers respectively, thus permitting to extract iteratively the n and k of the ZnO(3), ZnO(4) and finally ZnO(5) layer.

Sample	Structure (thicknesses for the best fit)
O_2 410K 200nm	**Si/ZnO(1)$_{235nm}$/roughness$_{25nm}$**
O_2 410K 450nm	**Si/ZnO(1)$_{209nm}$/ZnO(2)$_{240nm}$/roughness$_{39nm}$**
O_2 410K 870nm	**Si/ZnO(1)$_{210nm}$/ZnO(2)$_{204nm}$/ZnO(3)$_{514nm}$/roughness$_{34nm}$**
O_2 410K 1270nm	**Si/ZnO(1)$_{247nm}$/ZnO(2)$_{43nm}$/ZnO(3)$_{535nm}$/ ZnO(4)$_{289nm}$/roughness$_{33nm}$**
O_2 410K 1750nm	**Si/ZnO(1)$_{227nm}$/ZnO(2)$_{195nm}$/ZnO(3)$_{468nm}$/ ZnO(4)$_{393nm}$/ZnO(5)$_{483nm}$/roughness$_{42nm}$**

Table 6.2. Structures used for fitting optical reflectance spectra of the films of the "thickness series".

Figure 6.5c shows the n and k spectra of the five ZnO(i) layers constituting the "O_2 410K 1750nm" film, revealing an in-depth gradient of optical properties. The refractive index in the visible increases from 1.8 to 2 from the susbtrate to the surface, an effect that can be related to the decrease of porosity as observed from the SEM cross-section view. Meanwhile, the slope of the UV absorption of the material

decreases, the most significant evolution occuring in a 500 nm-thick region starting from the substrate. Similar changes were observed by Malandrino et al.[52] after annealing nanoporous polycristalline ZnO films and attributed to an improvement of the crystal structure (reduction of the amorphous tissue and the presence of grain boundaries causing lower polarizability per unit volume). XRD and reflectance measurements thus point out an improvement of the crystal quality (less stress, better crystalline order) with the distance to the substrate.

It can be seen in figure 6.6a, which shows the full PL spectra of the five films, that the intensity of both PL bands (the UV band and the visible band) decrease as the film thickness increases. The faster decrease of the UV PL intensity provokes a decrease of the optical quality factor (as shown in the inset of the same figure). At this point, it has to be highlighted that, due to the absorption of the pump beam at 280 nm, the probe depth of PL measurements is estimated (from simulations based on the n and k spectra shown in figure 6.5c) to increase from around 100 nm (for the 200 nm-thick film) to 200 nm for the 1750 nm-thick film. This argument is very important for interpreting the influence of the film thickness on the PL. Indeed, in the case of thick films (thickness > 100 nm), only the outmost surface layers of the films are probed, in contrast with XRD or cross-section SEM measurements that probe the whole material. Deconvolution of the visible PL peaks (fig. 6.6c) shows that the contribution of the yellow-orange band in the visible PL (fig. 6.6c) decreases when the film thickness increases. From this result, it can be proposed that the surface zone of the "O_2 410K 1750nm" film presents a better stoichimetry than the one of the "O_2 410K 450nm" film (that presents a PL typical of an excess of oxygen). Correlation with XRD data suggests that the vertical gradient of stress, with lower (higher) stress close to the surface of the film (film/substrate interface), is due to a vertical gradient of interstitial oxygen. Deconvolution of the UV PL peaks (fig. 6.6b) shows that the relative weight of the excitonic contribution increases with the film thickness. This could be a consequence of a vertical gradient of crystal order following the gradient of stress. Since the UV PL intensity and optical quality factor decrease upon depositing more material (fig. 6.6a) while the crystal order and stoichoimetry of the surface layer improve, another parameter should influence the UV PL band. At the emission wavelengths of the free exciton and phonon replicas (between 378 and 420 nm), the absorption coefficient of ZnO

(fig. 6.5c) is very low (below 0.02) whatever the depth, thus permitting to discard a possible role of reabsorption of the emitted light in our measurement conditions (excitation and collection at near-normal incidence). A more probable interpretation of the “thickness effect” (on the intensity of the UV PL) may involve scattering of the emitted light by the rough lateral and top faces of the nanocolumns. An increasing gradient of lateral roughness has effectively been observed (from the substrate to the surface) by SEM, whereas thicknesses of 25 nm and 42 nm were obtained for the roughness layer of the thinnest and thickest film, respectively. The decrease of the UV PL (collected at near normal incidence) when thickness increases could therefore result from scattering of light away from the collection direction.

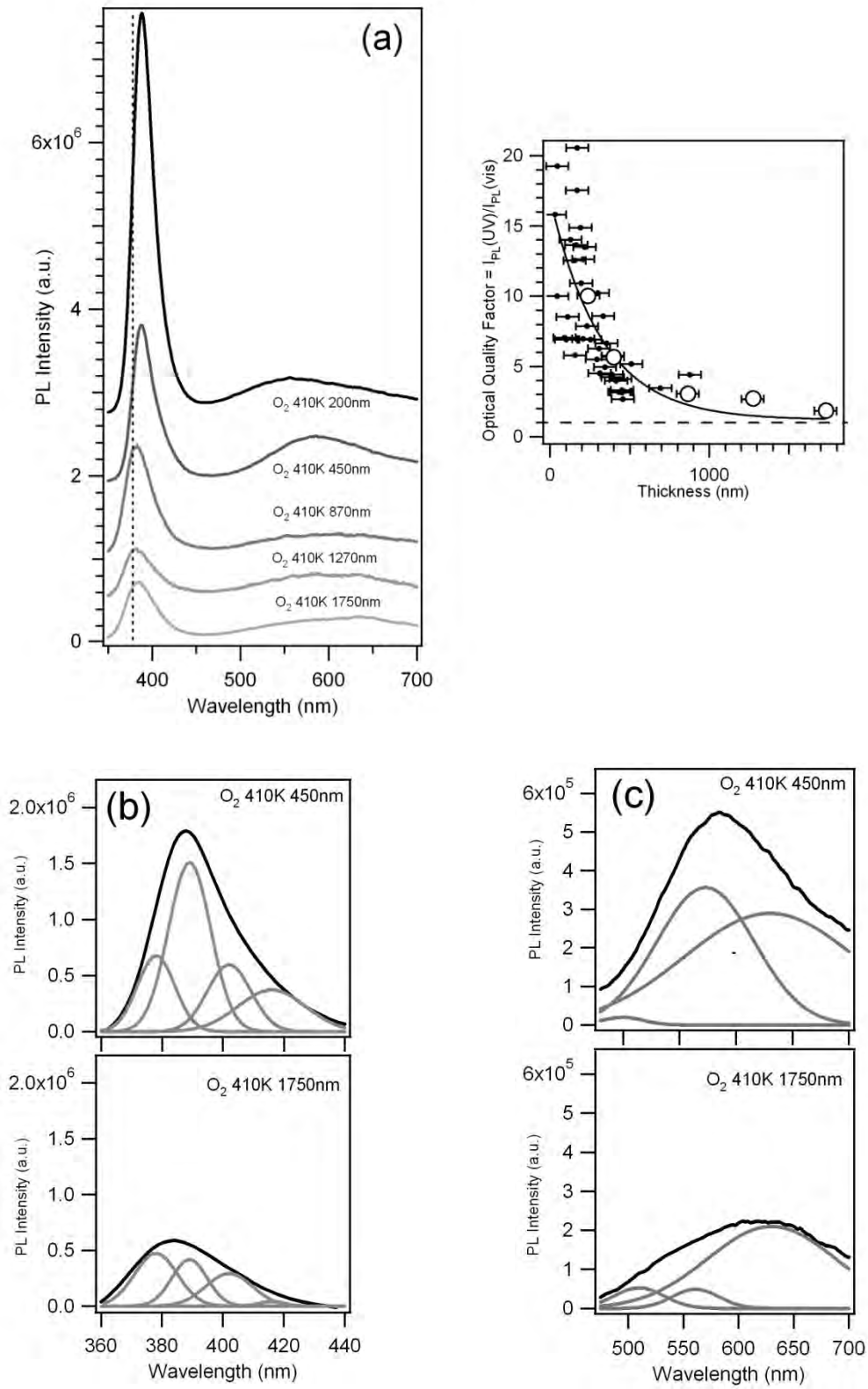

Figure 6.6. (a) Room temperature photoluminescence spectra of the thin films grown with a O_2 plasma at 410 K presenting different thicknesses and optical quality factor evolution versus thickness, (b) Spectra of the UV photoluminescence of two selected films and their corresponding Gaussian components, (c) Visible photoluminescence spectra of two selected films and their corresponding Gaussian components.

3.3. Influence of the plasma composition

Figure 6.7 presents the SEM cross-section and plan-view micrographs of the films grown at a 475 K substrate temperature and different nature of the plasma gas. A columnar nanostructure is observed from the cross section views whatever the plasma conditions, which however influence significantly the topology of the nanocolumns. In particular, at a given distance from the substrate, a smaller width is observed for the nanocolumns grown with O_2/H_2 and O_2/Ar plasmas. Let us remark that the columns grown in a O_2/H_2 are particularly smooth. The plan-view micrographs also demonstrate the role of the plasma on the in-plane structure of the films. An almost circular in-plane projected shape is reported in the case of nanocolumns grown with O_2 and O_2/N_2 plasmas, whereas those grown with O_2/H_2 and O_2/Ar plasmas present an elliptic projected shape without specific orientation.

Figure 6.8a shows XRD patterns of the films grown at 475 K with plasmas of different nature. As in the case of the films grown with a O_2 plasma, the films consist of ZnO in an hexagonal wurtzite phase with a preferential orientation of the c-axis perpendicularly to the substrate. The crystalline organization can be monitored through the degree of preferential orientation of the c-axis perpendicularly to the substrate (reflected by the relative intensity of the diffraction peaks) and by the size of the crystal domains along the [002] direction (shown in fig. 6.8b), which are both affected by the nature of the plasma. Films grown with O_2 and O_2/N_2 plasmas display a bigger size of crystal domains and a more pronounced preferential orientation and thus a better crystalline organization than those grown with O_2/Ar or O_2/H_2 plasmas. Moreover, as seen in figure 6.8c, the (002) peaks of the films grown with O_2/Ar, O_2/N_2 and O_2/H_2 plasmas are slightly shifted towards lower angles when compared to the unstressed value. This suggests that, in contrast with the film grown in O_2, tensile stress (that could be ascribed to the presence of interstitial defects) still exists.

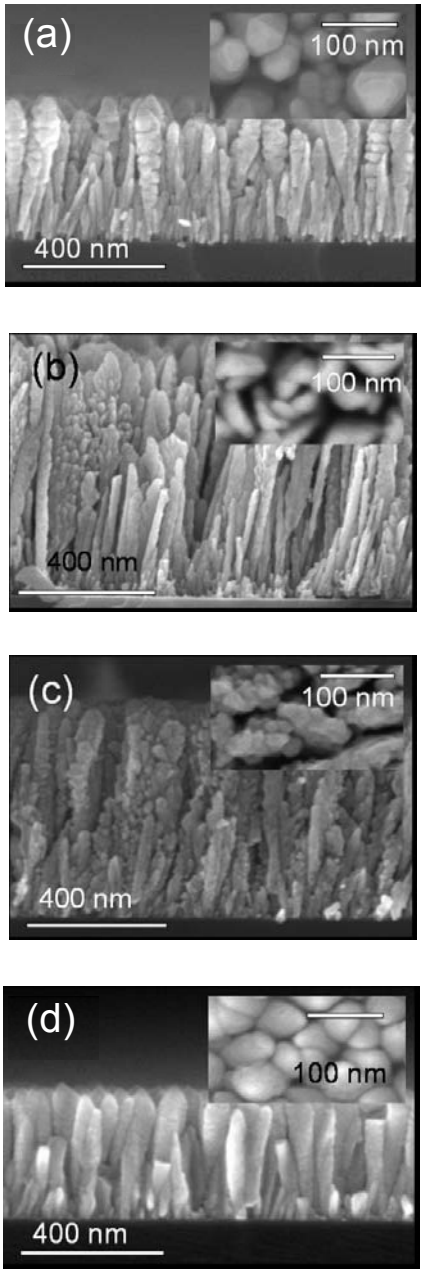

Figure 6.7. SEM cross section and plan view (insets) micrographs of the ZnO films grown at 475 K substrate temperature and with different plasmas: (a) O_2 plasma (O_2 475K 400nm), (b) O_2/H_2 plasma (O_2/H_2 475K 800nm), (c) O_2/Ar plasma (O_2/Ar 475K 700nm), (d) O_2/ N_2 plasma (O_2/ N_2 475K 300nm).

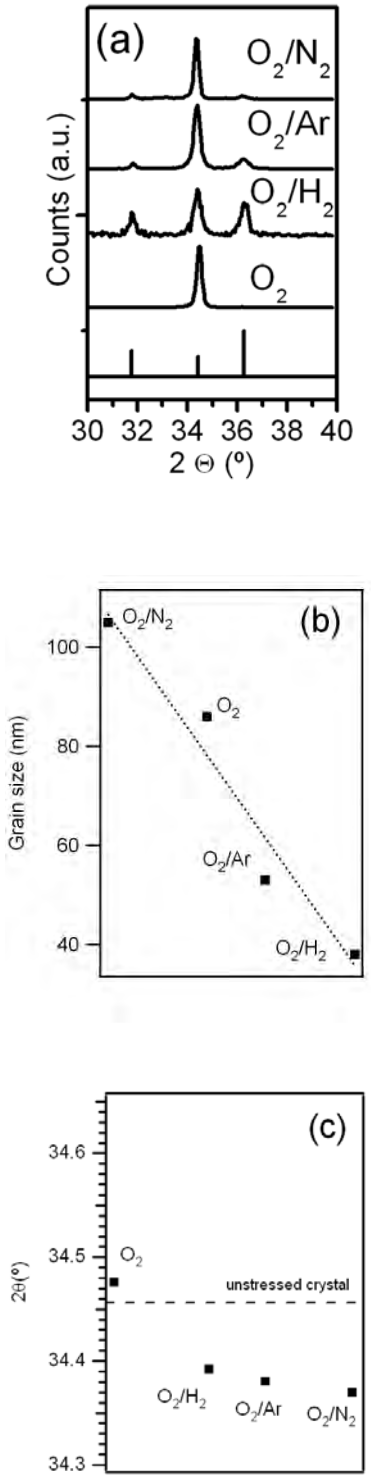

Figure 6.8. (a) θ–2θ x-ray diffraction spectra of the films grown at a 475 K substrate temperature and with different compositions of the plasma. (b) Evolution of the ZnO crystal size along the vertical axis determined from the (002) peak width as a function of the plasma composition. The dotted line is a guide for the eye. (c) Evolution of the angular position of the (002) wurtzite diffraction peak as a function of the plasma composition. The dashed line represents the angular position of the (002) peak of stress free wurtzite ZnO crystal.

The different micro and nanostructure of the films prepared with the aforementioned plasma gas compositions are likely the result of a different growing mechanism occurring in each case. In fact, the growing processes must be very dependent on the nature of the intermediate species of Zn formed in each case and/or on the generation of lattice defects by the interaction of the growing film with activated species of the plasma gas (e.g., Ar*, H*. N*, N_2^*, etc.). Note for example the presence of relatively heavy Ar ions bombarding the growing films in the case of mixtures O_2/Ar mixtures. Such dependence has been reported previously for TiO_2 grown by PECVD where the different decomposition degree of the precursor with plasmas of O_2 or mixtures O_2/Ar and O_2/N_2 leads to the formation of films with quite different structures and microstructures.[31]

It can be seen in figure 6.9a that the film grown in a O_2/N_2 plasma presents no UV PL peak but a broad band in the 400-500 nm range that might be linked to the presence of donor levels below the valence band induced by the incorporation of nitrogen to the film. Growing the films in a O_2/H_2 plasma enhances the intensity of the UV PL when compared to a film grown in O_2. A very high optical quality factor is obtained (see inset of fig. 6.9a) for this film, despite of its 800 nm thickness and small grain size. Indeed, in addition to previous XRD data, the UV PL of this film (fig. 6.9b) presents a strong phonon replica and its visible PL is markedly influenced by the yellow-orange band characteristic of O-rich materials (see note in supporting information S2). The intense UV PL of this film might arise from the passivation of active recombination centers by H_2 during the growth[53], a feature that would contribute to suppress non-radiative de-excitation routes of the exciton and to enhance the UV luminescence. One can note the smoothness of the columns grown in a O_2/H_2 plasma, that may prevent scattering of the emitted light (in contrast with the columns grown with a O_2 plasma) thus leading to a better collection of the UV PL in our measurement conditions.

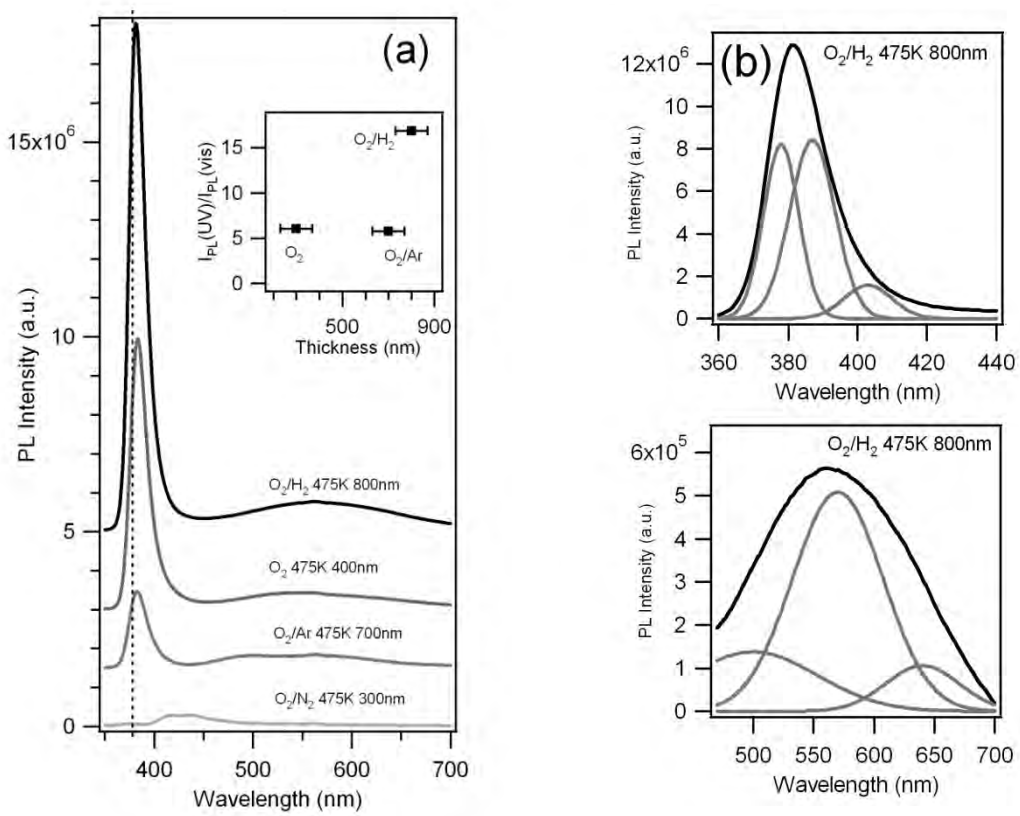

Figure 6.9. (a) Room temperature photoluminescence spectra of the thin films grown with at 475 K with various plasmas, (b) Spectra of the UV photoluminescence and Visible photoluminescence spectra of a film grown in a O_2/H_2 plasma and the corresponding Gaussian components.

4. Conclusions

By means of the PECVD technique at substrate temperature as low as 475 K, it has been possible to grow nanocolumnar ZnO thin films with a preferential c-axis orientation, low concentration of defects and strong UV PL. Films microstructure, crystallinity and PL can be tuned both in the UV and visible ranges by modifying the substrate temperature, nature of the plasma gas , and film thickness. Enhancement of the UV PL is obtained upon increasing the substrate temperature and attributed to the improvement of the crystal order. In a O_2 plasma, growing thicker films induces a decrease of the UV PL, showing that it is necessary to limit the thickness of deposited material to obtain films of optimal optical quality. This “thickness effect” is likely to be linked to the microstructure of the films rather than to their crystalline structure. The thickness limitation can be overcome by growing the material in a O_2/H_2 plasma, in which thick films with a high optical quality factor were obtained.

In addition, the correlation between the data extracted from XRD, reflectance and PL spectra permits to get a deep insight into the in-depth structure of the films, showing these two techniques can be combined for a precise non-destructive characterization of ZnO films.

Acknowledgments

This work was supported by the MICINN (projects FUNCOAT CDS2008-0023, MAT20010-21218) and Junta de Andalucía (Project P09-TEP-5283). J.T. acknowledges the Spanish Ministry for Research and Innovation for financial support (Juan de la Cierva Grant JCI-2009-05098).

Supporting Information Available : (S1) Lorentz deconvolution of the (002) diffraction peaks of the films, (S2) Composition of the plasma. This information is available free of charge via the Internet at http://pubs.acs.org.

References

(1) Djurisic, A.B.; Leung, Y.H. *Small* **2006**, *2*, 944.

(2) Konenkamp, R.; Word, R.C.; Godinez M. *Nanolett.* **2005**, *5*, 2006.

(3) Hung, M.; Mao, S.; Feick, H.; Han, H.; Wu, Y.; Kind, H.; Weber, E.; Russo, R.; Yang, P. *Science* **2001**, *292*, 1897.

(4) Djurisic, A.B.; Leung, Y.H.; Tam, K.H.; Ding, L.; Ge, W.K.; Chen, H.Y.; Gwo, S. *Appl. Phys. Lett.* **2006**, *88*, 103107.

(5) Kohan, A.F.; Ceder, G.; Morgan, D.; Van de Walle, C.G. *Phys. Rev. B* **2000**, *61*, 15109.

(6) Borseth, T.M.; Svensson, B.G.; Kuznetsov, A. Y.; Klason, P.; Zhao, Q.X.; Willander, M. *Appl. Phys. Lett.* **2006**, *89*, 262112.

(7) Zhang, D.H.; Xue, Z.Y.; Wang, Q.P. *J. Phys. D : Appl. Phys.* **2002**, 35, 2837.

(8) Lin, B.; Fu, Z.; Jia, Y. *Appl. Phys. Lett.* **2001**, *79*, 943.

(9) Wei, H.; Wu, Y.; Wu, L.; Hu, C. *Mater. Lett.* **2005**, *59*, 271.

(10) Yang, Y.; Qi, J.; Liao, Q.; Zhang, Y.; Yau, X.; Huang, Y.; Tang, L. *Appl. Phys. A* **2009**, *94*, 799.

(11) Ohashi, N.; Sekiguchi, T.; Aoyama, K.; Ohgaki, T.; Terada, Y.; Sakaguchi, I.; Tsurumi, T.; Haneda, H. *J. Appl. Phys.* **2002**, *91*, 3658.

(12) Van Dijken, A.; Meulenkamp, E.M.; Vanmaekelbergh, D.; Meijerink, A. *J. Lumin.* **2000**, *87*, 454.

(13) Wang, Z.L. *Mater. Sci. Eng. R.* **2009**, *64*, 33.

(14) Ahn, M.W.; Park, K.S.; Heo, J.H.; Park, J.G.; Kim, D.W.; Choi, K.J.; Lee, J.H.; Hong, S.H. *Appl. Phys. Lett.* **2008**, *93*, 263103.

(15) Liao, L.; Lu, H.B.; Li, J.C.; Liu, C.; Fu, D.J.; Liu, Y.L. *Appl. Phys. Lett.* **2007**, *91*, 173110.

(16) Baratto, C.; Todros, S.; Faglia, G.; Comini, E.; Sberveglieri, G.; Lettieri, S.; Santamaria, L.; Mabdalena, P. *Sens. Actuators, B* **2009**, *140*, 461.

(17) Van Dijken, A.; Meulenkamp, E.A.; Vanmaekelbergh, D.; Meijerink, A. *J. Phys. Chem. B* **2000**, *104*, 1715.

(18) Van Dijken, A.; Meulenkamp, E.A.; Vanmaekelbergh, D.; Meijerink, A. *J. Phys. Chem. B* **2000**, *104*, 4355.

(19) Wang, Y.; Zhao, F.; Xie, P.; Liang, S.; Deng, S.; Xu, N. *Opt. Commun.* **2007**, *276*, 186.

(20) Djurisic, A.B.; Choi, W.C.H.; Roy, V.A.L.; Leung, Y.H.; Kwong, C.Y.; Cheah, K.W.; Krishnaswamy, T.; Chan, W.K.; Liu, H.F.; Surya, C. *Adv. Funct. Mater.* **2004**, *14*, 856.

(21) Djurisic, A.B.; Leung, Y.H.; Tam, K.H.; Ding, L.; Ge, W.K.; Chen, H.Y.; Gwo, S. *Appl. Phys. Lett.* **2006**, *88*, 103107.

(22) Bahnemann, D.W.; Kormann, C.; Hoffmann, M.R. *J. Phys. Chem.* **1987**, *91*, 3789.

(23) Li, Y.; Meng, G.W.; Zhang, J.D.; Phillipp, F. *Appl. Phys. Lett.* **2000**, *76*, 15.

(24) Wang, L.; Zhang, X.; Zhao, S.; Zhou, G.; Zhou, Y.; Qi, J. *Appl. Phys. Lett.* **2005**, *86*, 024108.

(25) Laudise, R.A.; Ballman, A.A. *J. Phys. Chem* **1960**, *64*, 688.

(26) Park, W.I.; Kim, D.H.; Jung, S.W. ; Yi, G.C. *Appl. Phys. Lett.* **2002**, *80*, 4232.

(27) Li, Y.; Feneberg, M.; Reiser, A.; Schirra, M.; Enchelmaier, R.; Ladenburger, A.; Langlois, A.; Sauer, R.; Thonke, K.; Cai, J.; Rauscher, H. *J. Appl. Phys.* **2006**, *99*, 054307.

(28) Wu, J.J.; Liu, S.C. *J. Phys. Chem. B* **2002**, *106*, 9546.

(29) Wu, C.L.; Chang, L.; Chen, H.G.; Lin, C.W.; Chang, T.F.; Chao, Y.C.; Yan, J.K.; *Thin Solid Films* **2006**, *498*, 137.

(30) Liu, X.; Wu, X.; Cao, H.; Chang, R.P.H. *J. Appl. Phys.* **2004**, *95*, 314.

(31) Borras, A.; Cotrino, J.; Gonzalez-Elipe, A.R. *J. Electrochem. Soc.* **2007**, *154*, 12.

(32) Borras, A.; Yanguas-Gil, A.; Barranco, A.; Cotrino, J.; Gonzalez-Elipe, A.R. *Phys. Rev. B* **2007**, *76*, 235303.

(33) Martín, A.; Espinós, J.P.; Justo, A.; Holgado, J.P.; Yubero, F.; González-Elipe, A.R. *Surf. Coat. Technol.* **2002**, *151*, 289-293.

(34) Bekermann, D.; Gasparotto, A.; Barreca, D.; Bovo, L. *Cryst. Growth Des.* **2010**, *10*, 2011.

(35) Zang, Y.; Bahlawane, N. *J. Phys. Chem. C* **2010**, *114*, 5121.

(36) Yang, B.; Kumar, A.; Feng, P.; Katiyar, R.S. *Appl. Phys. Lett.* **2008**, *92*, 233112.

(37) Gracia, F.; Holgado, J. P.; González-Elipe, A. R. *Langmuir* **2004**, *20*, 1688.

(38) Winter R.; Korzec D.; Engemann J. *Surf. Coat. Technol.* **1997**, *91*, 101.

(39) Barranco, A.; Cotrino, J.; Yubero, F.; Espinos, J.P.; Benitez, J.; Clerc, C.; Gonzalez-Elipe, A.R. *Thin Solid Films* **2001**, *410*, 150.

(40) Fang, Z.B.; Yan, Z.J.; Tan, Y.S.; Liu, X.Q.; Wang, Y.Y. *Appl. Surf. Sci.* **2005**, *241*, 303.

(41) Choim J.H.; Tabatam H.; Kawaim T.J. *Cryst. Growth* **2001**, *226*, 493.

(42) Ashrafi, A.B.M.A.; Binh, N.T.; Zhang, B.P.; Segawa, Y. *Appl. Phys. Lett.* **2004**, *84*, 2814.

(43) Voss, T.; Bekeny, C.; Wischmeier, L.; Gafsi, H.; Börner, S.; Schade, W.; Mofor, A.C.; Bakin, A.; Waag, A. *Appl. Phys. Lett.* **2006**, *89*, 182107.

(44) Lima, S.A.M.; Sigoli, F.A.; Jafelicci, M.; Davolos, M.R. *Int. J. Inorg. Mater.* **2001**, *3*, 749.

(45) Shalish, I.; Temkyn, H.; Narayanamurti, V. *Phys. Rev. B* **2004**, *69* 245401.

(46) Matsumoto, T.; Kato, H.; Miyamoto, K.; Sano, M.; Zhukov, E.A. *Appl. Phys. Lett.* **2002**, *81*, 1231.

(47) Cui, J. *J. Phys. Chem. C* **2008**, *112*, 10385.

(48) Gao, M.; Cheng, R.; Li, W.; Li, Y.; Zhang, X.; Xie, S. *J. Phys. Chem. C* **2010,** *114*, 11081.

(49) Djurisic, A.B.; Leung, Y.H.; Tam, K.H.; Ding, L.; Ge, W.K.; Chen, H.Y.; Gwo, S. *Appl. Phys. Lett.* **2006**, *88*, 103107.

(50) Fan, H.B.; Yang, S.Y.; Zhang, P.F.; Wei, H.Y.; Liu, X.L.; Jiao, C.M.; Zhu, Q.S.; Chen, Y.H.; Wang, Z.G. *Chin. Phys. Lett.* **2007**, *24*, 2108.

(51) Ong, H.C.; Du, G.T. *J. Cryst. Growth* **2004**, *265*, 471.

(52) Malandrino, G.; Blandino, M.; Fragala, M. E.; Losurdo, M.; Bruno, G. *J. Phys. Chem. C* **2008,** *112*, 9595.

(53) Ohashi, N.; Ishigaki, T.; Okada, N.; Taguchi, H.; Sakaguchi, I.; Hishita, S.; Sekiguchi, T.; Haneda, H. *J. Appl. Phys.* **2003**, *93*, 6386.

Supporting information

6.S1. Lorentz deconvolution of the (002) diffraction peaks of the films

The XRD patterns have been fitted using up to 4 Lorentz peaks centered at 34.19º, 34.29º, 34.39º and 34. 47º, numbered as nº1, nº2, nº3 and nº4 respectively. Examples of these fits are presented in figures 6.S1a and S1b, corresponding respectively to the "O_2 410K 200nm" and "O_2 410K 1750 nm" films. In the case of the 200 nm-thick film (fig. 6.4b), two Lorentz functions (nº1 and nº2) have been necessary to fit the (002) peak. A good fit has been performed with the 4 Lorentz peaks in the case of the 1750 nm-thick film (fig. 6.4c). Similar fits (not presented) show that the (002) peak of the "O_2 410K 450nm", "O_2 410 K 870nm" and "O_2 410K 1270nm" films can be reproduced using 2 (nº1 and nº2), 3 (nº1, nº2 and nº3) and the 4 Lorentz functions respectively. Despite of the crudeness of the fits, qualitative trends can be extracted. The fact that the diffraction peak of the thinnest film can be fitted with 2 Lorentz peaks (nº1 and nº2), both shifted towards low angles when compared to the unstressed value means that this film is, as a whole, under tensile stress. In contrast, fitting the diffraction peak of the thickest film requires to add peaks nº3 and nº4, suggesting that the overall diffraction signal contains contributions of unstressed and stressed regions of the material. The unstressed zones are very likely to be located at the surface of the thick film and not in the first 200 nm, since they are absent in the 200 nm-thick film.

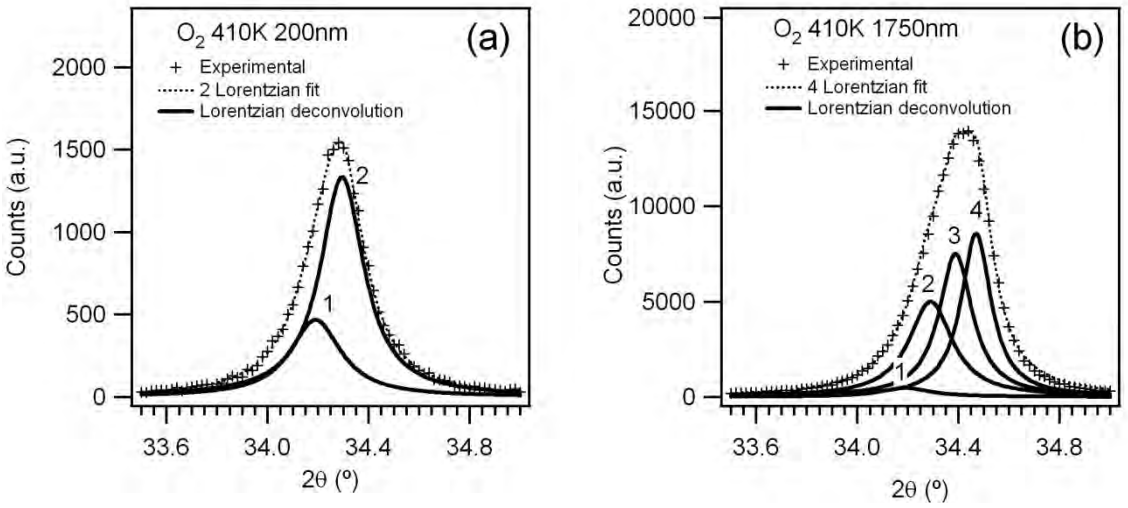

Figure 6.S1. Lorentz deconvolution of the (002) peak of (a) the "O_2 410K 200nm" film (2 Lorentz peaks) and (b) the "O_2 410K 1750nm" film (4 Lorentz peaks).

6.S2. Composition of the plasma

At first sight it might seem surprising that despite the reducing character of hydrogen O_2/H_2 (80%/20%) plasmas favor the formation of O-rich films. However, the optical emission spectroscopy (OES) analysis of these plasmas have shown that besides H^* and O* intermediate species, the very reactive OH* species are also very abundant (data not shown). We believe that both H* and OH* contribute very actively to the removal (as CO_2, H_2O or CH_4) of the $–CH_3$ groups attached to the Zn in the volatile precursor used for the synthesis, enabling a very effective incorporation of oxygen in the lattice network of the growing oxide.

Capítulo 7

Resumen y discusión global de resultados

RESUMEN Y DISCUSIÓN GLOBAL DE RESULTADOS.

7.- Discusión Global.

En este epígrafe se resumen y discuten brevemente los resultados más importantes recogidos en cada capítulo de la tesis resaltando las conclusiones más relevantes obtenidas en cada uno de ellos, siguiendo el orden secuencial del esquema de tesis de la figura 1.28.

7.1 Nanoestructuración superficial usando aceleradores de partículas.

Este bloque consiste en el estudio detallado de las características físicas y químicas de las nanoestructuras formadas, obteniéndose un modelo que explica las microestructuras desarrolladas atendiendo a parámetros como la movilidad, afinidad química etc. En el grupo de investigación donde se ha desarrollado esta tesis se ha publicado un artículo relacionado con esta temática que no forma parte de esta tesis pero es relevante para entender el capítulo 2 de esta tesis. Dicho artículo se muestra en el apéndice I. Además, su resumen y discusión se muestra en el apéndice II.

Surface nanostructuring of TiO_2 Thin Films by High Energy Ion Irradiation.

Este estudio constituye una ampliación del trabajo expuesto en el apéndice II, tanto desde un punto de vista experimental, ya que se introducen técnicas de medida que amplían el conocimiento de cómo se incorpora el ion a la matriz, como del conocimiento de cuáles son los principios que rigen el crecimiento de las microestructuras singulares generadas mediante implantación iónica, proponiendo un modelo de formación de las mismas.

El punto principal que aborda este trabajo es el estudio del efecto de la temperatura durante la irradiación, aunque se tienen en cuenta otros parámetros como la afinidad del ion de implantación con la matriz, ángulo de incidencia y dosis. A continuación se expone un resumen del trabajo realizado:

Microscopía (FESEM)

Mediante la microscopía FESEM se observaron los diferentes regímenes de nanoestructuración posibles dependiendo de parámetros experimentales, tales como son la temperatura durante la implantación o el tipo de ion a implantar.

La figura 2.2 muestra claramente cómo el cambio de la nanoestructura superficial depende de la temperatura.

Propiedades ópticas, estructurales y químicas relacionadas con la incorporación de N en la matriz.

En la figura 2.3 se muestra una mayor absorción en la zona del visible para las muestras implantadas a 400ºC frente a las muestras implantadas a temperatura ambiente. Esta absorción se debe tanto a la incorporación de nitrógeno en la red como a la reducción de titanio a especies Ti^{+3}. En la figura 2.3 se muestra una pérdida de cristalinidad de la fase Anatasa para la muestra a temperatura ambiente frente a la muestra sin implantar, efecto atribuido al daño recibido por la matriz. Por el contrario la muestra calentada a 400 ºC continuó siendo Anatasa, debido a que recristaliza la matriz a esa temperatura de trabajo. Por último, en la figura 2.3 se muestra mediante XPS, que la mayor cantidad de nitrógeno superficial implantado tiene una energía de enlace de 396.1 eV en todos los casos de implantación.

Imagen de la zona implantada mediante la micrografía HAADF-TEM y Perfil en profundidad del Nitrógeno y estado del mismo.

En las figuras 2.4 y 2.5 se muestra con mayor claridad mediante HAADF-TEM la diferencia entre la nanoestructuración en forma de "*Voids*" realizada a temperatura ambiente y la estructura de "*Nanorods*" desarrollada a 400 ºC. Por otro lado, en las figuras 2.4 y 2.5 se muestra mediante EELS cuál es el perfil en profundidad del nitrógeno en la zona implantada. También mediante EELS se pone de manifiesto que la muestra implantada a temperatura ambiente presenta nitrógeno molecular frente al nitrógeno en red que presenta la muestra a 400 ºC.

Los datos obtenidos mediante EELS podrían parecer contradictorios con los obtenidos mediante XPS para la muestra a temperatura ambiente, ya que la espectroscopia EELS muestra nitrógeno molecular, frente a nitrógeno incorporado en la red determinado

mediante XPS. Esta discrepancia se atribuye al carácter superficial de la técnica de XPS, que no detectaría ningún nitrógeno molecular de la superficie debido a su desorción.

Modelo de formación de la nanoestructura.

Como indica la figura 2.6, el modelo de formación de nanoestructuras en la zona de implantación se puede estructurar en tres fases. En la fase inicial del crecimiento de la nanoestructura la densidad de defectos puntuales aumenta debido a las colisiones binarias con los iones. En una segunda fase, la densidad de defectos aumenta hasta alcanzar una densidad crítica de vacantes puntuales generando pequeñas oquedades. La tercera fase depende de la movilidad de las vacantes. Por un lado, si la movilidad de las vacantes es baja, el desbastado superficial descubre las oquedades dando lugar a estructuras tipo "*sponge-like*" o "*voids*". Por otro lado, si la movilidad es alta, la acción combinada entre desbastado superficial y migración preferencial de vacantes en la dirección del haz descubren las oquedades formando los *nanorods*.

La formación de vacantes y su movilidad tiene como parámetro crítico la temperatura durante la implantación, pero viene corregida por el resto de parámetros experimentales. Por un lado, la dosis y el ángulo de incidencia modulan la densidad de vacantes, mientras que la afinidad química del ion con la matriz modula la formación de vacantes por ion implantado.

7.2 Control de las condiciones del plasma.

En la actualidad se están realizando innumerables esfuerzos para modificar el TiO_2 para mejorar sus propiedades de fotoactividad. Aunque se ha demostrado la actividad de las muestras N-TiO_2 en el visible, no se tiene un buen conocimiento de cuál es la cantidad necesaria de nitrógeno para inducir tal fotoactividad y ni tampoco el estado químico del nitrógeno, además de otras características a tener en cuenta como son estructura, microestructura, propiedades ópticas etc.

En la bibliografía se encuentran ejemplos de películas N-TiO_2 preparadas mediante magnetrón sputtering, evaporación, PECVD etc. Sin embargo, para el caso de crecimiento de películas N-TiO_2 mediante plasma, no está estudiado el papel que juega

el plasma en la incorporación de nitrógeno en las capas. Por ello, en este capítulo se ha estudiado la relación entre las características del plasma y la cantidad y estado químico del nitrógeno dentro de las muestras.

Entre los hechos más relevantes que se ha puesto de manifiesto en nuestro trabajo cabe señalar cómo la incorporación de N_2 y H_2, a un plasma de O_2, produce cambios en la descomposición del precursor, consiguiéndose además, incorporar nitrógeno en la película. En este capítulo se ha realizado un análisis crítico de las condiciones del plasma mediante espectroscopia óptica de emisión y sonda de Langmuir. En los casos que sean posibles se han correlacionado esos datos con el estado químico del nitrógeno dentro de la red medido mediante XPS.

Mediante sonda de Langmuir (tabla 3.1) se observa un aumento de la densidad de iones del plasma que contiene una mezcla de H_2 y N_2 frente a plasmas puros (sólo H_2 o N_2). Este aumento es atribuido a un incremento de la intensidad en la cola de la función de distribución de energía de los electrones, debido a la menor energía de ionización del H_2 frente al N_2. El aumento considerable de la densidad de iones es indicativo de un aumento de la reactividad del plasma, lo que produciría una mayor descomposición del precursor utilizado.

Por otro lado, mediante espectroscopia óptica de emisión se observa cómo la introducción de H_2, en un plasmas que contiene N_2, produce la formación de la especie intermedia NH*, además de observarse la serie de Balmer de emisión del Hidrógeno. Se muestran espectros de plasma cuya composición sea N_2/O_2 y $N_2/O_2/H_2$ en la figura 3.1. La especie NH* detectada en el plasma $N_2/O_2/H_2$ es más reactiva que otras especies observadas en los plasmas mixtos N_2/O_2, como es el caso de la especie N_2^+.

Esta variación de la reactividad del plasma se refleja en la incorporación de nitrógeno en las muestras de TiO_2. La figura 3.2 muestra espectros de XPS de las películas crecidas con plasmas N_2/O_2 y $H_2/N_2/O_2$. El espectro de la muestra crecida con un plasma de N_2/O_2 muestra la incorporación a la película de especies de nitrógeno con una energía de enlace de 400 eV. Sin embargo, la adición de H_2 al plasma produce una mayor incorporación de nitrógeno a la capa, además de un aumento considerable de la especie 396.1 eV frente a la de 400 eV. Ambos efectos deben se han relacionado con el aumento de especies reactivas en el plasma, así como un entorno más reductor durante el crecimiento.

7.3 Síntesis y propiedades de capas nanoestructuradas N-TiO_2.

Este capítulo se divide en dos partes. La primera de ellas corresponde al estudio teórico-experimental de muestras N-TiO_2 analizado su actividad bajo irradiación en el visible mediante el test de ángulo de contacto correlacionándolo con el estado químico del nitrógeno. La segunda de ellas, estudia la fotoactividad en el visible de las muestras N-TiO_2, discerniendo entre los conceptos de fotoactividad superficial y fotoactividad másica que involucra la conducción de la barrera de Schottky para propiciar la salida de foto-huecos a la superficie.

Band gap narrowing vs. formation of electronic states in the gap in N-TiO_2 thin films

En este artículo se intenta dilucidar cuál es la especie de nitrógeno activa en el visible. Para ello se han preparado de forma sistemática muestras N-TiO_2 mediante la técnica de deposición PECVD. Los parámetros experimentales que se variaron para incorporar nitrógeno en la red fueron principalmente la composición del plasma, realizando mezclas de nitrógeno y oxígeno, así como la composición del precursor de titanio, usándose los precursores TTIP sin nitrógeno en su estructura y los precursores TDMAT y TDEAT, los cuales tienen el enlace Ti-N.

Previo a la caracterización de las muestras, mediante OES se estudió las especies existentes en los plasmas mezclas de N_2 y O_2 (Figura 4.S1.a). Se observó la existencia de especies de nitrógeno fuera del equilibrio termodinámico como son N_2^* y N_2^+. Dichas especies incrementan su emisión conforme aumenta la relación N_2/O_2 en el gas del precursor.

En este trabajo se han puesto también de manifiesto otras cuestiones básicas en relación con la fotoactividad de muestras N-TiO_2.

Influencia del precursor utilizado.

Para analizar la influencia del precursor, se estudia el crecimiento de las muestras en un plasma puro de oxígeno utilizando los diferentes precursores (fig 4.1). Para el caso de capas preparadas a temperatura ambiente se obtuvo una relación de N/Ti en las nanoestructuras de 0.037, 0.017 y 0.0 para los precursores TDEAT, TDMAT y TTIP respectivamente (figura 4.S2). Para el caso del TTIP no se observa nitrógeno

incorporado a la red del TiO_2, seguramente debido a que no contiene nitrógeno en su estructura. Para las muestras crecidas usando los precursores TDEAT y TDMAT se observó mediante XPS que se desarrolla un pico a 400 eV que se ha asociado a especies Ti-NO y Ti-ON.

Influencia de la composición del plasma

En este trabajo se aumentó gradualmente la cantidad de nitrógeno en el plasma, estudiándose la absorción de las muestras obtenidas mediante Elipsometría y espectroscopia de absorción ultravioleta visible. En paralelo se analizó la cantidad y estado químico del nitrógeno mediante XPS, obteniendo los resultados que muestran las figuras 4.2-7.

En la figura 4.4 se observa qué para plasmas con una proporción de nitrógeno mayor al 90%, la cantidad de nitrógeno en la capa crece exponencialmente. En la figura 4.2 se observa que para muestras con un contenido inferior al 85 % las muestras presentan un nitrógeno en estado químico asociado al pico de energía de enlace 400 eV, frente a las muestras con un porcentaje mayor del 90 % que presentan nitrógeno en un estado químico asociado mayoritariamente al pico de 396.1 eV. Esta deferencia claramente muestra que la composición del plasma determina las características químicas del nitrógeno incorporado. Con una cantidad de nitrógeno relativamente baja se obtienen especies del tipo Ti-NO y Ti-ON observadas alrededor de 400eV. Por el contrario, con cantidades elevadas de nitrógeno se obtienen especies tipo Ti-N (banda a 396.1 eV).

Por otro lado, en la figura 4.6 se observa cómo el umbral de absorción medido mediante espectroscopia UV-Visible disminuye a medida que aumenta la relación N/Ti en la capa. Concretamente para muestras con un contenido de 90% N_2 en el plasma se observa una disminución drástica del umbral de absorción de energía que corre paralelo con un aumenta del contenido de nitrógeno en el plasma. Este resultado contrasta con la disminución paulatina para las muestras cuyo plasma contiene menor cantidad de N_2.

Para obtener el coeficiente de extinción de las muestras se utiliza la técnica espectroscópica elipsometría. En la figura 4.7 se ilustran los coeficientes de extinción de las muestras preparadas con 0 %, 85 % y 97 % de N_2 en el plasma. Para este último caso se observa un fuerte desplazamiento del "*gap*" de absorción hacia mayores longitudes de onda. En el caso de la muestra que contiene 85 % de N_2 en el plasma sólo se observa

un ligero desplazamiento hacia el visible que se describe cómo la superposición de un oscilador armónico centrado en 375 nm.

Además del estudio de las muestras N-TiO_2 crecidas mediante PECVD, se realizaron cálculos Ab-initio incorporando en la red del TiO_2 las especies de nitrógeno Ti-N, Ti-NO y Ti-ON a diferentes concentraciones. Los cálculos realizados han permitido obtener las curvas de densidad de estados que muestra la figura 4.9. En ella se observa cómo la introducción de la especie Ti-NO y Ti-ON en el TiO_2 introducen estados electrónicos discretos en el gap, frente al caso de la especie Ti-N, cuyos estados están cerca de la banda de valencia, contribuyendo a desplazar esta y produciendo la disminución de la anchura de la banda prohibida del semiconductor.

Por último, como se muestra en la figura 4.11 mediante el estudio de la evolución del ángulo de contacto bajo irradiación visible, se observa que las muestras que contienen las especies Ti-NO o Ti-ON son fotoactivas en el visible frente a las muestras que contienen la especie Ti-N que no son fotoactivas en el visible bajo este test. Este resultado se considera especial ya que altera la visión expresada en numerosos trabajos previos sobre el tema.

Chemical State of Nitrogen and Visible Surface and Schottky Barrier Driven Photoactivities of N-Doped TiO_2 Thin Films.

En esta parte del capítulo se ahonda más en el estudio del conocimiento de la fotoactividad en el visible de las muestras N-TiO_2 realizando un estudio comparativo entre dos ensayos de medida de la fotoactividad, para discernir cuáles son los requisitos para que una muestra sea fotoactiva en el visible. Por un lado, se realiza el estudio de la evolución del ángulo de contacto bajo irradiación en el visible. Estos experimentos reflejaran que las mismas presentan un marcado carácter superficial. Por otro lado, se realizó el ensayo de fotodegradación de colorantes, que ponen de manifiesto cómo la fotoactividad depende de cómo esté formado el “bulk” del semiconductor.

Las muestras utilizadas para este estudio se relacionan en la tabla 4.2.

Las características de estas muestras son las siguientes:

Microestructura (FESEM)

Las muestras crecidas mediante PECVD y PVD en los casos estudiados muestran una microestructura tipo columnar, exceptuando los casos de muestras preparadas bajo condiciones ECR o temperatura ambiente, cuya microestructura es homogénea debido al aumento de la temperatura electrónica del plasma y, como consecuencia de esto, del bombardeo sufrido por la película durante el crecimiento. Cabe mencionar que la película (F), la única preparada utilizando métodos de PVD, fue realizada en configuración rasante, por lo que las columnas crecidas no son perpendiculares al sustrato, consiguiéndose un aumento de la porosidad de las muestras.

Estructura (Espectroscopia Raman y XRD)

Las figuras 4.13 y 4.14 muestran los espectros Raman y diagramas de difracción de las muestras estudiadas en este capítulo.

Mediante XRD se observa que la muestra preparada a temperatura ambiente es amorfa. Sin embargo, las muestras preparadas a 250ºC presentan estructuras anatasa o amorfa dependiendo del protocolo utilizado. Las muestras A, B y REF muestran una estructura anatasa, ya que son condiciones parecidas o iguales al crecimiento de una capa de anatasa típica, utilizando un plasma de oxígeno puro. Sin embargo, seguramente debido al bombardeo sufrido por las muestras D y E, estas no muestran estructura anatasa mediante XRD. Por otro lado, en la muestra F se observa una mezcla de fases anatasa y rutilo.

Mediante espectroscopia Raman se pone de manifiesto que todas las muestras tienen la misma estructuras exceptuando la muestra D que presenta estructura anatasa. Esta controversia entre XRD y Raman para la muestra D se atribuye al carácter más local de la espectroscopia Raman, que podría medir una cristalinidad incipiente sin que esta se detecte mediante XRD.

Absorción en el visible (UV-Visible)

La figura 4.15 muestra los espectros UV-Visible de las muestras comparadas respecto al de referencia.

Las muestras que presenta absorción en la zona de la banda prohibida del semiconductor son la B, D, E y F. Adicionalmente a esta absorción que se atribuye al nitrógeno incorporado en la red, se observa que la muestra E tiene un aumento de la absorción a longitudes de onda mayores. Esta absorción se relaciona con la formación de Ti^{+3} dentro de la muestra. Como consecuencia de ello esta muestra presenta una cierta conductividad eléctrica, que apoya este tipo de argumento.

Estado químico del nitrógeno (XPS).

La figura 4.16 muestra los espectros de XPS de las muestras A-F. Se observan dos picos principales. El primero, cuya energía de enlace es de ~396.1 eV, se asocia a la especie Ti-N y el segundo, cuya energía de enlace es de ~400.0 eV se asocia a Ti-NO o Ti-ON. La principal diferencia experimental entre las muestras que desarrollan la banda Ti-NO y/o Ti-ON y Ti-N es el carácter oxidante o reductor del plasma/atmósfera para las muestras preparadas mediante PECVD/PVD. Se observa que para ambientes más oxidantes, la banda tiene una energía de enlace de ~400.0 eV. Sin embargo en ambientes más reductores se observa claramente el pico a 396.1 eV.

Fotoactividad (fotocatálisis y ángulo de contacto).

Las figuras 4.17 y 4.18 muestran la fotoactividad de las muestras N-TiO_2. En la figura 4.17 se observa la evolución del ángulo de contacto para la muestra irradiada. En la figura 4.18 se observa la evolución de la actividad fotocatalítica.

La principal discrepancia entre ambos ensayos se manifiesta en que las muestras A, B, C, F muestran fotoactividad con luz visible si se analizan con el ensayo de la medida de ángulo de contacto. Sin embargo, utilizando el ensayo de fotodegradación de colorantes, solamente la muestra F presenta fotoactividad en el visible.

En este trabajo se plantea cómo entender la controversia entre los datos de fotoactividad en el visible obtenidos para las diferentes muestras. Esta controversia se trata de relacionar en términos de fotoactividad superficial o másica que involucra la formación de una barrera de Schottky en las capas superficiales. Por un lado, las muestras A, B, C y F presentan fotoactividad superficial, cuya característica común es que todas las muestras presentan un estado químico del nitrógeno de 400.0 eV medido mediante XPS. Por otro lado, sólo la muestra F presenta actividad másica que requerirían formación de una barrera de Schottky como vector que permite la salida del

foto-hueco a la superficie. La muestra F presenta una estructura cristalina mezcla de las fases Anatasa y Rutilo. Esta fotoactividad másica en el visible se relaciona a que la heterounión de fases puede contribuir a la migración de los fotohuecos desde el interior hasta la superficie. Este punto se discute con más detalle en el capítulo 5. Sin embrago, en las muestras A, B y C aunque se pudiese generar el par electrón/hueco, parece que su recombinación antes de salir a la superficie es importante, haciendo que estas muestras no presenten actividad foto-catalítica con luz visible.

7.4. El problema de la intercara anatasa-rutilo.

Este capítulo intenta contribuir al conocimiento de las causas por las que muestras de óxido de Titanio, con mezclas rutilo-anatasa, presentan una mayor fotoactividad que la muestras con fases puras.

Esta mejora en la actividad fotocatalítica para las muestras de TiO_2 anatasa-rutilo es bien conocida debido a que la muestra comercial más utilizada, P-25 de Degussa, presenta dicha mezcla de fases. Diferentes sistemas basados en mezcla de estas fases de TiO_2, han mostrado también dicho aumento de fotoactividad. En este contexto se ha acuñado el término *Hot-Spot* para explicar dicho aumento de fotoactividad, refiriéndose a sitios de la superficie en contacto con el medio donde coinciden las fases anatasa y rutilo.

Para entender este aumento de la fotoactividad, se prepararon una serie de bicapas de TiO_2 compuestas por una capa de anatasa expuesta a la disolución y otra más interna de rutilo directamente depositada sobre el sustrato, tal y como muestra la figura 1.19. El estudio realizado consistió en variar el espesor de la capa de Anatasa y ver cómo variaba la fotoactividad de las muestras. Con este sistema se consiguen fotoactividades mayores que para capas de anatasa equivalentes, observándose un máximo para un espesor aproximado de 130 nm (figura 5.4). Este hecho se trata de explicar suponiendo que la bicapa produce una mejora en la conducción del fotohueco hacia la superficie del fotocatalizador, debido a una modificación de la barrera de Schottky por la heterounión. Esta modificación se refleja en un incremento de la altura de la barrera de potencial en el sistema anatasa-rutilo, mejorando el transporte de fotohuecos tal y como muestra en el modelo de la figura 7.1.

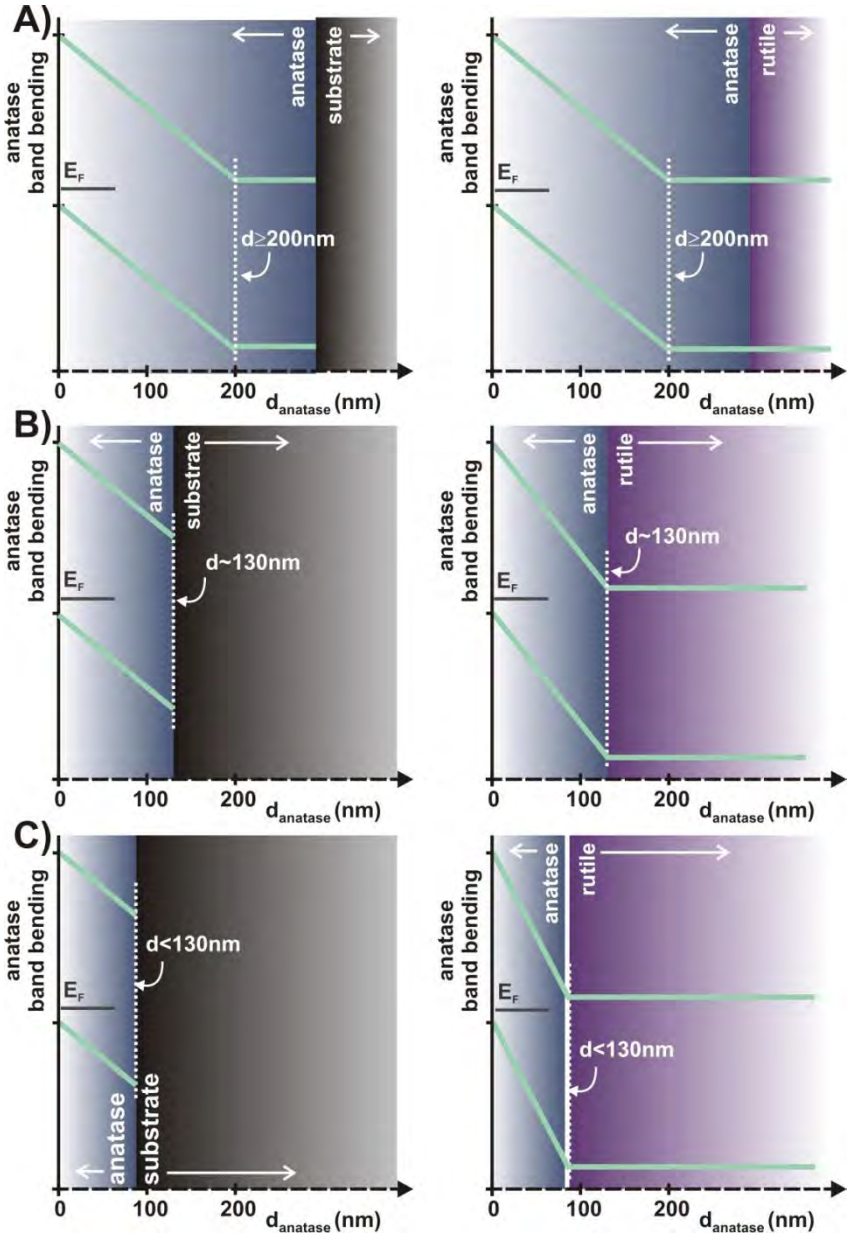

Figura 7.1. Esquema representativo de los sistemas Anatasa y Rutilo para diferentes espesores de la capa Anatasa. A) $d_{Anatasa} > 130$ nm; B) $d_{Anatasa}=d_{max\text{-}fotoactividad}$ y C) $d_{Anatasa} < 130$ nm. Izquierda) capa de anatasa depositada directamente sobre un sustrato aislante. Derecha) capa de anatasa depositada directamente sobre un sustrato de rutilo. Por simplicidad las diferencias entre "*band gap*" y función de trabajo entre anatasa y rutilo no son consideradas. La contribución del rutilo a la fotoactividad de los sistemas se asume despreciable y las bandas se representan por líneas rectas.

Para espesores menores de 130 nm de una capa de anatasa simple, aún no se ha terminado de formar la barrera de Schottky para la Anatasa, lo que va en detrimento de la fotoactividad. En el caso de la bicapa anatasa-rutilo y espesores comprendidos entre 130 nm y 200 nm la pendiente de la barrera de Schottky sería mucho más elevada favoreciéndose la migración de fotohuecos hacia la superficie, exaltándose así la

fotoactividad catalítica del sistema. Para espesores mayores de 200 nm, la exaltación de la fotoactividad se elimina debido a que la interfase se encuentra muy profunda y el sistema se comporta como una capa gruesa de anatasa.

En comparación con los resultados obtenidos para el sistema Rutilo-Anatasa, se ha estudiado la fotoactividad de capas simples de anatasa. Para espesores menores de 200 nm las muestras presentan siempre una menor fotoactividad que el sistema Anatasa-Rutilo.

De forma paralela al estudio de la actividad fotocatalítica, para entender mejor los procesos involucrados, se estudió la evolución del ángulo de mojado bajo irradiación UV para los distintos sistemas preparados. Este tipo de proceso no se ven afectados por ningún incremento significativo de la fotoactividad lo que se relaciona con el marcado carácter superficial del proceso, que no se vería afectado por efectos atribuibles a la formación de la barrera de Schottky.

7.5 Síntesis y propiedades de capas nanoestructuradas de ZnO

El ZnO es un semiconductor de banda ancha (3.37 eV). Una propiedad característica del ZnO es la fotoluminiscencia caracterizada por dos bandas de emisión. La primera banda se manifiesta en la zona del ultravioleta y se asocia con el excitón del material. La segunda banda se manifiesta en el rango del visible y se asocia a la recombinación de transiciones que involucran defectos de la red.

La motivación de este trabajo es la síntesis y control de las propiedades estructurales y de fotoluminiscencia de películas delgadas columnares de ZnO mediante el uso de la técnica de crecimiento PECVD. Los usos potenciales de estas nanoestructuras de ZnO pueden ser diodos electroluminiscentes, láseres de ultravioleta o sensores ópticos de gases.

Las características generales de las muestras de ZnO crecidas mediante la técnica de deposición PECVD son que las muestras no dispersan la luz en el rango del visible, presentan una microestructura columnar y una alta orientación de su estructura cristalina. Sin embargo, la forma de las columnas, el tamaño de grano y la

fotoluminiscencia de las muestras pueden ser controladas dependiendo de parámetros experimentales, como la temperatura, espesor de la muestra y composición del plasma.

El efecto de la temperatura se ilustra en las figuras 6.1 y 6.2. Se observa que, a medida que aumenta la temperatura, aumenta el tamaño de los motivos de la película observado mediante SEM, además de aumentar el tamaño de dominio cristalino. Por otro lado, en el espectro de fotoluminiscencia se observa un incremento en la emisión asociada al excitón a medida que aumenta la temperatura, así como una disminución de la banda asociada a defectos de oxígeno. Este aumento de la intensidad de emisión del excitón y disminución en la emisión del pico del visible se relaciona con el aumento del tamaño de dominio cristalino de la película y la disminución de la concentración de defectos.

El segundo parámetro es el efecto de espesor de la película cuyo efecto se ejemplifica en la figuras 6.4. Por un lado, a medida que aumenta el espesor de la película, disminuye el estrés de la misma. Ello se pone de manifiesto en el pico de difracción de rayos X, asociado al eje c de la wurtzita que se desplaza a mayores ángulos, acercándose al pico de difracción de una muestra de ZnO en polvo. Además, el ancho de columna y la rugosidad superficial aumentan con el espesor, tal y como se muestra en la figura 6.5. Por otro lado, en la figura 6.4 se pone de manifiesto una disminución en la emisión de fotoluminiscencia tanto del pico de emisión asociado al excitón como del pico de emisión asociado a los defectos. Esta disminución se atribuye a dos factores. Por un lado, la disminución del estrés hace que las muestras crezcan con cristales mejor formados, por lo que disminuyen los defectos de red asociados a oxígeno. Además, debido a la configuración en "*Font Face*" utilizada para la medida, al aumentar la componente dispersiva de las muestras hace que disminuya la intensidad medida de los picos de emisión de fotoluminiscencia

El tercer parámetro es la composición del plasma cuyo efecto se ilustra en las figuras 6.7 y 6.8. Se observa que el tamaño de los motivos de la nanoestructura depende del plasma utilizado. La adición de Hidrógeno o Argón al plasma produce una disminución del tamaño de los motivos frente al de las muestras crecidas con plasmas de oxígeno puro o mezcla nitrógeno y oxígeno. Se observan también un aumento/disminución del tamaño cristalino de partícula conforme aumenta/disminuye el tamaño del motivo de la nanoestructura. En paralelo, se observa un aumento de la intensidad del excitón cuando se incorpora H_2 en el plasma, así como una disminución de dicha emisión, cuando se

incorpora Ar al plasma. La disminución de la emisión de excitón con la adición de Ar en el plasma se puede relacionar con una disminución del tamaño de grano de la nanoestructura. Sin embargo, la adición de Hidrógeno del plasma produce un aumento de la emisión del excitón, que no se corresponde con los datos de difracción de rayos X, debido a que disminuye el tamaño de grano. Estas tendencias pueden ser explicadas atendiendo a que la incorporación de hidrógeno en el plasma produce especies reactivas OH^* o similares que pueden ser incorporadas en la película, pasivando los centros de recombinación de su superficie.

Capítulo 8

Conclusiones generales

CONCLUSIONES GENERALES.

Este capítulo presenta las principales conclusiones de la investigación realizada para la elaboración de esta tesis doctoral

1- Se ha elaborado una metodología para crecer nanoestructuras de óxido de titanio modificadas con nitrógeno mediante la técnica de deposición química desde fase vapor asistida por plasma de microondas. En general, las muestras presentan buena adhesión al sustrato para las experiencias realizadas y diferentes absorciones de luz en el rango del visible.

2- Se ha comprobado que dependiendo del plasma utilizado y/o composición del precursor utilizado, se puede controlar cantidad y estado químico del nitrógeno incorporado en la estructura del material.

3- Se ha conseguido crecer muestras N-TiO_2 que mediante XPS presentan un pico de nitrógeno a 400.0 eV. Estas muestras presentan fotoactividad superficial bajo irradiación visible frente a las muestras que presentan un pico de nitrógeno en 396.1 eV que no presentan dicha fotoactividad.

4- Las muestras N-TiO_2 que presentan fotoactividad catalítica en el visible presentan un pico de fotoemisión a 400 eV y una estructura cristalina mezcla de las fases anatasa-rutilo. La interfase anatasa-rutilo actúa como separador del par e^-/h^+ mejorando el transporte de los portadores de carga.

5- El pico de fotoemisión que aparece a 400.0 eV puede ser convolución de dos componentes, que se asocian a especies del tipo Ti-NO y Ti-ON. El pico que aparece a 396.1 eV se asocia a especies Ti-N.

6- Mediante cálculos "*ab-initio*" se ha calculado la densidad de estados electrónicos que se obtiene cuando se modifica la red del TiO_2 con nitrógeno. Las especies Ti-N producen un desplazamiento del gap hacia el visible, mientras que las especies Ti- NO y Ti- ON introducen estados localizados dentro del gap de energía.

7- Mediante elipsometría se puede obtener experimentalmente que las muestras que presentan especies Ti-NO o Ti-ON muestran estados localizados dentro del gap de energía, cerca de la banda de valencia. Para las muestras que tienen especies Ti-N se observa una disminución del gap de energía.

8- Se ha demostrado que existe un aumento de la actividad fotocatalítica en el UV para sistemas formados por una bicapa rutilo-anatasa, obteniéndose un máximo para espesores de la capa exterior de anatasa de 130 nm aproximadamente. Este aumento de la fotoactividad se atribuye a un aumento de la pendiente de la barrera de Schottky en esta bicapas. Sin embargo, la fotoactividad determinada por la variación del ángulo de contacto frente a la irradiación no se ve afectada por el espesor de la capa de anatasa. Esta falta de dependencia se asocia al carácter superficial del test utilizado.

9- Se ha elaborado una metodología para producir nanoestructuras de TiO_2 mediante la modificación de este óxido con aniones utilizando aceleradores de partículas. Las nanoestructuras obtenidas son del tipo *voids*, *sponge-like* o *nanorods*.

10- Las nanoestructuras obtenidas mediante implantación iónica se pueden explicar mediante un modelo de acumulación y movilidad de defectos introducidos en el material durante la implantación.

11- Las nanoestructuras tipo *nanorods* obtenidas mediante implantación iónica no han sido reportada en la bibliografía para ningún material implantado. Dicha nanoestrctura se consigue debido a la alta movilidad estructural del material durante la implantación.

12- Se ha elaborado una metodología para producir nanoestructuras de ZnO tipo columnar usando la técnica de deposición PECVD. En general, las muestras presentan una baja dispersión de la luz en el visible, una alta orientación cristalina y una microestructura columnar perpendicular al sustrato.

13- Se ha podido controlar el tipo de emisión de fotoluminiscencia de capas delgadas de ZnO preparadas mediante PECVD modificando las características estructurales y microestructurales de las mismas. En concreto ha sido posible preparar capas con emisión mayoritaria en el UV o en la zona visible del espectro.

Apéndices

APÉNDICE I.

Scripta Materialia 60 (**2009**) 574–577

Surface Nanostructuring of TiO_2 Thin Films by Ion Beam Irradiation

P. Romero-Gomez(a, A. Palmero(a,1, F. Yubero(a, M. Vinnichenko(b, A. Kolitsch(b, A.R. Gonzalez-Elipe(a

a) Instituto de Ciencia de Materiales de Sevilla (CSIC-Universidad de Sevilla). c/ Americo Vespucio 49, 41092 Sevilla (Spain)

b) Institute of Ion Beam Physics and Materials Research. Forschungszentrum Dresden-Rossendorf, POB 510119, 01314 Dresden (Germany).

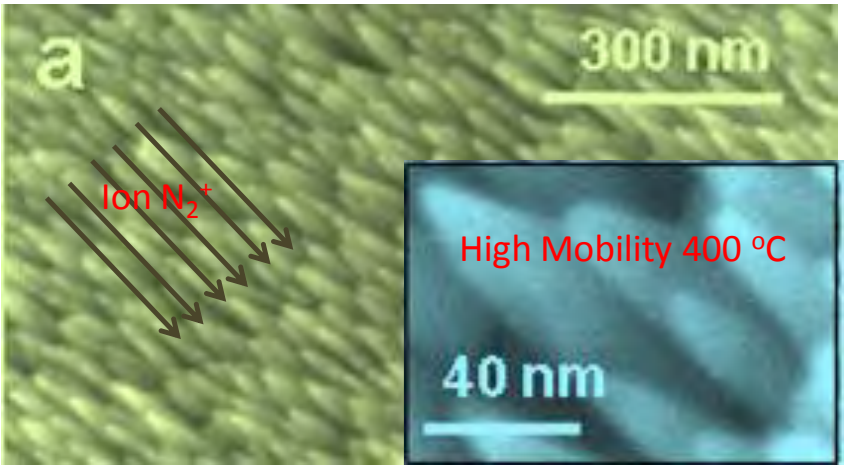

Title: Surface Nanostructuring of TiO_2 Thin Films by Ion Beam Irradiation.

Authors: **P. Romero-Gomez**, A. Palmero, F. Yubero, M. Vinnichenko, A. Kolitsch, A.R. Gonzalez-Elipe

Source: Scripta Materialia 60 (2009) 574–577

Surface Nanostructuring of TiO_2 Thin Films by Ion Beam Irradiation

P. Romero-Gomez[a], A. Palmero[a,1], F. Yubero[a], M. Vinnichenko[b], A. Kolitsch[b], A.R. Gonzalez-Elipe[a]

[a] *Instituto de Ciencia de Materiales de Sevilla (CSIC-Universidad de Sevilla). c/ Americo Vespucio 49, 41092 Sevilla (Spain)*

[b] *Institute of Ion Beam Physics and Materials Research. Forschungszentrum Dresden-Rossendorf, POB 510119, 01314 Dresden (Germany).*

Abstract.

This work reports a procedure to modify the surface nanostructure of TiO_2 anatase thin films through ion beam irradiation with energies in the keV range. The irradiation with N^+ ions leads to the formation of a layer with voids at a depth similar to the ion projected range. By setting the ion projected range few tens of nanometres below the surface of the film, well ordered nanorods appear aligned with the angle of incidence of the ion beam. Slightly different results were obtained by using heavier (S^+) and lighter (B^+) ions under similar conditions.

[1]Email: alberto.palmero@icmse.csic.es

Titanium dioxide (TiO_2) thin films possess outstanding properties that make them suitable for many technological applications. Their excellent optical transmittance, high refractive index, photoactivity, chemical stability, etc. have motivated the study of this material as well as the optimization of its properties and functionalities[1-2]. Within this context, surface nanostructuring of TiO_2 thin films turns out to be of great importance as the morphology of this material determines in a great extent many of its properties.

There are many examples of ion-beam-induced modifications of thin films in the literature[3]. For instance, Si and Ge thin films under He ion irradiation in the keV range develop microcavities in the material[4]. On the other hand, Ge, GaSb or InSb thin films show a so-called anomalous behaviour, i.e., they experience a clear swelling during the ion beam irradiation due to the formation of voids in the bulk[5-7]. These voids are formed as a result of the long-range migration of interstitial atoms and the movement of ion-induced point defects in the film[5]. Another remarkable effect has been reported for GaN thin films under ion beam irradiation. Here, an important stoichiometric imbalance takes place in the material due to the mass difference between ^{70}Ga and ^{14}N, producing Ga-rich and N-rich regions. Since many of these N atoms can not be easily incorporated into the network of the material, N_2 molecules are generated leading to the formation of nanometre-size bubbles embedded in the film[8-10]. Furthermore, there is evidence of migrating Ga interstitial atoms during the ion irradiation[11], thus suggesting a possible relation between the bubble formation mechanism and the ion beam induced movement of point defects. The mechanism for the bubble formation is still under research as there are cases of thin films containing randomly scattered N_2 molecules that do not come together and form a bubble. Formation of scattered N_2 molecules embedded in thin films subjected to low energy N^+ implantation has been reported for different materials, such as GaN[12], SiO_X[13] and Al_2O_3[14-15].

The behaviour of crystalline TiO_2 thin films under several tens keV ion beam irradiation has been extensively studied in the literature. It is known, for instance, that the TiO_2 network experiences an important depletion of oxygen due to the preferential sputtering[16-18]. To our knowledge, no indication of microcavities, anomalous swelling or bubble formation has been reported in the literature for TiO_2. The main aim of this letter

is to study the interaction of ions with energies in the order of several tens keV with a TiO_2 anatase thin film to develop a systematic method to modify its morphology and nanostructure. In the course of this investigation, it has been shown that this technique can be used as a novel approach for the surface nanostructuring of this material.

TiO_2 thin films with thicknesses between 300 and 500 nm were deposited at 523 K using the plasma enhanced chemical vapour deposition technique. The films, depicting the anatase structure, showed a high degree of crystallinity and a clear columnar microstructure perpendicular to the substrate. The details of the structure, microstructure and other characteristics of the material as well as the description of the deposition technique appear in ref.19. In figure A.1a-b, the cross-sectional and normal-view images of an as-deposited TiO_2 thin film obtained by scanning electron microscopy (SEM) are depicted. It consists of an arrangement of disordered grains agglomerated in the form of columns that extend from the substrate up to the surface. This microstructure will serve as a reference to compare with the results of the subsequent experiments. The ion irradiations were carried out at the Institute of Ion Beam Physics and Materials Research, Forschungszentrum Dresden-Rossendorf. The ion fluence was always set to $2.4\times10^{17}\ cm^{-2}$, whereas the ion penetration depth and the ion projected range (R_P) were calculated using the SRIM software[20]. In the cases where the irradiation was carried out at room temperature, the ion current was set low enough to keep the film temperature below 70º C (340 K).

The TiO_2 thin film was firstly irradiated using a 60 keV N^+ ion beam impinging the surface at 45° to the normal. These conditions imply an ion PD of around 200 nm and a R_p of around 100 nm. This means an average concentration of implanted nitrogen of $\sim10^{15}$ ions cm^{-2} nm^{-1} in the film and few tens of nanometres of material removed due to the sputtering. The normal and cross-sectional SEM image of the TiO_2 thin film after irradiation appears in figure A.2a-b In figure A.2b we have also depicted the calculated distribution of implanted ions in the film.

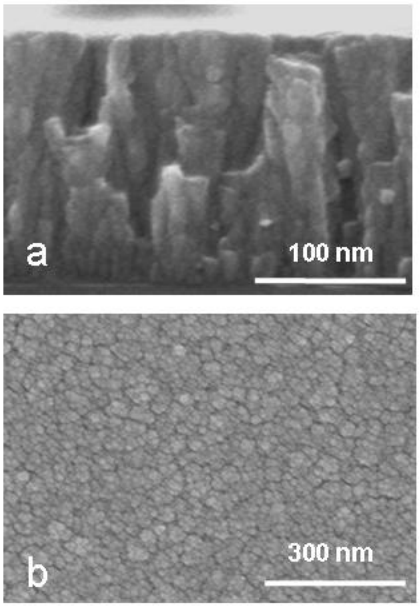

Figure A.1. Images of non-irradiated TiO_2 thin films obtained using SEM: a) non-irradiated sample, cross-sectional view, b) non-irradiated sample, normal view.

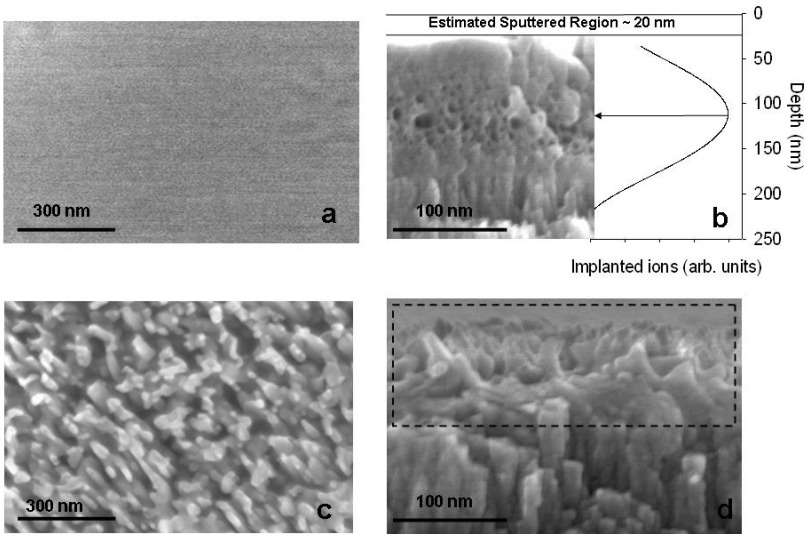

Figure A.2. Images of irradiated TiO_2 thin films with an angle of incidence of 45º and at room temperature obtained using SEM: a) N^+ ions with an energy of 60 keV, top-view, b) N^+ ions with an energy of 60 keV, cross-sectional view along with the calculated implantation profile, c) N^+ ions with an energy of 15 keV, normal view, and d) N^+ ions with an energy of 15 keV, cross-sectional view (the region of interest is framed). The substrate position is at the bottom of the cross-sectional images.

Figures A.2a-b evidence three important differences compared with figures A.1a-b: i) the columnar microstructure disappears in the implantation region, ii) the surface shows a very flat morphology, and iii) an intermediate layer containing spherical voids, with a diameter up to 10 nm, appears in the bulk of the material. The first feature can be understood by taking into account the ion-induced disorder in the material along the ion tracks, which also causes an important decrease of the crystallinity. This was corroborated by the loss of the X-ray diffraction (XRD) peaks observed for the original films (not shown). It is worth mentioning that the original columnar microstructure survives beneath the implanted region. The second feature indicates that the original pattern on the surface has been flattened: this phenomenon is well documented in the literature[21-22], where it has been explained by taking into consideration the competition among ballistic effects, surface diffusion and thermal spike-induced volume viscous flow. The third feature in figure A.2a-b, the appearance of a layer with nanometre-sized voids, is a remarkable phenomenon that, to our knowledge, is reported for the first time in the literature on TiO_2 thin films. Figure A.2a shows a clear relation between the appearance of voids and the ion projected range (R_P depth) in the material. Thus, it seems that the migration of ion-generated point defects (responsible for the mentioned anomalous swelling of Ge, GaSb or InSb thin films) and/or the formation of N_2 bubbles into the material might play an important role in the formation of these voids. This issue will be discussed later on.

Figures A.2a-b indicate that the microstructure of TiO_2 anatase thin films can be heavily modified through ion beam irradiation. Regarding the three abovementioned modifications produced by the N^+ ions, we propose a method to modify the film surface morphology: if the ion irradiation energy is set in such a way that R_P is close to the surface, apart from the well known processes responsible for the flattening of the surface (ballistic effects, surface diffusion and thermal spike-induced volume viscous flow), we will introduce a new competing mechanism (void formation) within the same spatial region. Thus, it is expected that this additional nanostructuring factor located in the top-most surface layers can affect the morphology of the film surface. This hypothesis is tested in the following experiments.

In figure A.2c we depict the top-view and cross-sectional SEM images of a film irradiated with N^+ ions with an energy of 15 keV and an angle of incidence of 45 degrees, keeping the film temperature below 340 K during the irradiation. These conditions imply an ion penetration depth of 100 nm, and a R_P of about 50 nm. Figure A.2c depicts a very different morphology to that in figure A.2a. In this case, a typical sponge-like disordered microstructure formed by nanometric elements that partially follow the direction of the ion beam is found. The cross-sectional SEM image (figure A.2d) shows that the typical columnar structure of the original film remains in the non-implanted part, whereas tilted and disordered nanorods are formed in the surface region. The Raman spectrum of this film is shown in figure A.3 along with the spectrum of a non-irradiated anatase TiO_2 material for the frequency range where the most intense TiO_2 anatase peak appears (i.e., 143 cm^{-1} corresponding to the E_g vibrational mode)[23]. This region is of particular interest because it provides important information about the structural changes of the material. The remaining part of the spectra is not shown as it provides redundant information about the anatase structure and has no relevance in this study. Comparing the two spectra in figure A.3, we find two important differences: i) the peak corresponding to the irradiated film is broader than that of the non-irradiated one, and ii) the peak associated to the irradiated film shows a small shift towards higher wavenumber. In general, the variations of Raman peak shape are usually caused by surface tension of grains, nonstoichiometry, disorder induced by minor phases, or phonon confinement effects with the grain size variation. However, for TiO_2 it was demonstrated that the changes observed in the Raman spectra were not related to any internal stress or grain size effects[23]. Thus, the redshift of the spectrum can only be linked to the increase of lattice parameter (loss of crystalinity), and the subsequent decrease of the phonon frequency, as well as to the presence of dangling bonds associated to the oxygen depletion[23]. This latter effect is expected due to the aforementioned preferential sputtering of oxygen atoms during irradiation, and agrees with the fact that the film becomes dark coloured and shows a high electrical conductivity, both features typical of partially reduced titanium oxide materials.

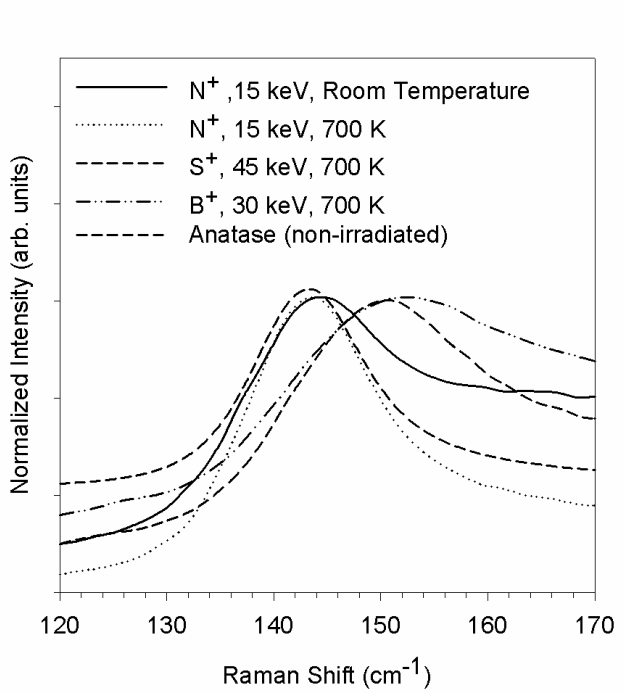

Figure A.3. Raman spectra of TiO_2 thin films under different irradiations.

In order to allow the film to recrystallize during the ion bombardment, we performed an experiment similar to the previous one, i.e. we irradiated with N^+ ions with an energy of 15 keV and an angle of incidence of 45º, but this time we set the film temperature to 700 K during the ion irradiation. These conditions ensure the recrystallization of the film into the anatase phase. The normal and cross-sectional SEM images depicted in figures A.4a-b correspond to this experiment. As in the previous case, the cross-section view depicts a typical columnar microstructure in the bottom part of the film. However, now the film termination consists of well ordered nanorods formed in the ion penetration depth region. Thus, in figure A.4a, presenting the normal-view in two scales, a regular pattern of nanorods with similar width ranging between 20 and 30 nm can be observed on the surface. The cross-sectional view (figure A.4b) shows that the nanorods have a length of approximately 100 nm and that they are quite well aligned along the ion beam direction. In figure A.3, the Raman spectrum of this film shows a sharper peak than that of the equivalent sample irradiated at room temperature, indicating a better crystallinity of the film[23], which is expected due to the higher film temperature during irradiation. This agrees with XRD measurements where the peaks of the anatase structure of titanium oxide could be detected (not shown).

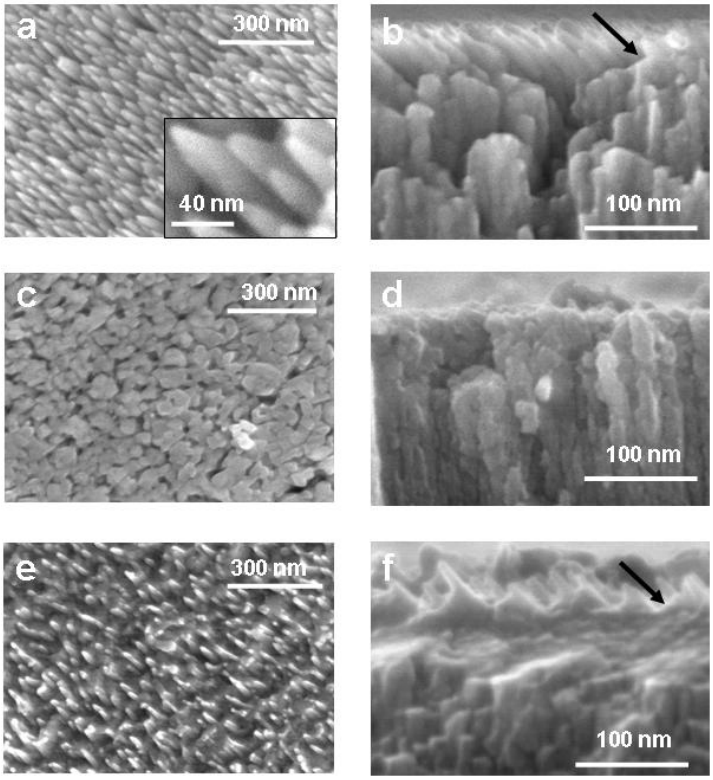

Figure A.4.- Images of irradiated TiO_2 thin films with an angle of incidence of 45º and at 700 K obtained using SEM: a) N^+ ions with an energy of 15 keV, normal view, b) N^+ ions with an energy of 15 keV, cross-sectional view, c) B^+ ions with an energy of 30 keV, normal view, d) B^+ ions with an energy of 30 keV, cross-sectional view, e) S^+ ions with an energy of 45 keV, normal view, f) S^+ ions with an energy of 45 keV, cross-sectional view. The black arrow indicates the angle of incidence of the ions. The substrate position is at the bottom of the cross-sectional images.

To know more about the proposed method for the modification of the surface topography, we performed another experiment using an ion with a similar atomic mass as nitrogen but that in no way can produce gas bubbles into the layer. Thus, we irradiated the TiO_2 thin film with a B^+ ion beam with an energy of 30 keV and an angle of incidence of 45º. The film temperature was kept equal to 700 K during the irradiation to allow recrystallization. Under these conditions, the ion penetration depth was 120 nm and R_P 60 nm, quite similar to the previous experiments with nitrogen. The normal-view SEM image of the irradiated film is depicted in figure A.4c, showing different features than in the previous cases. This time small cavities are formed on the surface of

the film, and no hint of nanorod formation is found. This becomes more evident in figure A.4d, where we depict the cross-sectional SEM image. Thus, this situation seems to represent an intermediate state where voids are formed on the surface of the material while other mechanisms are responsible for the flattening of the remaining surface regions. The Raman spectrum of this film also appears in figure A.3, and is characterized by a larger shift of the peak towards the right when compared with the non-irradiated spectrum. This points out that the reduction of the material due to the preferential sputtering of oxygen is much larger than that during nitrogen irradiation. The distinct chemical character of nitrogen and boron in the implanted state may also contribute to this difference: nitrogen is a very electronegative atom that tends to form nitride species when it is combined with metals, whereas boron may act as a cation when it is bonded to oxygen. Hence, different chemical structures are expected when they are implanted in TiO_2.

In a last experiment we employed a heavier ion, S^+, performing the irradiation with an angle of incidence of 45° and an energy of 45 keV, keeping the film temperature equal to 700 K. Thus, the ion penetration depth was about 50 nm, and R_P 30 nm. The normal-view SEM image of the film after irradiation with the S^+ ion is shown in figure A.4e, where we can find spaced structures similar to those in figure A.4a. The cross-sectional SEM view of the film (figure A.4f) shows that the surface is completely covered with nanorods aligned with the ion beam, although this time they are sharper and slightly less ordered than those formed by the nitrogen irradiation. Regarding the Raman spectrum (figure A.3), we find a clear shift of the peak towards the right as compared with the non-irradiated case. As we noted previously, this shift reveals a significant reduction of the oxide thin film[23].

This experiment with S^+ ions suggests that the formation of nanorods on the surface of the film, and thus the formation of voids during ion irradiation, is mainly associated to the migration of point defects during the irradiation and not to the formation of bubbles. This is supported by the fact that implanted S^+ cannot be released as a gas and must remain as defect ions within the TiO_2 structure. The different behaviour found with B^+ suggests that a certain threshold for the momentum and energy deposited on the TiO_2

and the different chemical character of the species are also important factors controlling the formation of nanorods. Our previous results, showing that ordered nanorods are only formed at 700 K also suggest that thermally activated diffusion is also important for these processes. Although this temperature is not very high for the mobilisation of stoichiometric TiO_2, it can be sufficient for the mobilisation of an oxygen depleted titanium oxide: the so called Magnelli phases (i.e., Titanium Oxides with a variable stoichiometry of the type TiO_x, x<2) are well known for their high mobility at not very high temperatures[24]. Similarly, for anatase films, a high mobility of Ti^{3+} species from the bulk to the surface has been directly observed using the scanning tunneling microscopy technique on partially reduced single crystals of this material heated in vacuum[25]. No further conclusion on the fundamental mechanisms responsible for the surface nanostructuring under ion irradiation can be achieved regarding our experiments, and more research, out of the scope of this letter, is required. However, from a phenomenological point of view, it seems that the parameters that determine the appearance of nanorods on the surface of the film are the ion penetration depth, the deposited amount of momentum and energy, the reduction of the network, and the thin film temperature during irradiation. Moreover, in the case of N^+ ion implantation we can not rule out the presence of N_2 bubbles in the material.

Summarizing, the previous results indicate that ion beam irradiation in the keV range can be employed to change the surface morphology of a TiO_2 thin film in a similar way as for the cellular structures reported for Ge, GaSb or InSb thin films[5] or other materials[26]. For TiO_2, the formation of well ordered nanorods as those shown in figures A.4a-b and Ae-f can be of the outmost importance for the improvement of the photocatalytic, photovoltaic or sensor[27] properties aimed for nanostructured TiO_2 thin films. Furthermore, the controlled formation of surface nanorods could be important for the improvement of the TiO_2 capabilities as electron collector or to enhance its sensitivity to gases.

Acknowledgements.- One of the authors (A. Palmero) acknowledges the I3P program of the Spanish Council of Research (CSIC). We thank the Spanish Ministry of Science and Education (project MAT2007-65764 and CONSOLIDER INGENIO 2010-CSD2008-

00023) and the European Union (project NATAMA 032583) for financial support. We also acknowledge the Institute of Ion Beam Physics and Materials Research at the Forschungszentrum Dresden-Rossendorf.

References

[1] O. Carp, C.L. Huisman, A. Reller, Prog. Sol. Stat. Chem. **32** (2004) 33

[2] A. Fujishima, T.N. Rao, D.A. Tryk, J. Photochem. Photobiol. C: Photochem Rev. **1** (2000) 1.

[3] A.R. Gonzalez-Elipe, F. Yubero and J.M. Sanz, Low Energy Ion Assisted Film Growth, Imperial College Press 2003.

[4] S.M. Myers, D.M: Follstaedt, G.A. Petersen, C.H. Seager, H.J. Stein, W.R. Wampler, Nucl. Inst. Meth. Phys. Res. B **106** (1995) 379

[5] N. Nitta, M. Taniwaki, Y. Hayashi, T. Yoshiiem J. Appl. Phys, **92(4)** (2002) 1799

[6] R. Callec, P.N. Favennec, M. Salvi, H.L'Haridon, M. Gauneau, Appl. Phys, Lett. **59(15)** 1991 1872.

[7] D. Kleitman and H.J. Yearian, Phys. Rev. **108** (1957) 901

[8] S.O. Kucheyev, J.S. Williams, C. Jagadish, J. Zhou, V.S. J. Craig, G. Li, Appl. Phys. Lett. **77(10)** (2000) 1455

[9] S.O. Kucheyev, J.S. Williams, J. Zhou, C. Jagadish, G. Li, Appl. Phys. Lett. **77(22)** (2000) 3577

[10] S.O, Kucheyev, J. E. Bradby, C.P. Li, S. Ruffell, T. van Buuren, T.E. Felter,

Appl. Phys. Lett. **91** (2007) 261905

[11] W. Jiang, Y. Zhang, W.J. Weber, J. Lian, R.C. Ewing, Appl. Phys. Lett. **89** (2006) 021903

[12] B.J. Ruck, A. Koo, U.D. Lanke, F. Budde, S. Granville, H.J. Trodahl, A. Bittar, J.B. Metson, V.J. Kennedy, A. Markwitz, Phys. Rev. B **70** (2004) 235202

[13] J.P. Holgado, A. Barranco, F. Yubero, J.P. Espinós, A.R. Gonzalez-Elipe, Nucl. Instr. and Meth. in Phys. Res. B **187** (2002) 465

[14] J.P. Holgado, F. Yubero, A. Cordon, F. Gracia, A.R. Gonzalez-Elipe, J. Avila, Solid State Comm. **128** (2003) 235

[15] J.P. Espinos, A.R. Gonzalez-Elipe, M. Mohai, I. Bertoti, Surf. Interf. Anal. **30** (2004) 90

[16] R. Asahi, T. Morikawa, T. Ohwaki, K. Aoki, Y. Taga, Science **293** (2001) 269

[17] M. Takeuchi, Y. Onozaki, Y. Matsumura, H. Uchida, T. Kuji, x Nucl. Instr. And Meth. in Phys. Res. B **206** (2003) 259 .

[18] N. Ishikawa, S. Yamamoto, Y. Chimi, Nucl. Instr. and Meth. in Phys. Res. B **250** (2006) 250

[19] A. Borras, C. Lopez, V. Rico, F. Gracia, A.R. Gonzalez-Elipe et al, J. Phys. Chem. C **111** (2007) 1801

[20] http://www.srim.org/

[21] S. Vauth, S.G. Mayr, Phys. Rev. B **77** (2008) 155406

[22] P. Mishra and D. Ghose, Nucl. Inst. Meth. Phys. Res. B 266 (2008) 1635

[23] J.C. Parker and R.W. Siegel, Appl. Phys. Lett. **57(9)** (1990) 943

[24] L. Liborio and N. Harrison, Phys. Rev. B 77(10) (2008) 104104

[25] M. Bowker, Phys. Chem. Chem. Phys. 9 (2007) 3514

[26] S.M. Allameh, N. Yao, W.O. Soboyejo, Scripta Mater. **50** (2004) 915

[27] S.E. Gledhill, B. Scott, B.A. Gregg, J. Mater. Res. **20** (2005) 3167.

APÉNDICE II. Resumen y discusión del artículo publicado en la revista Scripta Materialia 60 (**2009**) 574–577.

Surface Nanostructuring of TiO_2 Thin Films by Ion Beam Irradiation

En este artículo se estudia la nanoestructuración de materiales mediante aceleradores de partículas, un tema poco estudiado en la bibliografía sobre capas de óxido. Este trabajo de nanoestructuración se llevó a cabo mediante la implantación iónica, con energías en el orden de las decenas de KeV. Previamente a la implantación se calcularon los perfiles aproximados de implantación mediante la utilización del programa de cálculo computacional SRIM.

La nanoestructuración superficial desarrollada por el óxido de titanio mediante la implantación de iones en su superficie, tiene como parámetros fundamentales la dosis, el tipo de ion a implantar, el ángulo de incidencia del ión, así como, la temperatura del sustrato durante la implantación.

De todos estos parámetros, el más crítico es el efecto de la temperatura del sustrato durante la implantación superficial, ya que las muestras implantadas a temperaturas bajas, generan huecos ("*voids*") o estructuras tipo esponja ("*sponge-like*") (figura A.2), mientras que las muestras implantadas a 400ºC generan nanocolumnas ("nanorods") superficiales orientados con la dirección de haz de iones (figura A.4).

La formación de "*voids*" o nanoestructura tipo "*sponge-like"* se ha reportado en la bibliografía para otros materiales y su formación se explica debido a la acumulación de defectos y una posterior migración de los mismos. Sin embargo, la nanoestructura tipo "*nanorods"* no está reportada en la bibliografía para ningún tipo de material. Este tipo de nanoestructura en forma de "*nanorods"* orientados con el ángulo de incidencia del haz de iones se atribuye a una mayor acumulación de defectos de la red, junto con una mayor movilidad de esos defectos. Experimentalmente se observó también un aumento de la cantidad de defectos estructurales asociados a la reducción del óxido y/o defectos provocados por la incorporación del ion a la red. Esta reducción o formación de defectos en la red del óxido de titanio se observó mediante espectroscopia Raman

(figura A.3), mediante la observación de un desplazamiento del pico principal de la Anatasa a medida que aumenta con la cantidad de defectos en la red. La alta movilidad de la matriz es debida a que la temperatura utilizada durante la implantación es de 400 ºC. Al calentar la muestra a 400 ºC, se movilizan sus defectos. Además, la superficie del material formado por un subóxido de titanio (TiO_x), debido a los procesos de desbastado preferencial de oxígeno durante la implantación iónica, incrementa dicha movilidad.